VERY HIGH TEMPERATURE MEASUREMENTS:

APPLICATION TO NUCLEAR REACTOR SAFETY TESTS

A Dissertation

Presented in Partial Fulfillment of the Requirements for the

Degree of Doctorate of Philosophy

with a

Major in Nuclear Engineering

in the

College of Graduate Studies

University of Idaho

by

Clemente José Parga

March, 2014

Major Professor: Akira Tokuhiro, Ph.D.

Authorization to Submit Dissertation

This dissertation of Clemente José Parga, submitted for the degree of Doctor of Philosophy in Nuclear Engineering and titled "Very High Temperature Measurements: Application to Nuclear Reactor Safety Tests" has been reviewed in final form. Permission, as indicated by the signatures and dates given below, is now granted to submit final copies to the College of Graduate Studies for approval.

Major Professor: _____ Date:_____
Akira Tokuhiro

Committee Members: _____Date:_____
Christophe Journeau

_____ Date:_____
Mitchell Farmer

_____ Date:_____
Indrajit Charit

Mechanical Engineering: _____ Date:_____
Department Chair   John C. Crepeau

Dean of the College: _____ Date:_____
of Engineering   Larry Stauffer

Final Approval and Acceptance by the College of Graduate Studies:

Dean of the College:_____Date:_____
of Graduate Studies   Jie Chen

Abstract

This PhD research focuses on the improvement of very high temperature thermometry (1100ºC to 2480ºC), with special emphasis on the application to the field of nuclear reactor safety and severe accident research. Two main projects were undertaken to achieve this objective:

- The development, testing and transposition of high-temperature fixed point (HTFP) metal-carbon eutectic cells, from metrology laboratory precision (±0.001ºC) to applied research with a reasonable degradation of uncertainties (±3-5ºC).

- The corrosion study and metallurgical characterization of designed refractory alloys as prospect Type-C thermocouple (service temp. ≤ 2300ºC) sheath material to extend the survivability of TCs used for molten metallic/oxide corium thermometry (≤ 2000ºC).

Numerous metal-carbon eutectic systems [Fe-4.3wt.%C (1153°C), Co-2.6wt.%C (1324°C), Ti-0.4wt.%C (1646.5ºC), Ru-2.5wt.%C (1954°C), Mo-2.5wt.%C (2205°C), Nb-1.5wt.%C (2354ºC) and Re-1.3wt.%C (2480°C)] were studied to determine their feasibility as high temperature fixed points (HTFP). It was concluded that simpler eutectic systems (i.e. Co-C, Ru-C and Re-C) show better repeatability than complex systems (i.e. Mo-C and Nb-C), comprising multiple eutectics, intermediate phases and/or polymorphs. However, furnace and graphite cell thermal characteristics also have significant impact on the eutectic reproducibility. Nonetheless, this work allowed for the production of three refined metal-carbon HTFP cells (Co-C, Ru-C and Re-C), that are now available for on-site calibration of temperature sensors utilized in nuclear-grade experimental facilities, not suitable for calibration elsewhere.

The design and corrosion behavior analysis of various Re-W-Ta-(B) alloys [Re-10W-10Ta-(0.1B), Re-25W-35Ta-(0.1B), Re-40W-20Ta-(0.1B), Re-05W-52Ta-(0.1B)(mole %), "pure" tungsten and tantalum] in molten stainless steel (304L-SS) up to 2000ºC, was made to establish their viability as TC sheath material for corium in-melt thermometry. Among the materials tested, Re-10W-10Ta-

0.1B resists the SS corrosion up to1850ºC, representing a 150ºC improvement over the current tungsten sheath; its improved corrosion resistance is due to the formation of more thermally/chemically stable intermetallic compounds and the boron effect.

This PhD research allowed an improvement of the experimental capabilities for molten corium thermometry by facilitating thermometer calibration (Co-C, Ru-C and Re-C HTFP cells) along with the development of an alloy (Re-10W-10Ta-0.1B) with better corrosion resistance/thermal stability in molten oxide/metallic corium than commercial TC sheath material. Additionally, within the HiTeMS project, it contributes to the investigation of high-temperature metal-carbon eutectics, and their introduction as HTFP in the next International Temperature Scale (ITS).

Acknowledgements

I would like to thank my fiancée Cintia Gutiérrez-Peña for all her support throughout this 3.5-year research contract in CEA Cadarache, France. It would not have been possible without her. I greatly appreciate her decision to be part of this journey. I want to acknowledge my family for their continued support throughout my life and professional career. Thanks to the staff at STRI/LMA for their warm welcome and support during my internship in this wonderful lab; special thanks to José Monerris and Gérald Fritz. I acknowledge the staff at the University of Idaho, especially Alice Allen, because they made this long-distance degree possible. I would like to acknowledge my PhD committee for their willingness to be part of this venture: Dr. Farmer, Dr. Charit, and especially to Dr. Journeau and Dr. Tokuhiro for their guidance and support throughout my PhD degree. I am very thankful for the opportunity of being part of the European HiTeMS Joint Research project. Through this project I immersed myself and met such wonderful people in the field of metrology, among them I would like to mention Mohamed Sadli and Frédéric Bourson from LNE/Cnam, their support and involvement in this PhD research is greatly appreciated. Furthermore, I want to acknowledge the labor of Medhat Zebian, whom worked under my guidance during his 6- month internship at LMA. I am very happy to say I met wonderful people during my stay in France and abroad, some of them which I am proud to call friends. I thank them for sharing their culture and being part of my personal/professional development and adaptation process in France/Europe. I will mention a few, even though I would need several pages to credit them all. Special thanks to Vaclav Tyrpekl, Cyril Acien, Olomuyiwa Omotowa, Dmitry Grishchenko, Dmitriy Meshcheriakov, F. Boussard, L. Ferry, Dr. Piluso, Matthias Vanderhaegen, Maxim Guyot, Mathieu Sanchez-Brusset, Claude Brayer, Y. Bullado, L. Brissonneau, B. Tormos, Benoit Loeillet, N. Cassiaut-Louis, B. Valentin, Patricia & Johanna Correggio, J-M. Ruggieri, C. Suteau, J-F. Haquet, F. Compagnon, M. Valerian, Paris & Dente family, Julien Summo, Cynthia Joly-Flores, Olga Aresheva, Hector Sanchez, Vidia Carpio, Paul Caballero, Alberto Gonzalez, Cesar Peña, Diana Geoffriaud, Felipe Bedoya, Marcelo Chaug, Alejandro Pinto, César de Santiago and the people I might have forgot to include.

Table of Contents

List of Figures

List of Tables

List of Acronyms

ANL.- *Argonne National Laboratory.*

ATP.- *Absolute Thermoelectric Power.*

BCC.- *Body Centered Cubic.*

BDBA.- *Beyond-Design-Basis-Accidents.*

BSD.- *Backscatter Diffraction.*

BWR.- *Boiling Water Reactor.*

CEA.- *Commissariat à l'Energie Atomique et aux Energies Alternatives (French Atomic Energy and Alternative Energies Commission).*

CTE.- *Coefficient of Thermal Expansion.*

DBA.- *Design-Basis-Accidents.*

ECCS.- *Emergency Core Cooling System.*

EDM.- *Electric Discharge Machining.*

EDS.- *Energy Dispersive Spectroscopy.*

EIA.- *United States Energy Information Administration.*

EMF.- *Electromotive Force.*

EMPR.- *European Metrology Research Programme*.

EURAMET.- *European Association of National Metrology Institutes*.

FCI.- *Fuel-Coolant-Interaction.*

GHG.- *Green House Gases.*

HCP.- *Hexagonal Closed Packed.*

HiTeMS.- *High Temperature Metrology for industrial Applications.*

HPCI.- *High Pressure Coolant Injection.*

HV.- *Vickers Hardness.*

IC.- *Isolation Condenser*

INES.- *International Nuclear and Radiological Event Scale.*

INL.- *Idaho National Laboratory.*

ITS-90.- *International Temperature Scale of 1990.*

LMA.- *Laboratoire pour la Maitrise des Accidents Graves (Severe Accidents Mastery Laboratory).*

LNE-Cnam.- *Laboratoire National de métrologie et d'essais- Conservatoire national des arts et Métiers (French National Metrology and Tests Laboratory – National Arts and Trades Conservatory.*

LOCA.- *Losss-of-Coolant-Accident.*

LPCI.- *Low Pressure Coolant Injection.*

LWR.- *Light Water Reactor.*

M-C.- *Metal-Carbon.*

MCCI.- *Molten Corium Coolant Interaction.*

NEA.- *Nuclear Energy Agency.*

NPP.- *Nuclear Power Plant.*

OECD.- *Organization for Economic Cooperation and Development.*

OM.- *Optical Microscope.*

PCV.- *Primary Containment Vessel.*

PORV.- *Pilot Operated Relief Valve.*

RBMK.- *Reaktor Bolshoy Moshchnosti Kanalniy (High Power Channel-type Reactor).*

RCIC.- *Reactor Core Isolation Cooling.*

RHR.- *Residual Heat Removal.*

RIA.- *Reactivity Insertion Accident.*

RPV.- *Reactor Pressure Vessel.*

SA.- *Severe Accident.*

SAM.- *Severe Accident Management.*

SBO.- *Station Black-Out.*

SEM.- *Scanning Electron Microscope.*

SFP.- *Spent Fuel Pool.*

SI.- *Système International d'Unités (International Units System).*

SNL.- *Sandia National Laboratory.*

SPRT.- *Standard Platinum Resistance Thermometer.*

TC.- *Thermocouple.*

TMI-2.- *Three Miles Island Reactor #2.*

USA.- *United States of America.*

XRD.- *X-Ray Diffraction.*

Chapter 1. Introduction

1.1 Nuclear Energy in the World

Since our ancestors first roamed the earth, more than a hundred thousand years ago, the evolution of humankind has been strictly tied to energy; an excellent example is the discovery and mastering of fire, which can be considered as an unprecedented step on the evolution of humanity. Likewise in our contemporary era, energy, particularly in the form of electricity, is essential for an economic and social development, as well as a close linkage to a better quality of life. In figure 1 it can be observed how the evolution in the energy demand roughly after the industrial revolution is tied to technological development.
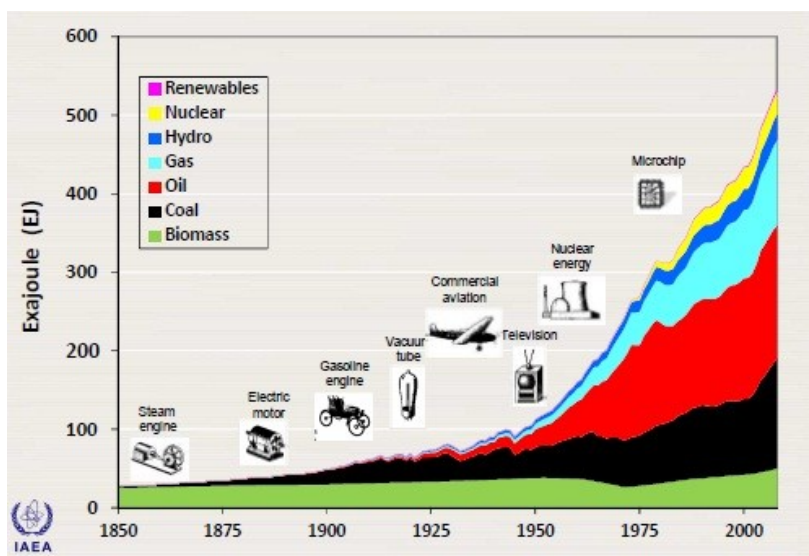
Figure 1.1. Historical energy supply by energy source from 1850-2008 (10^{18}Joules).

In 2002, the electricity consumption in the United States of America (USA) added up to 3,839 TWh (Terawatt-hour = 1×10^9 kilowatt-hour) which represented around one quarter of the worldwide consumption, or 40% of the consumption in OECD member countries (Organization for Economic Cooperation and Development): 70.4% of this generated from fossil fuels (coal, gas and petroleum), 20.3% from nuclear power, 6.6% came from hydroelectric, and the rest (2.7%) from other renewable sources like biomass, geothermal, wind, solar and ocean tide/wave. In 2006, the world electrical energy consumption was slightly over 16.25 PWh (16.25×10^{12} kilowatt-hour), of which 16%

(2.6PWh) of the demand was supplied by the nuclear power industry; this represents 23% of the electrical consumption in the OECD member countries. Furthermore, on December 31, 2011 the nuclear reactor fleet around the world added up to 435 nuclear power reactors, with a total electric power capacity of 369 GWe (Gigawatt-electric: 1×10^9 watts of electrical power). At the end of the year 2011, 65 reactors were under construction, of which at least 44 in Asia, where most of the expansion for the nuclear power industry is anticipated in the near and long term; for example, 35 out of the 45 most recent reactors that have been connected to the grid are mostly based in the Far East, especially in China and India. In contrast, during the second half of the 20th century most of the deployment of the nuclear reactor fleet was undertaken by several western countries, an exception is Japan and the Soviet Union. Nonetheless, on 2008, 57% of the nuclear power capacity was still shared among three countries: USA, France and Japan. Finally, the electricity generation from nuclear power around the world is expected to almost double by 2035, from 2.6 PWh in 2008 to 4.9PWh [1-5].

The nuclear power deployment was conceived after the first self-sustained nuclear chain reaction took place on December 2nd, 1942 in the graphite pile built at the Stagg Field Stadium of the University of Chicago; this program was led by Enrico Fermi as part of the ambitious Manhattan Project. Essentially, the device that made this possible was a gas-cooled graphite-moderated reactor, which was carefully designed and consisted of 40 tons of uranium metal and oxide lumps, which contained the fissile material (i.e. U^{235} isotope), distributed in a matrix of 385 tons of graphite bricks, where carbon served both as the neutron moderator and reflector material; while in operation, air was drawn into the hot core cavities, due to natural convection, and was enough to dissipate the heat generated by fission in the 2kW reactor [6].

The Nuclear Energy Agency (NEA) part of the OECD forecasts that electrical energy demand will increase by a factor of 2.5 by 2050, relative to the worldwide demand in year 2008 [1]. Moreover, according to the 2011 International Energy Outlook prepared by the U.S. Energy

Information Administration (EIA) the electricity generation will increase by 84 percent (or a factor of 1.84) to 35.2 PWh in 2035 from the reference value of 19.1 PWh in 2008 (19.1×10^{12} kilowatt-hour). Additionally, the total energy consumption, which includes energy not used to produce electricity: i.e. liquid fuels, natural gas and biomass used for transportation and heating purposes, is expected to grow by 53 percent relative to the 2008 demand (148 PWh) [4]; this means that approximately 13 percent of the total consumption based on year 2008 comes from electrical power generation. There is a consensus that the energy demand prospect is driven by the vigorous long-term economic growth in many emerging countries, i.e. Brazil, China and India. A summary of the perspectives on the electricity demand growth are shown in figure 2 on a per-capita basis and as a function of country(ies)/region; and in figure 3 the world energy demand increment is presented by fuel type.
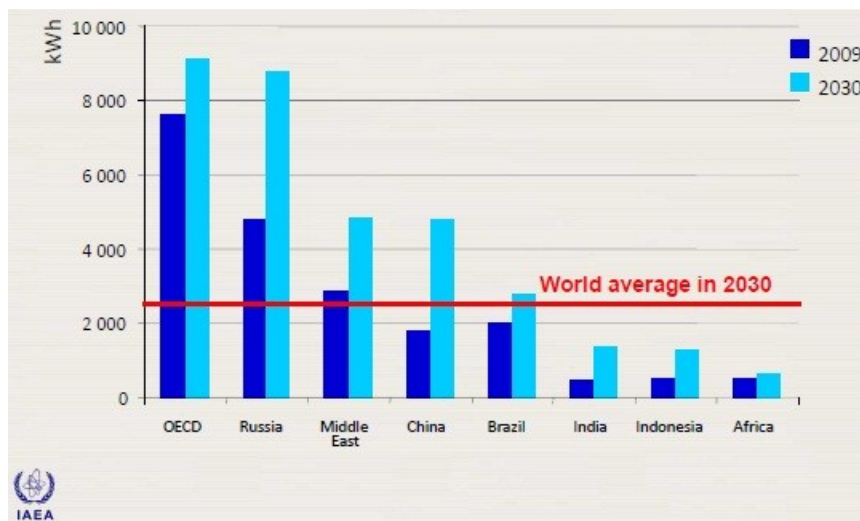
Figure 1.2. Per-capita energy demand perspectives in OECD and non-OECD countries.
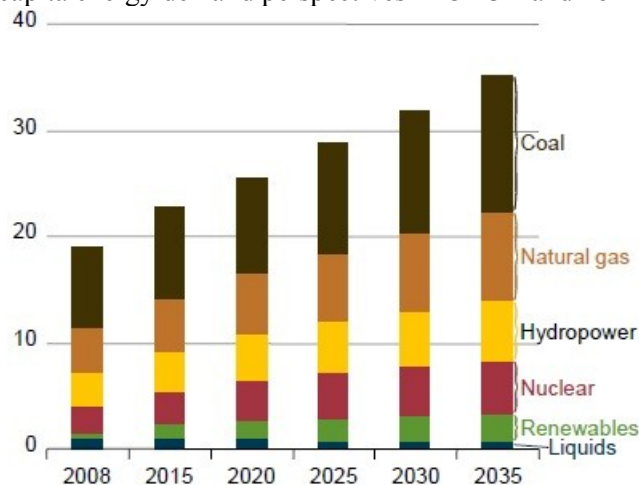
Figure 1.3. Anticipated world net electricity generation by fuel type: 2008-2035 (10^{15}watts) [4]

In this modern era we are confronted with a big dilemma: In what manner can we fulfill the current and expected worldwide energy demands in an environmentally-conscious manner? The enormous quantities of fossil fuels burnt since the industrial revolution (end of the 18th century) have significantly increased the concentration of green house gases (GHG) in the atmosphere, mainly carbon dioxide. This has become a matter of great concern to the public in general because of the GHG's detrimental effect on the Earth's ecological equilibrium and evidential global warming effect [7]. The consensus among scientists is that a minimum of 50 percent reduction in 2005 GHG emissions must be achieved by 2050 in order to limit the average temperature increase to 2-3°C in order to avoid a dangerous climate change [2]. The introduction of green technologies in electrical energy supply sector can be of great aid in achieving this environmental challenge. For example the increase on the share or mix of the electricity sources coming from renewable energies, nuclear power along with carbon sequestration in coal-fired plants is envisaged as a feasible way to face this ecological task. Among these options nuclear power is a mature technology with a large-scale energy deployment and almost zero CO_2 emissions that could be easily deployed over the next decades. Nonetheless, there is still a public concern about safety, disposal of nuclear waste and nuclear weapon proliferation. On one hand, the nuclear industry has failed to inform the general public, about the basics of the atomic energy exploitation and its advantages as a source of energy [8]. On the other hand, the stigmatization of the nuclear power industry as a result of three main nuclear accidents over the past 60 years has slowed down its expansion and undermined the civil nuclear energy renaissance: Three Mile Island (TMI-2 reactor) accident in Dauphin County, Pennsylvania, USA on March 28, 1979 rated level 5 (Accident with wider consequences) in the International Nuclear and Radiological Event Scale (INES); The Chernobyl plant reactor 4 disaster near Pripyat, Ukraine (then Ukrainian Soviet Socialist Republic) on April 26, 1986 was rated as level 7 (Major Accident) in the INES; and the Fukushima Daiichi nuclear power plant disaster in Ōkuma, Fukushima, Japan following the Tōhoku earthquake and tsunami on March 11, 2011 also labeled as level 7 under INES.

1.2 Nuclear Reactor Severe Accident

The nuclear power plants are designed considering the worst case scenarios; embedded are numerous redundant active and passive safety systems, along with specifically devoted emergency systems inside one or multiple containment structures (i.e. cladding, steel vessel and reinforced concrete containment); these might be essential for reactor operation and/or have the purpose of serving as mitigation and barriers to the release of radioactive materials to the environment under normal and severest accident conditions. In order to understand the stresses or loadings acting upon the reactor containment system in an accident scenario it is important to consider the main sources of energy release that can be encountered in order to halt or mitigate the accident evolution [8]:

- The *stored energy* comprises the sensible and latent heat stored in the reactor fuel, coolant, vessel and structure at the start of an accident. This is essentially the heat accumulated in the reactor core generated by the fission chain reaction under normal reactor operation and thus relates to designed power, pressure and temperature.

- The *nuclear transient energy* is the heat produced immediately after fission during a nuclear excursion. Under normal reactor operation conditions, the kinetic energy of prompt neutrons and gamma rays plus fission products, is transferred in the form of heat to the fuel as they diffuse through the reactor core, cladding and coolant materials. In contrast, during a nuclear excursion a change on the reactor reactivity causes a quick increase of more than several times the normal operating reactor power; this instantaneous excess heat results on a focused temperature/pressure spike, where local melting and/or vaporization of the fuel can take place because generation of energy is much faster than heat conduction; this can cause permanent damage to the reactors core constituents. Additionally, temperature, pressure and fission product poisons transients, can destabilize normal reactor working and result in damage to the nuclear reactor.

- The *decay heat* involves the continuous energy release due to radioactive decay of certain unstable isotopes. In a nuclear reactor the main source of decay heat are the fission products and

actinides, as they emit ionizing radiation in the form of alpha, beta particles and gamma rays. Also, but to a minor extent, moderate transmutation of containment and structural elements due to neutron capture, or interaction with ionizing radiation, can be another source of decay heat, but insignificant when compared to actinides and fission products' energy release. Anyhow, since radioactive decay for several fission products daughters and/or precursors, can be a lengthy and energetic process, continuous cooling of the reactor, even after reactor SCRAM, need to be maintained for years to compensate for the heat generated from decay of fission products.

- The *chemical reaction energy* denotes exothermic chemical interactions among reactor core constituents that might be undesirable due to its potential as accident initiators or consequence of them. For example, under an anomalous reactor situation higher than normal design temperatures could be reached, which in turn can lead to severe accident scenarios, for example loss-of-coolant-accident (LOCA), coolant evaporation and core uncovering in light water reactors. At this state, aggressive chemical interaction between coolant (like superheated liquid and vapour) and core metallic alloys (i.e. zirconium-based fuel cladding) can lead to degradation and loss of functionality of containment and structural materials. Typical interactions are Red-Ox type reactions among reactor constituents, i.e. dry/wet oxidation and corrosion will be accentuated under higher than normal service temperatures and abnormal pressures. The reaction specifics will also depend on the reactor type and condition.

- The *site-related energy sources* take into consideration both man-made and natural forces that originate from outside the nuclear power plant. On one hand, the man-made external accident initiators include airplane or other heavy vehicle crashes, industrial or chemical explosions, sabotage and acts of war or terrorist attacks. Also, internal initiators as equipment malfunction, tube rupture or failure of any mechanism necessary for the proper nuclear reactor operation. Additionally, natural forces with the capacity of endangering plant normal functionality and potential accident initiators are tornadoes, hurricanes, high winds and strong storms, floods and high waves like tsunamis, earthquakes and other seismic waves like those cause by volcanic

explosions. All the previous man-made and natural potential major-accident originators should be evaluated in a probabilistic manner and according to their intensity, in order to take them into account for the NPP design on a site-specific basis [9].

Furthermore, due to the extensive deployment of Western type light water reactors (LWRs) around the world we will focus our talk to sources that can lead to a nuclear reactor severe accident (SA) in these type of reactors; therefore, we will restrict our discussion primarily to pressurized water reactors (PWR) and boiling water reactors (BWR), and where pertinent we refer to Russian RBMK graphite-moderated water-cooled channel type reactor. Fundamentally, severe accidents are extremely improbable ($\sim 10^{-6}$ frequency/reactor year) events which could result on the partial or total meltdown of the reactor core. They might or might not be provided for in the design of the plant, i.e. beyond-design-basis-accidents (BDBA) and design-basis-accidents (DBA) as LOCAs. Severe accident initiators might be energetic nuclear excursions or overpower transients, loss of coolant accidents, loss of on-site and off-site power, or any event that results on the failure to remove radioactive decay heat from the fuel elements after reactor emergency SCRAM or normal shut-down. The initial thermal output from radioactive decay just after shutdown of a 1000-MWe reactor operating at full power and having reached equilibrium conditions between the production of radionuclides and their radioactive decay is equal to 7% of its total thermal output; or 2% of its electrical output considering an operating efficiency of around 33% for current LWR, thus without cooling an initial 20 MW output due to decay heat is enough to melt the fuel and cladding. This value will rapidly drop to about 16 MW, then 9 MW after 1 and 5 days, respectively [5, 9-11].

In the late seventies, studies on severe accident phenomenology in LWR were scarce besides preliminary studies performed by the WASH-1400 team as part of the U.S. Environmental Protection Agency, Office of Radiation Programs. After the TMI-2 accident the need to acquire understanding on the progression and consequences of severe accidents was evident, consequently, experimental and analysis research and development (R&D) programs were launched in the USA and Europe. In severe

accident scenarios, complicated material interactions between molten fuel, coolant, containment and structural materials render the SA phenomenology a complex process. A general description of core melt progression during a severe accident will be provided based on experimental results found through SA experimental programs and understanding of the TMI-2 accident progression:

1.2.1 In-Vessel Severe Accident Progression

If after reactor intentional or emergency SCRAM, there is a failure to remove radioactive decay heat by imbedded systems designed to cool the reactor under normal operation (i.e. forced or natural convection, conduction, irradiation of heat or a combination of cooling mechanisms) and/or emergency cooling systems (such as the emergency core cooling system, ECCS), the fuel elements will steadily increase in temperature leading to core meltdown. Even if the core is still partially or completely immersed in water, if no heat sink is provided, the coolant temperature will steadily escalate as result of steady evaporation and/or boiling of water, thus increasing the pressure inside the reactor vessel. Therefore, if core cooling is not re-established on time, the core will eventually uncover and fuel temperature will ramp up to temperatures well over 2500°C, until it reaches the fuels melting temperature (UO$_2$ T$_m$~2800°C). Afterwards, the accident progression, will be influenced by operator manoeuvres, reactor specifics and reactor condition (i.e. fuel burn-up). Therefore, even though an accident does not follow an exact succession of events, a detailed description of an accident progression, assuming loss of external and on-site electric power, will be presented to illustrate the complex phenomena taking place during core meltdown and evolution of the severe accident scenario.

Therefore, if no means to bring the reactor to a cold shutdown are provided, the heat produced by radioactive decay will be enough for the temperature to escalate until it reaches the water saturation temperature (at the existing pressure inside the vessel), causing coolant boiling and evaporation. As water boils off pressure will increase and there will be a need to relieve the pressure inside the reactor vessel to avoid premature failure. This can be done through relief valves that can

either ventilate the water vapour into steam recombining systems, or the containment building. If not, overpressure could damage the reactor head or other important segments of the primary cooling loop; for example a weak spot that has been considered is the failure of one of the reactor piping hot-legs, which would lead to rapid loss of coolant. This scenario has been considered as a DBA and that would lead to a rapid loss of coolant, this type of event is called a LOCA. Anyhow, if we assume that the vessel's pressure is constantly relieved as water continues to evaporate, but cooling systems are not re-established. Then, there will be a continuous decrease of the water level until partial uncovering of the core is reached. At this moment the conversion of decay heat into latent heat of evaporation due to water boil-off will cease and the temperature of the fuel bundles will continue to increase until it reaches 1000°C. At this moment, the vigorous oxidation of zirconium cladding by water vapour will take place (with a simultaneous production of hydrogen: $Zr + 2H_2O_{vapor} \rightarrow ZrO_2 + 2H_2$), greatly accentuating the core heat-up rate due to the combining effect of decay heat and the very exothermic zirconium oxidation (6.45 kJ/g of Zr). In turn, the oxidation of metallic structures such as the control rods' stainless steel cladding and its neutron absorbing material (Ag-In-Cd alloy used in most PWR or boron carbide, B_4C, in BWR) will further increase the production of hydrogen inside the pressure vessel. The hydrogen production will pose a great problem not only because there will be a concomitant increase in pressure inside the steel vessel, (recombining systems only work for condensable gases as water vapour), but also since the venting of gases to the containment building will be precluded if air is present in the atmosphere. Because the oxygen in the air can react with hydrogen to form water ($2H_2 + O_2 \rightarrow 2H_2O + 120$ kJ/g of hydrogen), and result in an explosive production of a significant amount of heat (combustible hydrogen/air proportion lies between 4 and 74%). A hydrogen detonation can be ignited by sparks (electric short-circuits), hot surfaces (piping), or deflagration (caused by convection of air and flow obstacles that could produce turbulent currents) inside the containment building. In order to avoid a hydrogen explosion, the atmosphere of the relatively smaller BWR containment building is inerted by injecting nitrogen. This is not the case in

PWRs since their larger containment building reduces the probability of reaching an explosive hydrogen concentration. Water vapour also acts as an hydrogen explosion inhibitor.

Furthermore, besides the partial oxidation of some structural elements, an increase in temperature will promote the melting of low melting point materials, like the control rod absorber materials in PWR (Ag-In-Cd alloys melting range: 777 to 827°C). In its liquid form this alloy will react with the internal stainless steel cladding wall, and promote the formation of low temperature eutectics, which will affect the structural stability of the rods and premature failure. In the case of the BWR, the melting of absorber ceramic material will take place at slightly higher temperatures (B_4C melting range: 1200 to 1400°C). Afterwards, the lower melting temperature phases and molten material could flow downwards and relocate/resolidify to form blockages in the colder parts of the core, impeding the convective flow or forced flow through the reactor core (in case the recirculation of coolant could be established). Furthermore, as temperature continues to rise any unoxidized zirconium alloy cladding material would eventually melt (zircaloy melting point 1850°C) and wet the oxide fuel pellets to produce low temperature eutectics phases and consequently fuel pin candling. Finally, if very high temperature is reached (between 2600°C and 2865 °C) the remaining refractory ceramic materials will melt, such as fuel pellets and previously oxidized zirconium. Therefore, the first barrier to the release of fission products will have been breached, which is of a lot of concern, especially due to the release of volatile fission products as ^{81}Br, ^{137}Cs, ^{131}I, ^{85}Kr, ^{87}Rb, ^{129}Te, ^{133}Xe, in the reactor vessel. Among them, the more toxic fission products, i.e. ^{137}Cs and ^{131}I, will dissolve into water in the form of CsI and CsOH, which will diminish the probability and quantity of radioactive material that could be released to the environment in the case of a total breach of the containment barriers.

At this stage, a molten pool will form at the top half or hottest part of the reactor core that will eventually melt through by growing axially and laterally as it ablates more fuel pins, containment and structural materials. If not cooled, the molten mass will eventually flow downwards in the form of jet

or small liquid droplets, impinging on the bottom of the stainless steel vessel. If there is any water left on the vessel lower head, the fuel-coolant-interaction (FCI) could trigger a vapour explosion, creating an energetic pressure spike that could fail the reactor top head bolts, or eject a control rod. This will create a path for the release of fission products to the containment building. Furthermore, the interaction of the molten fuel mass with the coolant can cause the partial fragmentation of the molten phase into solid debris, resulting on a very rapid conduction of heat from the debris to the water which can in turn cause a violent generation of steam causing shock waves or explosions. At this point, this complex melt can be called corium, and it consists of a non-miscible oxide phase (mainly UO_2 and ZrO_2 from fuel elements and some fission products) and a metallic phase (Fe, Cr, Mo from stainless steel and Ag-In-Cd or Boron/boron carbide from control rod materials) with a composition that depends on the proportion of ablated material in the core and fuel burn-up. Afterwards, a crust will be formed on top of the molten mass, if the corium is in a sub-oxidized state some uranium might diffuse into the steel and become part of the metallic phase, making it denser than the ceramic phase and therefore it will sank to the bottom, this phenomenon is called the first inversion. Moreover, if unoxidized zirconium is still present in the metallic corium it will eventually react with the oxygen present in the reactor pressure vessel (RPV) atmosphere (steam) and/or with urania (red-ox: $Zr+UO_2{\rightarrow}U+ZrO_2$). Therefore, the metallic phase will become lighter relative to the ceramic phase, and the second inversion will take place, where the metallic liquid will relocate to top and float in between the oxide and solid top crust. Finally, since the heat lost by radiation through the top free surface or crust is low compared to the convective heat flowing to the RPV the steel vessel wall will continuously heat up, and finally, due to the heat focusing effect and exacerbated by the fact that in most of the current reactor pressure vessels there is a thicker bottom head than the thinner vertical wall, a weak spot will exist where the molten mass will eventually melt through part of the steel and the corium will be ejected into the reactor pit due to the pressure difference and gravity forces. Therefore if not enough cooling of the steel vessel is promoted (i.e. some reactor have wet reactor pit

cavities or flood the dry cavity under sever accident scenarios in order to try to cool down and contain the corium inside the vessel) the vessel wall will be breached at the most susceptible site [9-11].

1.2.2 Ex-Vessel Severe Accident Progression

The ex-vessel scenario starts just after the corium melts through the RPV and it is discharged into the reactor pit. As previously mentioned, depending on the reactor design, the reactor pit might consist of a wet-cavity filled with water or a dry cavity. In the case of the wet cavity, the molten corium will fall into the flooded pit and react with water in a similar way as the FCI in the RPV; afterwards the molten corium and/or debris will reach the concrete basemat. On the other hand, if the reactor consists of a dry pit, the hot corium will react and start ablating the concrete; in a dry reactor pit molten corium spreading is usually promoted as a mean of cooling by irradiation of heat. When molten corium comes into contact with the basemat, degradation of the concrete takes place, and this process is usually referenced as the molten corium concrete interaction (MCCI). If no effective mean is provided to extract the radioactive decay heat produced by the fission products, the molten corium will steadily interact with the reactor containment foundation and will ablate its way through the thick reactor basemat (from 2 to 5 meters thick concrete depending on the reactor) until it reaches the underlying soil.   The molten corium mass will continue to penetrate the underlying layers until the decay heat is dissipated by thermal conduction, through spreading and mixing with humidity and aggregates in the soil, this phenomenon has sometimes been called "The China Syndrome".

Nuclear reactor basemat is made of concrete, which is essentially a mixture of cement, water and aggregates which consist of variable proportions of silica (SiO_2) and limestone ($CaCO_3$); limestone rich concretes are usually used in U.S. NPP and silica rich concretes used in European NPP reactor. The lava-like molten corium will be at temperatures between 1200 and 2300°C when in physical contact with the reactor basemat; at this point the concrete will heat up and go through several stages of degradation. Initially once it reaches 100°C physically bound water will start evaporating from the concrete, followed by dehydration of chemically bound water at 550°C. Afterwards, decarbonation

of cement and carbonate aggregates ($CaCO_3 \rightarrow CaO + CO_2$) will take place in the 700 to 900°C temperature range. The evolved gases will flow through the molten corium and exothermically react due to partial oxidation of the remaining liquid metallic phase to produce hydrogen and carbon monoxide. These combustible-non-condensable gases will reach the reactor containment building increasing the risk of an explosion ignited by a spark or deflagration; if energetic enough, damage to the reinforced concrete structure could take place generating paths for the release of any volatile fission products available in the atmosphere.

Finally, depending on the of proportion limestone/silica ($CaCO_3/SiO_2$ ratio), concrete will start melting at temperatures between 1100 and 1450°C, and calcia and silica will be incorporated into the corium. Additionally, between 1300 and 2200°C a period of stabilization or quasi-equilibrium is reached between the residual decay heat and the thermal losses through the corium-concrete interface and free corium surface. The corium will slow its progression as it steadily cools down; the metallic part will solidify first, due to its higher thermal conductivity and because most of the non-volatile fission fragments will be dissolved in the oxide phase of the corium. The initial active erosion of the concrete lasts about an hour and will penetrate through approximately 1 meter of concrete, and the degradation rate drops to a few cm/hour depending on the intrinsic concrete properties; the concrete ablation progress will stop once temperatures below the concrete decomposition are reached (<11000°C). A pessimistic analysis entails that if no external means for cooling the corium mass are provided it is believed that the reactor containment will be imminently breached in a matter of days up to a month, depending on the thickness of the basemat [11-16].

It should be understood that the MCCI is a long-lasting scenario and entails the understanding of a variety of coupled phenomena that make the analysis of its behaviour a complex process [11]:

- High temperature concrete decomposition and basemat ablation kinetics.
- Corium thermohydraulics, convective heat transfer and gas sparging in the molten pool. For example, convective heat transfer to the concrete wall due to transient effects is very

important in the initial stages of physical contact between corium and the basemat. Also, the production of large quantities of vapour from the physically/chemically tied/free water, as well as the CO_2 from the carbon aggregates, will increase the mixing and agitation of the melt, thus heat transfer.

- Thermodynamic and physico-chemical properties of the multicomponent corium melt undergoing significant compositional changes due to the incorporation of concrete constituents; complex red-ox type reactions between molten and evolved gases phases i.e. water vapour and carbon dioxide and production of hydrogen and carbon monoxide from concrete dehydration and decarbonation.

- Large/sluggish solidification range and mushy/slurry behaviour of corium-concrete molten mass.
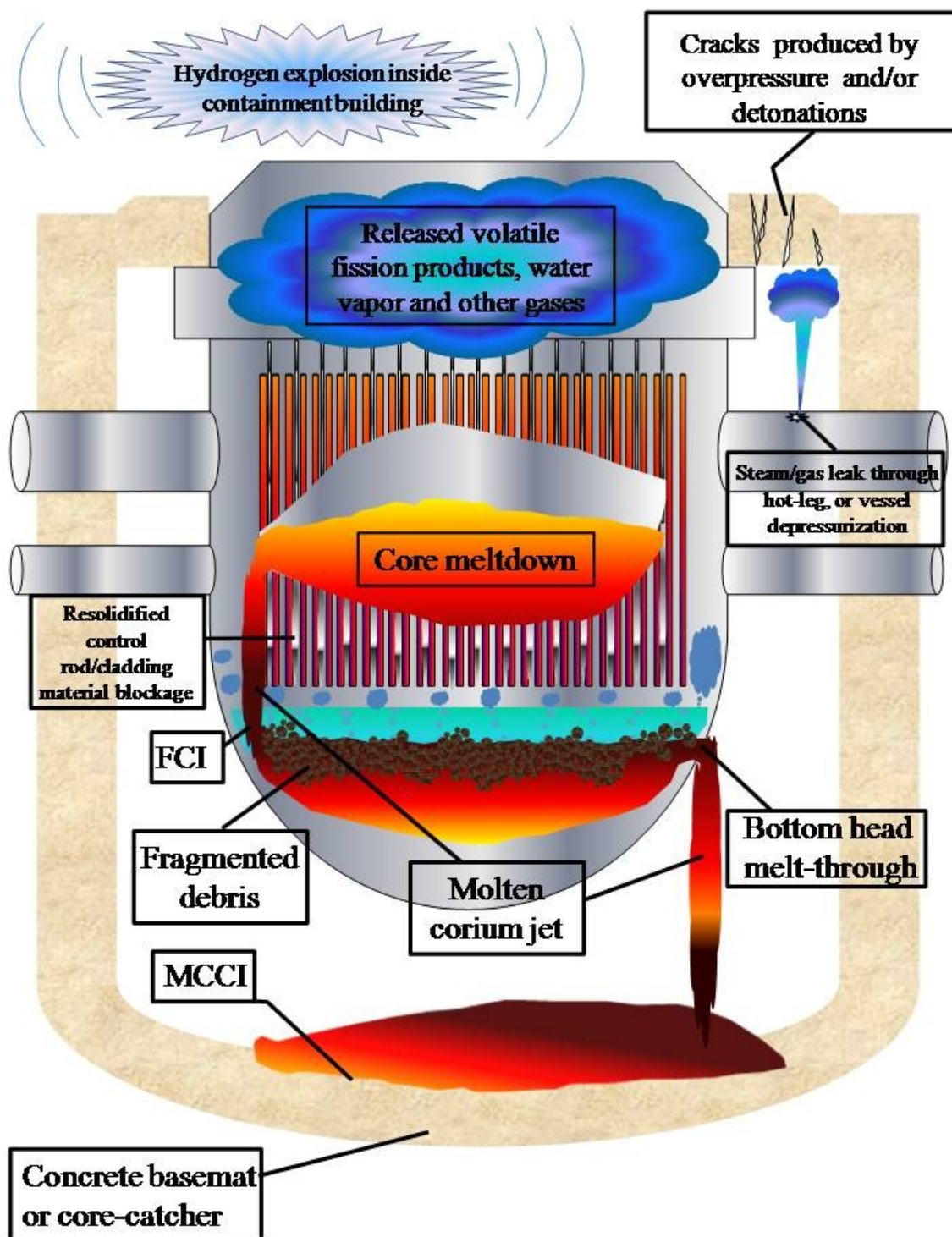
Figure 1.4. General nuclear reactor severe accident progression sketch.

1.2.3 The Three Mile Island (TMI-2) Nuclear Accident

On Wednesday, March 28, 1979, around 4:00 am, a failure on the intermediary cooling loop stopped the flow of water to the steam generator. Additionally a backup emergency feed water system should have started working to make up for the failure on the main loop, unfortunately due to a previous maintenance error after a systems test the main valves were left closed impeding the flow of cooling water. Moreover, the turbine stopped working since no more steam was flowing to it which in turn caused an immediate reactor scram by automatically dropping the control rods into the core. Temperature and pressure started rapidly increasing due to the absence of removal of sensible and decay heat from the reactor core; this in turn caused an increase on the level of the expansion tank, which is usually half-filled by water and steam in order to dampen any changes in pressure during normal reactor operation. Consequently the fast pressure increase opened the pilot operated relief valve (PORV), as it should, letting some of the steam flow through the piping into a collection tank which serves as a scrubbing agent in case there is any radioactive material. Thus, the reactor pressure decreased and the PORV should have closed afterwards, but the valve stuck open resulting on the continuous loss of coolant, and this was the start of a series of events that lead to reactor core meltdown.

Furthermore, a combination of malfunction of the main and backup cooling system critical parts, plus misleading temperature and pressure sensors which impeded the operators understanding that they were dealing with a LOCA. Due to the important coolant loses the pressure was low enough and the ECCS went-off, providing some extra water into the system, unfortunately, the operators were misled and thought they had an over pressurisation of the primary loop even though in reality the opposite was taking place due to coolant loss through the stuck open PORV; since the pressure sensor relied on the pressurizer tanks level the loss of coolant through the PORV and consequent depressurization on the main system caused a decrease on the saturation temperature of water, thus steam formed and expanded causing an increase in pressuriser tank, which would mean an increase in

pressure under normal operating conditions. As a result of the apparent, but erroneous, pressure increase reading, the operators were afraid that the reactor might go "solid" (if water filled the reactor it would act as an hydraulic press which could in turn blow off the reactor vessel head or cause fracture at the vessel walls) and decided to shut-down the ECCS. Once again, from the start of the ECCS the operators could have realized they were actually facing a LOCA, because this system only works if the reactors pressure drops below 11 MPa (~1600 psi), compared to the reactor normal operating pressure of 15.5MPa (~2250 psi), but they probably failed to do so since they were currently under very high stress levels as a result of numerous alarms ringing all around the control room, and they had never been trained for such scenarios.

Therefore, the water levels in the primary cooling system continued to drop as the coolant escaped and pressure decreased over the next couple of hours, causing the primary loop circulating pumps to violently cavitate due to the passage of a two phase liquid water and vapour mixture; the strong vibrations forced the operators to shut-down the pumps in order to avoid destroying them under this abnormal working conditions. Afterwards, the water level drop so low that core uncovering took place, and the temperature of the fuel rods kept increasing due to residual heat until it reached high enough temperatures to start the oxidation of the zirconium based fuel cladding and the release of hydrogen into the containment building which ignited latter in the afternoon causing a 2 bar pressure spike (the containment building resisted the explosion since it was designed to withstand a 5 bar pressure). Furthermore, the very exothermic reaction added up to the rapid increase in temperature and the fuel rods began to melt; this ignited several alarms due to an increase in the radioactivity levels resulting from the release of volatile fission products. At this instant, around 6:22am the operators finally realized that the PORV was stuck open, and immediately closed a backup valve, restarted the pumps and filled the system with water. Even though, they prevented further core melting, approximately half of the core was already molten and reacted with the fresh water to form a bed of solid debris on top of the molten pool which in turn formed and exterior crust

when it encountered the reflow of coolant into the reactor vessel. The poor thermal conductivity of the fragmented debris and crust impeded an efficient heat extraction and partial remelting of the corium took place which finally broke through the crust and found its way to the reactor vessel bottom. Fortunately, the coolant reflow into the vessel was able to provide sufficient cooling of the molten mass avoiding the breaching of the steel bottom head cap by either corium impingement or wall melt through [10,16,17]. Figure 5 is a schematic depiction of the initial state of the PWR and the post-accident appearance of the TMI-2 reactor vessel interior.
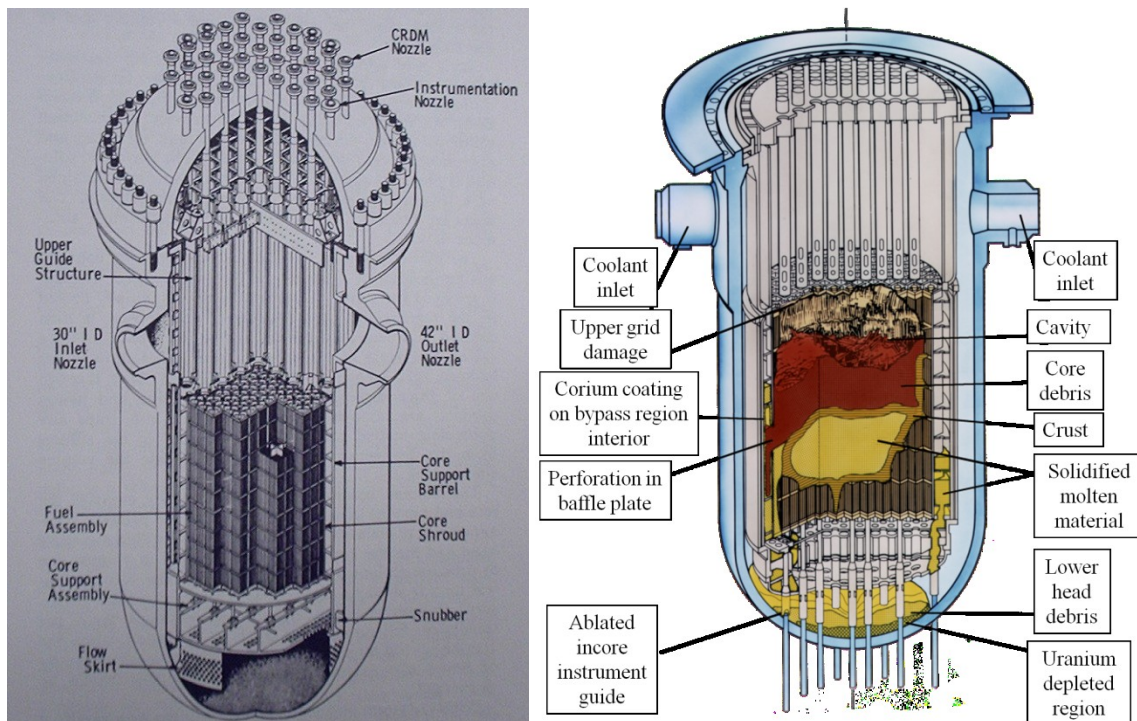
Figure 1.5. TMI-2 BWR before and after the accident.

1.2.4 The Chernobyl NPP Reactor-4 Nuclear Disaster

Contrary to Western type LWR, the RBMK (Reaktor Bolshoy Moshchnosti Kanalniy, "High Power Channel-type Reactor") is a uranium dioxide fuelled graphite-moderated reactor consisting of thousands of high pressure tubes through which coolant (ordinary water) flows, instead of a steel reactor vessel, to cool down the massive graphite core. The Chernobyl NPP consisted of four RBMK-1000 units that were each paired to two turbogenerators that provided 500MWe.

On April 26, 1986 a reactivity insertion accident (RIA) in Chernobyl reactor no. 4 resulted on the failure of several pressure pipes an caused an explosion that blew up the reactors 200-tonne upper lid, or biological shield, along with and expulsion of significant quantities of fuel and moderator material into the premises of the NPP site and produced a radioactive cloud that travelled through a large portion of Europe. Ironically, the events that lead to the greatest nuclear disaster known to date started with the intention of performing a reactor safety test to predict the reactors electricity autonomy in the event of a power failure. The series of events that lead to the nuclear disaster started with the initial demand to perform a test in order to understand if in the case of an abrupt reactor trip, the massive steam turbines' rotating inertia was able to generate enough electricity as it slowed down to keep the primary cooling pumps running during a 30-second span while the back-up diesel generators turned on an made up for the loss of power. It is important to mention the fact that this test was scheduled to be performed just before the regular reactor shut-down and maintenance, which means that the fuel burn-up was very high, and the accumulated fission product inventory was at the maximum for the designed reactor fuel lifetime, in other words, in the case of an accident the release of radioactive material would be at its most critical point. Unfortunately, there was a lot of political pressure since the test had already been delayed before, and the orders were to perform it without interrupting the regular reactor scheduled maintenance, so it was a now or never situation. Furthermore, that day the team in charge of performing the test was composed of the first-shift reactor operators and a group of electrical engineers that were especially sent onsite to perform the test, but lacked knowledge on the nuclear reactor system functionality and neutron physics.

The unit-4 power down rate started at 1am on April 25th and the generated power was halved over the following twelve hours. At 1:05pm one of the turbines was shutdown since a single turbine was to be used for the test and the reactor was at 50% capacity already, therefore it was enough to maintain the 4 main reactor cooling pumps running. The next step was to further reduce the power to 30%, but the electricity controller or soviet authority in Kiev refused the further down rate due to the

current electricity demand and told the operators to keep the reactor power generation online until further notice. However when they received the order to proceed with the power reduction 9 hours had already elapsed, plus the first-shift operators were gone, so the restless electrical engineers were to continue the test with the night-shift staff, which were not too well informed about the test in progress and seemed to be less experienced with reactor operation and physics than the earlier personnel. Nonetheless, they proceeded with the test and continued with the reactors power decrease, unfortunately, the operators made a mistake and failed to reset the automatic control rods to its set point and the reactor dropped to 30 MWth or 1% of full power, which in turn made the reactor operation very unstable due to the xenon poisoning effect. During normal reactor operation radioactive xenon gas (^{135}Xe) is a daughter or by product from the decay of the fission fragment ^{135}Te, which decays by negative beta particle emission into ^{135}I, and afterwards into this noble gas which has a longer half life than its parent radionuclide. The downside is that ^{135}Xe has an exceptionally large thermal neutron capture cross-section ($3x10^5$ barns) and produces the so called xenon poisoning, which is an anomalous effect that can by itself bring the reactor to total shut down. For example if the reactor involuntarily scrams or falls to very low power, as in the case of unit-4, the xenon will start building up to a maximum which is proportional to the normal reactor operation neutron flux, making it difficult to ramp up the reactors power if not enough excess reactivity is available, or additional fissile material.

Furthermore, the fact that the reactors power fell to such a low level due to operator mistake, not only promoted the build up of radioactive xenon, but also the coolant fell below its saturation point, and the previous vapour condensed into liquid water, adding up to the anomalous neutron absorption (Liquid water has a higher absorption of thermal neutrons than vapour since the macroscopic cross-section is directly proportional to the density of the material). At this point the operator had probably disabled several emergency systems in order to take out almost all the control rods, well below the 30-rod lower limit permitted for safe reactor operation and emergency shut-

down, with the purpose of overcoming the reactivity decrease due to the two neutron scavenging effects. Moreover, since the reactor was not designed to function under this low power the operator had to take upon the control of the pumps in order to regulate the flow, which is a rather difficult task to do manually, eventually the power started to slowly increase up to 200 MWth (around 7% of the full power), when the operator thought this was as stable as they were going to get the reactor and at this moment they decided to go on with the test. Just before starting the test they had to overwrite a final safety measure which was the fatal last blow before the reactor was essentially unleashed to run freely if a reactivity excursion were to occur. Basically the operator disabled the feature that automatically drops the emergency control rods into the core whenever loss of the remaining turbine occurs, since he was told to do keep the reactor running in case they needed to run a second test.

At 1:23:04am the remaining turbogenerator was disconnected, and as its rotating inertia decreased the power fed to the main pumps went down accordingly, in turn this reduced to flow and temperature began to increase until the water started to boil. Opposite to western LWR the RBMK has a positive void coefficient, this means that water boiling does not result on a reactivity reduction, but adversely the opposite takes place since graphite is the neutron moderator and as water started boiling its neutron absorption efficiency decreased and this set free a rapid increase in neutron flux or reactivity excursion. At this moment, the operator noticed a fast increase in the reactors thermal power so he executed an emergency scram, by freely dropping the emergency rods into the core, unfortunately one of the drawbacks of this reactor was the relatively large time frame (20 seconds) it would take to completely introduce the rods into the highest neutron density part of the core, compared to the 4 seconds it took for the reactor runaway and explosion. In other words, the exponential increase in reactivity came with a subsequent rapid upsurge in temperature which pulverized the fuel elements, failed the fuel cladding then mixed with water and provoked an intense production of steam which resulted on an almost instantaneous failure of the containment tubes along

with a very energetic explosion which destroyed the reactor core, blew the massive top concrete lid and partially destroyed the reactor building.

Moreover, as a consequence of the thermal explosion part of the reactor core was ejected into the atmosphere, exposing the environment to the radioactive fission products contained in the fuel, along with the oxidation of the red-hot graphite and fire ignition in the reactor hall. Thousands of burning graphite blocks pieces, and fuel debris were expelled into the night sky were most of the solid particles and graphite blocks fell back into the premises of the NPP site as the turbines building roof caught fire as a result of the burning graphite that fell on the rooftop. Extinguishing the fire became the priority to the firemen since the fumes could further propel high into the atmosphere the gaseous and volatile radioactive fission products, increasing the nuclear fallout area. Thousands of military personnel and firemen came into the scene and during days, with the aid of helicopters, dumped huge quantities of boron compounds, sand, clay, dolomite and lead into the reactor pit in order to reduce the probability of recriticality, to shield the environment from further ionizing radiation coming from the reactor core, and promote the mixing of materials with the molten corium mass that had started to engulf the reactors basement structure. One of the tasks to avoid contamination of groundwater due to the MCCI was to dug an almost 2 meter tunnel below the reactor structure in order to install a bottom cooling plate connected to a refrigeration system which helped to extract the decay heat and solidify the lava like material. Unfortunately, the emergency work came along with the sacrifice several people in the emergency crew, or the so called "liquidators", whom perished due to acute radiation exposure not to long after being in the Chernobyl nuclear disaster site. With time the molten corium ablation of the structure stopped as it cooled down and solidified, leaving behind traces of its flow through the reactors bottom piping, were the famous Elephant's foot was found in one of the basement corridors. Not too long after the disaster great efforts were made to build a big containment structure (completed on November 19th, 1986), originally called the Sarcophagus, in order to seal the emanation of radioactivity and impede further propagation of radioactive material into the

environment by impeding any rainwater entrance and further degradation of the imperilled RBMK reactor. Overtime this structure has become so unstable that the plans to construct a new one are underway under the funding of the G-7 countries [11, 13-15, 18].
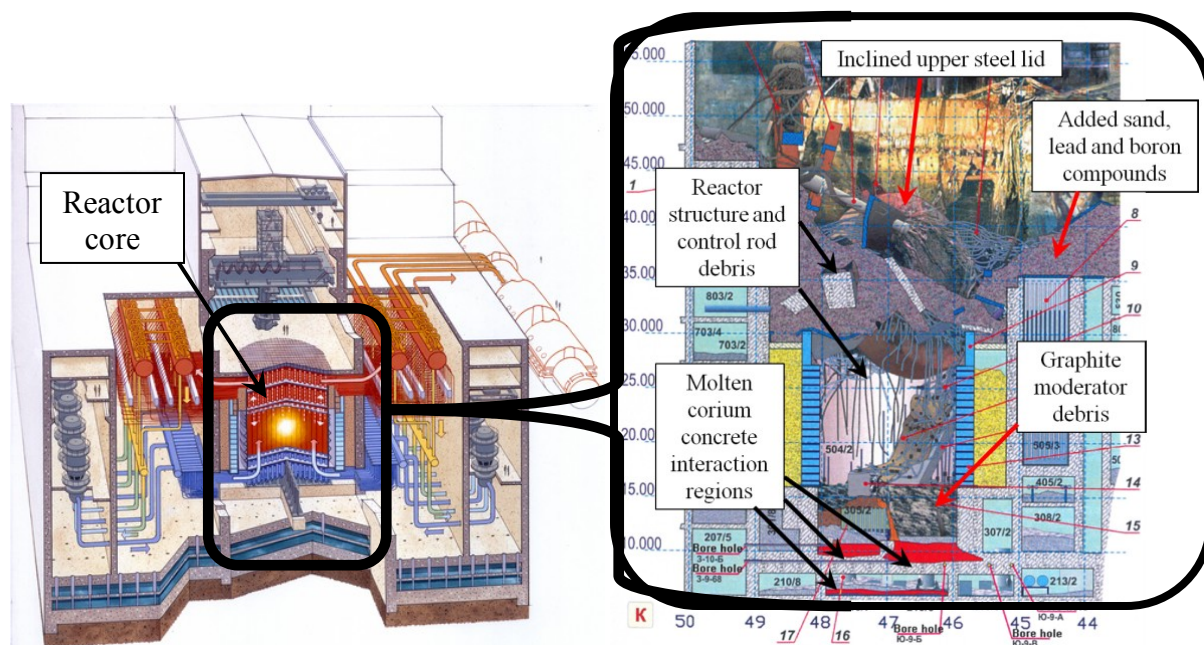
Figure 1.6. Chernobyl-4 RBMK reactor core before and after the disaster.

1.2.5. The Fukushima Daiichi Nuclear Site Disaster

The Fukushima Daiichi NPP site is composed of six BWRs from which unit 1-5 are of a Mark-1 type and unit 6 is a Mark-2 type reactor. The rated reactor power for unit-1 is 460MWe, then unit-2 through -5 have each a 784MWe power capacity and finally the most modern of the on-site reactor fleet is unit 6 with an electric output 1100MWe. On March 11, 2011 at 14:46 JST the Tōhoku earthquake with an epicentre approximately 130 kilometres from the Fukushima NPP site took place with an intensity of 9.0 in the Richter scale, being the strongest reported in Japan, and the 5th in strength since seismic recordings started on year 1900. The movement of the Pacific Plate against the Honshu underlying plate triggered a colossal Tsunami that reached a maximum height of 40.5 meters and travelled as much as 10 kilometres inland in the Sendai area. Due to the intense ground acceleration units 1-3, which were currently in operation, came to an automatic emergency scram, and the back-up diesel generators started working, since the off-site power supply was lost due to the

destruction of electric grid by the violent seismic shock. The diesel generators took over the cooling of the reactors through the Residual Heat Removal (RHR) system, driven by smaller external electric pumps in the secondary circuit which are connected to the two jet-pump recirculation circuits. They circulate water from the pressure vessel to RHR heat exchangers, finally dumping the heat into the sea.

Furthermore, over an hour after the earthquake a 14-meter tsunami wave hit the Fukushima Daiichi site and flooded the rooms containing the emergency diesel generator which were at an elevation of 10 meters; originally the NPP was constructed taking a 5-meter tide into the design basis. Therefore when the tsunami wave arrived it submerged almost all the diesel generators, causing the sudden stop of all but the emergency generators in Unit-6. Therefore, the only source of electricity left were the backup batteries which provide electricity to instrumentation and basic emergency systems. Unit-1 is equipped with an isolation condenser (IC) system which directs the reactor steam to an external condenser, this passive core cooling system is run by a battery DC power. Units 2-5 have a Reactor Core Isolation Cooling (RCIC) which injects water from the condensate storage tank, or the suppression pool, and can provide make-up water to the RPV, but it does not conduct the heat to a heat sink, so this system will work until the water in the storage tank or suppression pool heats up and reaches its saturation temperature. This system is controlled by batteries and is driven by a small steam turbine which uses the steam produced by the residual heat in the fuel. Therefore the RCIC worked until the suppression pool water boiled, at 11am on March 12th in Unit-3, and until 2pm on March 14th in Unit-2. Additionally in Units 1-3, there is an ECCS with a high-pressure and low-pressure component. The high pressure coolant injection (HPCI) system works over a wide pressure range and uses pumps powered by steam turbines. It requires only DC battery power and takes water from the storage tank and the large water suppression chamber or torus beneath the reactor. The Low-Pressure Coolant Injection (LPCI) mode, for use below 700 kPa, utilizes the suppression pool water and a core spray system. All the ECCS sub-systems are electrically driven and require some power to

operate valves which can be provided by the batteries. Finally, as part of the Severe Accident Management (SAM) countermeasure, a system which allows for the injection of water into the RHR system via the fire extinguisher system is available. Unfortunately, due to the batteries have a low energy storage capacity, and are designed to last over a period of 4 to 8 hours before they run out of energy. Therefore, after the energy from the emergency batteries totally consumed no means were quickly provided to re-establish the primary cooling system or a hit sink. This was in part due to the difficult, say impossible, task to reach the NPP site caused by the catastrophic condition left behind by the tsunami. Therefore, this resulted on a total station black-out (SBO) that lasted for a very long time.

At that time Units 5 and 6 were already in the cold shutdown state, but Unit-4 was of special concern since it had been recently shutdown for major renovation and all of its fuel had been removed and stored in the spent fuel pool (SFP) for removal of the significant amount of residual heat generated (~3 MWth). It is important to mention that one drawback of the Mark-1 design is that its SFP is located outside the primary containment vessel (PCV) on the reactors buildings top floor, which was not structurally designed to withstand any significant static or dynamic pressure increase and its filled with air at atmospheric pressure, opposed to the RPV and PCV which have a higher pressure bearing capability (RPV> 8.24MPa and PCV: 0.28-0.43MPa) and are under an inert nitrogen atmosphere in order to avoid any hydrogen explosion when mixed with air. Furthermore, it is believed that Unit-1 went through an almost complete core meltdown (70 to 80%), in which corium flowed to the reactor head bottom. This is estimated since no water (heat removal) was provided to the core for more than 14 hours, which is a very long time period when compared to the estimated 2-hour lapse needed for sufficient fuel uncovering and intense oxidation of fuel cladding. Hence due to cladding oxidation, large quantities of hydrogen were produced and had to be vented to the PCV. Unfortunately, the hydrogen seemed to have filtered to the containment building top floor, probably through cracks created either by the earthquake or due to over pressurization of the PCV.

Consequently on March 13th at 15:36 hydrogen combination with oxygen in the air caused an energetic explosion that blew the roof away in Unit-1. It was also believed that the reactor bottom steel head had been breached and molten corium had reached the reactor PCV pit due to an increase in the radioactivity, but up to date there have not been any confirmations on this hypothesis.

On the other hand, Unit-2 was left without water cooling for over 6 hours after the RCIC system stopped working. Eventually sea water injection was provided, but cooling was not re-established fast enough and core meltdown took place in Unit-2, which relocated and breached the reactor lower head 5 hours after fuel uncovering. This is asseverated since a large increase in the PCV pressure was recorded. Therefore, venting had to be performed due to the high pressure and elevated steam/hydrogen concentration. The steam and hydrogen were directed towards the suppression pool for recombination and condensation of the steam. However, since hydrogen is not a condensable gas, it cannot be recombined with this system, and an explosion took place which damaged the reactor suppression pool. Finally, after 7 hours the RCIC and HPIC stopped working in Unit-3, water injection stopped and fuel uncovering took place leading to core meltdown and relocation to the bottom head. It is believed that the RPV was also breached in Unit-3, since the pressure increased over the design limits for the PCV and venting to the stack was needed, but the emergency membrane did not rupture and the hydrogen/nitrogen mix plus volatile fission products leaked to the reactor building through cracks and caused an explosion which blew the roof away. It is believed that some of the hydrogen produced in Unit-3 travelled to Unit-4 through common venting system causing the ignition of debris, and a fire in reactor building number 4 which damaged the roof top. Water was provided to the Unit-4 SFP with the aid of fire trucks, cement trucks, and helicopters to avoid depletion of water. This event was greatly feared since it could have resulted on failure of the spent fuel and large release of fission products. Until now no confirmation is available on whether the molten fuel breached the RPV and if it had reacted with the concrete basemat [11-12]. An illustration

of the Mark-1 type BWR is shown in figure 1.7. This is the same reactor type of the Fukushima

Daiichi NPP site Units 1 to 5.
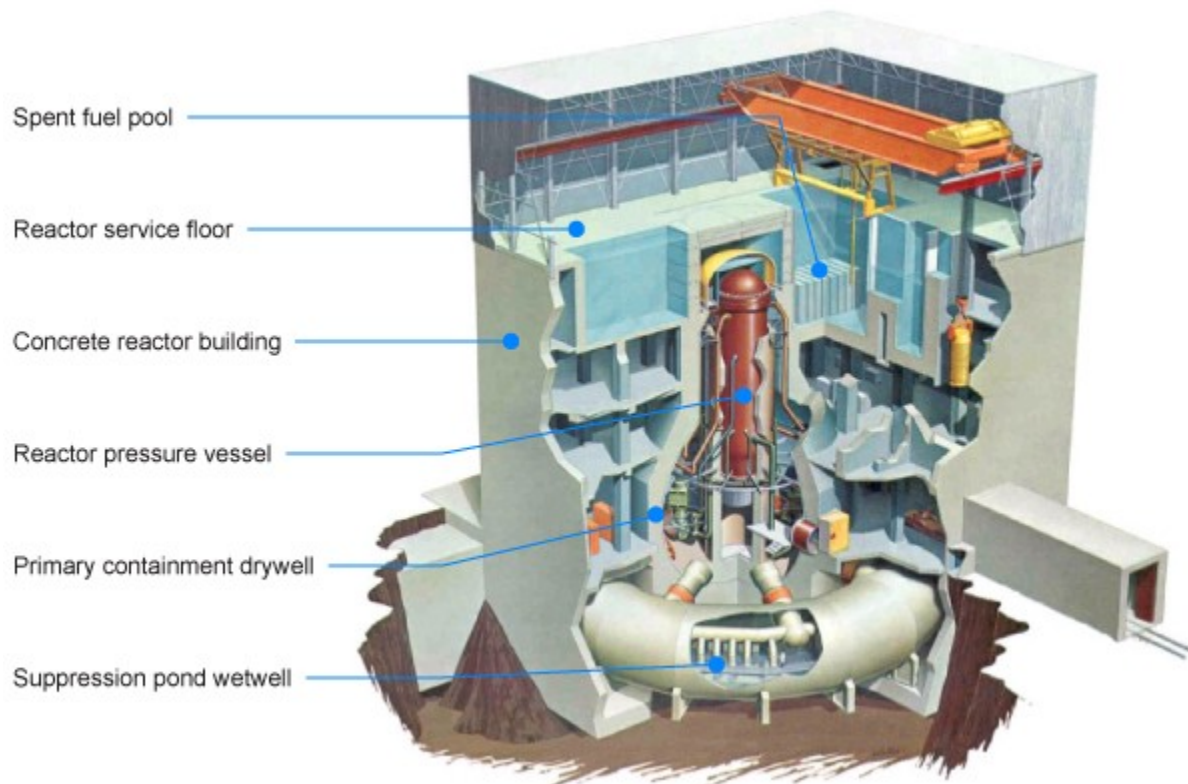
Figure 1.7. Schematic of the Mark-1 Boling Water Reactor.

Chapter 1 - References

1. OECD/AEN, "Perspectives de l'Énergie Nucléaire 2008" AEN N°6349 (English version: OECD/NEA, "2008 Nuclear Energy Outlook" ISBN 978-92-64-05410-3), 2008, pp. 20-21, 50.

2. OECD/NEA, "Nuclear Energy in Perspective" OECD, November 2010, pp. 1-8.

3. IAEA, "Nuclear Technology Review" printed by the IAEA in Austria, September 2012, pp. 7.

4. DOE/IEA, "International Energy Outlook 2011" DOE/IEA-0484, September 2011, pp. 1-4.

5. D. Bodansky, "Nuclear Energy: Principles, Practices, and Prospects" 2nd Ed., ISBN 0-387-20778-3, Springer Science+Bussines Media, Inc., New York, 2004, pp. 6, 381-383.

6. S. Glasstone and A. Sesonske, "Nuclear Reactor Engineering" ISBN 0-442-02725-7, Litton Educational Publishing, Inc., New York, 1967, pp. 23, 260-269.

7. L. Xu, R. B. Myneni, F. S. Chapin III, T. V. Callaghan, J. E. Pinzon, C. J. Tucker, Z. Zhu, J. Bi, P. Ciais, H. Tømmervik, E. S. Euskirchen, B. C. Forbes, S. L. Piao, B. T. Anderson, S. Ganguly, R. R. Nemani, S. J. Goetz, P. S. A. Beck, A. G. Bunn, C. Cao, J.C. Stroeve, "Temperature and vegetation seasonality diminishment over northern lands" Nature Climate Change, 2013; DOI: 10.1038/nclimate1836, pp.1-6.

8. D. Klein, M. Corradini, "FUKUSHIMA DAIICHI: ANS Committee Report" The American Nuclear Society Special Committee on Fukushima, March 2012, revised June 2012, pp. 1-40.

9. E.E. Lewis, "Nuclear Power Reactor Safety" John Wiley & Sons, New York, 1977, pp. 434-531.

10. J.N. Lillington, "Light Water Reactor Safety: The Development of Advanced Models and Codes for Light Water Reactor Safety Analysis" ISBN 0-444-89741-0, Elsevier Science B.V., Amsterdam, 1995, pp. 6, 21-31.

11. B.R. Sehgal, "Nuclear Safety in Light Water Reactors: Severe Accident Phenomenology" ISBN: 978-0-12-388446-6, 1st Ed., Elsevier Inc., Amsterdam 2012, pp. 45-78, 369-374.

12. K.R. Robb and M.T. Farmer, "Enhanced Ex-Vessel Analysis for Fukushima Daiichi Unit 1: Melt Spreading and Core-Concrete Interaction Analyses with MELTSPREAD and CORQUENCH" (Report: ORNL/TM-2012/455) prepared by Oak Ridge National Laboratory for the U.S. Department of Energy under contract DE-AC05-00OR22725, February 2013, pp. 1-96.

13. S.A. Bogatov, A.A. Borovoi, , S.L. Gavrilov, A.S. Lagunenko, E.M. Pazukhin, V.A. Khvoschinskiy, "Development of the Models for Nuclear reactor Fuel Behavior during Active Phase of Chernobyl Accident" International Science and Technology Center and the Russian Research Center Kurchatov Institute, Project No.2916, 01/02/2007, pp. 1-147.

14. E.M. Pazukhin, "Fuel-Containing Lavas of the Chernobyl NPP Fourth Block: Topography, Physicochemical Properties, and Formation Scenario" Radiochemistry; Journal Volume: 36; Journal Issue: 2; Nov 1994, pp. 109-154; Translated from Radiokhimiya, vol. 36, No. 2, Mar-Apr 1994pp. 97-142.

15. S.A. Bogatov, A.A. Borovoi, A.S. Lagunenko, E.M. Pazukhin, V.F. Strizhov, and V.A. Khvoshchinskii "Formation and Spread of Chernobyl Lavas" ISSN 1066-3622, Radiochemistry, 2008, Vol. 50, No. 6, pp. 650–654. Original Russian Text 2008, published in Radiokhimiya, 2008, Vol. 50, No. 6, pp. 565–568.

16. B.R. Sehgal, P. Piluso (Eds), K. Trambauer, B. Adroguer, F. Fichot, C. Müller, L. Meyer, W. Breitung, D. Magallon, C. Journeau, H. Alsmeyer, C. Housiadas, B. Clément, M.L. Ang, B. Chaumont, I. Ivanov, S. Marguet, J.-P. Van Dorsselaere, J. Fleurot, P. Giordano, M. Cranga, "SARNET Lecture Notes on Nuclear Reactor Severe Accident Phenomenology", CEA-R-6194, ISSN 0429-3460, September 2008.

17. B.A. Osif, A.J. Baratta, T.W. Conkling, "TMI 25 Years Later: The Three Mile Island Nuclear Power Plant Accident and Its Impact" ISBN 0-271-02383-X,The Pennsylvania State University Press, 2004, University Park, PA, pp. 21-32.

18. IAEA, "Assessment and Management of Ageing of Major Nuclear Power Plant Components Important to Safety: PWR Pressure Vessels" IAEA-TECDOC-1120, ISSN 1011-4289, Vienna, 1999, pp. 4.

19. R.F. Mould, "Chernobyl Record: The Definitive History of the Chernobyl Catastrophe" ISBN 0-7503-0670-X-hbk, Institute of Physics Publishing, Bristol, 2000, pp. 15-49.

Chapter 2. Thesis Objectives - Very High Temperature Measurements

The author's PhD research has been focused on the improvement of temperature measurements in severe accident tests, especially the VULCANO MCCI test configuration; the doctoral dissertation research findings can be utilized for the improvement of very high temperature measurements in general via the use of new calibration techniques for high temperature thermometry.

Moreover, the PLINIUS experimental platform, part of Severe Accident Mastery Laboratory (LMA) in the French Alternative Energies and Atomic Energy Commission (CEA) Cadarache research centre in France, is devoted to the study of nuclear reactor severe accidents with the capability of using large masses of prototypic corium. PLINIUS is composed of 4 facilities: VULCANO, COLIMA, KROTOS and VITI. Details in table 2.1.

PLINIUS Platform

- ❖ VULCANO.- study of molten corium concrete interaction (MCCI) and corium rheology.
- ❖ COLIMA.- study the production of volatile fission products, i.e. aerosol formation on molten corium.
- ❖ KROTOS.- study of fuel coolant interaction (FCI) and steam explosions.
- ❖ VITI.- consists of an induction furnace intended for small scale material interaction tests (<300grs), and for research on thermo-physical, -chemical properties of materials.

Table 2.1. CEA Cadarache, PLINIUS experimental platform facilities.

2.1 Temperature Measurement and Uncertainty Sources in Severe Accident Tests

The nuclear reactor severe accident experimental research is very complex and demanding, especially when dealing with low-radioactivity prototypic materials such as depleted uranium dioxide. Additionally, to produce a corium melt, the high liquidus temperature of the UO_2-ZrO_2 system (>2500°C) must be reached, which possess a lot of difficulties and entails the use of adequate instrumentation and specialized equipment that is able to withstand such high temperatures and aggressive environment.

The temperature measurements are performed using a combination of intrusive (thermocouples) and non-intrusive (pyrometers) techniques during MCCI tests. Among other measurable parameters, temperature is essential to determine thermo-physical, -chemical and -dynamic properties of corium, along with concrete ablation phenomenology and heat convection from the melt to the concrete walls. Impediments for adequate temperature measurements in VULCANO MCCI tests [1] not only render the task of interpreting the temperature data difficult but can lead to erroneous conclusions and misunderstanding of the MCCI phenomena. Therefore, early in the thesis, the main task was to identify sources of error in high-temperature measurements in MCCI experiments. Therefore, upon performing a literature research on the subject, reviewing internal MCCI technical reports, attending SA seminars and conferences as well as fruitful discussions with LMA scientists and technicians, attending several SA tests in the VULCANO and KROTOS facilities, the author has gathered enough knowledge to identify the following important sources of uncertainty in temperature measurements with the aim to introduce improvements in SA thermometry of core melts:

- Accurate pyrometer measurements during molten corium-concrete ablation tests are disrupted by fine dust particles, fumes and gases evolved, (i.e. perturbations on the electromagnetic radiation by selective absorption bands of water vapour and carbon mono/dioxide), also emissivity of molten mass will be tied to the evolution of corium composition and temperature during progression of MCCI test [1-5].

- Induction heating, utilized to emulate fission product radioactive decay heat, can produce ambiguous thermocouple (TC) readings caused by electromagnetic interference and its impact on the thermoelectric Seebeck effect on which the TC rely for temperature measurements [5].

- Destruction of thermocouples by the very hot corium melt through the intense thermal shock and/or dissolution of the sheath materials caused by the large temperature gradients and high

heat fluxes between the molten corium (>2000°C) and the concrete test section (room temperature).

Based on the observations, the author of this dissertation has proposed two main line of actions to improve the certainty of in-melt thermometry in nuclear reactor severe accident tests.

2.1.1 Application of Metal-Carbon Eutectic Cells as High Temperature Fixed Points

During the evolution of the thesis extensive work on several high temperature metal-carbon eutectic systems was performed to gain insight on its solid↔liquid phase transformation reproducibility and behavior under extreme temperature ramps typical of SA tests. Moreover, eutectic cells can greatly diminish the impact of temperature-sensor-drift (aging) by providing a practical mean for on-site calibration of thermometry instruments, instead of more time-consuming recalibration at manufacturer facilities or metrology labs. Additionally, if coupled with thermometers they can serve as in situ reference points and aids for post-test correction of thermal data, i.e. they can be used as fixed points for in situ corium-melt temperature measurements.

2.1.2 Development of Refractory Alloy Protective Sheath in Contact with Molten Corium

In order to render a material that can perform under the very high temperatures and aggressive environments experienced in VULCANO MCCI tests, an extensive literature search and experimental work on liquid metal corrosion was performed to find a material with adequate properties to resist molten metallic/oxide corium. In parallel, this research will expand the thermodynamic database on this complex system for computer phase diagram estimations, and to obtain information on some mechanical properties and corrosion behavior of this metallic system. Consequently a refractory alloy system was explored as a possible candidate for in-melt thermocouple sheath.

2.2 Concept of Temperature

2.2.1 Temperature as a Physical Quantity and its Thermodynamic Basis

Among some of the most essential physical quantities, i.e. length, time, mass and temperature, the latest was for a long time the least understood, and it was not until relatively recent times that the more formal notions of temperature and methods to measure it were envisaged. The first attempts to establish a temperature scale were through the measurement of different substances' response to temperature changes, for example the expansion of gases like air as a function of temperature, and the liquid-expansion thermometers utilizing alcohol or mercury in a glass vial. In a simplistic way temperature can be defined as a measure of the hotness or coldness of a body, but in the fact that temperature is an intensive quantity, (i.e. it is independent of the size of the system or material present, and its non-additive) has render it more difficult to elucidate, even though it has great influence on the properties of matter, i.e. physical, chemical, optical, acoustical, mechanical, electrical, magnetic properties of materials. Temperature is formally defined as that thermodynamic quantity that takes the same value when two systems are brought into thermal contact and are allowed to reach thermal equilibrium. The heat might be transferred through physical contact, via a heat-conducting medium and/or by irradiation of heat. The basic unit of temperature, according to the Système International d'Unités (SI) is the Kelvin (K) which is an absolute temperature scale, opposed to the degree Celsius (°C), also called centigrade, temperature scale that is based on the triple point of pure water (0.01°C or 273.16K) temperature at standard pressure (1 atmosphere). Nonetheless, in order to maintain consistency the Kelvin has the same magnitude as the °C. The lowest possible temperature in the Kelvin scale is the 0 K, being the state of zero atomic vibrational motion or zero volume of a gas, and it corresponds to -273.15°C, and it is based on the ideal gas temperature relationship or ideal gas law:

$$PV = nRT \qquad \textbf{(1)}$$

An ideal gas is composed of randomly moving particles that do not interact among them, in reality noble gases and lighter gases like hydrogen, nitrogen and oxygen behave ideally under certain

limits but deviate from an ideal gas behavior under very low temperatures or high pressures and concentrations. Nevertheless, the ideal gas law denotes the state or behavior of a fixed quantity of an ideal gas, n, (number of moles, usually 1 mole is utilized for practical reasons), undergoing changes in pressure (P), volume (V) and/or temperature (T) and the relationship among these variables; R refers to the universal gas constant (8.314472 J/mole K). Nonetheless, lately there has been an endeavor to define the Kelvin in terms of fundamental constants [6]. Nevertheless, due to its simplicity and empirical/theoretical soundness the ideal gas law is widely used in the treatment and analysis of thermodynamic systems, since it can be related to the concept of internal energy of a system (U) or state, and its dependence on pressure, volume and temperature changes, i.e. U = U(P,V,T). For example, the evolution of thermodynamics was tied to the understanding of the relationship between heat and work and its relationship to internal energy of a closed system. We can clarify this by looking at mathematical statement of the first law of thermodynamics:

$$\Delta U = q - w \qquad \textbf{(2)}$$

This equation establishes a relationship between the changes in the internal energy (U) of a closed system as a function of added heat (q), and the subsequent subtracted work (w) or work performed by the system (usually called the P-V work, since it only takes into account compression-expansion work). The analysis of the first law of thermodynamics states the concept of energy conservation, and sets the notion of energy transit in the form of heat and work. Furthermore, through analysis of the Carnot engine cycle, Lord Kelvin proposed and association between temperature and heat presented on the following equation:

$$Q_2/Q_1 = T_2/T_1 \qquad \textbf{(3)}$$

This is a straightforward correlation between an energy exchange in the form of heat and a corresponding change in temperature of a closed system, which can be also regarded as the relationship between temperature and the internal energy of a system. Furthermore, concepts as the heat capacity of a substance, C, where:

$$C = q/\Delta T \qquad \textbf{(4)}$$

In the previous equation we can observe the relationship between added/extracted heat from a substance and a corresponding temperature change, except under a phase transformation where all the heat is being exhausted or given up (endothermic/exothermic) in the reaction, and temperature is invariant. Therefore, in order to describe changes of the total energy of a variety of systems (isobaric, isochoric, isothermal, adiabatic), and non-cyclic processes like chemical reactions were $\Delta U \neq 0$, other state functions have been derived to be able to gain more insight into the evolution of the system through its different stages. For example, enthalpy *(H)*, is function of state which relates to the change in total energy or amount of heat evolved/absorbed in a system undergoing volumetric changes at a constant pressure (H = U + PV) **(5)**. Another important thermodynamic term is entropy *(S)*, which can be regarded as the measurement of the irreversibility of a process, and it can be quite helpful when measuring the degree of irreversibility of a chemical reaction, like oxidation-reduction. It can be also looked at as the degree of disorder in a system, for example a pure substance in its liquid state will usually have higher entropy, due to the fairly disordered distribution of its particles, than the same substance in a solid state, were a more ordered crystalline state is present ($dS = \delta q_{rev}/T$) **(6)**. Also, for an isothermal-isobaric process the change in enthalpy of the substance can be related to the entropy change in the following manner: $\Delta S = \Delta H/T_m$ **(7)**.

Nonetheless, it is important to be able to conveniently utilize and relate thermodynamic principles between theory and practice, therefore, the derivation of auxiliary functions has been pursued in order to adapt to a variety of environment were systems are under different conditions. Among several ways of representing the equilibrium states of existence of a system, the constitution or phase diagrams are widely used due to the important information which can be extracted from these graphs and its convenience of use. These diagrams are based on equilibrium through minimization of the Gibbs free energy of the system. The substance state is based on the combination of potentials of intensive thermodynamic properties as temperature, pressure and the chemical potential of the different species present; the previous determine the equilibrium state and also acts as

the driving force towards the systems' lowest energy configuration. Isobaric diagrams are the most popular phase diagrams since a substance's equilibrium state, (liquid, solid, crystalline configuration), can be traced as a function of temperature and chemical composition variations [7-9].

Therefore, it can be concluded that temperature is an essential and convenient parameter for the understanding of a system's thermodynamic behavior as it goes through transients and various equilibrium states.

2.2.2 International Temperature Scale: Ag, Au, Cu fixed points & Plancks Radiation Law

The International Temperature Scale was first introduced in 1927 and it was based on the assignment of values to a selected number of fixed points based on very reproducible phase equilibrium temperatures, as triple, freezing, melting and boiling points of selected substances. They were sensibly distributed and interpolation among them is utilized with specified type of thermometers (i.e. platinum resistance thermometers) and assigned formulae. This scale has evolved through time in order to improve its accuracy and agreement with thermodynamic temperatures, being International Temperature Scale (ITS-90) the most current.

The high temperature side of the ITS-90 is defined using the equilibrium freezing point of silver (961.78°C), gold (1064.18°C) and copper (1084.62) at a standard pressure of 101325 Pa (1atm) as reference points. Above the solidification temperature of silver, T_{90} is defined using Planck's radiation law,

$$\frac{L_\lambda(T_1)}{L_\lambda(T_2)} = \frac{\left(exp\left(\frac{c_2}{\lambda T_2}\right)-1\right)}{=\left(exp\left(\frac{c_2}{\lambda T_1}\right)-1\right)} \quad \textbf{(8)}$$

where T_2 refers to any of the three metals' freezing point, L_λ is the spectral radiance (in vacuum) of a blackbody at the specified wavelength, λ, of either T_1 (the unknown temperature) and T_2 (T_{90} reference point), and finally c_2 is the second radiation constant (0.014388m.K). Therefore, high temperature measurements can be performed through the employment of a calibrated monochromatic

optical pyrometer focused on the hot body to be measured [5, 9]. Nonetheless, there are ongoing activities towards an updated ITS which will extend the scale to higher temperatures through the introduction of higher-temperature physical points [10].

2.3 High-Temperature Measurement (>1400K)

As it was previously mentioned, the ITS is based on the utilization of diverse phase equilibrium temperatures of substances as reference points to establish the scale. For example, it utilizes the vapor pressure of liquid ^{3}He and ^{4}He from 0.65 to 5 K, being the lowest achievable temperature, going through the triple point of water at 273.16K up to the melting point of copper at 1357.77 K. Above this temperature and due to the absence of a method that complies with the stringent demands of the ITS (repeatability < 10mK), extrapolation of Planck's radiation law above the melting point of copper is still currently the only accepted method. Nonetheless, due to the impracticality of this approach and its inherent drawbacks, i.e. real materials' emissivity depends on temperature, can be directionally dependent as the angle of incidence/reflection changes, can have spectral variations, and depends on thickness and surface finish of material. Therefore the previous parameters will affect emissivity and can introduce significant errors when using monochromatic optical pyrometers for temperature measurements. Consequently, more practical types of thermometers have been introduced, with higher degree of simplicity with, lower cost, and acceptable drift in temperature measurements. These thermometers balance out their advantages and disadvantages, due to the fact that they introduce an error in temperature measurement which can be usually tolerated in most typical industrial applications and laboratory needs worldwide. These thermal sensors can be categorized in two groups: contact and non-contact thermometers [5, 11].

2.3.2 Contact Thermometers

A contact thermometer needs to be in physical contact with the body or medium whose temperature is being measured. Among the contact thermometers, the resistance thermometers and thermocouples are widely used at low (<0ºC), intermediate (0ºC<T<1100ºC) and high temperatures

(>1100ºC). The basis of resistance thermometers is the relationship between a material's electrical conductivity and the dependence of this property on temperature. Due to their larger electrical conductivity, metals and alloys are usually the choice for the resistance thermometer sensing material. For example, a metal's electrical resistivity, inverse of conductivity, is directly correlated to temperature, and can be expressed empirically by,

$$\rho_T \; = \; \rho_o \; + \; aT \quad (9)$$

where ρ_o and α, are constants of the particular metal which take into account the initial deformation condition and other crystalline lattice defects of the metal (i.e. internal strains, impurities, vacancies, movement of dislocations, etc.). Increase in thermal vibrations of the atoms and any other phenomena that affects the transport of electrons through the matrix also influences resistivity. Thus, ρ_T is a function of temperature.

Due to its excellent repeatability (<10mK) the standard platinum resistance thermometer (SPRT) is widely used in thermometry labs to set-up standards and for calibration of other thermal instruments.   Over time the cost of the SPRT has diminished owing it to improvements in manufacturing techniques; this has widened its application in other fields besides thermometry labs. Unfortunately, even though platinum has a reasonably high melting point (1772ºC), the SPRT use is only recommended up to the melting point of silver (961.78ºC) and down to cryogenic temperature (< -150ºC). Above this high temperature limit, microstructure defects, coefficient of thermal expansion difference and chemical interaction with other elements in the thermometer assembly (ceramic substrate) will introduce mechanical strains and impurities in the platinum wire, causing it to drift; this can generated erroneous readings that might be unacceptable for use in low tolerance applications as thermal treatment of superalloys used in gas turbine engines and metrology. Other metal resistance thermometers which can perform as well as or outperform SPRT in specific temperature ranges have become available; among them we have the Cu, Pt-Rh, Rh-Fe, Pt-Co, Ni and its alloys resistance thermometers. Unfortunately, as well as Pt, any metal will inherently suffer from degradation if used

outside its scope of intended application, thus restricting its use to specific environments and temperature limitations. Additionally, other types of thermometers that also depend on changes in the electrical conduction of a material as a function of temperature have been introduced, i.e. thermistors and semiconductor thermometers. These devices use semiconducting materials like germanium, carbon and some metal oxides as the thermal sensing lead. Semiconductor materials depend on the conduction of electrons/vacancies between their filled valence band across the band gap up to their empty conduction band; since the mobility of electrons and vacancies is influenced by temperature variations, a relationship can be established between current flow and temperature [5, 12].

Moreover, we will continue with the introduction of other type of thermometers, previously mentioned, which are called thermocouples. Thermocouples, as it name infers, are composed of two distinct metallic wires (A and B) joined at its tips (below 1 and 2), one called the hot junction (temperature sensing point) and the other one the cold junction (kept at a known constant temperature). The thermocouples rely on the thermoelectric potential or Seebeck effect as the physical principle. For example, if the junctions are exposed to different temperatures, a small current will flow around the circuit, producing an electric potential. The magnitude of the thermal electromotive force (emf) will depend on the compositions of the conductor wires and temperature difference, ΔT, between the junctions.
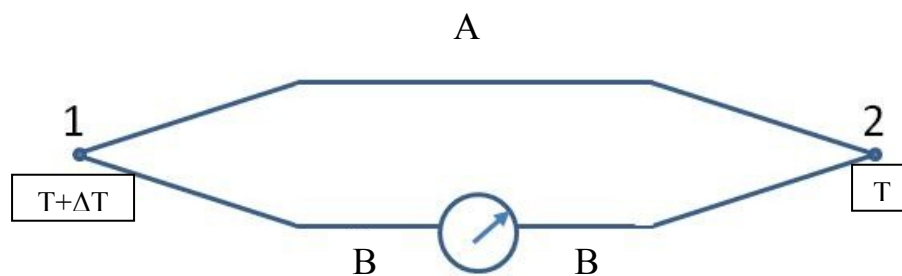
Figure 2.1. Electric circuit used for Seebeck and Peltier effect explanation.

On the other hand, the contrary of the Seebeck effect is the so-called Peltier effect. By analyzing the same circuit as before (but replacing the ammeter by a battery), Peltier observed that a

temperature difference is produced among the junctions (1 and 2) when a current flows through the circuit. The magnitude of the temperature difference depends on the intensity and direction of the current, *I*. The Peltier relationship is the following,

$$\Phi \ = \ PI \quad \textbf{(10)}$$

where *P* is the Peltier coefficient or constant of proportionality (in watts/amperes or volts), in this equation *I* is the current in amps, and finally the heat flow is represented by Φ (in watts or joules/sec). On the other hand, Thomson observed that when there is a temperature gradient along a single conductor and a current is flown through it, the heat content or flow is depends on the current *I* and the ΔT gradient. Therefore, Thomson developed the following relationship:

$$\Phi \ = \sigma \cdot I \ \cdot \varDelta T \quad \textbf{(11)}$$

In this equation, sigma is the Thomson coefficient (in WA/K or V/K). Finally, by combining the Peltier and Thomson relationships we can calculate the electromotive force magnitude or thermoelectric potential of the Seebeck effect caused by the temperature difference, ΔT amongst the two junctions (1 and 2) in the previous scheme.

$$E \ = \ \frac{dE}{dT} \cdot \ \varDelta T = P(T + \varDelta T) - P(T) + \sigma_A \ \cdot \varDelta T - \sigma_B \ \cdot \varDelta T \quad \textbf{(12)}$$

Physically, depending on the metal or alloy, thermocouples are designed and calibrated so one of the legs has a positive absolute thermoelectric power (ATP) relative to the other one, with a negative ATP. Therefore, as the temperature difference among the hot and cold junction increases, there will be a respective increase in the ATP difference among the positive and negative legs' that can be translated into a temperature reading. Tables can be found were either an ATP value or thermal emf (against the Platinum standard at 0ºC) of various metals and alloys are presented.

There are a variety of commercial thermocouple pairs available that can be utilized from low temperature up to intermediate or high temperatures. The choice of thermocouple largely depends on the demands regarding the tolerable temperature measurement error, the service temperature, and

working environment. Table 2.2 presents some thermocouples that can be utilized at moderate to high temperatures:

T/C Type	Positive Leg	Negative Leg	Temperature range ºC	Error, %	Service Environment Details
R	87Pt13Rh	Pt	0 to 1500 (1600)ºC	0.25	Oxidizing or Inert
S	90Pt10Rh	Pt	0 to 1500 (1600)ºC	0.25	Oxidizing or Inert
B	87Pt13Rh	Pt	0 to 1750 (1800)ºC	0.50	Oxidizing or Inert
K	NiCr: Chromel	NiAl: Alumel	0 to 1250 (1300)ºC	0.75	Lightly Oxidizing/Reducing, Inert or Low Vacuum
N	NiCrSi: Nicrosil	NiSi: Nisil	0 to 1250 (1300)ºC	0.75	Same as Type K, better stability at high temperatures
C	W5Re	W26Re	0 to 2100 (2300)ºC	1.00	Vacuum, Inert, Hydrogen, Non oxidizing
D	W3Re	W25Re	0 to 2300 (2500)ºC	1.00	Vacuum, Inert, Hydrogen, Non oxidizing
G	W	W26Re	0 to 2500 (2700)ºC	1.00	Vacuum, Inert, Hydrogen, Non oxidizing

Table 2.2. Compilation of thermocouples for intermediate and high-temperature use.

Furthermore, there is a family of Mo-Re thermocouples which is largely utilized to monitor the temperature in nuclear reactor or neutron flux environments. They can also be used up to moderately high temperatures (<2000ºC), and they pose several advantages over the tungsten containing thermocouples. For example molybdenum is more chemically stable than tungsten when in contact with reactor structural and coolant materials (i.e. carbon containing media). Also, molybdenum has a lower macroscopic absorption cross-section ($0.173cm^{-1}$) than tungsten ($1.21cm^{-1}$). And finally molybdenum, as well as tungsten, can be rendered more malleable through alloying with rhenium. Lately, investigations on the feasibility of utilizing molybdenum/niobium thermocouples for in-pile temperature monitoring have been pursued. This has been partially due to the increased service temperature of new generation of nuclear fission reactors, and scaling up of fusion reactor size and power density. Additionally, the increasing demand on stricter and more meticulous temperature control of irradiated samples in experimental reactors for R&D as well as for the production of isotopes for the medical industry [5, 12-16].

2.3.3 Non-Contact Thermometers

If correctly utilized non-contact thermometers, as radiation thermometers, are capable of providing very accurate temperature measurements under very difficult environments which sometimes render difficult or impossible the employment of any other temperature measurement

technique. They posses many advantages over contact thermometers, especially at high temperatures and in reactive environments, since they are not in physical contact with the substance whose high temperature is being measured. This will avoid the need for any intimate physical contact between the sensor and the media that could produce unwanted mechanical, chemical, and thermal interactions that could disturb, contaminate and influence the behavior of the thermometer and/or the system of interest. Unfortunately, non-contact thermometers only measure the surface temperature can be monitored, and not the interior or body surface of opaque media. However, optical thermometers pose several advantages over contact-thermometers specially when dealing with surfaces those posses a near black-body behavior, since in this case radiation laws can be easily applied. Nonetheless, in real life most of the situations are far from ideal, and departure from black-body conditions are usually the case, therefore it is important to understand the effect of changes in emissivity, absorption, and/or reflection of the material being measured. Therefore, it is important to understand the basis of their functionality, since this will be of great aid in selecting the adequate radiation thermometer for the job, not to forget it will also help interpret and reduce the influence of any optical or radiative phenomena arising from the system being monitored. Failure to do this could defeat the purpose of utilizing a radiation thermometer, because erroneous temperature measurements could lead the user to misinterpret temperature data. This could mislead into wrong conclusions tied to technical research, and/or frustration as a result of losses in the manufacturing line resulting from awkward temperature data.

Every radiation thermometer depends on the measurement of the total or partial thermal radiation emitted by a surface or body, in order to deduce a temperature measurement. Practically all objects emit electromagnetic radiation depending on the electronic, vibrational, and rotational energy levels of their constituent atoms or molecules. The electromagnetic spectrum covers the range from the relatively long radio waves, passing through the infrared and visible, down to the cosmic rays (10^{-14} m) (see figure 2.2). In order to refer to distinctive parts of the electromagnetic spectrum, it has been divided into different segments based on their wavelength (λ in meters), or frequency (in hertz or

cycles per second). Thermal radiation energy is nothing else than electromagnetic waves, flowing through space in the form of photons; as they traverse space these light quanta can interact with other objects and media encountered in their path (absorption, emission, scattering). Thermal radiation includes the electromagnetic waves emitted between the microwave (λ = 1 mm), and the whole visible spectrum (λ = 0.38-0.78 μm), but usually the portion utilized in radiation thermometry is limited to 0.5 up to 20 μm.
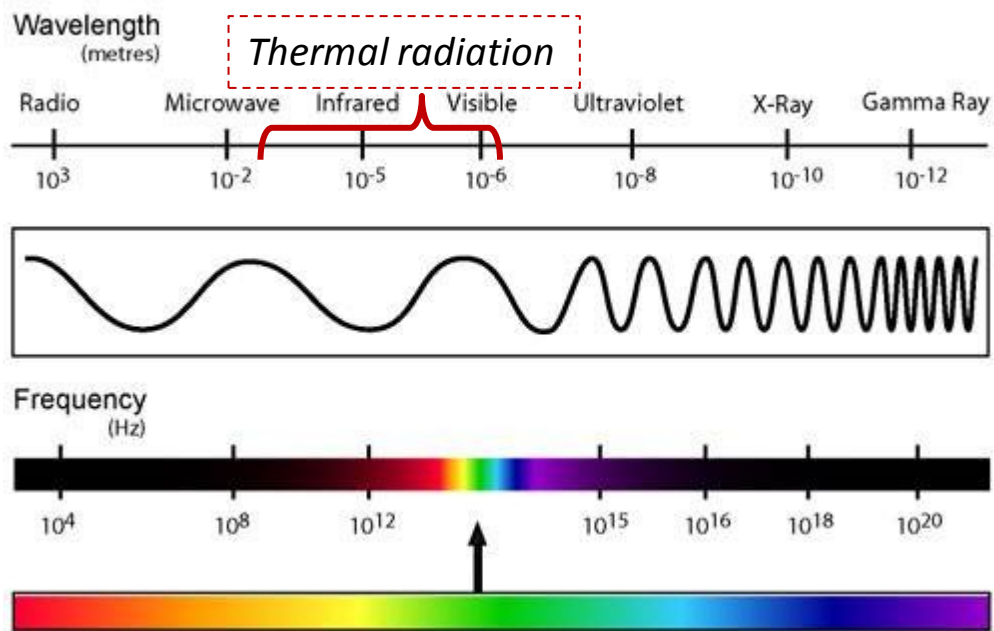
Figure 2.2. Electromagnetic spectrum [11].

Pyrometry relies on comparing real bodies with an ideal blackbody radiator, which is defined as a body that absorbs all radiation incident on it, irrespective of the wavelength, radiation energy direction, and polarization state. Similarly a blackbody always emits the maximum amount of radiation or radiant flux per unit area at any temperature (in both integrated and spectral fluxes). This leads to the following relationship,

$$\alpha = \varepsilon = \alpha_\lambda = \varepsilon_\lambda = 1 \quad \textbf{(13)}$$

where α is absorptivity (or absorptance) and ε is emissivity (or emittance). Furthermore, a blackbody is defined as a perfectly diffuse radiator, which means that it emits the same amount of radiant energy in any direction, at any wavelength. According to Stefan-Boltzmann law, the total emissive power of a black body in vacuum (neglecting the index of refraction of the medium) is,

$$M_b = \sigma T^4 \quad \text{(14)}$$

where M_b is in W/m^2, T is the absolute temperature of the body and σ is the Stefan-Boltzmann constant (5.670400x10^{-8} W·m^{-2}·K^{-4}). After Boltzmann's statistical thermodynamics formulation, we will now introduce Planck's theoretical expression of the spectral blackbody emissive power or spectral radiant exitance.

$$M_\lambda = \frac{2\pi h c^2}{n^2 \lambda^5 \left[\exp\left(\frac{hc}{n k_B \lambda T}\right) - 1\right]} \quad \text{(15)}$$

where h is Planck's constant (6.62606896x10^{-34}J·s) and k_B is Boltzmann's constant (1.3806504x10^{-23}J/K) and n is the index of refraction ($n = c_o/c$) which refers to the ratio of the speed of light in vacuum to its speed in any other media (i.e. air, vapor, other gases). For most engineering applications the index of refraction of air or other diatomic gases (i.e. H_2, N_2, O_2) is considered as unity, since they weakly interact with the emitted electromagnetic waves considered in the thermal radiation waveband. To simplify the previous equation it is better to formulate Planck's law substituting with the radiation constants, $C_1 = 3.7418\cdot10^{-16}$ and $C_2 = 1.4387\cdot10^{-2}$ and considering n equal to 1.

$$M_\lambda = \frac{C_1}{\lambda^5 \left[\exp\left(\frac{C_2}{\lambda T}\right) - 1\right]} \quad \text{(16)}$$

Furthermore, since in pyrometry we usually deal with low values of λT ($\exp(C_2/\lambda T) \gg 1$) it is practical to introduce Wien's approximation of Planck's law:

$$M_\lambda = \frac{C_1}{\lambda^5 \left[\exp\left(\frac{C_2}{\lambda T}\right)\right]} \quad \text{(17)}$$

Finally, a very useful equation, called Wien's displacement law, can be obtained by differentiating Planck's distribution law:

$$\lambda_{max}T = C_3 = 2897.7686 \ \mu m \cdot K \quad \textbf{(18)}$$

This simple equation, is the solution to Wien's transcendental equation #17, and is very practical since it serves to directly calculate the peak emission wavelength or temperature at which the maximum of the Planck's curve occurs. This is important to know since the wavelength at which the intensity of irradiation is the maximum, (λ_{max}), is an indication of the temperature of the radiating object. See figure 2.3.
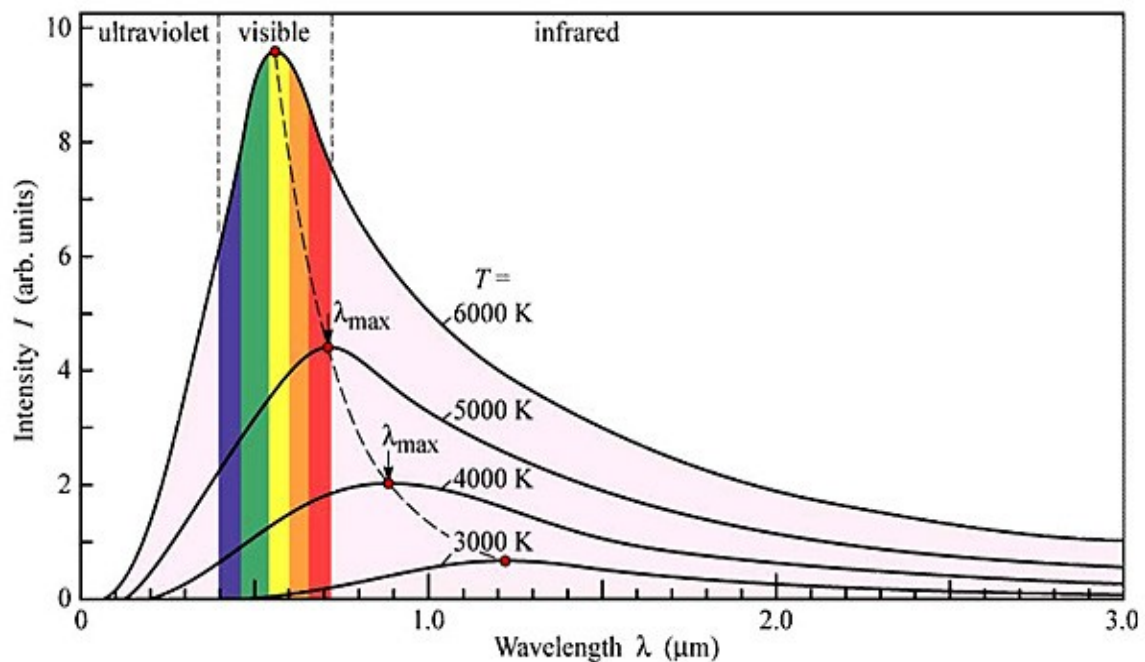
Figure 2.3. Black-body radiation curve and peak emission wavelength [11].

Even though, a real body will always emit less radiant energy than an ideal blackbody at the same temperature, by introducing a proportionality factor pyrometry makes use of the previous equations to estimate a real body's temperature. This factor is the real body's emissivity $\varepsilon_\lambda\ (\theta, T)$, and will always be less than 1; also it will depend on the observation angle and temperature. In

thermometry the spectral radiance of a real body is the basis for temperature calculation of optical sensors and is defined as:

$$L_\lambda = \frac{\varepsilon_\lambda\,(\theta,T)\cdot M_\lambda}{\pi} = \frac{\varepsilon_\lambda\,(\theta,T)}{\pi} \cdot \frac{2\pi h c_\circ{}^2}{\lambda^5\left[\exp\left(\frac{hc_\circ}{nk_B\lambda T}\right)-1\right]} \quad \textbf{(19)}$$

Now we will go through the principles of operation of several types of radiation thermometers. Radiation thermometers can be broadly classified into four categories:

Total-radiation thermometers

They measure the radiant energy in a broad waveband, and they have the advantage of being able to focus a large amount of energy at any temperature. Adversely, since they operate over a large spectral interval, it can be easily affected by sighting distance and atmospheric conditions such as moisture in the air, dust, or smoke and thus provide faulty data. This type of pyrometer relates the output signal *S(T)* to a blackbody source through the use of the following equation,

$$S(T) = F \int_0^\infty L_\lambda(T)s_\lambda d\lambda \quad \textbf{(20)}$$

where F is a constant tied to the geometrical factor that depends on the optical system, L_λ is the spectral radiance of a blackbody, and s_λ is the spectral responsivity of the thermometer, which is based on the transmittance of the optical components and detector responsivity. Assuming s_λ as being wavelength independent, the previous equation can be integrated and expressed in a more the familiar Stefan-Boltzmann format as:

$$S(T) = F' \int_0^\infty L_\lambda(T)d\lambda = \frac{F'\sigma T^4}{\pi} \quad \textbf{(21)}$$

This is the interpolating equation for total-radiation thermometers, and *F'* groups all constant factors. Nonetheless, the only way to realize a true thermometer of this kind is by using aperture optics and a blackbody detector, otherwise (as in industrial applications) the condition of constant responsivity is not fulfilled due to the lenses and/or mirrors and non-blackbody detectors. In this case

the previous relationships must be replaced by an empirical relationship correlating the thermometer and the target temperature.

Single-waveband thermometers

Also called monochromatic thermometers, they measure radiation energy in very narrow waveband range of the thermal spectrum. This can be advantageous since a precise waveband can be selected through the use of of filters in order to perform temperature measurements on materials with selective waveband optical properties. For example, glasses and plastics, are transparent at long and particular wavelengths, but are opaque or reflective in rather short wavelengths or outside the windows of strong transmittance in certain narrow spectral bands, respectively. Furthermore, the monochromatic pyrometer's wavelength can be carefully chosen such that as much as possible reduction on the interference of participating media can be achieved. For example water vapor (H_2O_{vapor}), carbon mono/dioxide (CO/CO_2), methane (CH_4) and other non-diatomic gases are show a strong absorption, emission and scattering of radiative energy are strongly wavelength dependent and they are the strongest at definite wavebands (also called atmospheric windows to refer to gases commonly found in the atmosphere). Additionally, sometimes significant interference can be encountered due to fine particle in environment between the sensor and the surface of interest (i.e. from combustion of fossil fuels and coal, or aerosols above any high temperature pool). Through careful selection of a pyrometer with an effective wavelength, which is significantly longer than the size of the air borne particles, we can strongly reduce any interference (i.e. scattering) on the emitted electromagnetic waves as they traverse the space between the irradiating body and the optical sensor. Anyhow, the criteria to select the best narrowband should be made taking into account the compromise between sensitivity and accuracy loss as the wavelength increases. Additionally, the ε_λ is an important parameter that influences the choice of narrow-waveband λ. Nonetheless, there is usually more concern on the effect of the measurement conditions since it has a more intense impact on the accuracy of the measurement.

Moreover, even though in reality single-waveband thermometers work in a very small waveband they are represented by a single wavelength, which is called the effective wavelength. This will avoid us the integration of equation(x), and we can rather utilize the following simple relation,

$$S(T) = GL_\lambda(T) \quad \textbf{(22)}$$

where and the utilization of the effective wavelength is necessary and G includes geometric and responsivity factors. Finally, in order to calculate the temperature of the surface of interest we derive Wien's approximation of Planck's law and use the following equation:

$$T = \frac{1}{\frac{1}{T_\lambda} + \frac{\lambda}{C_2} \ln \varepsilon_\lambda} \quad \textbf{(23)}$$

Where λ is the effective wavelength, ε_λ is the spectral emissivity of the surface, T_λ is the radiance temperature and T is the true temperature (T_λ is always $< T$ except when the source is a blackbody $\varepsilon_\lambda = 1$).

Ratio thermometer

Also addressed as bichromatic pyrometers, they measure the ratio of the energy in two narrow wavebands (wavelengths λ_1 and λ_2). This type of thermometer possesses several advantages over the previous two since it does not depend on the target size, emissivity and optical path obscuration, provided these are the same over the two wavelengths (*grey-body* condition), which is not usually the case for most materials and media. The sensitivity and accuracy is inferior than the monochromatic thermometers for the same spectral region. They are usually not used for laboratory precision measurements, but they are often preferred in applications were emissivity is not know or there is a considerable departure from blackbody conditions. We will know go through the measuring principle of the two-color thermometer, and the basic equation is,

$$R(T) = G' \frac{\varepsilon_{\lambda_1} L_{\lambda_1}(T)}{\varepsilon_{\lambda_2} L_{\lambda_2}(T)} \quad \textbf{(24)}$$

where *R(T)* is the ratio of the spectral radiance at the two different wavelengths times *G'* a constant that represents the ratio of the spectral responses at each wavelength and geometrical factor, finally ε_{λ_1} and ε_{λ_2} correspond to the spectral emissivity at each wavelength. By applying a similar treatment as for single-waveband thermometers we can calculate the true temperature of a body with monitored by a ratio thermometer with the following equation:

$$T = \frac{1}{\frac{1}{T_R} - \frac{\lambda_1 \lambda_2}{C_2(\lambda_1 - \lambda_2)} \ln \frac{\varepsilon_{\lambda_1}}{\varepsilon_{\lambda_2}}} \quad \textbf{(25)}$$

where T_R and T are respectively the measured and calculated true temperature, and the rest of the variables/constants have already been previously introduced.

Multi-waveband thermometers

They permit the implementation of more complex emissivity-wavelength relationships to avoid the problems encountered by ratio thermometers due to differences in emissivity of the material at different wavelengths, and when more information on the emitted radiation is needed. Anyhow, there is a consequent decrease in sensitivity and accuracy of the measurements, and it also entails an augmented complexity and increased measurement precision requirements. Therefore, they should only be utilized in special situations where their use is justified, and if it allows the elimination of emissivity dependence in the measurement. For example, a three-wavelength thermometer is preferred if the emissivity of a material varies linearly with wavelength, and the wavelengths are selected such that the following relationships hold true over the range of interest: $\lambda_2 = (\lambda_1 + \lambda_3)/2$ then $\varepsilon_{\lambda_1} \cdot \varepsilon_{\lambda_3} \approx \varepsilon^2_{\lambda_2}$. In this case the ratio thermometer becomes independent of emissivity since the ratio equation is the following [5, 11]:

$$R = \frac{\varepsilon_{\lambda_1} \varepsilon_{\lambda_3}}{\varepsilon^2_{\lambda_2}} \cdot \frac{L_{\lambda_1} L_{\lambda_3}}{L^2_{\lambda_2}} \quad \textbf{(26)}$$

2.4 Severe Accident Research and Test Section Instrumentation at the PLINIUS Platform

  2.4.1 VULCANO Facility –Molten Corium Concrete Interaction (MCCI)

   Among the experimental facilities compromised in the PLINIUS experimental platform for severe accident R&D, VULCANO is devoted to the study of molten corium interaction with reactor pit or basemat concrete materials (MCCI) [1, 17], along with spreading (rheology research) of corium over a variety of ceramic based refractory materials focused on the validation of core-catcher materials. The following section will be devoted to an explanation on the experimental section and instrumentation utilized in the MCCI tests.

   The experimental section in the VULCANO facility (Figure 2.4) is composed of three main parts: oxide melting furnace, metal melting furnace and concrete crucible test section. They are described as follows:
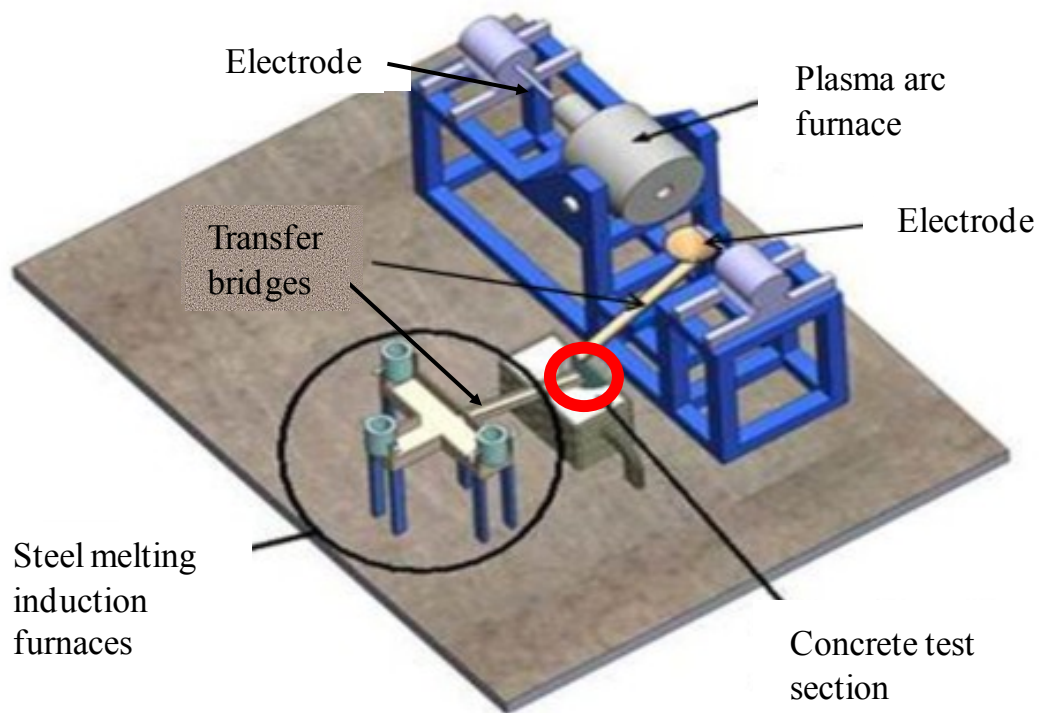
Figure 2.4. VULCANO facility experimental section.

- The drum type rotary plasma-arc furnace (VULCANO furnace) [18-19] (Figure 2.4.) is used to melt the oxide fraction of the corium (UO_2-ZrO_2 based). The rotating furnace is filled through the introduction of straw-type arm that is connected to the container of the oxide mix and it moves back-and-forth in order to produce a more or less uniform layer of powder inside the furnace. This furnace can hold more than a hundred kilograms of refractory ceramic oxides (internal cylinder dimensions Ø: 400mm, length: 600mm), from which almost 90% is melted and transferred into the concrete test section, and the remaining part separates/protects the water cooled stainless steel furnace interior from being in direct contact with the high temperature molten oxide mass (>2800ºC). The self-crucible technique is possible since a primary charge composed of ZrO_2 powder is initially introduced into the furnace and heated up such that enough thermal energy is provided to form a protective layer of sintered zirconia (the adequate sintering temperature is between 80% and 99% of the absolute melting temperature). Additionally, in order to improve the sintering process, the powder needs to be simultaneously heated and under compression, and this is provided by regulating the furnace rotation speed (rpm) which in turn influences the centrifugal forces imposed on the zirconia mass, to produce an adequate compaction of the material. Finally, after each fill-up of the furnace and since the powders density depends on particle size and is always much lower than the theoretical density, it is necessary to perform a couple of filling/melting steps (besides the initial charge of protective zirconia) with increasing urania content to finally produce the desired corium melt composition and afterwards transfer it to the concrete test section. The melting is performed by introducing two electrodes into the drum, initially inerting the furnace interior with argon, which serves as the gas media to formerly ignite the arc and form the plasma that will heat up the oxides through irradiation of heat.

- The high-frequency induction furnace [20] (Figure 2.5.) section is composed of three crucibles with the capacity of holding 8 kilograms of molten stainless steel each one (around

one liter in volume). Cold crucible induction heating technique is utilized, and each unit is composed of a water cooled induction copper coil embedded into a multilayer configuration composed of an exterior refractory ceramic mortar separated by a thinner mica foil (electrical insulator) and a sacrificial adobe interior material (adobe is a natural building material made from sand, clay, water, and some kind of fibrous or organic material) that has been previously compacted (green compaction) into a crucible form and then sintered up to 1500ºC. The 304L-stainless steel (304L-SS) is added systematically to the crucible in the form of spheres and heated just above its melting temperature (~1500ºC), before transferring it to the concrete test section. Temperature of the steel is monitored through the use of two type-C thermocouples implanted in the crucible bottom material, and a bichromatic pyrometer is used to monitor the liquid metal top surface at one of the three crucibles. The crucibles are covered by a ceramic plate in order to improve the heating efficiency, or reduce the heat losses and interaction (oxidation) of the metal by the air in the closed environment. However, we can expect an oxide slag to naturally form on top of the metal that will protect the liquid below from further oxidation. A sketch is shown below of the induction furnace used to melt the 304L stainless steel (SS).
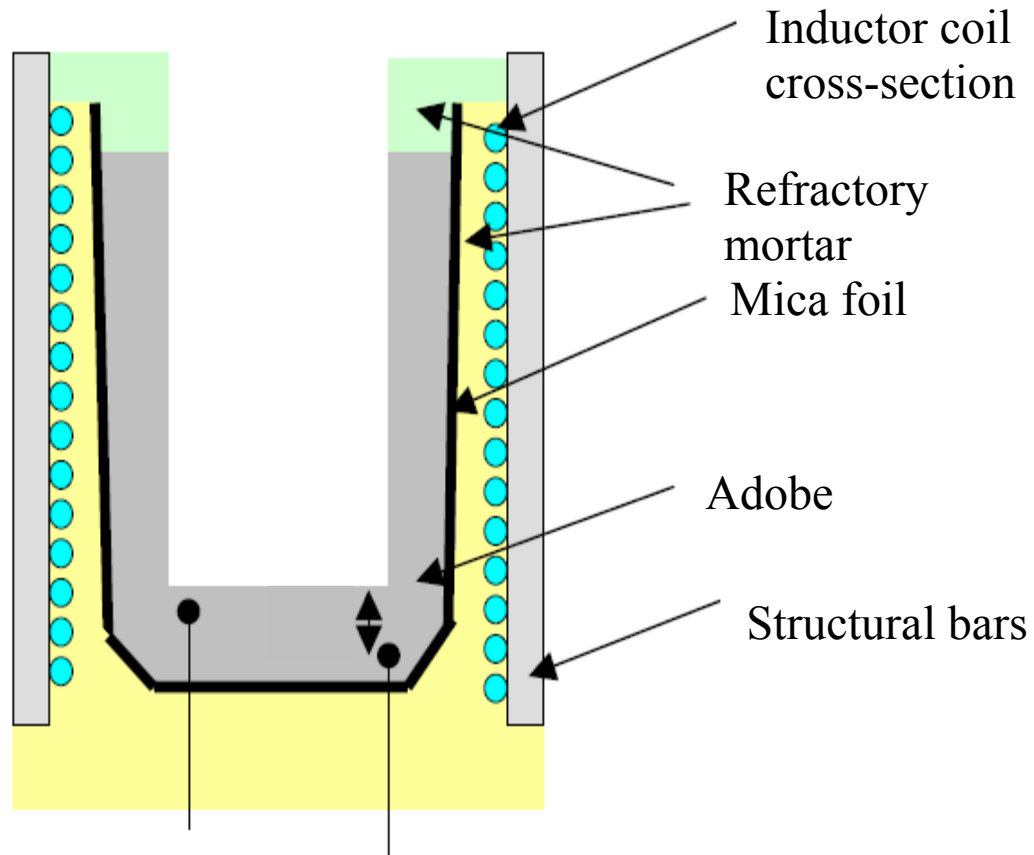
Figure 2.5. VULCANO induction furnace for melting of metallic phase.

- The concrete crucible test section [21] (Figure 2.6 and 2.7.) consists of a concrete block (600 x 300 x 400 mm) with an empty semi-cylinder (Ø: 300mm, height: 250mm) which will catch/hold the molten corium mass. The concrete is usually silica or limestone based concrete (sometimes a more exotic ferrous concrete type is used) which might also contain gravel materials of varying size and shapes. The skeleton of the test section is equipped with more than a hundred type-K thermocouples, and about eight type-C thermocouples (with an added protective refractory sheath made in tungsten or zirconia) that serve to trace concrete ablation front and corium temperature, respectively, they are placed in three azimuths 45º, 90º and 135º. The use of the type-K low temperature thermocouples is very practical since they serve

as markers to trace the concrete ablation front, because their maximum service temperature is in the same range as the concrete ablation initiation temperature (~1300ºC).
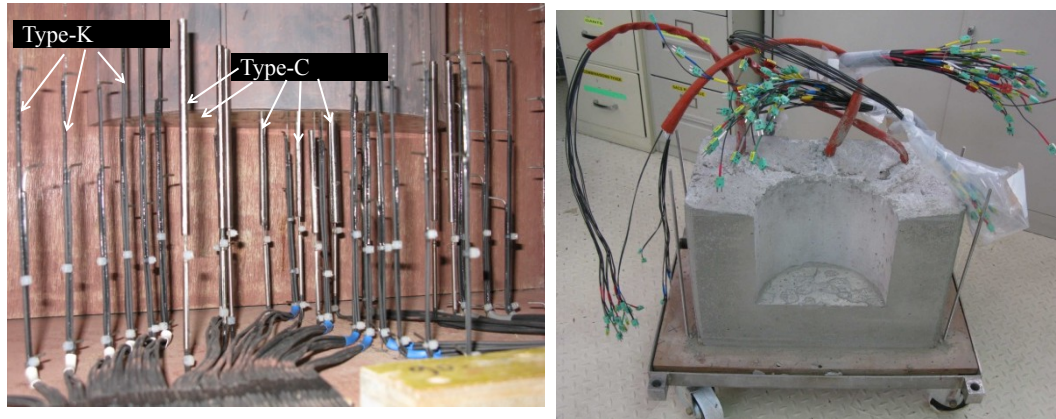
Figure 2.6. VULCANO MCCI test concrete crucible test section.

Moreover, the concrete part is surrounded by a set of zirconia/concrete plates which in turn are surrounded by four water cooled copper coils (only three of them are active induction coils), and a cold copper plate on the bottom. The cooled zirconia plates serve as the ultimate protective barrier in case of an unnoticed corium melt-through the concrete. The poured corium is kept hot using induction heating, since through the use of this novel heating technique (Joule heating) radioactive decay heating can be emulated [1, 17, 20].
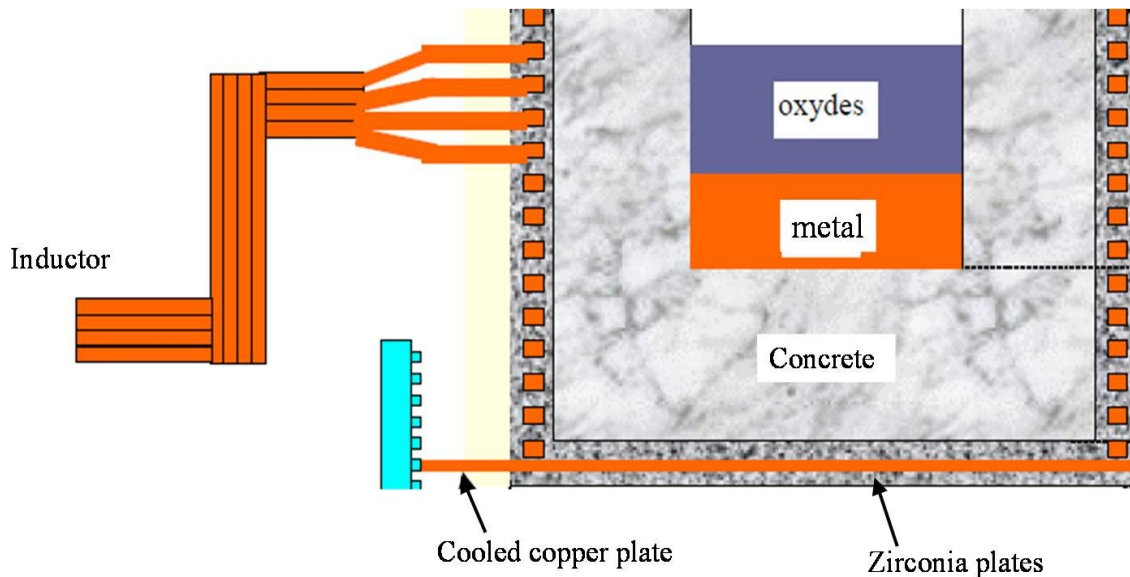
Figure 2.7. Schematic of VULCANO facility induction furnace for residual heat simulation.

Furthermore, in the following section the optical thermometers utilized in VULCANO MCCI tests will be presented with pertinent technical details (Table 2.3) and its point of measurement (Figure 2.8.):

Pyrometer ID	Wavelengths, μm	Tempeature range, ºC	Measurement point
Ircon 1	0.95 & 1.05	700-1800	Inside VULCANO furnace
Impac 1	0.95 & 1.05	1250-3300	Inside VULCANO furnace
Maurer 1	0.92 & 1.04	1000-3000	Centered normal to the test section semi-cylinder bottom
Impac 2	0.95 & 1.05	1250-3300	Test section center
Impac 3	0.95 & 1.05	1250-3300	Mobile and coupled to a video camera
Impac 4	0.95 & 1.05	1250-3300	At the start of the molten metal transfer bridge
Impac 5	0.95 & 1.05	1250-3300	Inside one of the metal melting furnaces

Table 2.3. VULCANO facility pyrometer details.
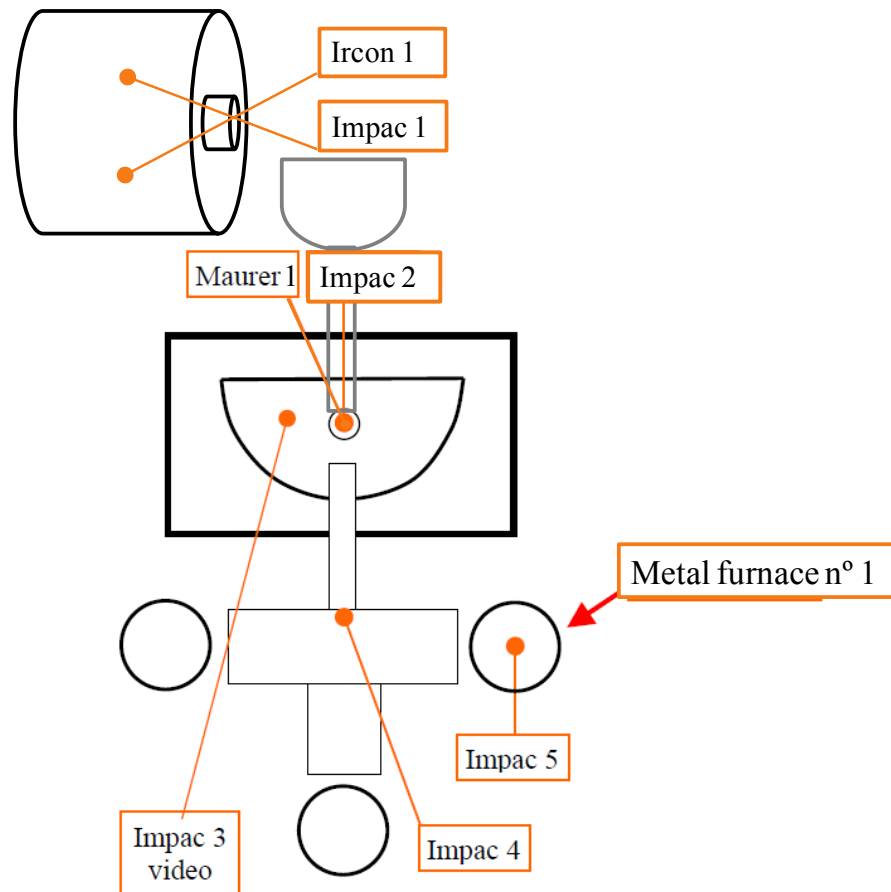
Figure 2.8. Contact thermometers used in VULCANO MCCI test.

It is important to conclude that even though this PhD research on very-high temperature measurements has been focused in the VULCANO MCCI test, the thermometry techniques studied and materials developed can be applied to other experimental facilities in the PLINIUS platform (KROTOS, COLIMA, VITI) at CEA Cadarache. Along with other nuclear reactor safety and severe accident experimental tests in Idaho National Laboratory (INL), Argonne National Laboratory (ANL), Sandia National Laboratory (SNL), among other facilities around the world [22-23].

Chapter 2 - References

1. C. Journeau, P. Piluso, P. Correggio, L. Ferry, G. Fritz, J-F. Haquet, J. Monerris, J-M. Ruggieri, M. Sanchez-Brusset, C. Parga, "Contributions of the VULCANO Experimental Programme to the Understanding of MCCI Phenomena" DOI: 10.5516/NET.03.2012.703 Korean Nuclear Society, Nuclear Engineering and Technology, Vol. 44, No. 3, April 2012, pp. 261-272.

2. R.G. Eldridge, "Water vapour Absorption of Visible and near Infrared Radiation" Applied Optics, April 1967, Vol. 6, No.4, pp. 709-713.

3. E.K. Plyler, "The Infrared Absorption Bands of water Vapor" Physical Review, Volume 39, January 1, 1932, pp. 77-82.

4. J.R. Howell, R. Siegel, M.P. Mengüç, "Thermal Radiation Heat Transfer" 5th Ed. CRC Press, ISBN: 978-1-4398-0533-6, Boca Raton, Florida, 2011, pp. 441-491, 747-785.

5. Eds. W. Göpel, J. Hesse, J.N. Zemel, Vol. Eds. T. Ricolfi, J. Scholz, "Sensors: A comprehensive survey/Vol 4: Thermal Sensors" VCH Verlagsgesellschaft mbH, Weinheim, Federal Republic of Germany, 1990 ISBN 0-89573-676-4, pp. 119-223.

6. J. Fischer, S. Gerasimov, K.D. Hill, G. Machin, M.R. Moldover, L. Pitre, P. Steur, M. Stock, O. Tamura, H. Ugur, D.R. White, I. Yang, J. Zhang, "Preparative Steps Towards the New Definition of the Kelvin in Terms of the Boltzmann Constant" International Journal of Thermophysics, vol. 28, 2007, pp.1753-1765.

7. D.R. Gaskell, "Introduction to the Thermodynamics of Materials" 4th Edition, Taylor and Francis Group, New York, 2003, pp. 1-176.

8. P.R.N. Childs, J.R. Greenwood and C.A. Long, "Review of Temperature Measurement" Review of Scientific Instruments, Vol. 71, Number 8, August 2000, pp. 2959-2978.

9. J. Fischer and B. Fellmuth, "Temperature Metrology" Institute of Physics Publishing, Reports on Progress in Physics, Vol. 68, 2005, pp. 1043-1094.

10. G. Machin, P. Bloembergen, J. Hartmann, M. Sadli and Y. Yamada, "A Concerted International Project to Establis High-Temperature Fixed Points for Primary Thermometry" International Journal of Thermophysics, Vol. 28, pp.1976-1982.

11. J.R. Howell, R. Siegel, M.P. Mengüç, 'Thermal Radiation Heat Transfer" 5th Ed. CRC Press, ISBN: 978-1-4398-0533-6, Boca Raton, Florida, 2011, pp. 1-42, 87-139, 441-491, 747-785.

12. W.D. Callister Jr., "Materials Science and Engineering: An Introduction" 5th edition, John Wiley and Sons, Inc., New York, 2000, pp. 605-616.

13. S. Glasstone and A. Sesonske, "Nuclear Reactor Engineering" ISBN 0-442-02725-7, Litton Educational Publishing, Inc., New York, 1967, pp. 23, 260-269, 804-807.

14. S. K. Danishevskii, S. I. Ipatova, P. P. Oleinikov, L. D. Oleinikova, E. I. Pavlova, N. I. Smirnova, L. I. Trakhtenberg, "Molybdenum-Rhenium alloy Thermocouples" Measurement Techniques, April 1966, Volume 9, Issues 4, pp. 508-512.

15. J.-F. Villard, S. Fourrez, D. Fourmentel, A. Legrand, "Improving High-Temperature Measurements in Nuclear Reactors with Mo/Nb Thermocouples" International Journal of Thermophysics, October 2008, Volume 2009, Issue 5, pp. 1848-1857.

16. J.L. Rempe, D.L. Knudson, K.G. Condie, S.C. Wilkins, "Evaluation of Specialized Thermocouples for High-Temperature In-Pile Testing" INL/CON-05-00944, Proceedings of ICAPP '06, Reno, NV, USA, June 4-8, 2006, paper 6068.

17. L. Carenini, J-F. Haquet, C. Journeau, "Crust Formation and Dissolution during Corium Concrete Interaction" Proceedings of ICAPP 2007, Nice, France, May 13-18, 2007, Paper 7312.

18. C. Jégou, G. Cognet, A. Roubaud, J.-M. Gatt, G. Laffont, F. Kassabji, "Plasma transferred arc rotary furnace for corium melting", J. High Temp Mater. Proc.1, 1998, 409-420.

19. G. Cognet, G. Laffont, C. Jégou, J. Pierre, C. Journeau, F. Sudreau, A. Roubaud "Utilisation d'un four tournant à arc plasma transféré pour fondre et couler des mélanges d'oxydes autour de 2000°C", Ann. Pharm. Fr., vol. 57, 1999, pp. 131 – 136.

20. C. Journeau, P. Piluso, J-F. Haquet, S. Saretta, E. Boccaccio, J-M. Bonnet, "Oxide-Metal Corium –Concrete Interaction Test in the VULCANO Facility" Proceedings of ICAPP 2007, Nice, France, May 13-18, 2007, Paper 7328.

21. Journeau, C., Boccaccio, E. , Jégou, C., Piluso, P., Cognet, G., "Flow and solidification of corium in the VULCANO facility", 5th World conference on experimental heat transfer, fluid mechanics and thermodynamics, Thessaloniki, Greece, September 24-28, 2001.

22. S. Lomperski, "OECD MCCI Project: Enhancing Instrumentation for Reactor Materials Experiments", OECD/MCCI-2002-TR02, pp. 1-7.

23. C. Journeau, "Contribution des Essaies en Matériaux Prototypiques sur la Plate-forme PLINIUS a l'étude des Accidents Graves de Réacteurs Nucléaires" CEA Cadarache, DEN/DTN/STRI/LMA, CEA-R-6189, ISSN-0429-3460, ver. 1, Dec, 2008, pp. 14-77.

Chapter 3. High-Temperature Metal-Carbon Eutectic Fixed-Point Cells

3.1 Metal-Carbon Eutectic Alloys and their Application as Fixed Points

Just after the introduction of the ITS-90, there was a call to find a mean to reduce high temperature measurement uncertainty ($\leq$ 0.1%) above the Ag (961.78°C), Au (1064.18°C) and Cu (1084.62°C) melting point. By extrapolating from these temperature reference points the ITS-90 uses the ratio form of Planck's radiation law as a practical way of achieving a close approximation to thermodynamic temperature. Nonetheless, as temperature increases, uncertainties spread as T^2 introducing inadmissible errors in high temperature applications. Also, the issue of pure substances reacting with crucible material at relatively high temperatures; since the chemical activity of any substance augments with temperature, there is a corresponding increase in the probability of introducing impurities in the fixed point material that will deteriorate its repeatability and long-term stability. Therefore, in order to respond to the demands of high temperature thermometry, Yamada presented in year 1999 the first results on radiometric observations of certain metal-carbon eutectic alloys solid $\leftrightarrow$ liquid transformation (Ni-C, Pd-C, Pt-C, and Ru-C), contained in graphite crucibles with black cavities, as a mean to provide practical high temperature physical temperature references [1]. The use metal-carbon eutectics contained in a graphite cell (or crucible assemblage) possesses multiple advantages:

- A eutectic mixture melts/solidifies at a precise temperature, as a pure substance does; this makes it conceivable for application as a fixed point.

- Undesirable chemical reactivity between the phase change material and the crucible is avoided since the cell material is an intrinsic part of the eutectic alloy system.

- The low cost, ease of machinability, very high temperature sublimation points (the highest of the elements) and inherent graphite properties render it an optimal container material. Graphite can be tailored to improve the cell's mechanical, thermal, and optical performance (not to forget graphite's close to black body radiation behavior which is great for radiation thermometry, emmisivity~1). For example, the eutectic cell can be designed such as to

include carbon-carbon composite fabrics (anisotropic properties) as part of the graphite cell in order to optimize the cells thermal behavior (thermal homogeneity and reduction of heat losses in desired directions).The implementation of adequate black-cavity/thermowell for radiation and contact thermometry.

- The great variety of high temperature metal-carbon eutectic systems expands the choice for the selection of an adequate reference point for the intended application and temperature range of interest. For example above the copper point some of the available metal-carbon eutectics points are Fe-C (1153°C), Co-C (1324°C), Ni-C (1329°C), Pd-C (1492°C), Pt-C (1738°C), Ru-C (1953°C), Ir-C (2290°C) and Re-C (2474°C).

In order to introduce metal-carbon eutectics as secondary reference points into a new ITS and allow for its practical utilization as high temperature reference points in industry, a variety of metrology institutes, universities and industrial partners have engaged in the joint task of conducting research and development in high-temperature metal-carbon eutectic fixed-point cells [2-8, 11-13]. Among several past international projects in this realm, the author of this dissertation has been actively involved in the High Temperature Metrology for Industrial Applications (HiTeMS > 1000°C) project, within the collaboration of CEA as a non-funded partner. The HiTeMS Joint Research project is funded by the European Metrology Research Programme (EMPR) participating countries within the European Association of National Metrology Institutes (EURAMET) and the European Union.

3.1.1 Eutectic System Definition

A eutectic system is a mixture of chemical compounds or elements that have a single chemical composition at a lower temperature than any other composition made up of the same ingredients. In a phase diagram the eutectic is an invariant point fixed by a specific composition (C_E) and temperature (T_E) at which the eutectic mixture transforms upon heating or cooling. The eutectic represents an equilibrium point were the lowest Gibbs free energy is attained for the coexistence of three phases: one liquid phase L with the eutectic composition C_E and two distinct solid phases α and

β with compositions $C_{\alpha E}$ and $C_{\beta E}$ respectively. Therefore, the eutectic reaction is expressed as the following, $L(C_E) \leftrightarrow \alpha(C_{\alpha E}) + \beta(C_{\beta E})$ where a liquid L transforms congruently into two dissimilar solid phases, α and β upon steady cooling, and the inverse reaction takes place upon steady heating [15-16]. A simple binary eutectic phase diagram at standard pressure is shown below (figure 3.1) with the pertinent regions of equilibrium phase stability as a function of temperature and chemical concentration, along with the eutectic point and other important reference lines of transformation:
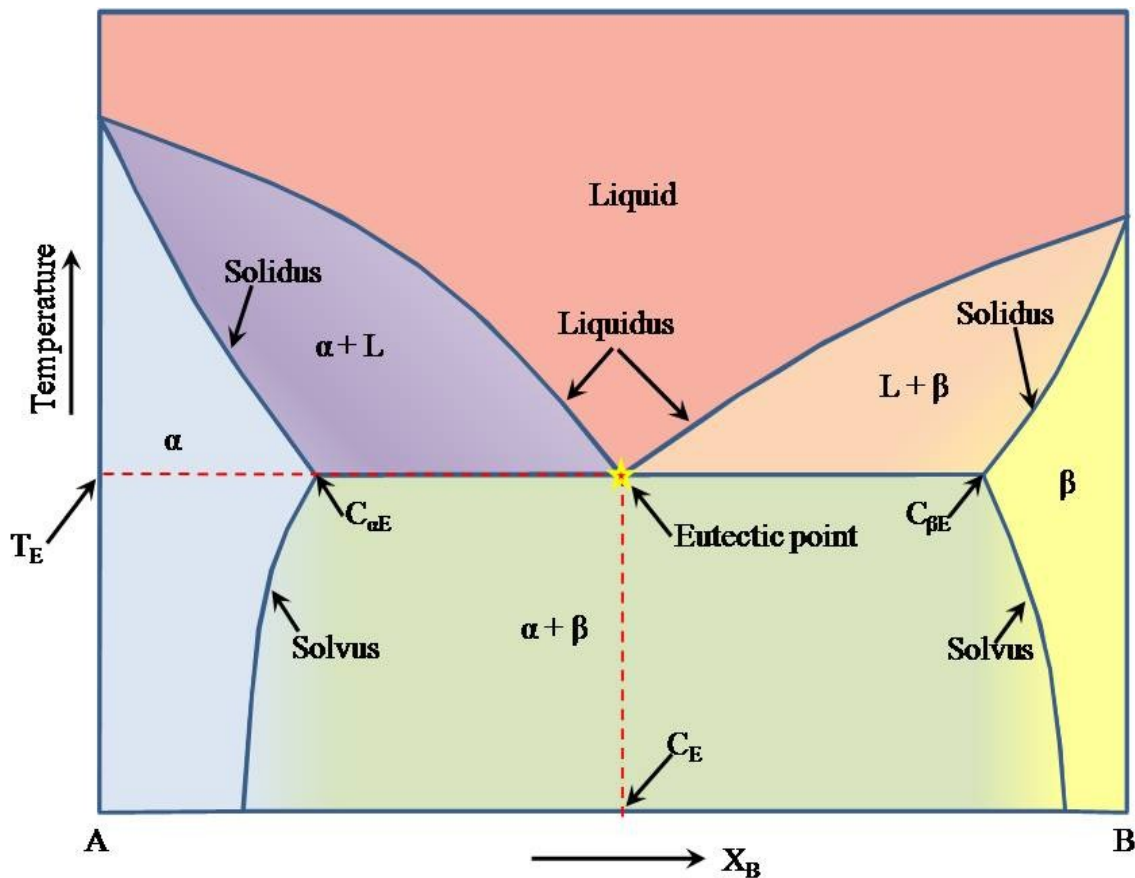
Figure 3.1. An overview of a simple binary eutectic phase diagram.

3.1.2 High Temperature Metal-Carbon Eutectic Alloy Selection

An extensive literature review was performed to conceive a list of known metal-carbon (M-C) eutectic systems above the melting point of copper. Based on scrutiny of the available systems several of them were selected according to the following criteria:

- Priority was given to eutectic points that fell within the solidification range of corium-concrete mixtures, due to their potential as reference points for in-melt thermometry.

- The alloys' eutectic temperature should be evenly spread to cover as good as possible the temperature range of interest, with the aim of facilitating interpolation among them and to improve temperature measurement certainty.

- Another important factor was material availability and price, in order to have more flexibility and less expense in case destructive or one-time use of the cell is unavoidable, as in severe accident tests in which most of the contact thermometers do not survive the end of the experiment.

- It was important to select systems that were in parallel with the research being performed by metrology institutes, especially within the HiTeMS framework, in order to facilitate comparison and discussion over results. This interweave of work would then facilitate and optimize the improvement of cell performance and repeatability thanks to the interdisciplinary collaboration of scientists and engineers specialized in different realms of science.

- Finally, other metal-carbon systems were selected in order to explore more in depth the eutectic transformation behavior of considerably well known simple system under non-equilibrium conditions, along with other less understood complex eutectic systems containing multiple intermediate equilibrium phases. This was done with the sole aim of understanding their response to more pragmatic environments like those commonly found in industrial applications, and to enrich the availability of data for computer code refinement and validation.

In figure 3.2 is shown a curve plotting with several metal-carbon eutectic systems, including the tested systems (encircled) and the selected eutectics (*) along with the molten corium-(silicious) concrete solidification range.
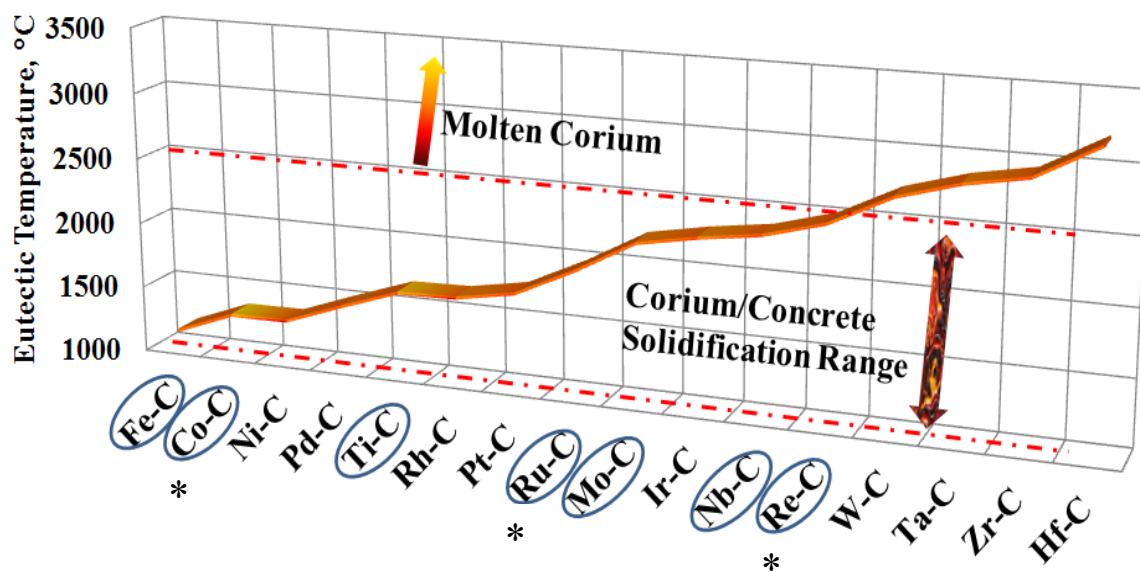
Figure 3.2. This graph highlights several high temperature metal-carbon alloys' eutectic temperature, juxtaposed with the molten corium-concrete solidification range.

Afterwards Table 3.1 contains a summary of pertinent thermophysical and thermodynamic data on various high temperature metal-carbon eutectic systems [1-5, 8, 12-14, 17-25, 27, 51]. These parameters were important for the alloy selection, and interpretation of results for the understanding of the behavior of the eutectic transformation in the systems investigated; highlighted in blue are the systems on which experimental work was performed. The pertinent metal-carbon phase diagrams are contained in Appendix A. Additionally, more details and specifics on the eutectic cells utilized for this study are included in table 3.2 and 3.3.

Material	T melting, °C	Enthalpy of fusion, ΔH, J/g	Heat Capacity, Cp, J/g·K @25°C	Material crystal structure
Fe	1539	247,3	0,449	BCC_1< 912°C FCC < 1394°C BCC_2
Co	1495	272,5	0,45	HCP< 422°C <FCC
Ni	1453	290,3	0,445	FCC
Pd	1555	157,3	0,244	FCC
Ti	1670	295,6	0,522	HCP< 882°C <BCC
Rh	1964	258,4	0,243	FCC
Pt	1768	113,6	0,133	FCC
Ru	2334	381,8	0,238	HCP
Mo	2620	390,7	0,251	BCC
Ir	2450	213,9	0,131	FCC
Nb	2477	323	0,265	BCC
Re	3180	324,5	0,137	HCP
W	3422	284,5	0,132	BCC
Ta	3014	202,1	0,14	BCC
Zr	1855	230,2	0,278	HCP< 886°C <FCC
Hf	2231	152,4	0,144	HCP< 1743°C <FCC
C	3367	9741,1	0,709	Graphite, Hexagonal

Alloy System	Eutectic reaction solid constituents	T eutectic, °C	Intermediate phases, metal carbides
Fe–C	$Fe+Fe_3C$	1153	Fe_3C
Co–C	Co+C	1324	None
Ni–C	$Ni+C, (Ni+Ni_3C)$	1329, (1025)	Ni_3C (metastable)
Pd–C	Pd+C	1492	None
Ti–C	Ti+TiC, TiC+C	1646.5, 2776.4	TiC
Rh–C	Rh+C	1657	None
Pt–C	Pt+C	1738	None
Ru–C	Ru+C	1954	None
Mo–C	$Mo+Mo_2C, \delta MoC+C$	2205, 2589	$\beta Mo_2C, \beta' Mo_2C, \eta, \delta, MoC$
Ir-C	Ir+C	2290	None
Nb–C	$Nb+Nb_2C, NbC+C$	2354, 3364	$\gamma\beta Nb_2C, \beta Nb_2C, Nb_4C_3, Nb_6C_5, NbC$
Re–C	Re+C	2480	None
W–C	$W+\gamma W_2C, \gamma W2C+\alpha WC$	2715, 2747	$\gamma W_2C, \beta W_2C, \alpha W_2C, \alpha WC, WC$
Ta–C	$Ta+Ta_2C, Ta_2C+C$	2774, 3476	Ta_2C, TaC
Zr–C	ZrC+C	2927	ZrC
Hf-C	HfC+C	3180	HfC

Table 3.1. Thermophysical and thermodynamic data on high-temperature metal-carbon eutectic alloys.

3.2 Metal-Carbon Eutectic Fixed Point Tests' Experimental Details

3.2.1 Graphite Crucible Design and Fabrication

One of the challenges for the development of the high temperature metal-carbon eutectic fixed points was to envisage and test a variety of cell designs in order to get some insight on the cell response and robustness under important mechanical stress caused by thermal constraints and constituent material expansion/contraction. Especially for the large temperature variations experienced in industrial and applied R&D furnaces. The design of CEA's pyrometer and thermocouple graphite cells was based on extensive technical literature review of other metal-carbon eutectic cell that were being developed worldwide in national metrology institutes under the Himert project (Novel High temperature, Metal-carbon Eutectic fixed points for Radiation Thermometry, Radiometry and Thermocouples) predecessor of HiTeMS project. The author of the dissertation recognizes the significant fruitful interaction with several scientists (M. Sadli, F. Bourson, G. Failleau among others) at the French common laboratory of metrology at *Laboratoire National de métrologie et d'essais- Conservatoire national des arts et métiers* (LNE-Cnam) near Paris for their feedback and collaboration on the development of our cells [12-13, 24-30]. Furthermore, 5 different graphite cell designs (identified as *A, B, C, D* and *E*) were conceived by the author, from which A through C were constructed from type 2333 polygraphite provided by Groupe Carbone Lorraine, and graphite cells D and E from graphite type TM1 bought from POCO Graphite Inc. In addition, graphite cells A to C are the first generation of cells, and they are all pyrometry cells with the exception of A in which a small thermowell was machined in the bottom of the crucible for simultaneous pyrometer/thermocouple temperature measurements. The normal emissivity of the black cavity for all the graphite cells was calculated to be over >0.999 [31]. On the other hand, with the aim of reducing the fill-up steps LNE-Cnam developed a quite clever, nonetheless more complex, filling method with a special graphite cell to accommodate these changes. This method virtually allows for a 100% cell fill-up, in just one or two steps, therefore this greatly increases the cell fill-up efficiency, by reducing the time and energy invested and reducing the possibility of contaminating the eutectic material with impurities in the

environments by avoiding excessive handling of the cell. Basically, this filling method makes use of a piston like mechanism which pushes the hypoeutectic mix into the cell while is hot inside a vertically oriented high temperature ceramic tube furnace [8]. Nonetheless, this method would be unpractical in the VITI furnace; therefore a simpler but longer approach was developed.

Furthermore, the knowledge acquired with testing of the first generation of cells lead to the refinement of cell design and allowed for the realization of the second generation of graphite cells. This resulted in the development of a thermocouple-devoted graphite cell (design D) with an improved thermocouple thermalisation, through the implementation of a longer thermowell. Additionally, the conception of enhanced pyrometry cells (design E) was possible through the reduction of cell size, which did not only result on an improved temperature homogeneity and reduction in heat losses, but also there was a significant cost reduction by minimizing the eutectic material needed to fill-up the cells, this is particularly important for cells containing precious metals (Platinum, Palladium, Iridium, Rhodium, Ruthenium, Rhenium). Finally, all the cells were machined from graphite blocks by "Dornberger & fils" company. Before any eutectic mix fill-up and testing, all graphite cells were baked at 350°C for 24 hours inside a small box furnace opened to the environment; this step was performed with the aim of volatilizing machining lubricant, organic residues and/or any absorbed moisture. A sketch of the multiple metal-carbon eutectic graphite cells is presented in Figure 3.3:
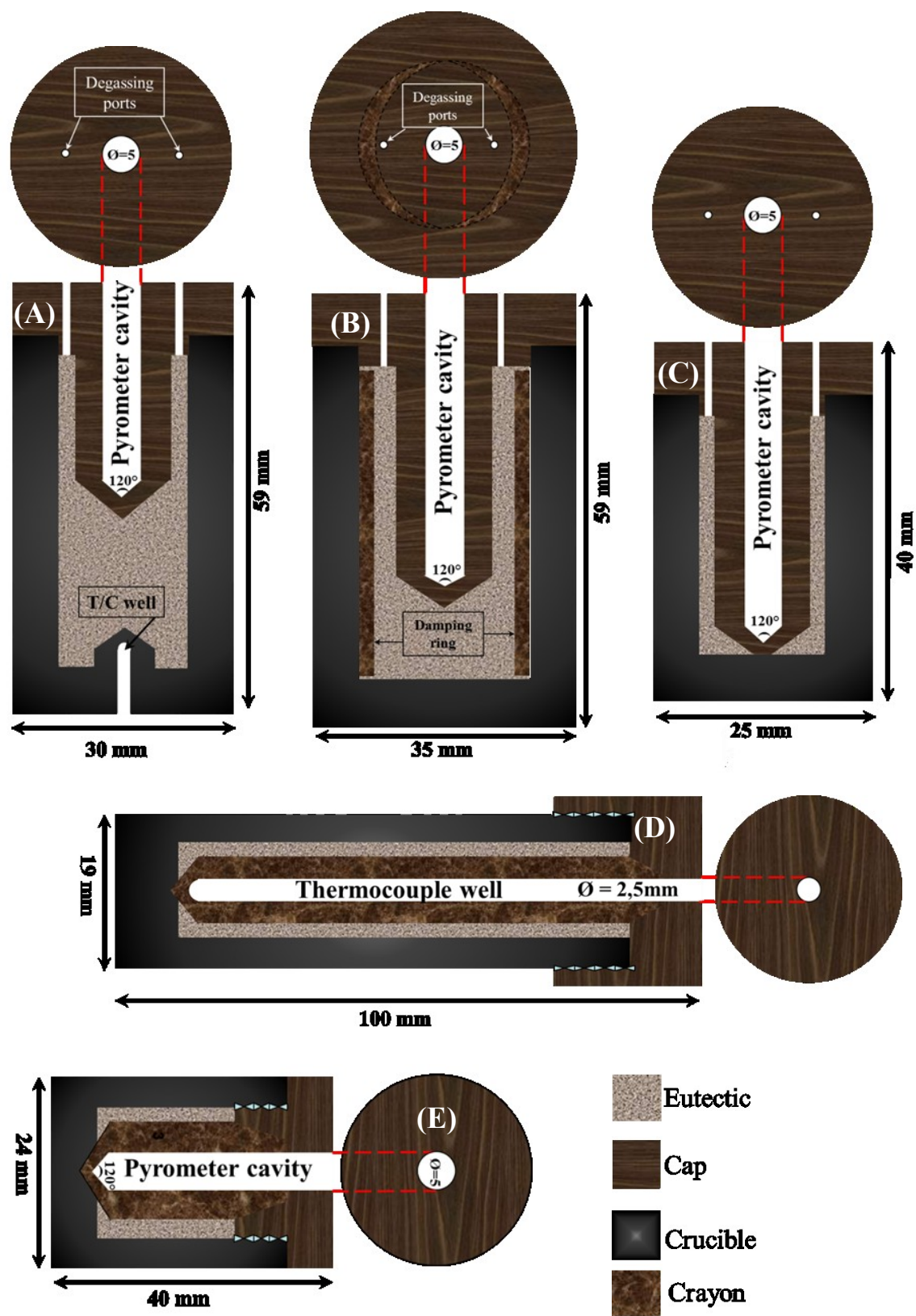
Figure 3.3. Sketch illustrating the design of various eutectic graphite cells tested.

3.2.2 Eutectic Cell Preparation and Material Specifications

The metallic powders were mixed with the graphite granules, inside a glove box under flowing argon (5 L/min), in a proportion slightly below the eutectic composition (hypoeutectic composition). Using a hypoeutectic mix was recommended since previous tests performed in metrology institutes using hypereutectic compositions, resulted in the fracture and failure of certain component of the graphite cell (pyrometer cavity, crucible, or cap) most probably due to coefficient of thermal expansion (CTE) difference between the eutectic solid phase constituents and the unreacted graphite particles. Nevertheless, this issue was partially solved by introducing an hypoeutectic mix (besides trying to match the graphite used for the construction of the cell to the metals CTE), since the composition of the melt will naturally (thermodynamically) tend toward the eutectic metal/carbon proportion to reduce the overall Gibbs free energy of the mix, hence the rest of the carbon needed to attain the eutectic composition is dissolved from the graphite cell walls at relatively high temperatures ($>0.8T_m$). Moreover, before introducing the blend in the cell, it was sealed inside a plastic bottle and randomly mixed for 30 minutes in order to promote a homogeneous distribution of the particles. Afterwards, the mix was introduced into the graphite cell (under flowing argon) and the cell was transported in order to place inside the induction furnace.

Due to the particular design of the first generation of eutectic graphite cells (A through C) there was a single opportunity to fill-up the dedicated eutectic cavity since once the hypo-eutectic blend was heated up above eutectic temperature, then melted and reacted with the graphite the cell components became welded together. As a result, this lead to the conception and implementation of modifications into the second generation of cells (D and E). These design improvements were applied successfully into the machining of the 2nd generation graphite cells, allowing for the realization of multiple hypoeutectic blend refills, among other improvements to generation two; the capability of increasing the eutectic mass inside the cell greatly improved the cells performance. Table 3.2 and 3.3 presents the details pertinent to each cell that was tested along with the data on the hypoeutectic blend and material technical data:

Cell #	Cell Design	Cell Type	Graphite cell weight, grams	Cell Cavity volume, cc	M-C Eutectic Alloy	Metal Purity, (metal basis)	Metals Provider	Particle size/form
1	A	Pyro/TC	68,12	6,3	Fe-4.3C	99%	Alfa-Aesar	-20mesh/powder
2	A	Pyro/TC	67,91	6,3	Fe-4.3C	99.98%	Alfa-Aesar	1-2 mm/granules
3	A	Pyro/TC	67,42	6,3	Fe-4.3C	99.998%	Alfa-Aesar	-22mesh/powder
7	B	Pyro	88,25	6,4	Ti-0.4C	99.995%	Alfa-Aesar	3.175 mm/slug
8	B	Pyro	88,35	6,4	Co-2.6C	99.998%	Alfa-Aesar	-22mesh/powder
9	B	Pyro	90,59	6,4	Mo-2.5C	99.999%	Alfa-Aesar	-22mesh/powder
11	C	Pyro	25,26	1,5	Nb-1.5C	99.8%	Alfa-Aesar	-325mesh/powder
12	C	Pyro	25,23	1,5	Ru-2.5C	99.9%	Degusa	unknown/fine powder
15	D	TC	54,49	5,2	Ru-2.5C	99.9%	Acros Organics	-200mesh/powder
16	C	Pyro	29,94	1,5	Re-1.3C	99.999%	Zhuzhou Kete	-140mesh/powder
17	E	Pyro	29,10	2,6	Re-1.3C	99.999%	Zhuzhou Kete	-140mesh/powder
18	E	Pyro	29,04	2,6	Co-2.6C	99.998%	Alfa-Aesar	-22mesh/powder
19	E	Pyro	28,71	2,6	Ru-2.5C	99.9%	Acros Organics	-200mesh/powder

Table 3.2. Metal-Carbon eutectic material and graphite cell details.

Cell #	M-C Eutectic Alloy	Hypoeutectic mass, grams	Hypoeutectic, wt.% Carbon	Metal mass, grs	Hypoeutectic carbon mass, grams	Carbon mass dissolved from crucible, grams	Hypoeutectic volume% in cavity
1	Fe-4.3C	16,73	3,9	16,08	0,65	0,073	37,3
2	Fe-4.3C	20,47	3,9	19,68	0,79	0,088	45,7
3	Fe-4.3C	18,77	4,0	18,03	0,74	0,064	41,9
7	Ti-0.4C	20,30	0,4	20,22	0,08	0,004	71,2
8	Co-2.6C	8,60	2,0	8,43	0,17	0,052	16,4
9	Mo-2.5C	12,61	2,0	12,36	0,25	0,062	21,2
11	Nb-1.5C	5,28	1,0	5,23	0,05	0,026	42,2
12	Ru-2.5C	4,82	2,0	4,73	0,10	0,024	29,0
15	Ru-2.5C	9,99	2,1	9,79	0,20	0,045	17,5
16	Re-1.3C	13,89	1,1	13,74	0,15	0,098	19,1
17	Re-1.3C	12,10	1,1	11,97	0,13	0,029	22,5
18	Co-2.6C	4,80	2,0	4,70	0,10	0,029	35,9
19	Ru-2.5C	10,10	2,3	9,87	0,23	0,026	24,9

Table 3.3. Metal-Carbon eutectic cell fill-up material details.

The graphite used in the hypoeutectic mix was bought from Alfa-Aesar, in the form of small flakes (-10 mesh) with a 99.9% purity (metal basis). The impurity chemical analysis quantification for most of the materials is included in Appendix C.

3.2.3 Thermal Cycling

After each eutectic cell was carefully filled-up with the hypoeutectic mix, the next step was to place it inside VITI furnace vessel for subsequent thermal cycling around the eutectic temperature. After the cell was located inside the induction coil, then the furnace vessel was tightly sealed, in order to start the evacuation of air with the aid of a mechanical pump. Once a medium vacuum was achieved, the mechanical pump was turned off, and high purity argon gas (Alphagaz 2 Argon from AirLiquide) was injected into the vessel to attain a pressure of 0.5 bar gauge. This procedure was systematically performed for three consecutive times, before beginning the heat up, as a mean of eliminating residual oxygen.

Afterwards, the crucible and its contents where heated up (at an average of ~25°C/min, compared to usual metrology laboratory heating rates of 5-10 ºC/minute.) to a temperature just below the eutectic melting point and kept until temperature stabilized. Subsequently the temperature was ramped up above the eutectic temperature in order to melt the solid eutectic metal-carbon alloy; then temperature was again stabilized before proceeding with the cooling step in order to promote the solidification of the eutectic alloy. A steady thermal cycling was repeated for at least three times to reproduce similar heating/cooling rates as shown in figure 3.4 in order to measure the eutectic transformation temperature repeatability. Additionally, supplementary temperature ramps were applied with significant variations in heating/cooling rate in order to evaluate the eutectic transformation behavior under substantial temperature fluctuations.

Furthermore, since the thermal cycling stimulates the continuous transformation of the eutectic alloy between solid and liquid states, figure 3.5 shows a temperature-time curve illustrating a typical melting/solidification curve is presented along with the microstructural alterations taking place during the solid↔liquid (or $\alpha + \beta \leftrightarrow L$) transformation.
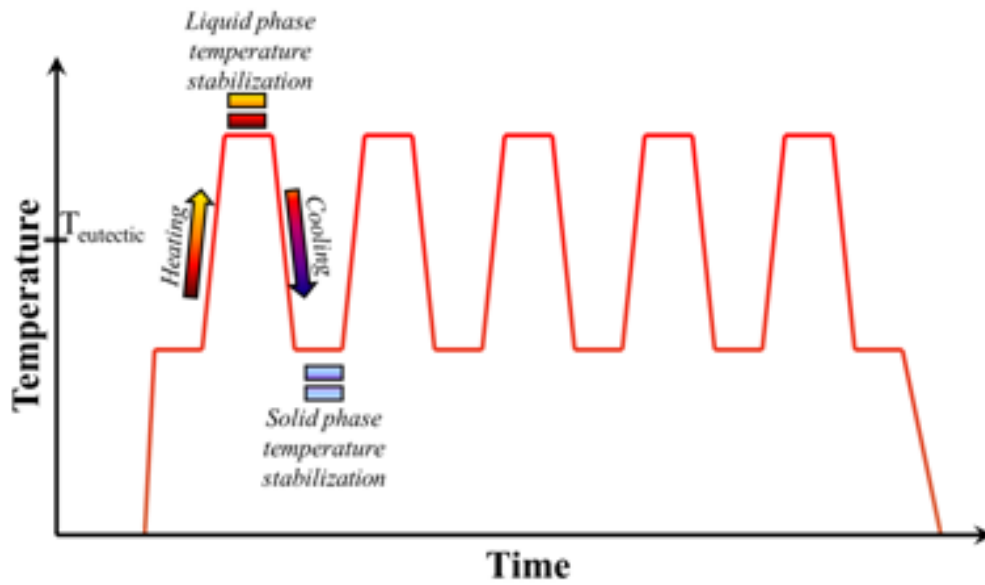
Figure 3.4. Sketch illustrating the thermal cycling sustained by the eutectic cell.
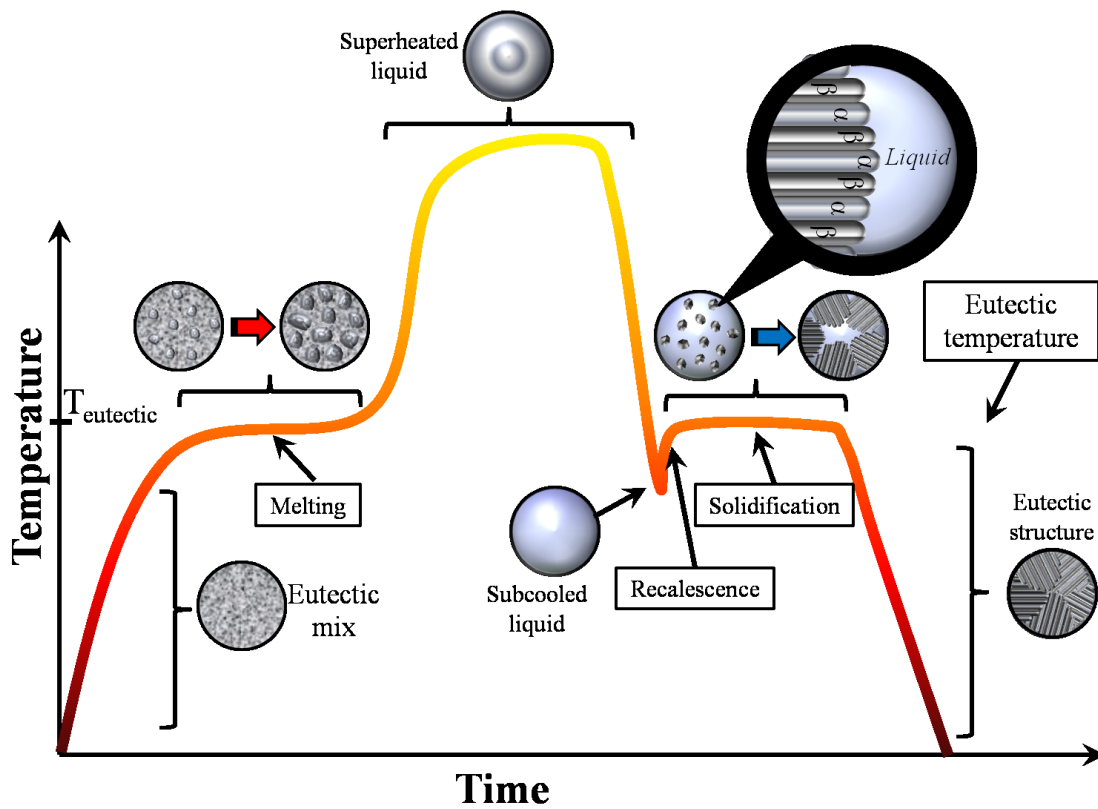
Figure 3.5. Illustration of a eutectic melting/solidification curve showing detailed micro-scale transformation taking place.

Figure 3.5 denotes the different stages observed in a typical melting/solidification curve for a eutectic alloy, tied to the micro-scale morphing taking place. To start, if we move from left to right

and follow the reddish temperature-time curve we observe an initial sharp slope or heat-up period. Alongside there is a representation of the state of the metal-carbon mix in its initial powdery form. Upon heat-up we should understand that even before reaching the actual eutectic temperature the powder particles are already reacting with each other, or sintering process, where there is active diffusion among the chemical species at a temperature just above 80% of the absolute melting temperature. Afterwards, we observe an important decrease in the slope and what is observed as a plateau in the curve. At this stage, there is a temperature arrest an all the heat entering the material is invested in the melting of the solid particles. The actual atomic process taking place is the breaking of the atomic bonds of the crystalline particle in order to transform from a ordered structure into a relatively disordered liquid phase. The energy invested in the transformation is called the latent heat of transformation, also called enthalpy of fusion which; and as this reaction involves the absorption of heat then it is called an endothermic process. At the micro-scale level we can observe how the first embryos of liquid nucleate and grow until all the solid eutectic mix has transformed into liquid phase having the exact eutectic composition. Then temperature rises again until it reaches the equilibrium temperature which is a function of the balance between the energy or heat going into the eutectic cell (provided by the furnace heating elements, induction coil, etc.) and the thermal energy leaving the cell by conduction, convection and/or irradiation of heat. At the micro-scale we can observe a superheated liquid with some agitation due to convective currents.

Furthermore, if we now decrease the furnace power input in order to cool-down the cell to a temperature below the eutectic temperature (cooling step in figure 3.4). In Figure 3.5, the eutectic alloy temperature is dropping from the stabilized superheated liquid stage, down the slope, until it reaches a temperature below freezing point, which is referred as subcooled (or undercooled) liquid. How come the liquid be at a temperature below the solidification temperature, but still in liquid phase? At the thermodynamic freezing temperature the probability of a solid embryo reaching the critical size to become stable nuclei is extremely small. But as subcooling increases the critical size decreases, hence the probability of nucleation of a stable nuclei increase, and once it nucleates, the

solidification continues through the growth of the solid nuclei. The driving force for solidification is the difference in Gibbs free energy between the liquid and the solid, since the energy associated with the crystalline structure of the solid is less than the energy of the liquid, hence freezing will eventually take place. Nonetheless, the time it takes for the nucleation of the solid will not only depend upon undercooling. For example if a solid was to grow freely from a subcooled liquid, it would have to attain more or less the configuration of crystal in its solid phase to freeze. Therefore, the availability of nucleation sites, as solid impurities in the melt and crucible walls can facilitate the nucleation of stable nuclides.   As can be seen freezing is a more complex process than melting, just from the fact that moving from an ordered to a disordered state will always be easier than changing from a disorder (liquid) to order (solid crystal) state. Anyhow, after this brief explanation on the kinetics and thermodynamics of solidification we will continue our walk-through the temperature-time curve.

Therefore, once the first solid nuclei reach the critical size and start to grow we observe the recalescence or exothermic process where the liberation of the latent heat of transformation takes place and we reach a maximum that is considered as the solidification temperature. Afterwards, we arrive to another plateau were the eutectic liquid transforms into solid through the formation of two distinct solids (α and β) which grow into the subcooled liquid. Once all the liquid has solidified, the temperature curve slopes down until it reaches its equilibrium temperature and stabilizes.   This process is again repeated and as the thermal cycling continues the metal-carbon eutectic continuously transforms from a solid into a liquid and backwards.

In theory, an ideal eutectic melting-solidification curve (temperature vs. time profile) would show an almost perfect flat plateau at the eutectic temperature as for a pure material. But in real-life things are far from being ideal, and instead of a perfectly flat plateau there is noticeable change in slope showing a definite transformation range that is affected by thermal gradients, inclusions in the alloy, superheating/undercooling temperature, and previous thermal history, among others, will have

an effect on the phase transformation behavior. Additionally, other parameters which depend on the instrumentation set-up and operation basis will indirectly affect the temperature measurement, for example the size of source effect for pyrometers, thermocouple degree of thermalization, and other phenomena which disturbed the measurements will introduce uncertainties which need to be considered. All these parameters will play a more or less important role on the reproducibility and behavior of the eutectic transformation, especially under non-equilibrium conditions.

Finally, this subsection serves as an explanation on the general features of the eutectic melting/solidification curve and its respective material micro-scale modifications. Nonetheless, it should be understood that a slightly different behavior can be observed depending on the eutectic system and thermal conditions. Therefore, after providing the experimental details on the VITI facility and instrumentation utilized in the tests, the results on the thermal cycling of multiple metal-carbon eutectic alloy cells will be presented to get insight on its repeatability and behavior under different circumstances.

3.3 VITI Induction Furnace and Instrumentation Details

The VITI ("VIscosity Temperature Installation") facility [9-11] is composed by a copper induction coil contained in a continuously cooled (water flow: ~4 m^3/hour) stainless steel vessel (volume: 70 L). The VITI furnace is utilized to perform experiments on material compatibility, study of thermo-physical/chemical properties of materials, small scale severe accident tests, aerodynamic levitation of small droplets of molten materials, and more, due to its flexibility in configuration. The induction coil is powered by a 24 kW generator with a frequency of 30 kHz (IDP 12-30 generator by Induction Partner Development), allowing for the heating up of samples to a maximum temperature of 3000°C. The furnace vessel can function under medium vacuum using a mechanical pump (2015SD Pascal Dual Stage Rotary Vane Vacuum pump manufactured by Alcatel Adixen) or inert atmosphere (argon, helium, nitrogen), and with diluted reactive gases in gas mixtures.

The thermal cycling of the high temperature metal-carbon eutectic fixed point cells was conducted under a flowing argon atmosphere with a relative pressure of 0.8 bar (approx. ~2 atm absolute). The VITI furnace heating of the samples is usually performed by indirectly heating a graphite susceptor with electromagnetic induction (Joule heating) which afterwards transfers its energy to the sample mainly by thermal radiation of heat. Nonetheless, based on calculations performed on the magnetic field penetration depth of this particular heating experimental set-up, it is presumed that the eutectic graphite cells coupled to the induced electromagnetic field and also heated up directly by induction heating [32]. Furthermore, a porous graphite bell is placed in between the susceptor and the copper coil to improve temperature uniformity and reduce heat losses.

During the experiments, two commercial bichromatic pyrometers, and sometimes a thermocouple (for thermocouple well containing cells) were utilized to measure temperature. The eutectic cell temperature was measured by looking vertically into the black cavity through a quartz window using an IMPAC ISQ 5-TV bichromatic pyrometer (λ_1: 0.9μm and λ_2: 1.05μm). Additionally, an IMPAC ISQ-LO bichromatic pyrometer (λ_1: 0.95μm and λ_2: 1.05μm) was used as a control pyrometer by measuring the temperature of the cell wall or sometimes by pointing at the graphite susceptor. A type C thermocouple (provided by Thermo-Est) was used to trace the melting/solidification curves in the pertinent tests. Before the start of our tests the IMPAC ISQ 5-TV pyrometer was sent to the manufacturer for calibration, and afterwards an in-house test on the pyrometer utilizing an incandescent tungsten filament system was performed with and without the silica quartz window to measure the transmittance/interference effect of the window on the temperatures measurements. No perceivable changes in temperature reading were observed when the quartz window was placed in between the pyrometer and the hot source. The pyrometer measurement uncertainty on a black body source is: for temperatures below 1500°C is 0.5% and above 1500°C is 1% of measuring value. Finally, a LabView 8.2 kit was utilized as the instrumentation-computer interface (Lab View Version 8.2.1 by National Instruments, 2007), which allowed to command the generator power input (furnace heating) and to control/record the furnace instruments' data

acquisition (Temperature, pressure, gas flow, video recording). The following photographs (figure 3.6) display the layout of the VITI induction furnace and instrumentation utilized in the tests, plus the internal view of the vessel with the configuration for the experiments.
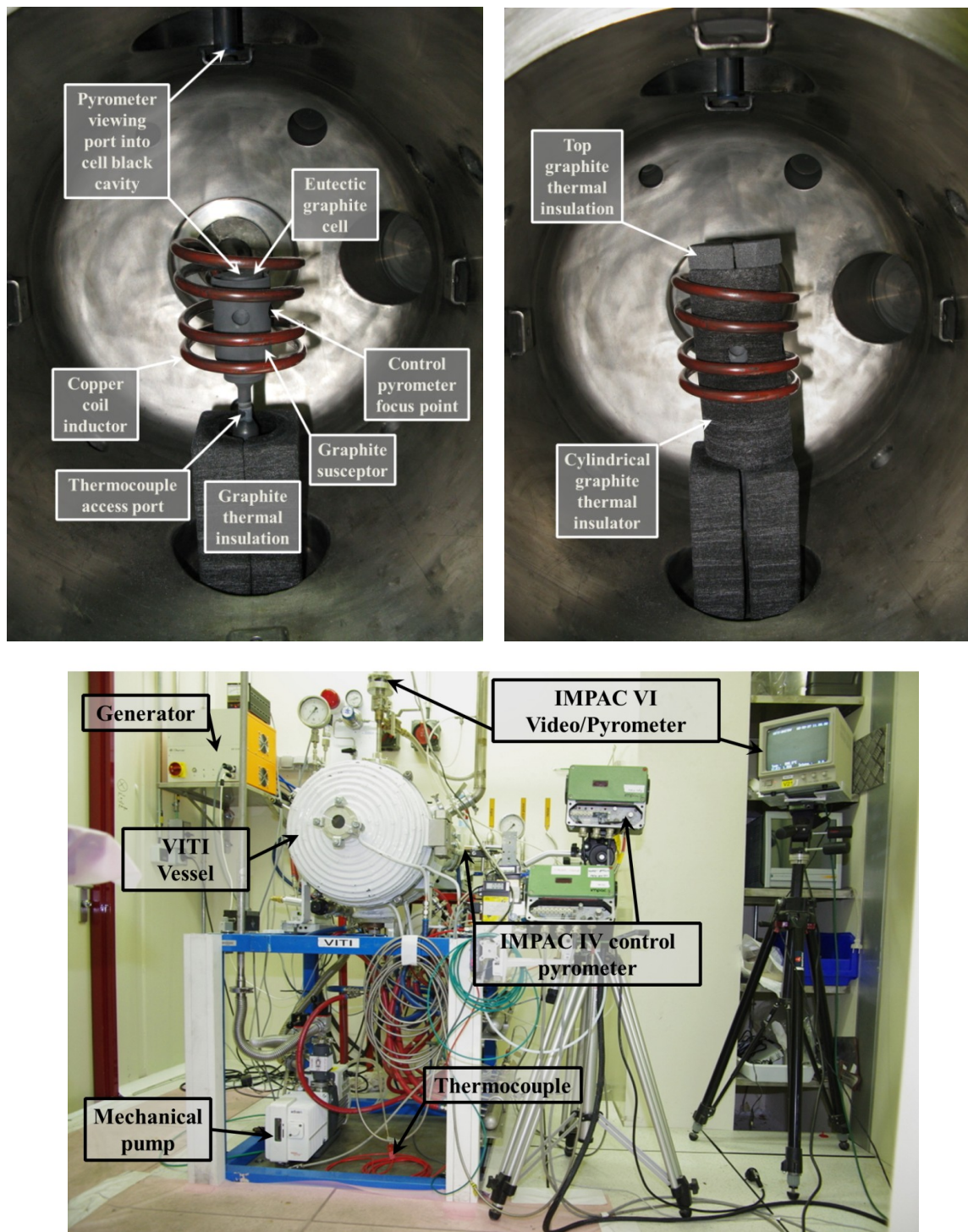
Figure 3.6. Photos of VITI facility and experimental configuration for the M-C eutectic experiments.

3.4 Results of Metal-Carbon Eutectic Cells Non-Equilibrium Non-Steady-State Transformation Experiments in VITI Furnace

If we look back at the characteristic melting/solidification curve (figure 3.5), we can observe that the melting "plateau" region displays an inflection point in the curve. This temperature has been selected as the melting temperature for all the tests performed on the selected metal-carbon eutectic system's transformation temperature. Similarly, the solidification temperature has been selected as the maximum temperature reached after the recalescence, or in case there is no discernible maximum, but instead a change in slope as for melting, then again the inflection point has been selected as the freezing temperature. This procedure for the selection of the transformation temperature has been agreed among all the partner laboratories conducting research on the high temperature metal-carbon fixed point cells with the purpose of setting a standard procedure for the selection of the transformation temperature with the aim of achieving an adequate comparison and interpretation of the obtained results [7-8, 12-14, 24-25, 28].

3.4.1. Iron-Carbon (Fe-Fe₃C) System – Iron Purity Impact on Eutectic Temperature

To start with, a summary of the results on the tests performed in the iron-carbon eutectic are presented (figures 3.7-3.9). The Fe-C cells (#1 to 3) melting/freezing temperatures are plotted against the heating/cooling rate.

Fe-C		Melting				Solidification				Eutectic
Test #	Iron purity, %	Average heating rate, °C/min	Mean temperature μ, °C	Standard deviation σ, °C	Thermometer error, ±°C	Average cooling rate, °C/min	Mean temperature μ, °C	Standard deviation σ, °C	Thermometer error, ±°C	Ref. temp., °C
1st Pyro	99	64,2	1144,3	1,5	5,7	40,8	1135,0	0,7	5,7	
2nd Pyro	99	56,0	1138,7	1,2	5,7	40,5	1121,1	0,3	5,6	
1st Pyro	99,98	59,0	1145,8	0,1	5,7	47,6	1140,3	0,1	5,7	
2nd Pyro	99,98	61,2	1139,7	0,4	5,7	38,7	1130,2	0,5	5,7	
1st Pyro	99,998	59,0	1157,4	3,1	5,8	42,8	1127,5	1,8	5,6	
2nd Pyro	99,998	59,2	1143,6	0,4	5,7	42,2	1127,0	0,7	5,6	1153
3rd Pyro	99,998	70,1	1150,3	0,6	5,8	63,3	1144,0	0,5	5,7	
1st TC	99	55,6	1091,8	1,2	10,9	42,4	1083,3	0,4	10,8	
2nd TC	99	50,2	1097,1	1,0	11,0	44,1	1088,5	0,9	10,9	
1st TC	99,98	51,9	1107,1	1,0	11,1	47,3	1103,9	0,6	11,0	
2nd TC	99,98	58,4	1126,5	0,3	11,3	47,0	1118,2	0,5	11,2	

Table 3.4. Summary of results on the Iron-Carbon cells no. 1 through no. 3.
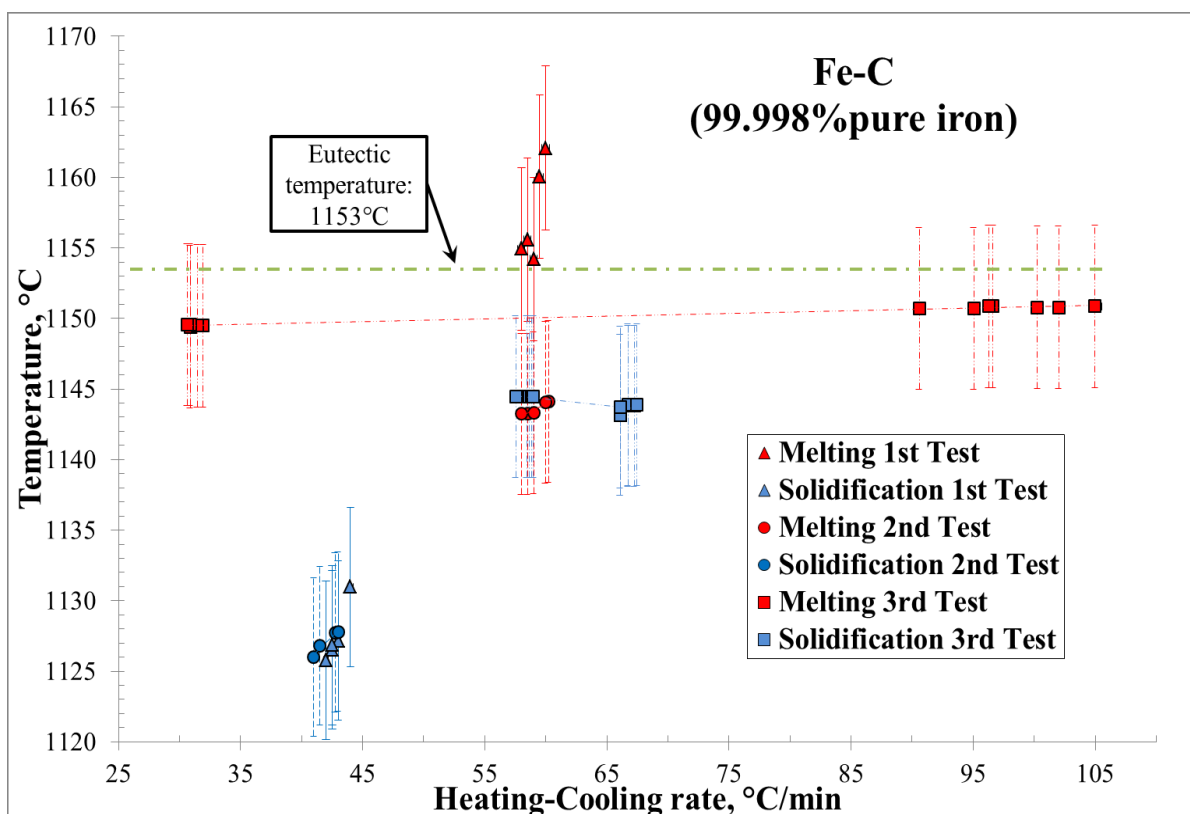
Figure 3.7. Melting/solidification temperature−heating/cooling rate, Fe-C #3 (99.998% iron purity).
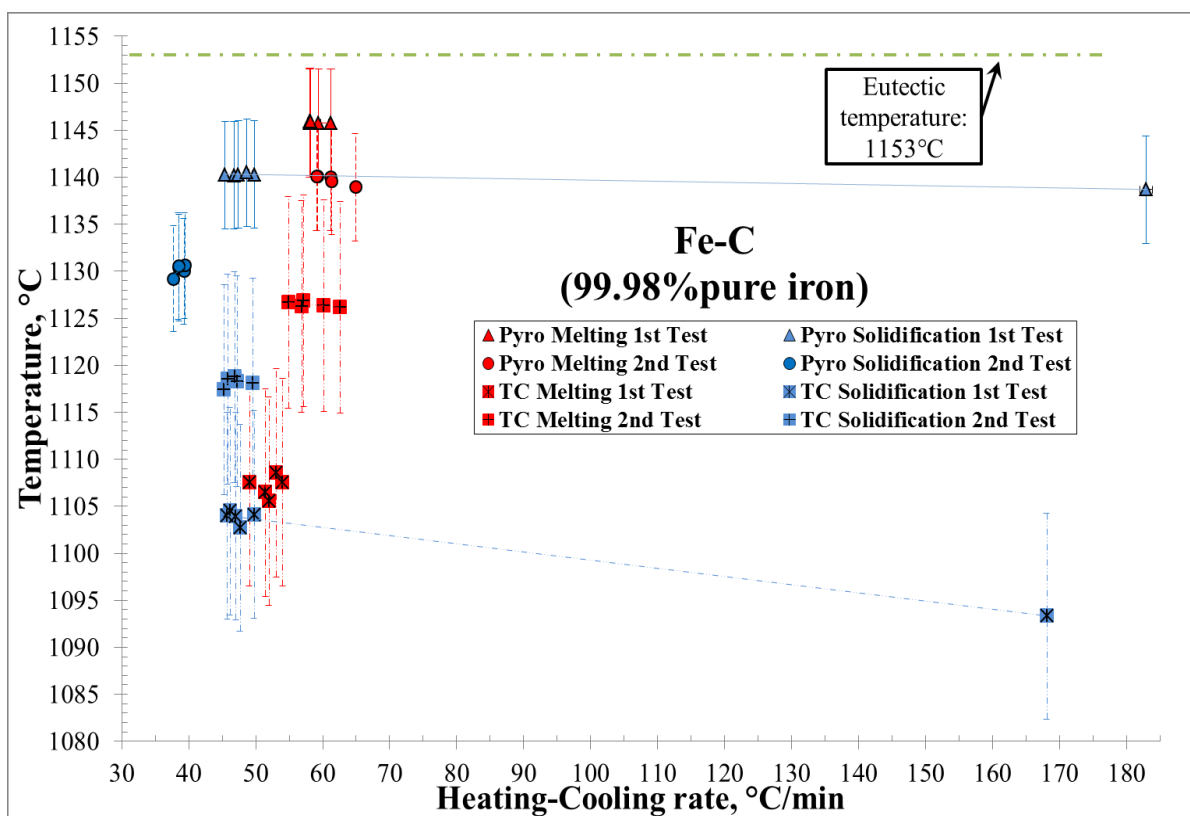
Figure 3.8. Melting/solidification temperature−heating/cooling rate, Fe-C #2 (99.98% iron purity).
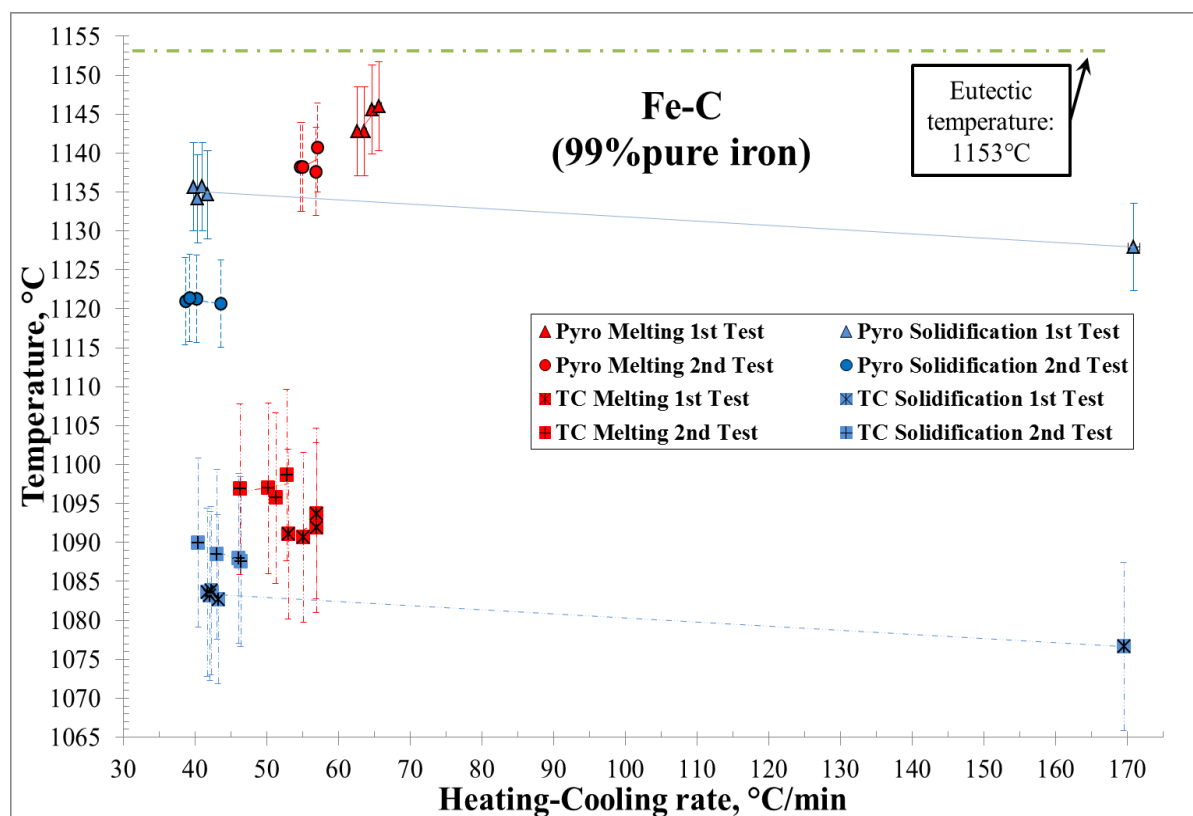
Figure 3.9. Melting/solidification temperature−heating/cooling rate, Fe-C #1 (99% iron purity).

The three previous graphs consist of a plot for the iron-carbon eutectic cells number 1 to 3 displaying the measured melting (denoted as red symbols) and solidification (illustrated with blue symbols) transformation temperature. Multiple tests at different time frames (it means the cells were taken out of the furnace and put back in at some other time) were performed on each cell with the purpose of perceiving any to variations in behavior due to slight positioning fluctuations or ageing. For the highest purity iron eutectic cell #3 (99.998%Fe), three tests were performed with similar experimental configuration, where only the pyrometer measurements are shown [unfortunately, the TC well was damaged while inserting the TC; hence it had to be sealed with a graphite piece and not used anymore]. On the other hand, Fe-C cells number 1 and 2 were tested twice, and pyrometer/TC measurements were performed in parallel in both tests. Additionally, the plots include linear trend lines (where pertinent) to facilitate the visualization of the effect of heating rate on the cell. Finally, an error bar is included for each dot to denote the thermometers precision as a function of temperature (provided by the fabricant). On the other hand, it is important to state that the difference between the

cavity pyrometer (eutectic cell cavity) and the control pyrometer (pointing at the crucible exterior wall) for all the tests varied around 20 to 30°C, being the exterior wall the lowest or relatively coldest temperature. An attempt to calculate the latent heat of fusion/solidification was made, but no consistent information was obtained due to the inherent design of the VITI furnace and the significant heat losses. This type of study is favored in an adiabatic system with a capability to perform fine measurement of temperature/heat variations via calorimetry or differential thermal analysis (DTA) in an especially designed apparatus.

Furthermore, table 3.4 shows a summary of the eutectic transformation temperature (similar heating/cooling rate) for all the multiple Fe-C cells in order to cross-compare the results among the cells repeatability and to visualize the effect of purity on the eutectic transformation. Moreover, figures 3.10 and 3.11 are graphical representations of table 3.4 illustrating the melting temperature and solidification temperature, respectively, for several thermal cycles performed at an average heating rate of 1°C/sec, and solidification rate of 0.7°C/sec
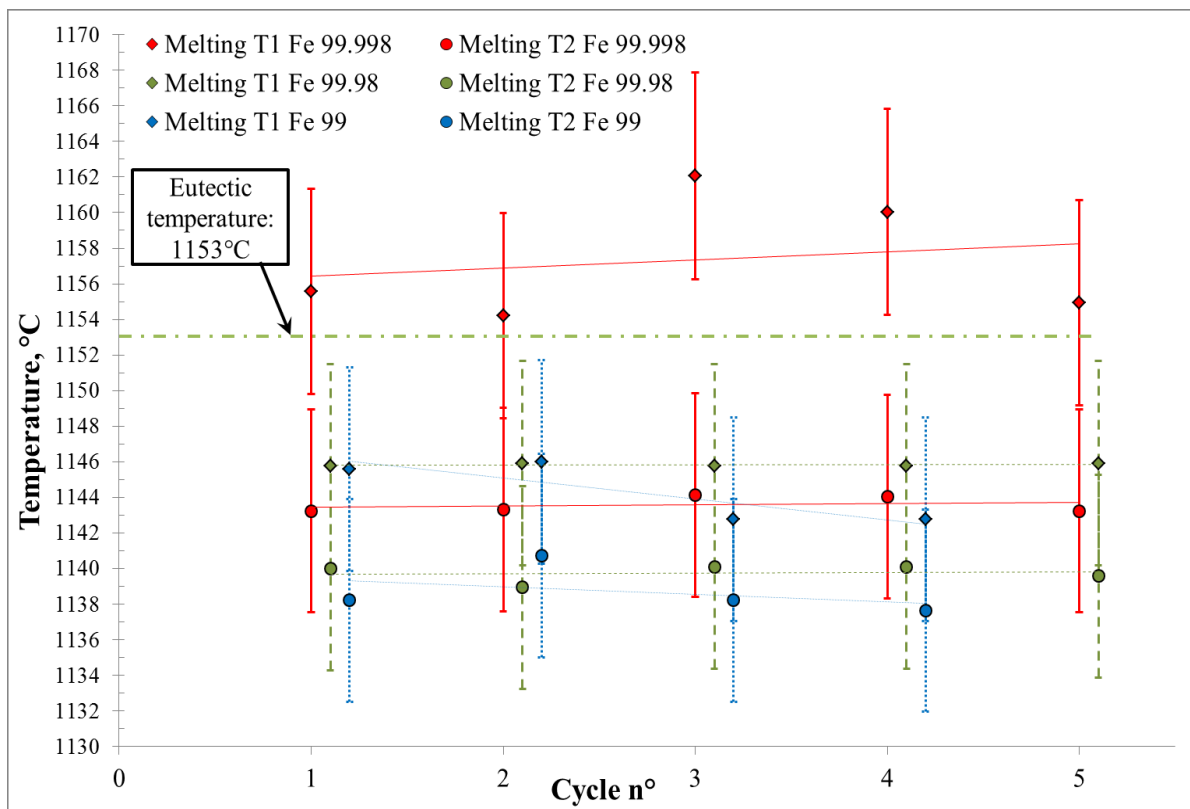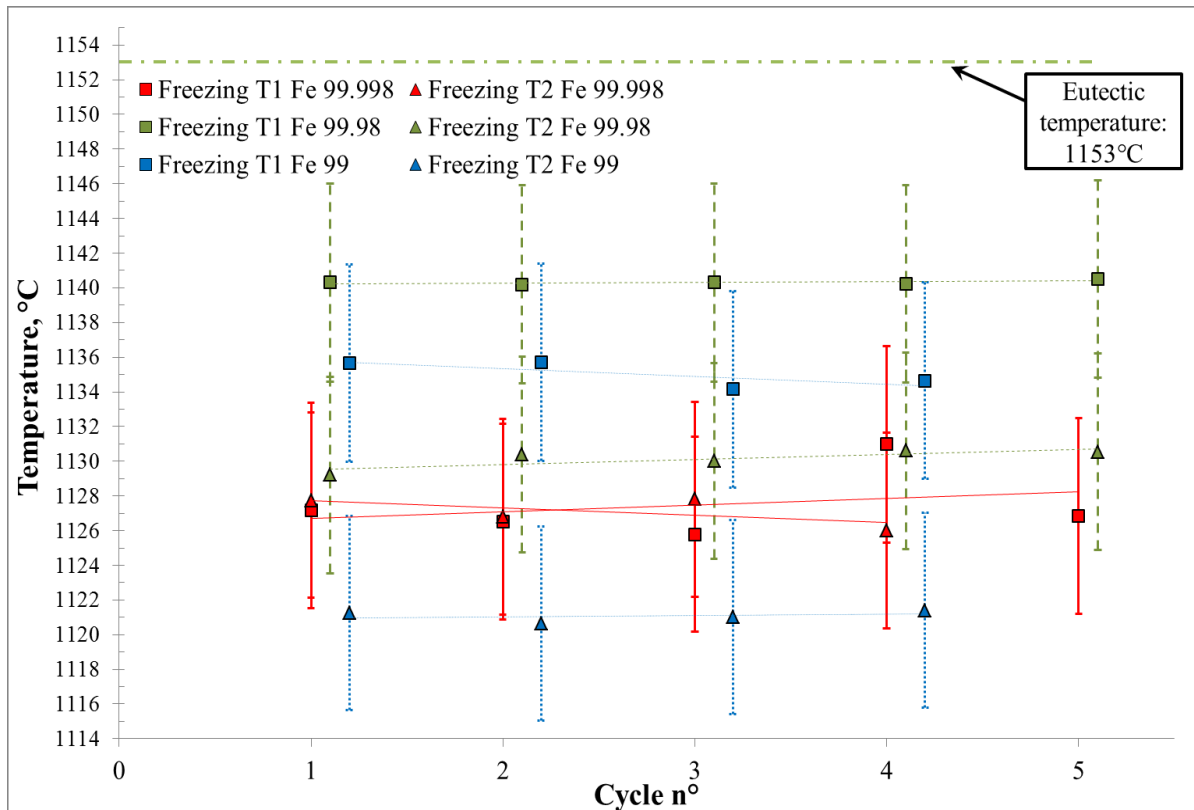
Figure 3.10. and 3.11. Comparison among the Fe-C eutectic cells melting and solidification temperature under similar heating/cooling rate.

Moreover, in order to better, or more vividly, illustrate the differences that can arise from even such low iron powder purity variations, the following section includes a metallurgical analysis (metallography and Vickers micro-hardness testing) on three metal-carbon. Additionally, in order to avoid destruction of the Fe-C cells, three simple graphite crucibles were prepared with the exact same hypoeutectic blend as for cell no. 1 to 3, (99%, 99.98% and 99.998% iron) and then thermally cycled for 4 times (under argon atmosphere). The crucibles were heated up to melting, then cooled down until solidified to promote a complete reaction between the carbon and iron with the aim of achieving chemical and microstructural homogeneity.
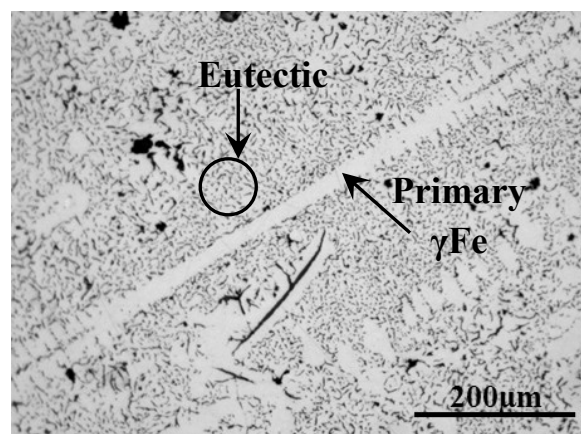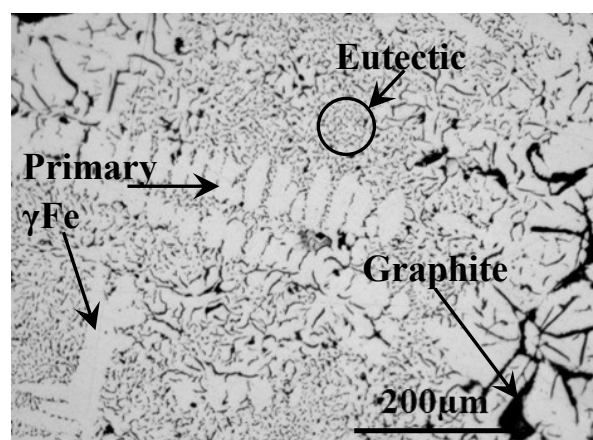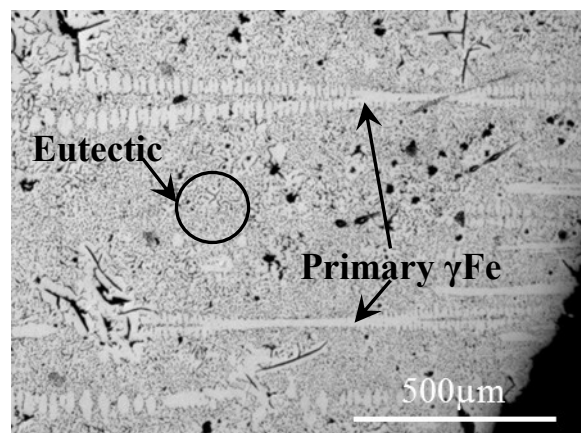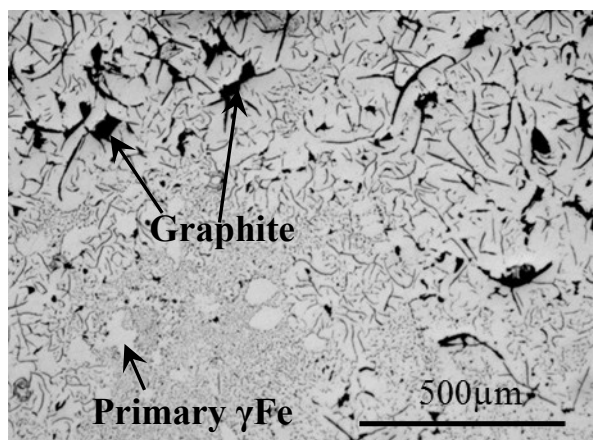
Figure 3.12. Micrographs showing the Fe-C eutectic microstructure of (99% pure) iron and carbon.
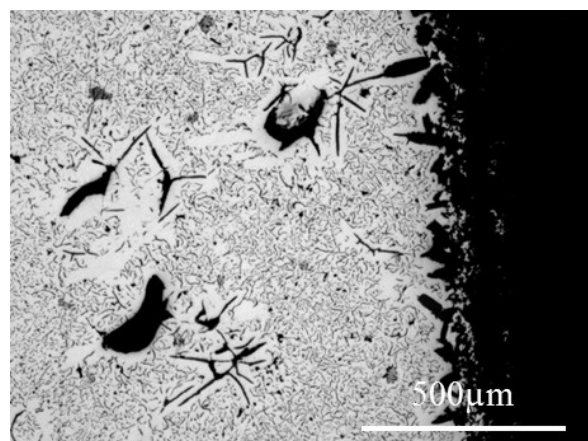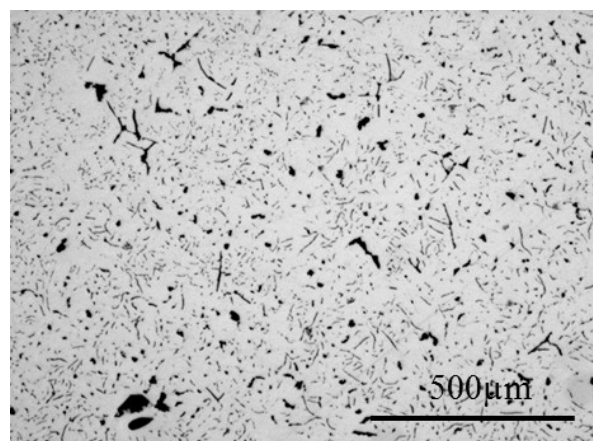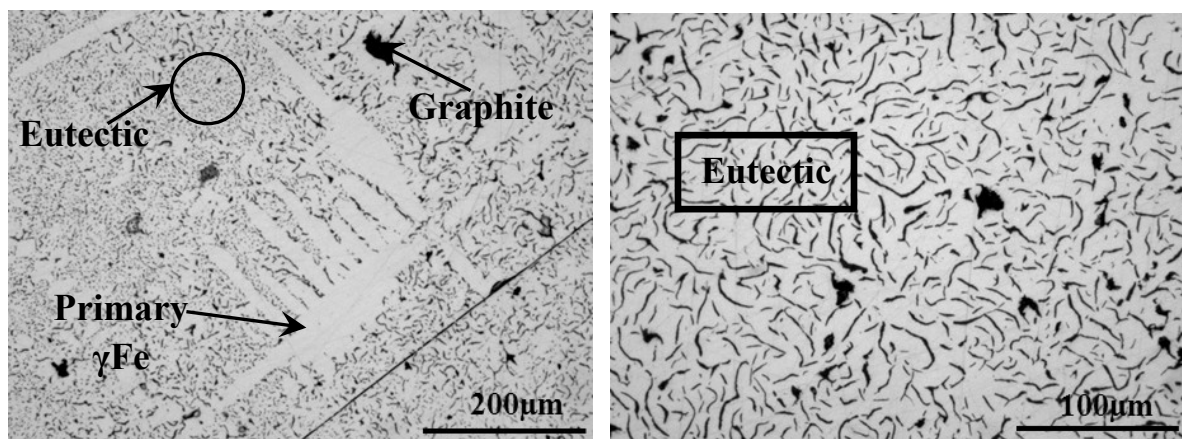
Figure 3.13. Micrographs showing the Fe-C eutectic microstructure of (99.98% pure) iron and carbon.
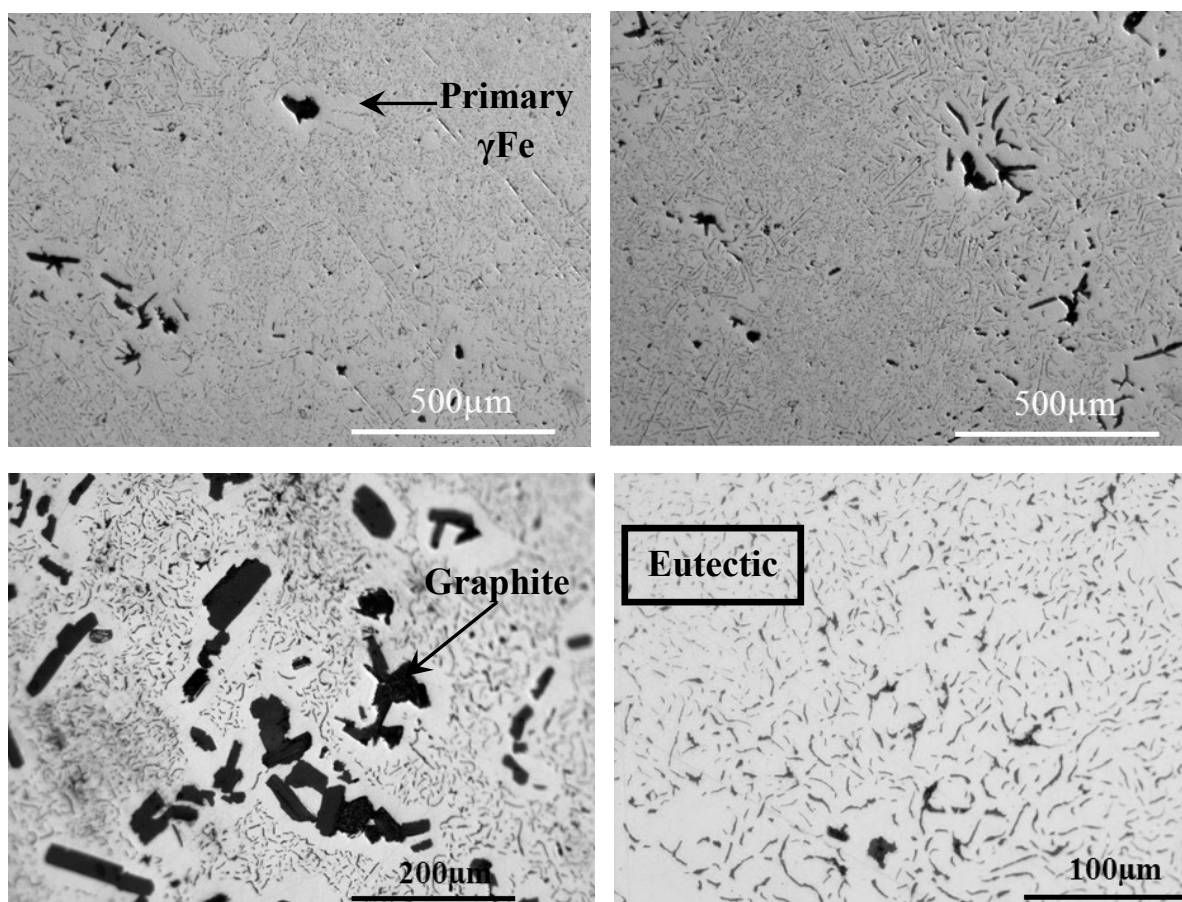
Figure 3.14. Micrographs showing the Fe-C eutectic microstructure of (99.98% pure) iron and carbon.

The previous micrographs (Figure 3.14) are the result of the metallurgical preparation of the sectioned iron-carbon eutectic cells. The cylindrical graphite cell was fine cut into two halves along its axis with the aid of a diamond disc coupled to a Buehler IsoMet low speed saw. Afterwards, the two samples were grinded in a water cooled turntable machine with silicon carbide grinding paper

(80, 120, 180, 220, 320, 400, 500, 600, 800, 1200, 2400), then polished on a fine cloth (Struers MD-Plan or similar) sprayed with a Struers DP-S diamond suspension (with particle size 6µm, 3µm and 1µm) along with a red lubricant (Struers DP-Red Lubricant) and final fine polish with a 0.04 µm silica particles suspended in water. The samples were rinsed in water, ethanol and afterwards dried with a warm air gun. Then the previous micrographs were captured with an optical microscope (Olympus BX51M) coupled to a video camera system controlled via computer software (Analysis 5.0, Soft Imaging System GmbH). The pictures are presented at several magnifications in order to focus in some microstructural details and phase morphology that aid in highlighting the differences among the samples. Additionally, a bar graph is presented were the mean Vickers micro-hardness of the microstructure constituents for each sample are shown in order to pinpoint the big differences that can arise in mechanical properties because of significantly low impurity content variations. The micro indentures were made in 20 seconds with a 100 lbs. force using a PolyVarMet/Micro-Duromat 4000 microscope/hardness equipment by Reichert-Jung.
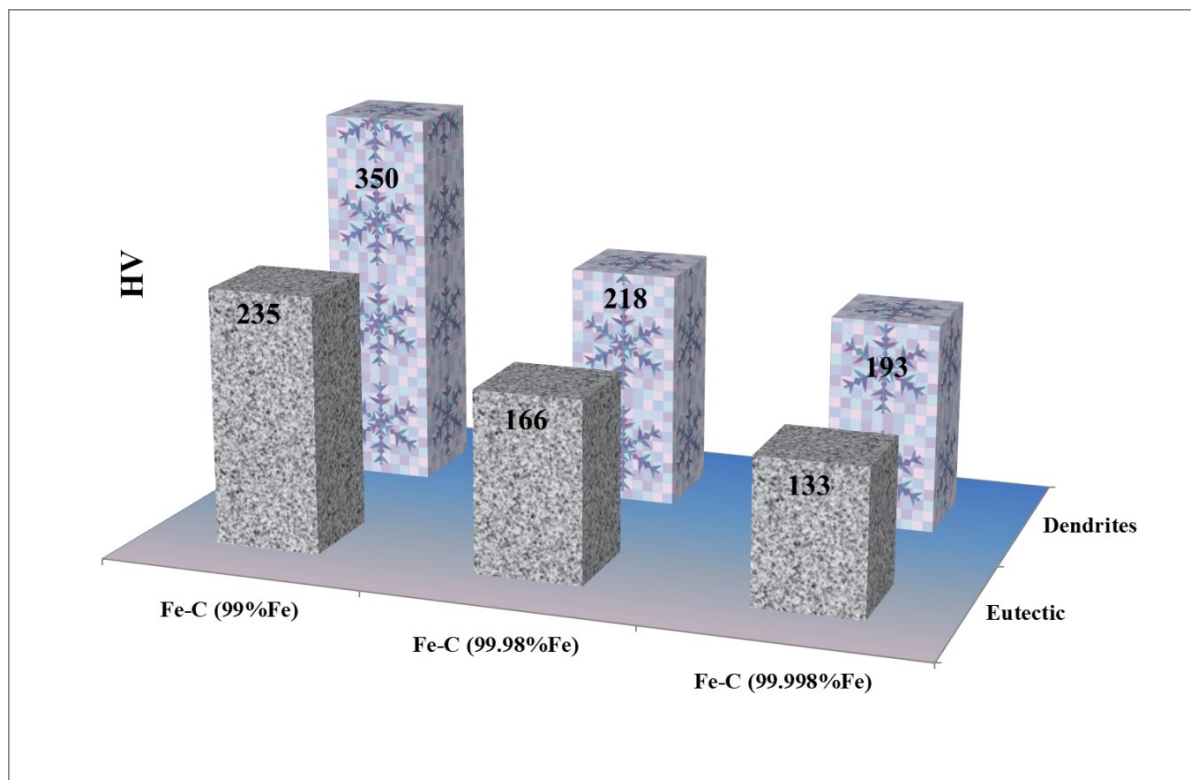
Figure 3.15. Vickers micro-hardness testing of various iron-carbon eutectic samples.

3.4.2 Discussion of Impurity and Thermal Effects on the Eutectic Transformation (Fe-C Eutectic System)

In order to understand the effect of impurities or foreign inclusions in the Fe-C eutectic, its fusion and solidification transformation temperatures, three graphite cells were filled-up with a hypoeutectic blend composed of a different degree of iron powder purity (99 to 99.998% weight percent iron, in metal basis).

The 99% pure iron cell (Fe-C cell #1) underwent two tests (figure 3.9) where thermal cycling of the cast iron eutectic alloy was accomplished by repeating a minimum of four consecutive comparable thermal profiles (approx. heating: 1°C/sec and cooling: 0.7°C/sec), and at the last thermal cycle the superheated liquid was cooled at a relatively faster rate (~2.8 °C/min), with the aim of looking at the solidification behavior and sensibility under rapid heat extraction. The pyrometer measurements of the first test on "Fe-C cell #1" (99% pure iron) showed a lower average melting/freezing temperature than the 1153°C reference eutectic temperature with -9°C and -18°C, respectively; a 5°C recalescence was observed in all the solidification curves. On the other hand, the thermocouple measurements were approximately 50°C underneath the pyrometer measurements with similar curve inflection at the transformations points, but not such an evident recalescence. The final faster cooling showed a 7°C lower solidification temperature, for both the pyrometer and thermocouple, for a fourfold increase in cooling rate. Additionally, the pyrometer results on the "Fe-C cell #1" (99% pure iron) second thermal cycling test showed a depression in melting/freezing temperatures corresponding to a mean temperature difference of around -14°C and -32°C for the melting and freezing point, respectively; the solidification curve does not show a discernible recalescence as in the previous test but instead it looks more like a slightly inclined solidification plateau. On the contrary, the thermocouple temperature measurements show a slight increase of around 6°C in the mean transformation temperature, with respect to the first test; similar features are observed in the thermocouple curve when compared to the initial test.

The previous results give important insight on the sensitivity of the cells repeatability as a function of thermometer type, plus a glance at the influence of variations in heat extraction rate (cooling rate); this topic will be analyzed in more detail in the following paragraphs where tests performed on higher temperature eutectic cells (Co-C, Ti-C, Ru-C and Re-C) are discussed. Furthermore, the relatively lower temperature measured by the thermocouple can be understood by considering the difference in the basis of measurement of both thermometers. On one hand the, thermocouple is an intrusive sensor, which means it will be directly in contact with the sample of interest and under the influence of the same environment. Hence the sensor will be affected by thermal gradients along the sample, heat exchange between surfaces and other media (gases, liquid and solids) in the experimental section, electromagnetic interference, chemical reactivity between the TC sheath and the sample contact surface, and/or neutron irradiation or charged particle. First in order to reduce the heat losses along the thermocouple (Heat pump effect [33]) the thermocouple sheath should be as fine as possible to limit the exchange surface and to avoid excessive sensor material that would otherwise influence the temperature measurements as a result of the thermal inertia of the sensor materials. Also, the thermocouple hot juncture needs to be adequately anchored to the hot sample, this means it needs to be in very intimate contact with the sample of interest. If possible the thermocouple tip should be inside part of the volume of the hot body (i.e. submerged in a hot liquid, inside a borehole, or welded to the surface it will greatly depend on the application) in order to avoid any disturbance in the temperature measurement caused by non-adequate TC/sample interface contact, gases or foreign surfaces that could exchange heat with the thermometer (in the form of radiation, convection and/or conduction). Moreover, a feasible thermocouple thermalization is important to reduce the magnitude of the temperature gradient along the axis of the thermocouple and heat pump effect. Lack of thermalization will lead to erroneous measurements that could be higher or lower than the actual temperature of the sample. Therefore, thermalization can be improved by increasing the portion of the TC inside the sample, for example for a cylindrical piece, there should be at least a 5:1 ratio between the thermocouple insertion and cylindrical piece diameter. This means that

the portion of the TC inserted (preferably along the central axis of the sample to reduce the influence of temperature gradients in the radial direction) should have a magnitude of five times the diameter of the cylindrical piece. Finally, thermocouple physical deterioration will influence its service life and reliability therefore it is of great importance to select adequate thermocouple sheath materials based on the service environment. This means that chemical interaction (corrosion, wet/dry oxidation/reduction, carburization, nitration, hydration, sulfurization, etc.) between the TC materials and the medium should be kept to a minimum by utilizing relatively inert materials for the selected environment; under very aggressive mediums special techniques to protect the integrity of thermocouple might be necessary, i.e. sacrificial material utilization, galvanization, protective coatings, over-sheathing, etc. Lastly, when the sensor needs to perform under service environment in which it will be under neutron irradiation or other particle bombardment, materials with low interaction cross-sections should be chosen in order to reduce as much as possible the influence of atomic transmutation and lattice defect creation, on the thermocouples reliability [23, 28, 31-41]. On the other hand, when performing pyrometer measurements, the black cavity should have an emissivity very close to one (<0.999), this can be done by utilizing a relatively long cavity along with diaphragms to reduce the cavity aperture. Also the pyrometer focal spot or sight should be well positioned inside the black cavity bottom to reduce the size of source effect. The size of source effect can impact the measurement if there are other colder/hotter surfaces in the field of view that will interfere with the irradiation of heat from the cavity. In reality the spot size of an optical sensor focuses in an area that does not have clear exterior limit, but diffuses outward. Therefore, the energy measured by the pyrometer is mostly leaving the calculated focal spot, but outside these limits there is a relatively small quantity of energy captured by the optical sensor; graphically this looks as a bell distribution in which some limits are set for the measurement area, even though a small part is also measured outside this range [29-31].

Furthermore, the 99.98% pure iron cell (Fe-C cell #2) was tested twice (figure 3.8) by imitating the thermal cycles of Fe-C cell #1. The first test on cell no. 2 using pyrometer measurements

resulted on a mean melting/solidification temperature of -7°C and 13°C, respectively. Besides a 3°C recalescence observed for the first solidification cycle, no obvious recalescence can be observed for the rest of the cycle. And the last solidification temperature performed under relatively faster cooling rate (183°C/min.) shows a less than 2°C depression in the transformation temperature compared to the milder cooling rate (60°C/min.) of the first thermal cycles. Moreover, the second test on cell #2 shows a further decrease in the transformation temperature of -13°C and -23°C for the melting/solidification with respect to the reference value of 1153°C. Furthermore, the thermocouple measurements for the first and second test show -46°C and -26.5 differences between mean melting temperature, an additional -49°C and -35°C difference on the average freezing temperature relative to the reference temperature, respectively.

Finally, there were three tests (figure 3.7) conducted in the high purity iron (99.998%) Fe-C eutectic cell #3, such that the two emulated the same thermal cycling and experimental configuration as for the 1st and test performed on the previous Fe-C cells (1 and 2). For the first test the mean melting/solidification temperature difference is around +4°C and -25.5°C, respectively. The second test shows again a depression on the mean transformation temperatures of around -9°C and -26°C for the melting and freezing point, respectively, but it was more pronounced on for the melting than freezing. The thermal curves for the first two tests are almost identical (see appendix B), no recalescence is observed and but instead a discernible change in the curve inclination for both melting and solidification sites. On the other hand, the third test on Fe-C cell #3 was different than the rest since wider variations in heating/cooling rates were undertaken, especially on the heating, along with the addition of more graphite felt around the cell in order to improve thermal homogeneity and reduce the heat losses. Moreover, the cell was thermally cycled more than 10 times at heating rates ranging from 30-105°C/min which resulted on a mean melting temperature of 1150.3°C and standard deviation of ±0.6. Additionally, the cooling rate was varied between 57 and 68°C/min, leading to a mean freezing temperature of 1144°C and a 0.5 standard deviation.

By looking at figure 3.10 and 3.11 were a plot of the comparison between the three Fe-C cells, we can deduct from the experiments that the melting/freezing temperatures decrease as a function of increase in impurities, and this might vary depending on the concentration and nature of the impurities, but for very low concentrations this trend seems to be valid as long as the impurities stay in solution, which also depends on temperature. Therefore, the highest purity material (>99.99%) should be used to avoid depression in the eutectic temperature caused by impurities.

Moreover, the results observed show that the melting points are always higher than the freezing points. This effect is influenced by multiple phenomena; among them the influence of the thermal behavior of the test zone (cell and furnace design) seems to have the greatest impact, i.e. low purity concentration, non-equilibrium melting solidification kinetics and thermodynamics. This can be confirmed by looking at the last test on cell no. 3, in which thermal isolation of the cell was improved by the addition of extra layers of carbon felts. This resulted on a reduction in the temperature gap between melting and freezing temperatures of more than 10°C compared to the first configuration, and also a less marked effect of heating/cooling rate on the transformation temperature. Nonetheless, the inherent difference in fusion and solidification kinetics and non-equilibrium thermodynamics will also account to some extent in the variations on transformation behavior and temperature. For example, important difference between the solidification and melting points measured far from the equilibrium thermal conditions between the cell and the furnace is a phenomenon common to a large majority of the eutectic systems under high rates of cooling. This variation might be also explained by looking at the complex kinetics during solidification which binds the nucleation of the first solid embryos, stabilization and growth to the undercooling magnitude, and availability of nucleation sites (i.e. solid impurities as oxides and crucible wall roughness). Impurities can be introduced as a result of the gradual diffusion of oxygen through the graphite cell wall porosity, reaching the metallic surface, until the adsorbed oxygen saturates the first atomic layers of metal and a fine oxide layer is nucleated until it reaches it equilibrium thickness and no further oxidation takes place, since the layer acts as a protective coating. For example, at room temperature

iron, like most metals, will immediately form a thin (several nanometers thick) oxide layer when exposed to air and moisture, resulting on the formation of predominantly Fe_2O_3 (probably with small quantities of Fe_3O_4). We can asseverate that as the inclusion content increases, the transformation temperatures will shift, usually decrease. Unless they are decomposed or reduced into their metallic form, most of the oxide products will float on top of the molten metal, in the form of a slag, and act as nucleation sites that will impact the observed solidification temperature. Furthermore, under very fast cooling or non-equilibrium cooling, the nucleation of metastable phases can take place during solidification. Hence, extra transformation steps might be present and the liquid might not form the expected crystalline phase, but instead nucleate an intermediate phase that serves as a transition between the equilibrium phases. This is very applicable for highly ordered lattice structures as metal carbides, where the probability of forming the structure under high cooling rates might be impeded due to the inability of the atom species to diffuse and arrange in a highly ordered lattice, from a relatively disordered liquid. This has been studied before and non-equilibrium phase diagrams have been produced for limited systems were the nucleation of metastable phases modifies the equilibrium transformation steps by introducing intermediate steps of local equilibrium [43-55].

Moreover, as stated previously in the Fe-C results section, three graphite crucibles were filled with a similar hypoeutectic mix prepared as for iron-carbon cells #1 to 3. Afterwards, each crucible was inserted into the VITI furnace and to go through the same thermal cycle as the iron-carbon eutectic cells in test 1 (melting/solidifications for at least 5 times). Then, the crucibles were prepared for metallurgical analysis. The optical micrographs of these samples are presented in figure 3.12-3.14, starting from the lowest purity iron powder up to the highest purity metallic powder (99wt.% Fe, 99.98wt.% Fe and 99.998wt% Fe). First, in figure 3.12 we can observe several micrographs at different magnifications of the lowest purity iron-carbon eutectic (99%Iron). The sample's microstructure is composed of a very heterogeneous microstructure. Large primary austenite dendrites (γ-iron FCC) can be observed as they branch out all over the microstructure. Moreover, a black flaky graphite structure is in the micrographs, the carbon phase has a wavy form, and is usually

surrounded by a white phase that could also consist of γ-Fe (FCC), or it might have transformed into lower temperature ferrite (α-Fe BCC). Then, a finer spotty-looking dark microstructure prevails on the micrographs, this is the eutectic structure and it is composed of the dark metal carbide, called cementite (Fe_3C), embedded in a white matrix phase or secondary austenite (white) iron-rich phase. Afterwards, the micrographs corresponding to iron-carbon eutectic (99.98%Iron purity) ingot are shown in figure 3.13. This pictures show a more homogeneous microstructure with a relatively smaller phase fraction of graphite flakes and finer primary austenite dendrites. The eutectic structure dominates the picture, and it can be seen more in detail in the last micrograph. And finally, the microstructure for the highest purity iron powder-carbon eutectic (99.998%Iron purity) is shown in figure 3.14. This microstructure is very homogeneous showing a mostly eutectic microstructure with the exception of some islands of graphite flakes surrounded by the white phase. By zooming into the graphite phase, we can observe a much squared, step-like interface morphology, which differs greatly from the previously observed rounded interface between the graphite flakes and the metal matrix. This plane interface denotes a lack of interaction among the two phases, which means that the carbon needed to reach the equilibrium eutectic composition, has been reached and the diffusion of atomic species is limited to the coarsening of the eutectic constituents, or if kept for a long time at a lower temperature (<727°C) the austenite will slowly convert into ferrite, as it expulses the carbon since ferrite dissolves 35.5 times less carbon than the FCC iron phase. In essence, these microstructural differences among the samples gives us information on the effect of foreign atoms in the eutectic, even for concentrations of less than 1wt.%. This will certainly impact the phase transformation temperature. Therefore, it is very important to avoid the introduction of impurities in the eutectic alloy.

Furthermore, a Vickers micro-hardness test was performed on all the iron-carbon crucibles previously sectioned and observed under the optical microscope. The average values for the hardness of the dendrites and eutectic phase have been compiled in a bar graph shown in figure 3.15. As it can be observed, there is a direct relationship between the increase in impurity content and the increase in

the micro-hardness of the distinct phases. This is due to a mechanism called solid solution strengthening, in which the inclusions will occupy lattice sites (substitutional or interstitial position, depending on the atom radii) in the alloy, that will stress the atom crystalline bonds due to the size mismatch, and this will result on an increase in the overall strength of the alloy up to a maximum. This test was performed in order to provide more evidence on how even such a low concentration of impurities will produce a non-negligible impact on the mechanical properties of the alloy; therefore, this will also impact, to a more or less extent, the melting/solidification temperature and behavior of the alloy.

The aim of the research on the iron-carbon eutectic was to understand the effect of varying amounts of impurities on the eutectic cell performance. The studies were performed in three iron-carbon alloys which differ on the iron purity of the base materials (99wt.% Fe, 99.98wt.% Fe and 99.998wt.% Fe). Upon thermal cycling of the eutectic cells containing the eutectic ingots it was observed that as the impurity content in the system increases, there is a tendency to decrease the melting/solidification temperature of the alloy. Additionally, a metallurgical analysis (optical microscopy and Vickers micro-hardness testing) of the three samples was performed, to complement the thermal curves. The metallographic observations allowed for a comparison between the microstructural features of each alloy, and served as a way to proof how even such relatively small concentration of impurities will cause a non-negligible change in phase concentration and morphology of the alloy. Furthermore, to support the metallography, a Vickers micro-hardness test was performed on particular phases found in the three alloys. This test lead to a more plausible understanding of the impact of impurity content in the strength of an alloy, since there was a direct relationship between an increase in impurity content and increase in the hardness of individual phases in the microstructure. In conclusion, the highest purity material available (>99.99%) is recommended to avoid the effect of impurities on the eutectic temperature. On the other hand, the type-A cell used for the analysis of the iron-carbon eutectic allowed for a simultaneous pyrometry/thermocouple measurement of the eutectic behavior. This enabled a comparison between the two thermometry

methods and more important to understand the advantages and disadvantages of each thermometry technique. Nonetheless, among other tests, the results on the thermal cycling of Fe-C eutectic cells allowed for an improvement in cell design for both pyrometer and thermocouple cells, but also to allowed to envisage the application of these cells as *in situ* reference points in a broad spectrum of high temperature applications, besides nuclear reactor safety and severe accident research.

3.5. Cobalt-Carbon (Co-C) System - Eutectic Response to Heating/Cooling Rate Variations

Afterwards, in this subsection the results obtained on the tests performed on the Cobalt-Carbon eutectic cell #8 are presented. In figure 3.16, a plot of three tests performed for the eutectic cell in different dates show the response of the cobalt-carbon cell to increments in heating and cooling rate.
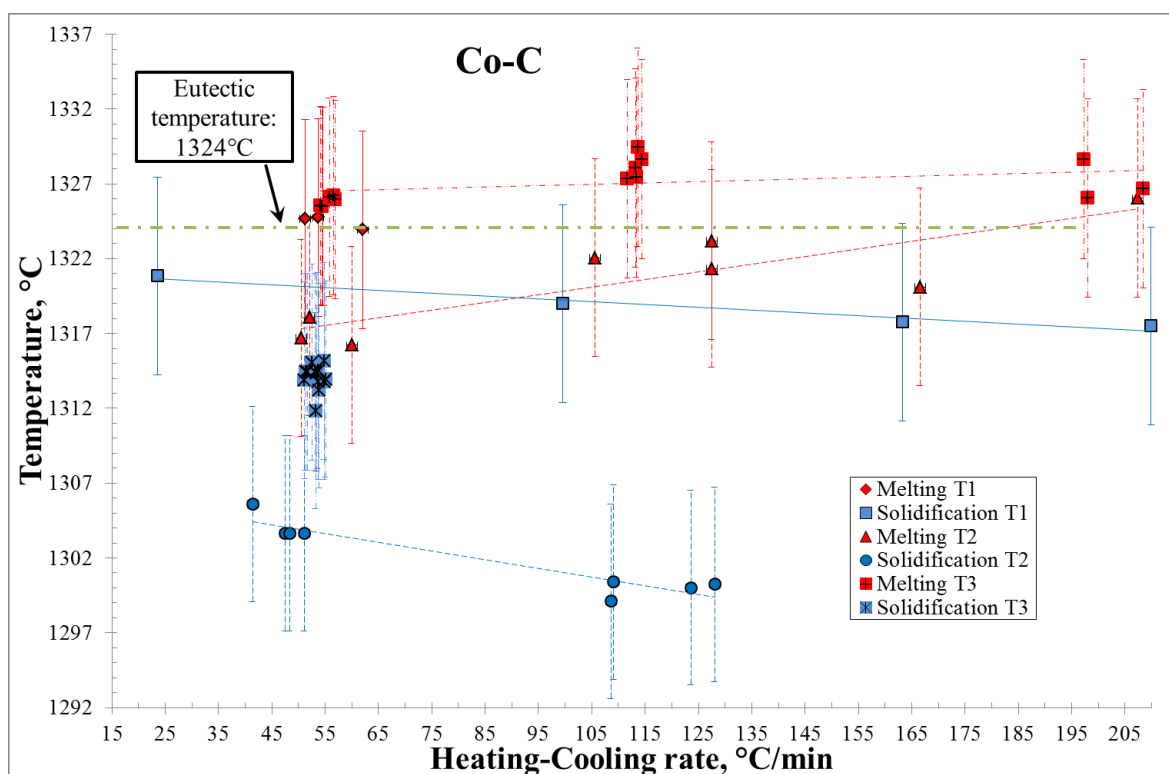
Figure 3.16. Melting/solidification temperature as a function of heating/cooling rate, Co-C cell #8.

Table 3.5 presents a compilation of the data points previously plotted, along with some statistical parameters that serve as indications of the repeatability of the transformation temperature,

and finally the reference value or best estimate for the cobalt-carbon eutectic is from French metrology lab [8, 25] shown at the end. Finally, the difference between the cavity pyrometer (eutectic cell cavity) and the control pyrometer (pointing at the crucible exterior wall) for the 1st and 3rd test varied around 5 to 20°C, being the exterior wall the lowest or relatively colder temperature, except in the second test where there was a colder temperature recorded at the cavity of around minus 25° to 30°C.

Co-C	Melting				Solidification				Eutectic
Test #	Heating rate, °C/min	Melting temperature, °C	Mean temperature μ, °C	Standard deviation σ, °C	Cooling rate, °C/min	Solidification temperature, °C	Mean temperature μ, °C	Standard deviation σ, °C	Reference temp., °C
1st	62,0	1323,9	1324,7	0,5	23,5	1320,9	1318,8	1,3	
	53,7	1324,7			99,6	1319,0			
	51,3	1324,7			163,3	1317,8			
	54,6	1325,5			209,9	1317,5			
2nd	60,0	1316,2	1320,5	3,2	48,3	1303,6	1302,0	2,2	
	50,5	1316,7			109,1	1300,4			
	52,0	1318,1			41,4	1305,6			
	105,7	1322,1			108,6	1299,1			
	127,5	1323,2			47,5	1303,6			
	127,5	1321,3			128,1	1300,2			
	207,4	1326,0			51,1	1303,6			
	166,6	1320,1			123,6	1300,0			
3rd	54,2	1325,6	1327,0	1,3	53,1	1314,4	1314,1	0,8	1324
	56,6	1326,2			53,4	1314,4			
	54,4	1325,5			51,7	1314,4			
	56,9	1326,0			55,1	1314,0			
	55,9	1326,1			54,8	1313,8			
	113,6	1329,5			51,4	1314,4			
	114,4	1328,6			51,2	1313,9			
	113,2	1328,1			53,9	1313,2			
	111,7	1327,3			53,8	1313,8			
	113,3	1327,4			53,2	1311,8			
	197,3	1328,6			52,5	1315,1			
	198,1	1326,0			53,7	1314,5			
	208,5	1326,7			54,8	1315,2			

Table 3.5. Summary of transformation temperatures for the cobalt-carbon eutectic cell #8.

3.5.1 Heating/Cooling Rate effect on Melting/Solidification Temperature of Co-C Eutectic

The Co-C eutectic alloy cell (Co-C cell #8) was subjected to three tests to study the eutectic behavior in a range of heating/cooling rate variations ranging from less than 50°C/min to over

200°C/min. The first thermal cycling was analyzed and a mean melting temperature was found to be slightly over the reference value by +0.7°C and the solidification mean temperature was around -5°C below the value found in literature (eutectic temperature of 1324°C), for a cooling rate ranging from 23.5°C/min. to 210°C/min. with a standard deviation of 1.3°C. Furthermore, during the second test an overall decrease in the transformation temperature was observed obtaining a mean melting temperature difference of -3.5°C (Heating rate: 60-167°C/min, σ: 3.2°C) and -22°C for the freezing point. Moreover, the last test produced a mean melting temperature of 1327°C or +3°C over the reference value, and a solidification temperature of -10°C. Nonetheless, it is important to point out that even though significant variations in heating rates were promoted, ranging from 50°C/min to over 200°C/min, and if we combine the results of all the tests a mean melting temperature of 1324.6°C is obtained with a maximum standard deviation of 3.2°C during the second test. The repeatability of the melting temperature is quite impressive if we take into consideration the important variations in heating ramp, and not to forget that the standard deviation in the worst case is still below the ±7°C instrumental error. On the other hand, even though the freezing temperature repeatability under large variations in cooling rate falls below the instrumental error, the overall mean solidification temperature is still 11°C below the reference eutectic temperature rests was around 22°C lower than the mean melting temperature during the second test. Finally, a discernible change in solidification curve shape was observed between the first and subsequent tests, since we could initially observe some recalescence in the first but this was not anymore the case for the following tests under similar cooling rates.

3.6. Titanium-Carbon (Ti-TiC) System - Eutectic reaction Response to Heating/Cooling Rate

Subsequently, in this part the results obtained on thermal cycling of the Titanium-Carbon eutectic cell #7 are shown. The Ti-C cell was tested twice in the VITI furnace, and the results are plotted in figure 3.17. This plot shows the response of the titanium-carbon cell to variations in heating and cooling rate. Also, table 3.6 presents more detailed data on the results obtained during the testing of this graphite cell. The temperature difference between the cavity temperature and the outside graphite

wall for the first was of plus 50°C and minus 20-30°C in the second test.

Ti-C	Melting				Solidification				Eutectic
Test #	Heating rate, °C/min	Melting temperature, °C	Mean temperature μ, °C	Standard deviation σ, °C	Cooling rate, °C/min	Solidification temperature, °C	Mean temperature μ, °C	Standard deviation σ, °C	Reference temp., °C
1st	65,0	1607,4			45,4	1603,7			
	68,3	1605,4			48,5	1602,3			
	71,1	1606,2	1605,4	3,0	50,9	1601,0	1599,2	4,1	
	67,6	1608,4			48,1	1596,5			
	52,5	1599,7			59,4	1592,5			1646,5
2nd	38,5	1605,4			68,5	1568,1			
	98,9	1610,8			86,1	1565,0			
	39,0	1600,5	1604,7	3,6	61,4	1567,6	1566,6	1,8	
	119,3	1601,9			125,9	1563,8			
	87,5	1605,1			142,8	1568,4			

Table 3.6. Summary of transformation temperatures for the titanium-carbon eutectic cell #7.
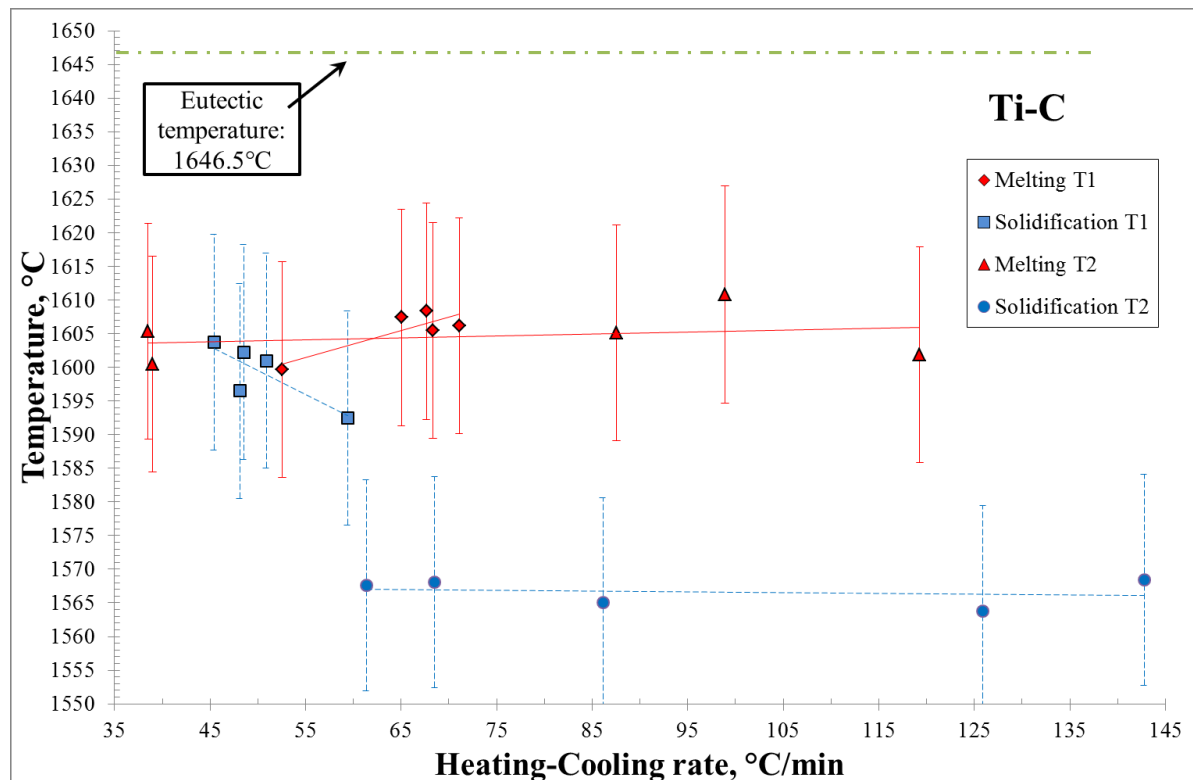
Figure 3.17. Melting/solidification temperature as a function of heating/cooling rate, Ti-C cell #7.

3.6.1 Heating/Cooling Rate effect on Melting/Solidification of the Ti-C Eutectic Temperature

The Ti-C systems low temperature eutectic (Ti-TiC) cell (Ti-C cell #7) was thermally cycled in two test by inducing a variety of heating and cooling rates in order to understand the impact on the melting and freezing behavior. The first test showed a mean melting temperature difference of -41°C

and freezing temperature of -47°C compared to the value found in literature (eutectic temperature of 1646.5°C) and a tendency for an increase in melting temperature as the heating rate increased and the a similar pattern was observed for the solidification temperature. Moreover, during the second test a wider range of heating/cooling rates were induced (~40°C/min to 140°C/min), however there was a linear and not a scaling behavior for an increase in heating rate as it was observed previously, plus the mean melting temperature was virtually the same as before. Anyhow, a significant decrease in the mean freezing temperature of 33°C was observed compared to the first test. Furthermore, it is important to point out that there exist intermediate metal carbide TiC and two eutectic points (Ti-Ti-C and TiC-C) in the Ti-C system (see Ti-C phase diagram in Appendix A). Therefore, even though we have introduced a hypoeutectic mixture in the cell, corresponding to the low temperature eutectic, the following reactions will take place as we approach the melting point. First, as the powder goes through the sintering temperature range atomic inter-diffusion between titanium and carbon becomes an important process. Then once the eutectic temperature is reached the first liquid nuclei appear and wetting of the solid phase. Since the availability of graphite in the cell is around 81wt.% C (graphite from crucible and flakes) compared to 19wt.% Ti, the melt that has formed will initially have the eutectic composition. Nonetheless, there will be a tendency towards the formation of the TiC compound, which can be very sluggish process. But as the melt is solidified and thermal cycling continues, there will be a composition shift toward the carbon rich side, as it forms more and more titanium carbide until it reaches its equilibrium composition. This might explain in part why we initially observe a marked tendency to an increase/decrease in melting/cooling temperature as a function of heating/cooling rate, respectively; but during the second test there is an almost linear behavior, or no sensitivity to changes in heat addition or extraction. Even though we should not discard the influence of the cells thermal inertia in the phase change, it should be understood that the tests were performed under the same experimental configuration. However, the standard deviation of the transformation temperatures remains below the instrumental error, even under significant changes in heating/cooling rate.

3.7 Ruthenium-Carbon (Ru-C) System - Eutectic reaction Response to Heating/Cooling Rate

In the next section, we will go over the results obtained for two ruthenium-carbon eutectic cells which include the pyrometer cavity (cell #12) and thermocouple well (cell #15). Three tests at times were performed on the Ru-C pyrometry cell #12; the melting and solidification temperatures as a function of heating and cooling ramp are plotted in figure 3.18.
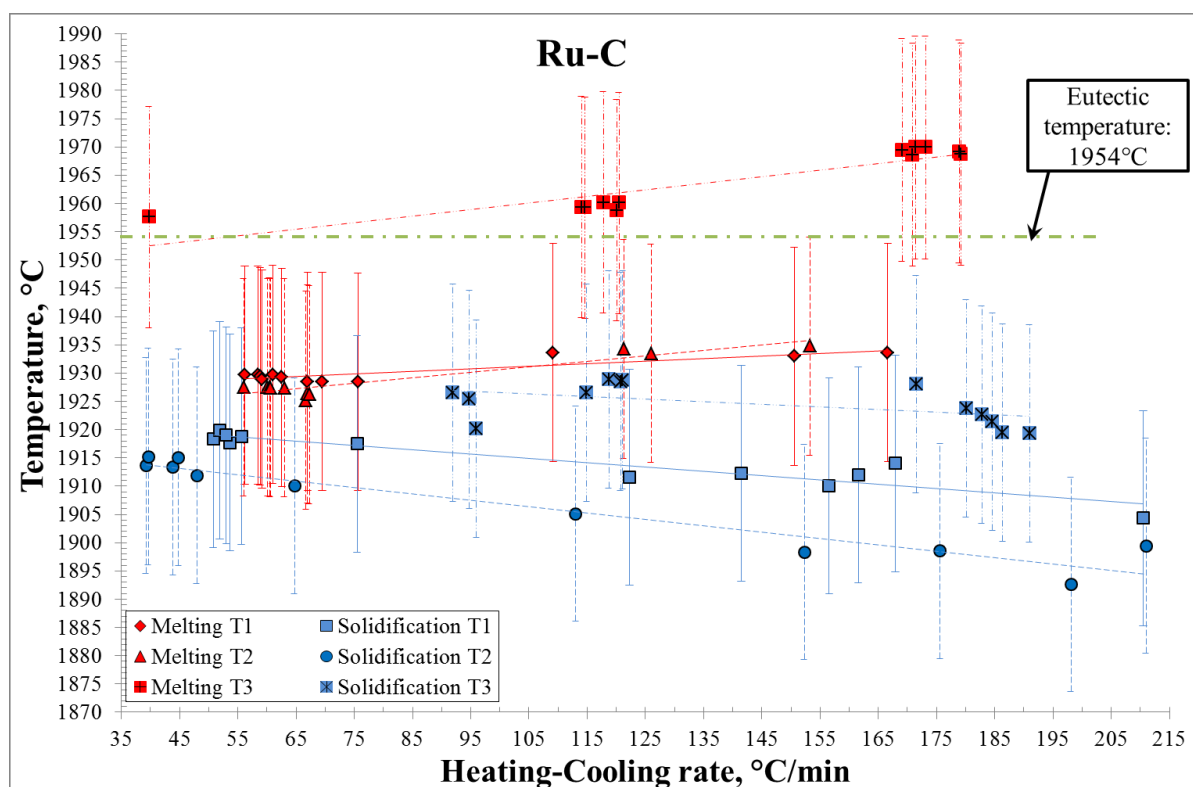
Figure 3.18. Transformation temperature as a function of heating/cooling, Ru-C pyrometry cell #12.

Additionally, a more detailed compilation of the results shown in the previous figure can be found in table 3.7. In this table is included the melting/solidification, mean temperature, and standard deviation which contains a wide range of heating/cooling rates which expands over a significant temperature range.

Finally, as well as for the pyrometry cell, the results on the thermowell-style Ru-C eutectic cell (cell #15) are respectively shown in figure 3.19 and table 3.8. This subsection serves to elucidate the different in the behavior of a non-intrusive thermometer as the pyrometer, and an intrusive thermometer like the thermocouple.

3.7.1 Heating/Cooling Rate effect on Melting/Solidification Temperature of Ru-C Eutectic

The Ru-C eutectic pyrometer cell (Ru-C cell #12) was also subjected to fluctuations in heating and cooling rates to study the impact in the melting and freezing behavior. The first test showed a mean melting and solidification temperature of -23°C and -38°C, respectively, when compared to the value found in literature (eutectic temperature of 1953°C). Additionally, during the second test there was a decrease of 2°C in the mean melting temperature and an 8°C in the mean freezing temperature.

Ru-C	Melting				Solidification				Eutectic
Test #	Heating rate, °C/min	Melting temperature, °C	Mean temperature μ, °C	Standard deviation σ, °C	Cooling rate, °C/min	Solidification temperature, °C	Mean temperature μ, °C	Standard deviation σ, °C	Reference temp., °C
1st	56,2	1929,7	1930,4	1,9	50,8	1918,3	1914,7	4,7	
	58,8	1929,4			53,6	1917,7			
	61,0	1929,7			51,9	1919,9			
	58,4	1929,7			53,0	1919,0			
	59,2	1928,9			55,6	1918,8			
	62,5	1929,3			122,3	1911,6			
	75,6	1928,4			75,5	1917,5			
	109,2	1933,6			156,6	1910,0			
	166,6	1933,6			141,5	1912,3			
	69,5	1928,5			210,5	1904,4			
	150,5	1933,0			161,6	1912,0			
2nd	63,1	1927,4	1928,9	3,3	39,7	1915,2	1906,7	7,8	1953
	60,6	1927,4			39,2	1913,7			
	56,0	1927,5			44,8	1915,1			
	60,1	1927,5			43,9	1913,4			
	60,5	1927,5			48,0	1911,9			
	67,0	1926,3			113,0	1905,1			
	121,3	1934,3			64,8	1910,0			
	153,2	1934,8			152,4	1898,4			
	67,3	1926,2			175,6	1898,5			
	126,0	1933,5			198,1	1892,7			
	66,7	1925,2			211,1	1899,5			
3rd	39,8	1957,6	1963,9	5,1	118,8	1928,9	1924,6	3,5	
	114,0	1959,4			121,1	1928,8			
	114,7	1959,3			120,8	1928,5			
	114,7	1959,3			114,9	1926,5			
	170,9	1968,6			94,8	1925,4			
	173,2	1969,9			91,9	1926,5			
	171,4	1969,9			96,0	1920,2			
	117,9	1960,2			182,8	1922,7			
	120,5	1960,1			180,1	1923,8			
	120,1	1958,8			171,5	1928,0			
	169,1	1969,4			184,6	1921,4			
	178,9	1969,2			191,0	1919,4			
	179,2	1968,7			186,4	1919,4			

Table 3.7. Summary of transformation temperatures for the eutectic Ru-C pyrometer cell #12.

And finally, the third test was conducted, with some modifications in the experimental set-up, by adding extra thermal insulation around the cell in order to reduce the heat losses. The mean melting temperature difference was +11°C and -28°C the mean solidification. The Ru-C system has demonstrated a high degree of repeatability, since there was a standard deviation of 5°C for the melting temperature under heating rates ranging from 40 to almost 180°C/min. and a mean melting temperature of 1942°C. Furthermore, a small standard deviation of less than 8°C was observed during cooling rates from 40°C/min to 211°C/min, which is quite impressive for a five-fold increase in cooling rate; nonetheless, there was a mean solidification of 1915.8°C.
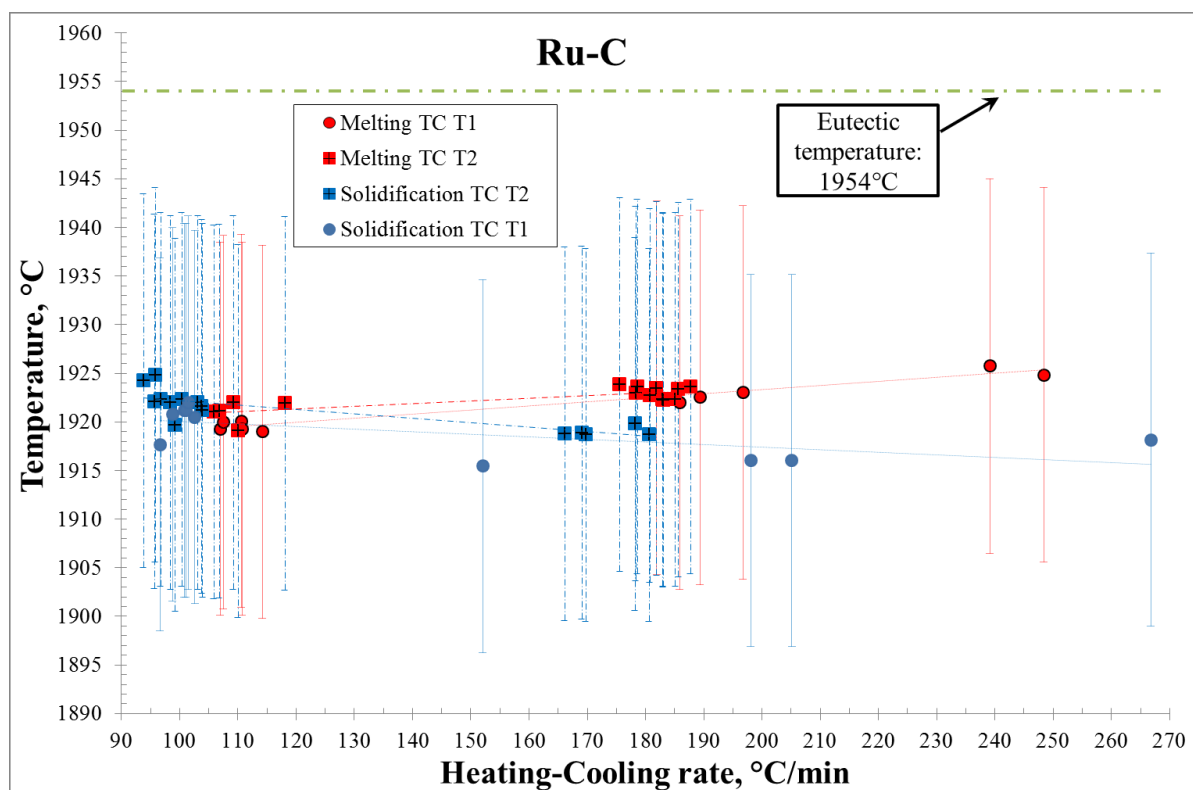
Figure 3.19. Transformation temperature as a function of heating/cooling, Ru-C thermocouple cell#15.

This system showed a very marked trend regarding the effect of heating/cooling rate on transformation temperatures and recalescence. For example it was observed that the melting temperature increases as function of an increase in the heating rate, and respectively the solidification transformation temperature decreases as the cooling rate is increased. This pattern can be visualized in figure 3.18. Besides, this eutectic system showed a marked increase in recalescence as a function of

increase in cooling rate, or undercooling, resulting on a recalescence of up to 32°C for a corresponding cooling temperature rate of 210°C/min (see Appendix B). Even though this behavior is not particular of the Ruthenium-Carbon eutectic system it has been pointed out because there was a clear increase in recalescence as a function of supercooling. It appears that most metals and alloys show a similar behavior, to a minor or larger extent, as they undergo liquid to solid transformation with increasing cooling rates. On the other hand, it should be also pointed out that there is definitely a thermal effect caused by the experimental configuration, since it was seen that once more thermal isolation was added there was a gain in temperature for both transformation temperatures. This effect will be more obvious when we compare the results obtained on the testing of certain eutectic cells in metrology labs.

Ru-C	Melting				Solidification				Eutectic
Test #	Heating rate, °C/min	Melting temperature, °C	Mean temperature μ, °C	Standard deviation σ, °C	Cooling rate, °C/min	Solidification temperature, °C	Mean temperature μ, °C	Standard deviation σ, °C	Reference temp., °C
1st	114,2	1919,0	1921,8	2,3	100,8	1921,2	1918,6	2,5	
	110,6	1920,1			102,6	1920,5			
	107,0	1919,3			98,8	1920,8			
	107,5	1920,0			101,1	1921,2			
	110,7	1919,3			101,5	1922,0			
	185,9	1922,0			873,1	1915,0			
	181,9	1923,5			96,6	1917,7			
	239,2	1925,7			152,1	1915,4			
	196,7	1923,0			198,1	1916,0			
	248,4	1924,8			205,1	1916,0			
	189,3	1922,5			266,8	1918,2			
2nd	110,0	1919,1	1922,4	1,2	93,9	1924,2	1921,1	1,9	1953
	105,9	1921,0			103,1	1922,0			
	109,3	1922,0			95,7	1922,1			
	118,1	1921,9			95,8	1924,8			
	106,8	1921,1			98,4	1922,0			
	178,6	1923,6			99,3	1919,7			
	178,3	1922,9			100,4	1922,3			
	183,0	1922,3			96,8	1922,3			
	183,1	1922,2			103,8	1921,6			
	187,7	1923,6			103,9	1921,2			
	181,9	1923,4			180,7	1918,7			
	180,7	1922,7			166,2	1918,8			
	185,7	1923,3			169,1	1918,9			
	175,6	1923,8			169,8	1918,7			
	185,1	1922,3			178,2	1919,8			

Table 3.8. Summary of transformation temperatures for the eutectic Ru-C thermocouple cell #15.

The Ru-C eutectic thermocouple-well cell (Ru-C cell #15) was thermally cycled during two tests. The mean melting temperature for the 1st test is 1921.8°C for a heating rate ranging between 107°C/min. up to 248°C/min. with a standard deviation of 2.3°C; moreover, the mean solidification temperature is 1918.6°C for a cooling rate extending from 96°C/min. up to 266°C/min. with a standard deviation of 2.5°C. Additionally, the second test resulted on a mean melting and solidification temperature of 1922.4°C and 1921.1°C, respectively for a heating/cooling rate spanning over 80°C/min., and a respective standard deviation of 1.2°C and 1.9°C, for the transformation temperatures. By looking at figure 3.19, it is evident that the thermocouple measurements seem to be less affected by rate changes or heat extraction rate than the pyrometer, and we could say that there is virtually no difference between the melting/solidification temperature at a temperature ramp of 100°C/min. and lower for this cell design. On the other hand, the thermocouples seems to be more sensible to the thermalization degree, nonetheless even for less than 20% of the cavity volume filled by the eutectic alloy the solid↔liquid transformation is clearly discernible. Hence this is very promising since a further reduction in since is possible, even though the mechanical strength of the cell might be the limiting factor, especially when trying to increase the length of the thermowell to improve thermalization and reduce the wall thickness to reduce size. Anyhow, the thermalization problem should be reduced by increasing the amount of material introduced in the cell. Unfortunately, the Ru-C cell #15 thermowell crayon broke while trying to unscrew the cell to refill it for the second test. Hence there might be a need to increase the strength of the crayon by either increasing the wall thickness or selecting stronger graphite. Also, especial attention needs to be placed when choosing the thermocouple sheath material in order to maintain the reaction between graphite and sheath to a minimum.

3.8 Rhenium-Carbon (Re-C) System - Eutectic Reaction Response to Heating/Cooling Rate

Moreover, this section presents the results on the highest temperature eutectic cell tested, the Rhenium-Carbon cell #16. Nonetheless, figure 3.20 and 3.21 present the results on the transformation temperature and recalescence magnitude before solidification for two tests on the Re-

C eutectic cell #16, as a function of variations in the stabilization temperature. Before continuing, it should be stated that this cell leaked some of the eutectic material while liquid through the bottom of the crucible. This might have been due to a non-discernible micro fissure at the bottom of the cell caused by handling or by thermal expansion/contraction stress concentration during testing. This is the reason why for some particularly high cooling rates, a double recalescence was observed (see figure 3.22 and 3.23). This double recalescence is due to the separate solidification of two independent pools of molten eutectic. Hence, the solidification of the exterior drop, observed as a double recalescence, is not accounted in the analysis of these tests, on the other hand, not a single melting temperature has been excluded since there is a very repeatable pattern and no noticeable double melting has been observed.
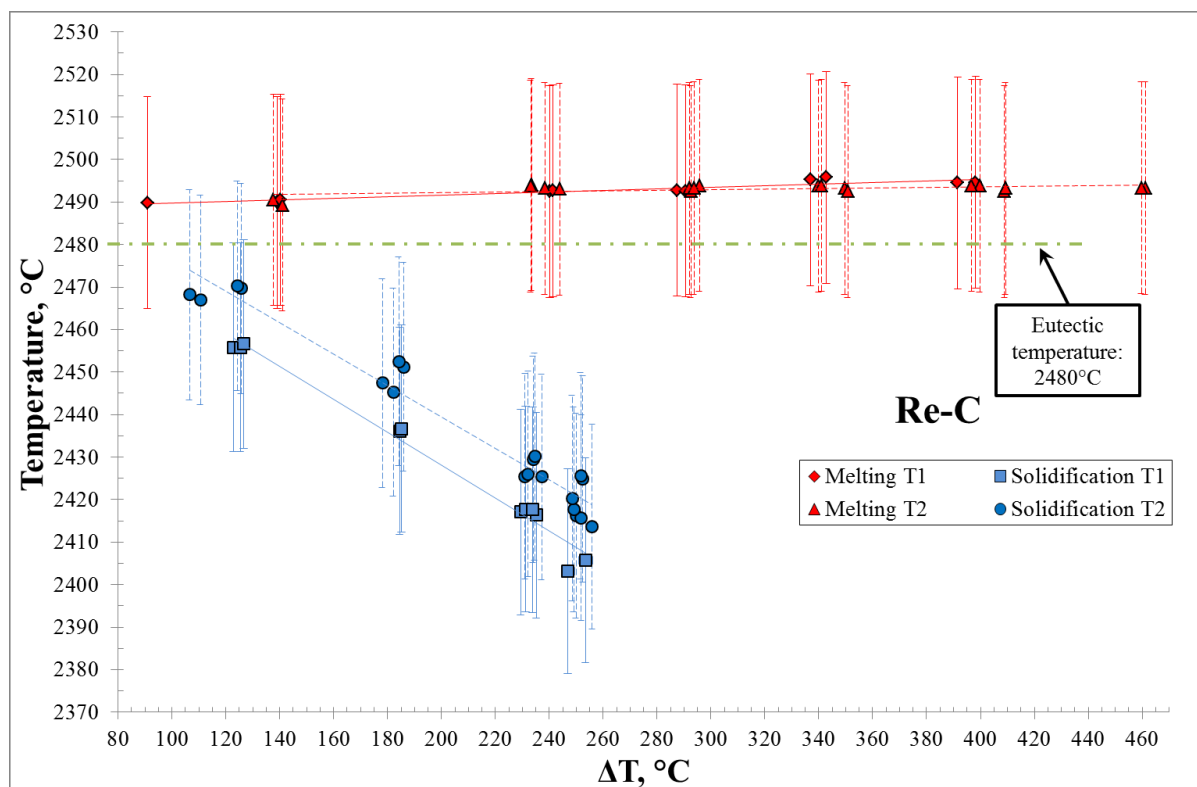
Figure 3.20. Transformation temperature as a function of the difference between minimum/maximum stabilization temperatures for Re-C cell #16.
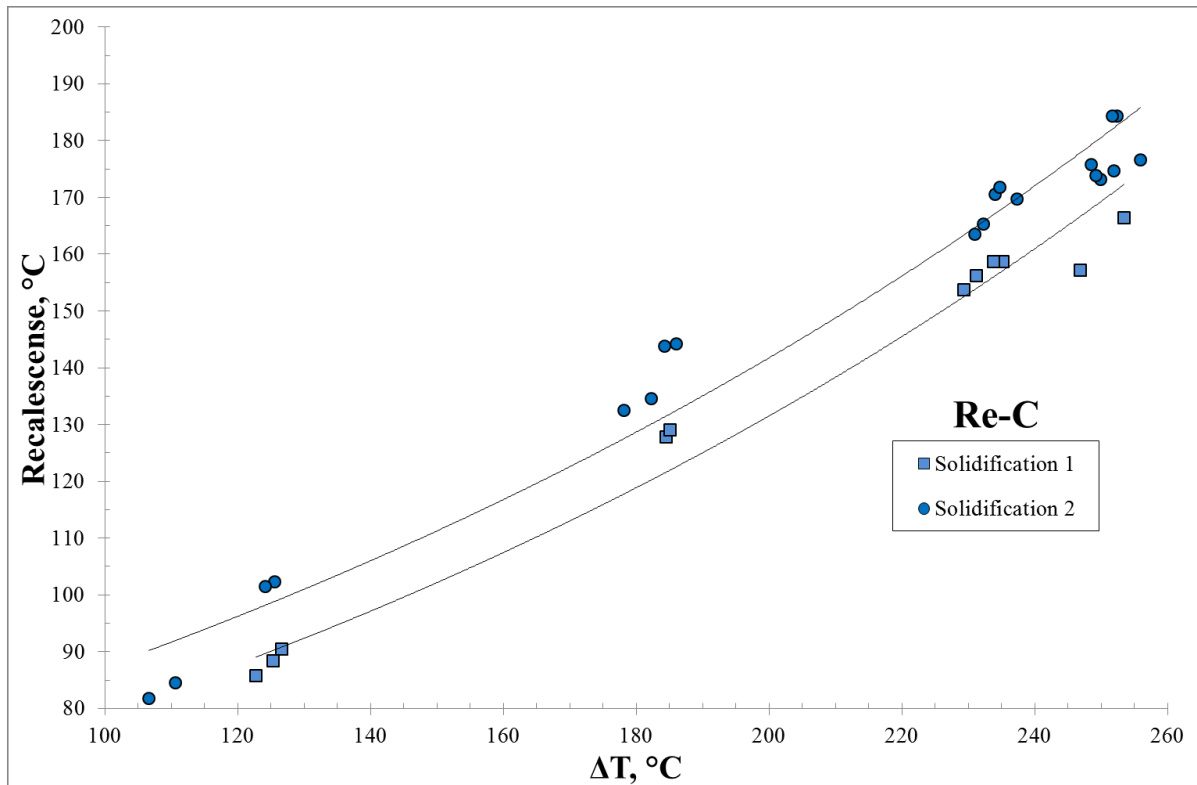
Figure 3.21. Recalescence temperature as a function of the difference between superheat stabilization temperature and minimum temperature just before solidification for Re-C cell #16.

Furthermore, opposite to the previous eutectic cell curves, the results on Rhenium-Carbon eutectic cell #16 transformation temperature has not been plotted as a function of heating/cooling rate. The behavior of rhenium-carbon eutectic transformation, especially due to rhenium, is very particular and will be discussed in more depth afterwards. Anyhow, in order to make more sense out of the Re-C plots, a more pertinent representation of its melting/cooling temperature behavior is illustrated by comparing it to the temperature difference between specific minima and maxima in the thermal curve. For example in figure 3.20, the melting temperature is plotted as a function of the difference between the solid state stabilization temperature (T_{solid}) and the superheated liquid stabilization temperature (T_{SHL}) after melting, or $\Delta T_{melting} = T_{SHL} - T_{solid}$. On the other hand, the solidification temperature, has been plotted as a function of the difference between the superheated liquid stabilization temperature (T_{SHL}) and the minimum undercooled liquid temperature (T_{UCL}) reached just before recalescence, hence $\Delta T_{solidification} = T_{SHL} - T_{UCL}$.
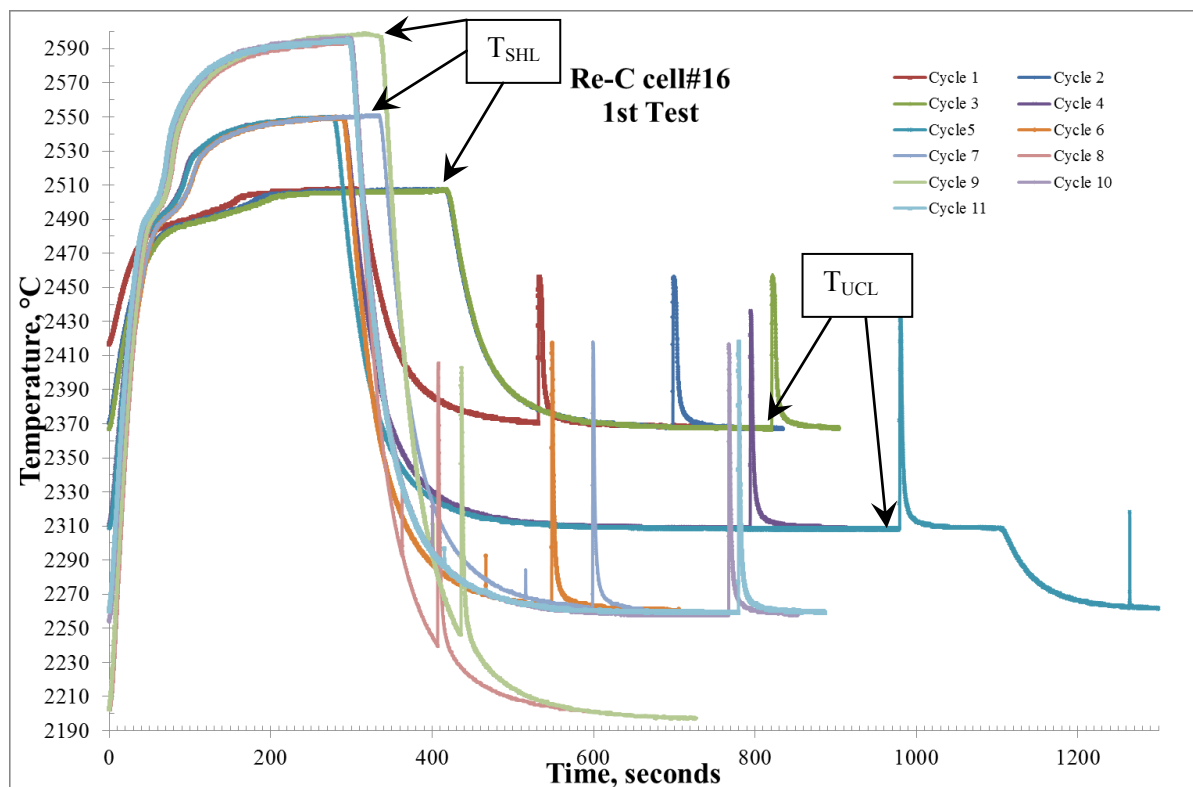
Figure 3.22. Thermal cycling of the Re-C cell #16 showing melting/solidification curve, test 1.

Moreover, figure 3.22 and 3.23 are the thermal curves corresponding to the 1st and 2nd tests performed on the Re-C cell #16, respectively. They have been included here, and not in the Appendix B, to illustrate the particular solidification behavior of this metal-carbon eutectic and its impressive recalescence. Finally, table 3.9 presents a summary of the transformation temperatures for the tests performed on the rhenium-carbon cell #16. It includes the mean melting/solidification temperatures, the standard deviation for the whole set of transformation temperatures, and finally the eutectic reference temperature for comparison.
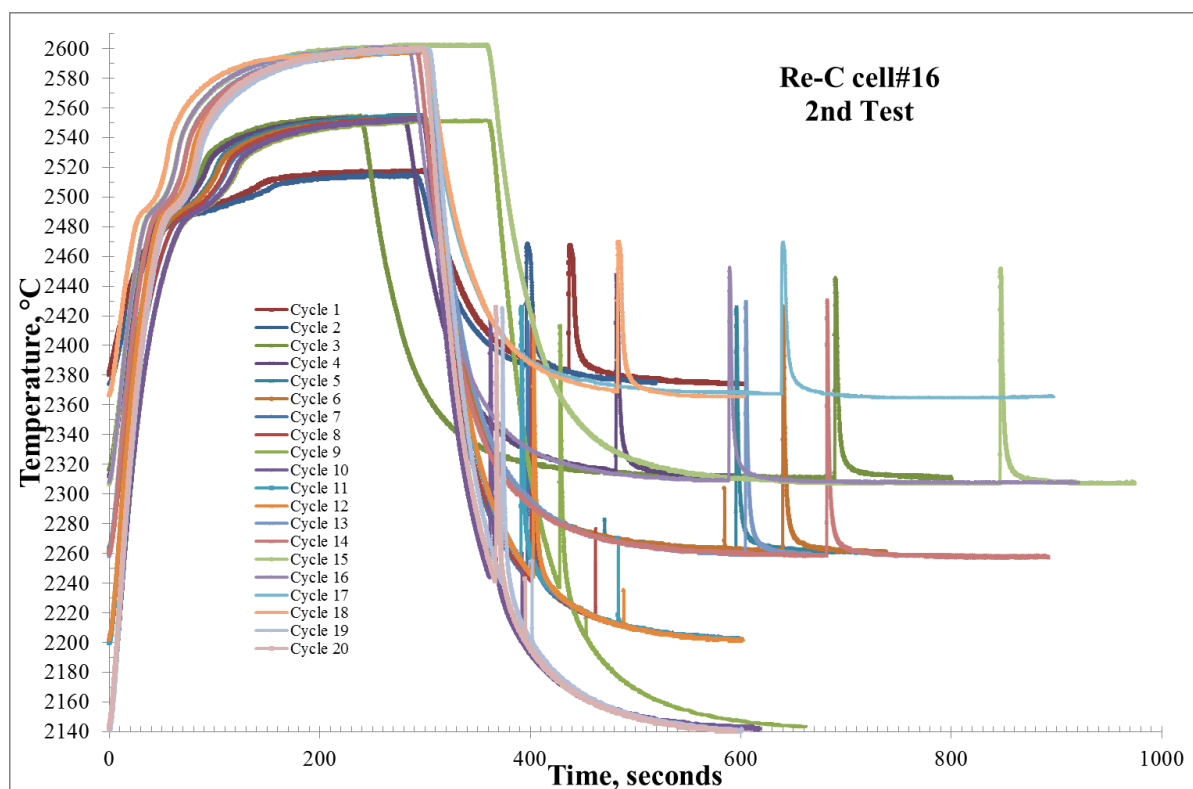
Figure 3.23. Thermal cycling of the Re-C cell #16 showing melting/solidification curve test 2.

3.8.1 Heating/Cooling Rate Effect on Melting/Solidification of the Re-C Eutectic Temperature

Finally, the highest melting point eutectic tested was the Re-C system (2480°C), for which two tests were withstood by the Re-C cell #16 under significantly fast heating and cooling rates. Nonetheless, it was more pertinent to plot the curves as a temperature versus ΔT, since rhenium-carbon solidification behavior is quite unique. Its solidification behavior is extremely influenced by the superheating temperature-time, which dictates the magnitude of undercooling temperature-time (Maximum observed undercooling: ~250°C, over 11 minutes), followed by a very large recalescence (maximum measured recalescence: ~185°C). On the other hand, Re-C eutectics melting temperature is relatively insensible to heating rate, when compared to its solidification behavior under variable superheating magnitude and time at molten state. The first test on Re-C cell #16 resulted on a mean melting/solidification temperature of 2492.8°C and 2429°C, for a standard deviation of 2°C and 19°C, respectively. Moreover, the second test resulted on a mean melting/solidification temperature corresponding to 2493°C and 2437.1°C, with a standard deviation of 1.2°C and 19.4°C, respectively.

It is evident that the melting temperature is more repeatable than the solidification just by looking at the standard deviation. This is not only the case for the rhenium-carbon system but in general the melting temperature seems to have better reproducibility than the solidification temperature to a larger or smaller extent in all the eutectics studied, and this is in part because of the inherent differences between the melting and solidifications kinetics.

Re-C	Melting				Solidification					Eutectic
Test #	ΔT, °C	Melting temperature, °C	Mean temperature μ, °C	Standard deviation σ, °C	ΔT, °C	Solidification temperature, °C	Mean temperature μ, °C	Standard deviation σ, °C	Recalescence, °C	Reference temp., °C
1st	90,8	2489,8			137,0	2455,8			85,8	
	139,1	2489,9			139,7	2455,8			88,4	
	140,2	2490,5			140,8	2456,6			90,4	
	240,2	2492,4			241,3	2436,1			127,8	
	241,3	2492,7			241,8	2436,7			129,0	
	287,4	2492,8	2492,8	2,0	284,9	2417,1	2429,0	19,3	153,7	
	290,6	2492,6			289,3	2417,8			156,2	
	391,5	2494,5			354,1	2405,8			166,4	
	398,2	2494,6			353,4	2403,2			157,2	
	342,8	2495,8			338,8	2416,3			158,7	
	336,9	2495,2			335,6	2417,6			158,6	
2nd	137,75	2490,5			135,2	2467,0			84,6	
	141,00	2489,3			128,6	2468,2			81,8	
	238,49	2493,2			243,9	2445,2			134,5	
	243,85	2493,0			239,7	2447,4			132,6	
	292,56	2492,4			292,8	2425,5			163,5	2480
	291,99	2493,2			291,3	2426,0			165,3	
	349,62	2493,2			309,6	2416,2			173,1	
	350,84	2492,4			312,8	2415,7			174,6	
	408,96	2492,4			314,4	2413,6			176,6	
	409,29	2493,2	2493,0	1,2	308,8	2417,7	2437,1	19,4	173,9	
	399,79	2493,8			343,3	2425,3			169,7	
	396,78	2493,9			354,1	2420,3			175,8	
	339,96	2493,7			339,1	2429,5			170,5	
	341,10	2493,9			341,7	2430,1			171,8	
	295,80	2493,9			295,0	2451,2			144,2	
	293,69	2493,3			291,8	2452,5			143,8	
	233,54	2494,1			233,2	2469,6			102,3	
	233,22	2493,7			229,9	2470,3			101,5	
	461,32	2493,3			358,8	2424,9			184,3	
	459,78	2493,3			358,5	2425,6			184,3	

Table 3.8. Summary of transformation temperatures for the eutectic Rhenium-Carbon cell #16.

The tests performed on Co-C, Ti-C, Ru-C and Re-C cells had the aim of elucidating the behavior of the eutectic transformation under the effect of heating and cooling rate fluctuations. It was observed that there is a tendency for the melting temperature to linearly increase as the heating rate increases, and likewise there is a linear depression in the solidification temperature as a function of an increase in the cooling rate. This was observed to a minor or greater extent in all the tests (1st

and 2nd test) performed on the selected eutectic cells using the same experimental configuration (thermal isolation and graphite susceptor). This is effect is due to the independent heat-up/cool-down of the fraction of primary liquid/solid formed during the non-equilibrium melting/solidification transformation. On the other hand, a third test was performed on the Co-C and Ru-C cells in order to perceive the influence of the addition of extra layers of thermal insulation (graphite felt) to reduce heat losses and increase the thermal homogeneity of the test section. In both cases the melting temperature was increased just above the reference value and the freezing temperature/cooling rate slope decreased, along with a slight increase in the solidification temperature. It is important to understand that even though the kinetics of melting and solidification are altered by the heat addition/extraction rate and direction, there is a more overwhelming effect produced by poor thermal homogeneity of the zone. This effect will diminish by increasing the eutectic alloy content in the cell (complete cavity fill-up), by improving the cell design (i.e. reduction in cell size, and addition of internal insulation to direct all the heat towards the cavity) and the furnace design (improvements on the thermal homogeneity and heat loss reductions of the test section). Although, there is an influence of the heating and cooling rate on the cells repeatability, the variations are below the instrumental uncertainty still under significant fluctuations in heating/cooling rate. Additionally, it has been observed that the melting inflection point has better reproducibility than the solidification temperature. Therefore, the melting temperature should be preferred over the solidification temperature for thermometer calibration. However, the first melting transformation temperature should not be considered, since it has poorer repeatability than the subsequent melting points. This behavior is due to the thermal history or aging effect, which depresses the first melting temperature relative to the following melting inflection points, and is a direct result of the lower-temperature (room temperature) microstructural state of the eutectic alloy while undergoing the first melting transformation.

3.9 Niobium-Carbon (Nb-C) and Molybdenum-Carbon (Mo-C) Complex Eutectic Systems

Moreover, Niobium and Molybdenum metal-carbon systems which also contain eutectic points were tested. They are particularly complex binary eutectic phase diagrams, due to the systems' multiple intermediate phases, and also because of the polymorphism of some carbides. See the Niobium-Carbon binary phase diagram in figure 3.24.
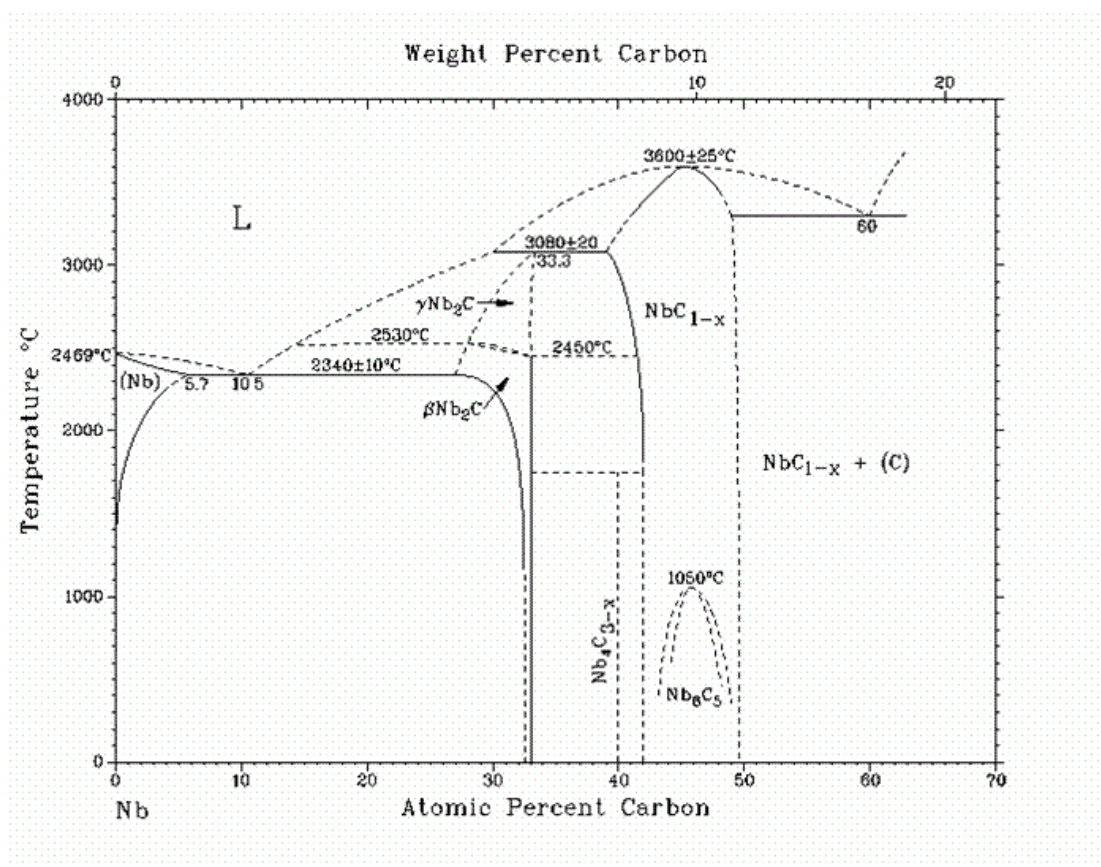
Figure 3.24. Niobium-Carbon phase diagram [J.F. Smith, O.N. Carlson, and R.R. de Avillez].

Furthermore, figure 3.25 is a plot of the curves obtained for the testing of the Nb-C eutectic cell #11. As it can be observed no discernible inflection in the curve or heat of transformation can be detected. This might due to the inherent nature of this multi-phase system, and the thermodynamic competition for the formation of several phases and its field or region of nucleation. The previous micrographs (Figure 3.26) are the result of the metallurgical preparation of the sectioned niobium-carbon eutectic cell. The cylindrical graphite cell was fine cut into two halves and they were prepared

for metallography following the same steps as for the iron-carbon eutectic cells in section 3.4.1. The micrograph on the left is the bottom corner section of the Nb-C cell, and multiple phase domain layers can be observed as rings growing outwards from the bottom right corner towards the top left angle. If we start by moving away from the bottom left corner going out from the concave section, there is a dark region where the pyrometer graphite cavity used to be, and then there are multiple layers as we move towards the top corner were the graphite cell wall is located. The entire ring-like regions are fields of stability of the niobium-carbon system, and they were formed due to the diffusion of carbon into the metallic niobium.
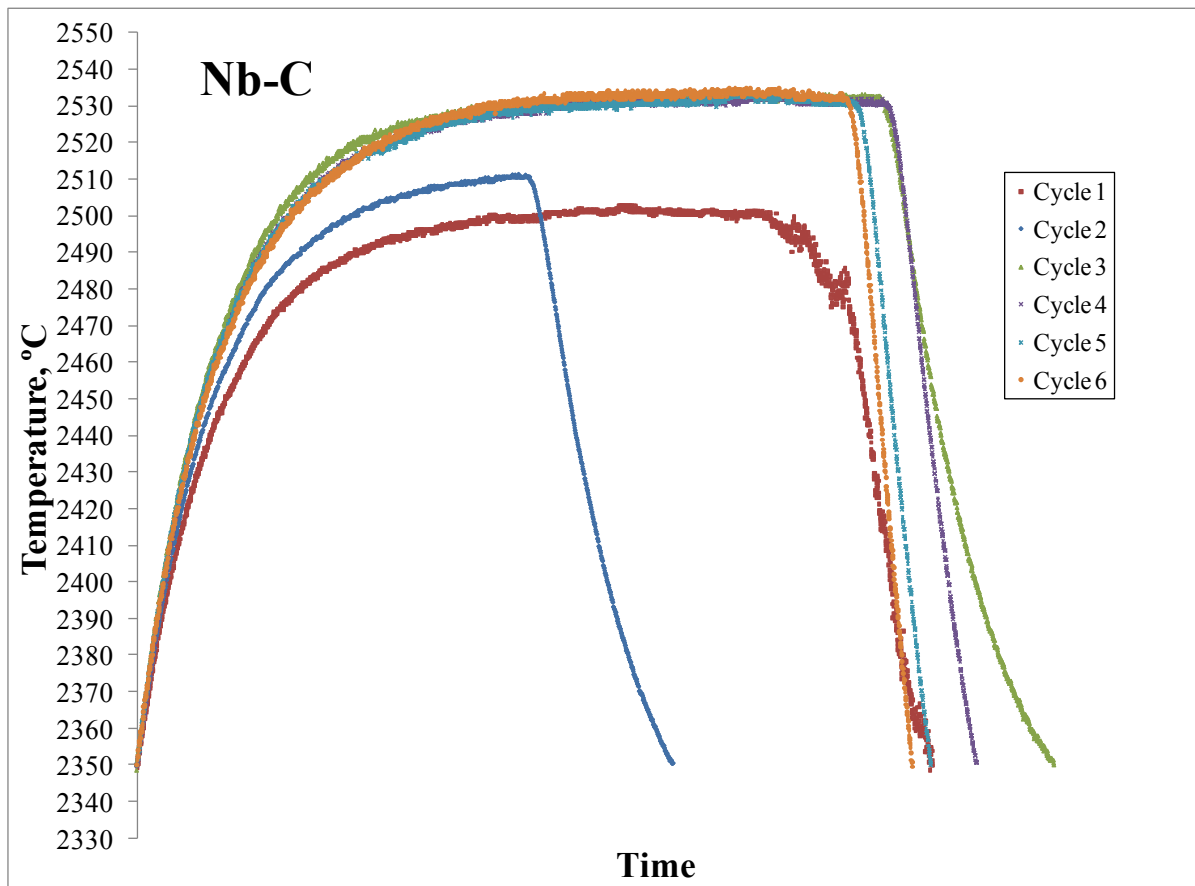
Figure 3.25. Thermal cycling of the Nb-C cell #11 showing melting/solidification curves.
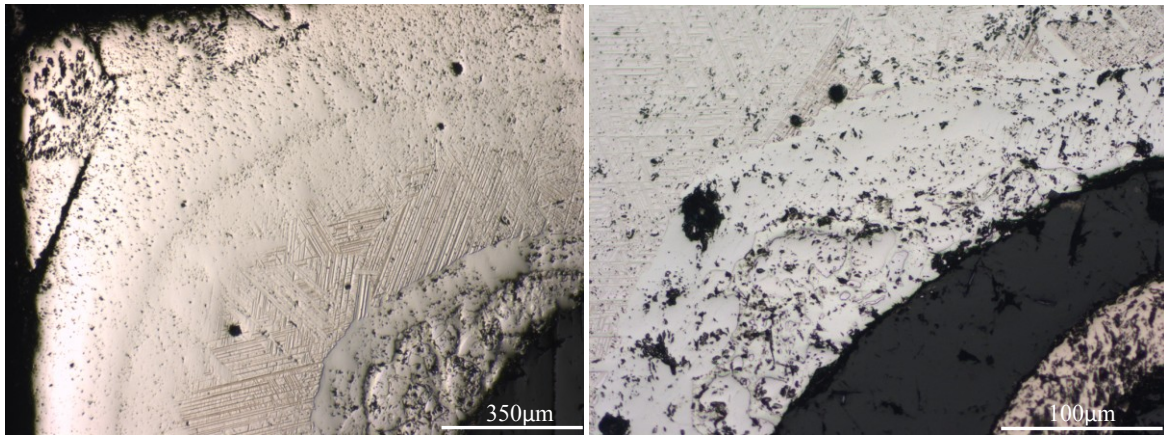
Figure 3.26. Niobium-Carbon cell #11 micrographs at different magnifications showing multiple phase layer domains.

For example the middle part which looks scratched, is the softer niobium rich region, and the following layer are a niobium-carbide two phase and the last layer before the graphite seems to be formed only by carbides. The second micrograph is a magnification of most inner layers, were a finer detail on the microstructure differences can be observed.
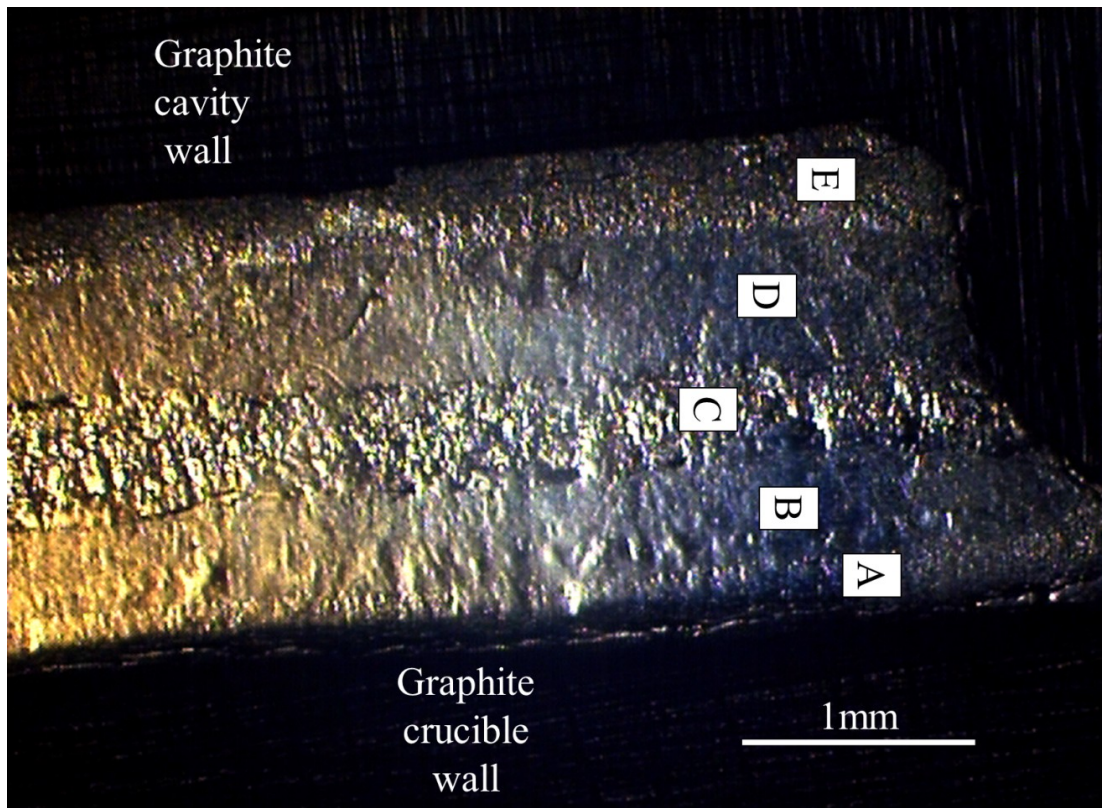
Figure 3.27. Niobium-Carbon cell #11 section utilized for micro-hardness testing showing the multiple phase layer domains with letters.

Furthermore, in order to better characterize the differences between the different phase fields a Vickers micro-hardness tests was performed on another region of the sample, which is the thinner region of niobium-carbon alloy moving upward from the bottom of the crucible in-between the graphite crucible and pyrometer cavity (Figure 3.27). This micrograph has been labeled to portray the multi-layer structure, and facilitate the relationship to the micro-hardness plot (Figure 3.28). The diamond-like indentures were made and a HV value measured utilizing a 200lbs force and 20-second penetration time. In Figure 3.28 a bar graph is tabulated for the Vickers micro-hardness of each region. In this bar graph it can be observed how the hardness decreases toward the middle layer C and it increases as we move towards the outside graphite layers. It should be noted that the micro-hardness values for the exterior part are relatively quite high and this is typical of metal-carbides. If we had performed a chemical analysis, we would see a similar pattern as for the hardness were the highest carbon concentration is at the most exterior layer (after the graphite walls) and it decreases as we move towards the middle. The carburization treatment is a classical manner to increase the hardness or strength of most of metals through the addition or carbon in solid solution or carbide precipitation.
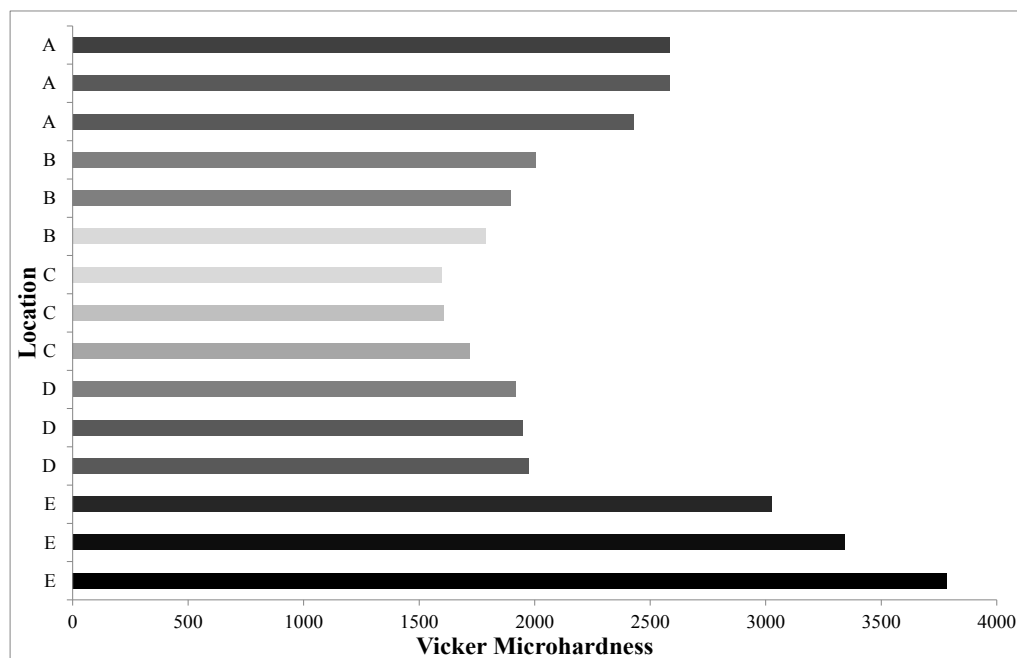
Figure 3.28. Vickers micro-hardness values for regions A through E in the macrograph in fig. 3.27.

Furthermore, besides studies on the Nb-C eutectic system, research on the Molybdenum-Carbon system was pursued. These two metal-carbon systems have multiple similarities and this can be confirmed by looking at their binary phase diagrams, which have a lot of resemblance (Figure 3.24 and 3.29). This is in part due to the shared body-centered-cubic crystal lattice and almost identical electron configuration between niobium and molybdenum, since they stand side-to-side in the periodic table of the elements.

Furthermore, figure 3.30 is a plot of the thermal cycling curves for the Mo-C cell #9. Upon heating the curves shows what it seems as a double transformation, barely discernible in some of the curves. On the other hand, upon cooling there are two distinct recalescence peaks that are related to the formation of two different phases, or the polymorphic transformation of the molybdenum-rich carbide. None the less is most probably due to the solidification of two different phases at different temperatures, since the solid state heat of transformation are usually too weak to be detected, if not done through calorimetry. Further explanation on this matter will be given in the discussion section.
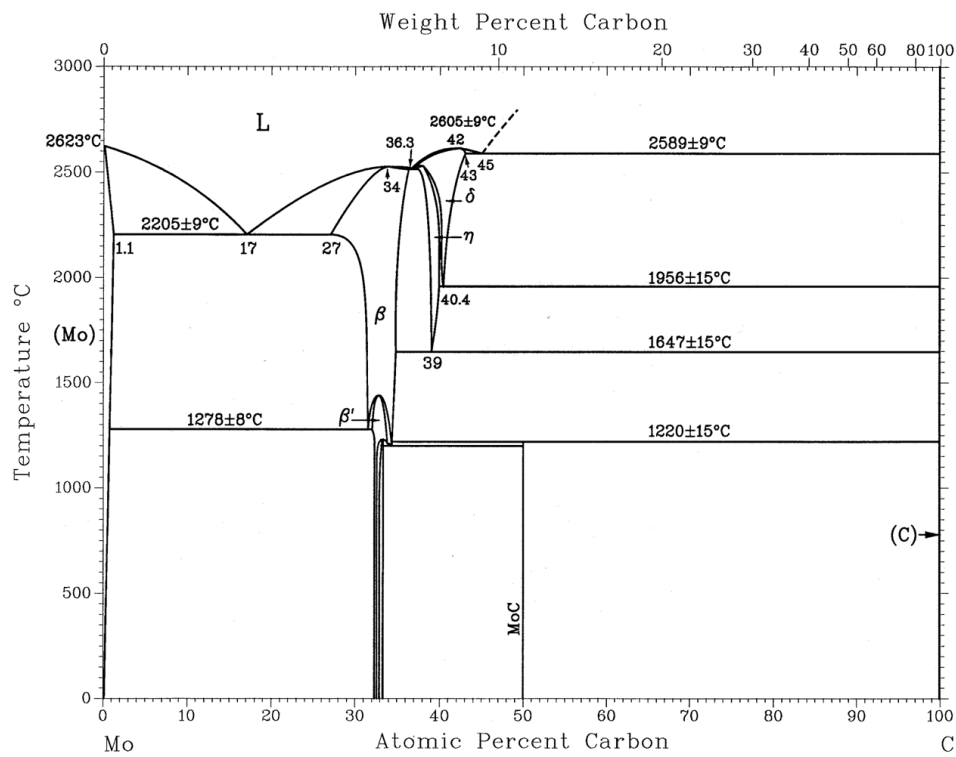
Figure 3.29. Molybdenum-Carbon phase diagram [54].

Furthermore, likewise as for the niobium-carbon cell, sectioning and metallurgical preparation for optical microscopy was performed on the Mo-C cell. And selected micrographs are shown in figures 3.31 to 3.33. These denote the variety of morphological features encountered throughout the alloy. In figure 3.31 we have an overall view of the microstructure throughout the cell, were metallic rich matrix is contrasted with a fine platelet like dark structure which nucleated near the walls of the graphite cell, along with a more irregular dark phase that formed towards the center of the molybdenum-carbon casting. Furthermore, figure 3.32 shows two micrographs at different magnifications were a section with cumulous graphite flakes is shown with a finer dark structure is embedded in the molybdenum-rich matrix in between the graphite elongated grains. More detail on this structure is observed on the right micrograph in figure 3.32. Moreover, figure 3.33 focuses on morphologies of two distinct carbides that have formed within the microstructure.
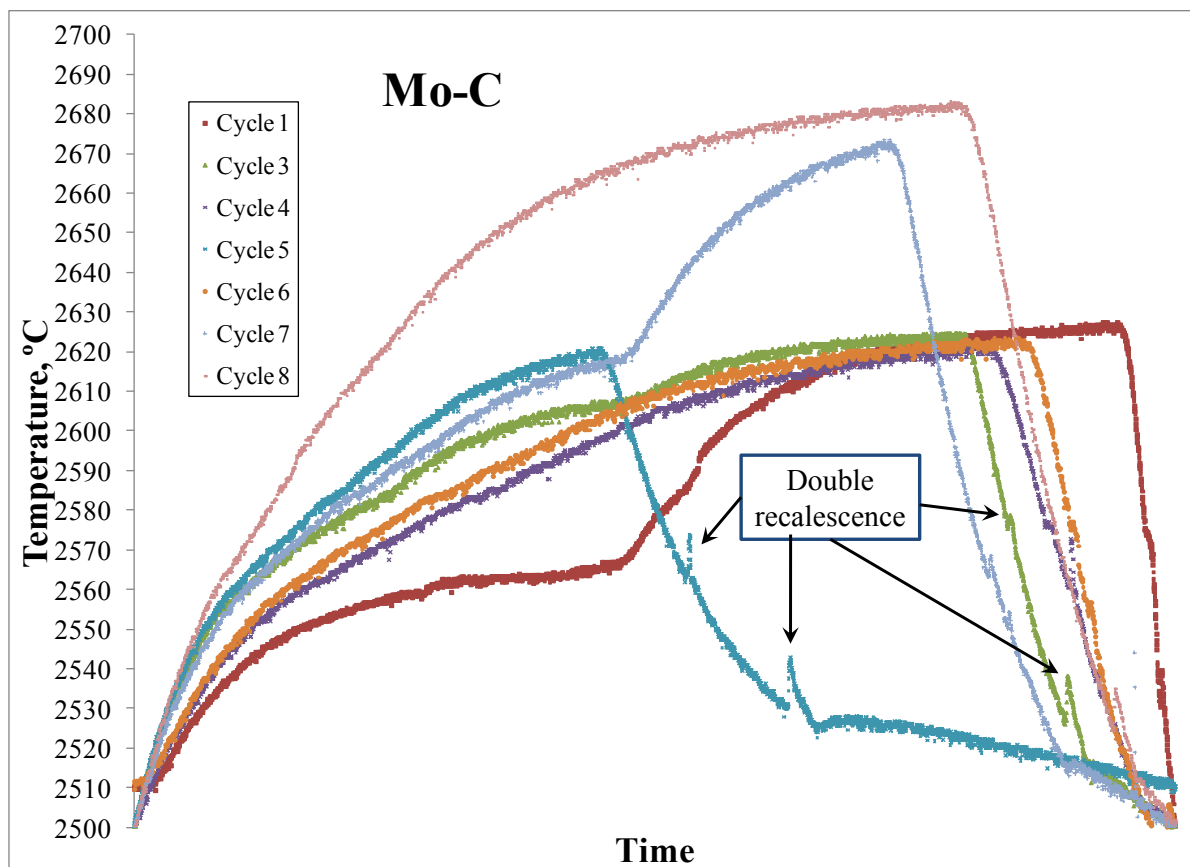
Figure 3.30. Thermal cycling of the Mo-C cell #9 showing melting/solidification curves.
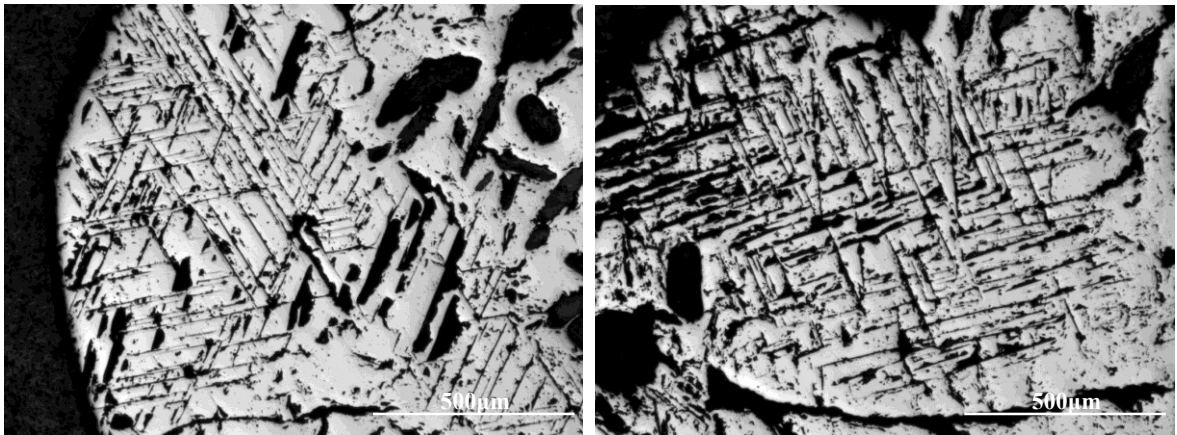
Figure 3.31. Molybdenum-Carbon micrographs showing the microstructure morphology.
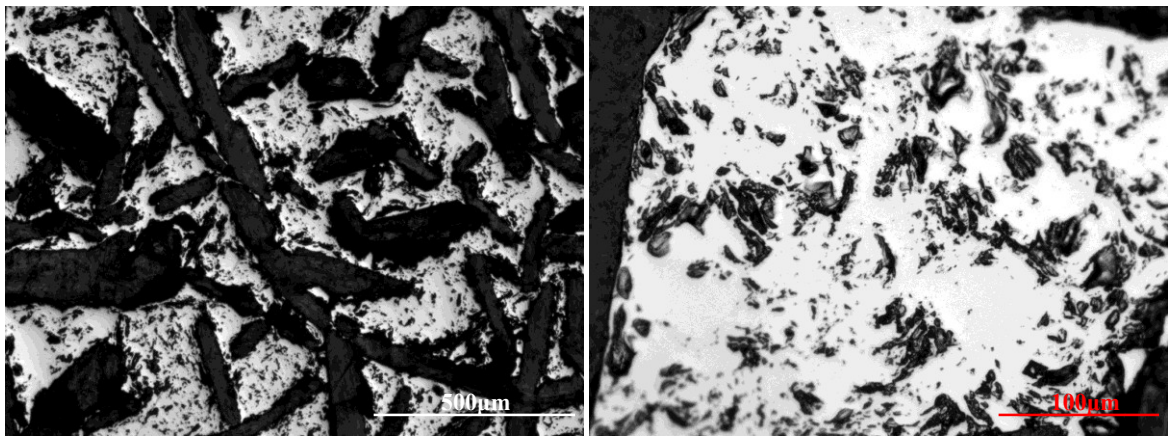
Figure 3.32. Molybdenum-Carbon micrographs showing more detail on microstructure facets.
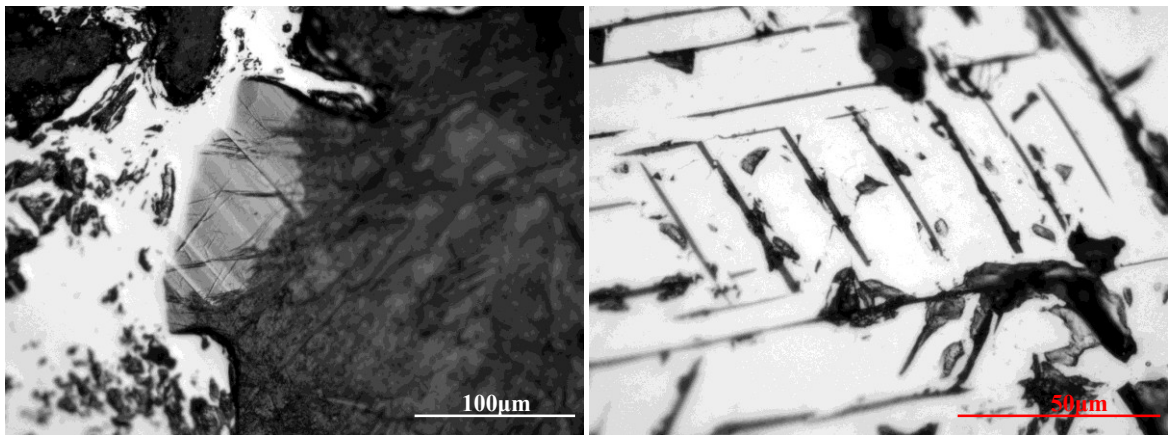
Figure 3.33. Higher magnification Mo-C micrographs showing diverse carbides morphology.

The first micrographs show the formation of irregular very-hard carbide in between a graphite flake and the white metallic structure. On the right, the second micrograph shows very well aligned dark platelets embedded in the microstructure, these platelets seem to be softer carbide that might be a combination of the lower and higher temperature polymorph of the molybdenum rich carbide. The

deformation of some platelets is evident, and it might be due to an incomplete solid state transformation of the carbide. Finally, a micro-hardness test was performed on the molybdenum-carbon alloy to validate the formation of multiple phases by looking at the distribution and variations in hardness as a function of the phase of indenture. The results have been plotted in figure 3.34 were we have highlighted the regions were the hardness readings were taken. A more in depth discussion will be given in the discussion devoted section to improve the strength on certain points already mentioned in this subsection.

3.9.1 Analysis of Simple vs. Complex Metal-Carbon Eutectic Binary Systems for Application as Eutectic Cells

Upon empirical study of several metal-carbon eutectic systems (Fe-C, Co-C, Ti-C, Ru-C, Re-C, Nb-C, Mo-C) and by analyzing their respective thermodynamic phase diagram some remarks can be made on the simpleness or complexity of a phase diagram. First of all, even though there are many high temperature metal-carbon systems there is a group that comprises eutectic equilibrium points at intermediate compositions.
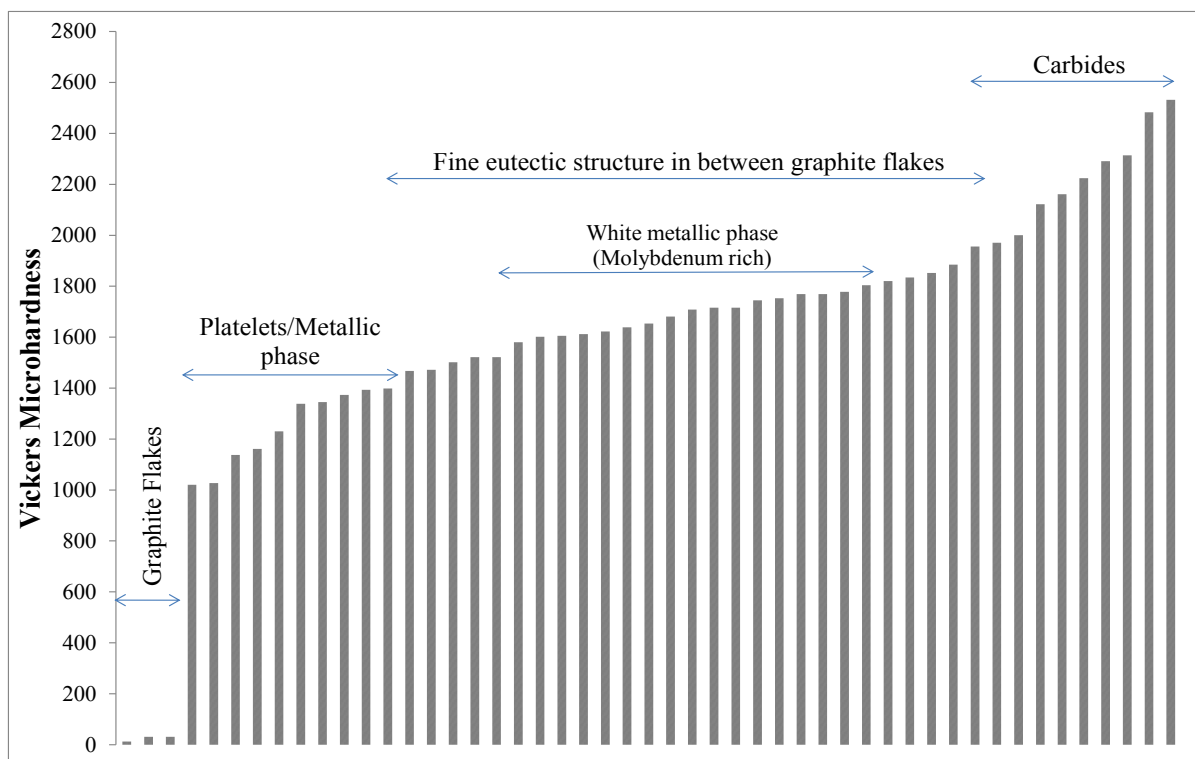
Figure 3.34. Vickers micro-hardness distribution plot for Mo-C eutectic cell ingot microstructure.

Furthermore, these eutectic systems can be sub-divided according to the complexity of their phase diagrams, by looking at the number of possible equilibrium or metastable constituents that can be formed under a range of compositions/temperature range and number of eutectic points. A list of metal-carbon sub-groups with their characteristics will be presented, starting with the simplest systems:

- A binary metal-carbon eutectic system with a single eutectic and no solid state allotropes, carbides or metastable phases: These binary metal-carbon systems contain a single eutectic equilibrium point (at concentrations below 30 at.% Carbon) which is formed by two solid constituents (a metal rich phase with low concentration of carbon dissolved and a graphite phase with some metal dissolved) below the eutectic temperature. This group comprises numerous noble metals part of the platinum group i.e. Pd-C, Rh-C, Pt-C, Ru-C, Ir-C and Re-C.

- A binary metal-carbon eutectic system with a single eutectic, along with an allotropic metallic phase or metastable carbide phases: In these category are included the ferromagnetic metals-carbon alloys, like the Co-C (cobalt has two stable crystalline structures), Fe-C (pure iron undergoes two metamorphic transformations in the solid state), and Ni-C (the nickel-nickel carbide forms under fast cooling rates, where the metastable Ni_3C replaces the equilibrium graphite rich phase). These three metals are side-by-side in the periodic table of the elements.

- A binary metal-carbon di-eutectic system comprising two eutectic points including multiple metallic or carbide phase allotropes: These systems are quite complex since they have more than one eutectic minima, contain one or more intermediate metal carbide phases, and have at least one constituent that goes through a low temperature lattice structure transformation or a sluggish transformation into a more ordered lower temperature structure. This sub-category includes the IVB group of metals Ti-C, Zr-C and Hf-C (the previous metals have two stable allotropes and can form a intermediate carbide when sufficient carbon is available, hence they comprise two eutectics points: a Metal-Metal Carbide and Metal Carbide-Carbon eutectic). Moreover, the Nb-C, Mo-C and W-C have similar features and contain at least two undeniable eutectic points and

what appears to be a midway minimum between two distinct metal carbides (M-γMC, γMetal Carbide-αMetal Carbide and αMC-C). And finally there is the Ta-C system which contains one metal carbide (TaC) and two eutectic points around (M-MC and MC-C). Table 3.1 and Appendix A include phase stability data and corresponding phase diagrams.

Furthermore, experimental work was performed in at least two eutectic systems contained in each category. This permits a parallel comparison and discussion of their performance during thermal cycling and metallurgical analysis of selected eutectic cells. In the first category, at least two Ru-C and Re-C cells were tested. It was observed that their melting transformation temperature is quite repeatable within each test (without taking into account the thermal impact of the cell design and hot zone configuration), and Ru-C eutectic solidification temperature is slightly less reproducible than the melting but still comparable. On the other hand, Re-C eutectic solidification behavior is highly dependent on the superheating magnitude, time at molten state and undercooling; the previous will dictate its recalescence range, solid nucleation time and solidification temperature repeatability. An explanation for rhenium's particular behavior is not deduced by looking at its metal-carbon system, but in general rhenium seems to be a metal with peculiar properties not shared by other metals. For example, it has no known ductile-to-brittle temperature which makes this metal very interesting for outer-space applications, has the third highest melting point of all elements at 3180ºC (only tungsten and carbon melt at higher temperature). It is known for its "ductilizing effect or rhenium effect" when alloyed, even in low proportions, with other brittle refractory metals as molybdenum and tungsten. And it has a wide variety of oxidation states (-1 to +7), among other particular features.

In the second category, at least two cells of Fe-C and Co-C were tested. These systems have adequate melting and solidification temperature reproducibility. Nonetheless, their solidification curve shape seems to moderately alter in each test, sometimes undergoing a small recalescence as in Fe-C (99.998%Fe) test 3, or a deterioration of their solidification temperature showing a wavy solidification instead of a plateau or a simple change of inclination, as in Co-C cell #3 test 2. Hence

these systems seem to have a moderate sensibility to thermal history and cooling rate on their solidification temperature because of the multiple phases that can form under different temperature composition regimes. Additionally, elements comprising various allotropes are susceptible to undergoing a modification of their region of stability, or stabilization/suppression of one of the crystallographic configurations due to the addition of even relatively small quantities (micro-alloying, ion implantation, adsorption, etc.) of other elements [53]. Even though, a lot of binary phase diagrams are available in the literature it is not always possible to analyze the effect of ternary or so, inclusions in the eutectic alloy, because the addition of other foreign atoms can exacerbate or mask the effects of some impurities. Therefore, it is important to evaluate the long term stability of the metal-carbon cells as a result of their exposure to the environment. Additionally, while not in use, the cells should be kept in a dry/inert environment to reduce exposure to humidity and contaminants in the environment.

In the third group of high temperature metal-carbon eutectics, one cell of Ti-C, Nb-C and Mo-C were tested. First, the Ti-C cell #7 melting and solidification temperatures were significantly below (>40°C) the expected eutectic temperature (Ti-TiC: 1646.5°C). A lack of material cannot be rendered responsible since more than 70% of the eutectic cavity volume was filled by the powder mix, and it represents the maximum fill-up achieved in any of cells tested. Even though, the melting and solidification can be detected in the curve, they are barely discernible since there is a very faint fluctuation in the inclination of the curve. Not to mention that during the second test the mean solidification temperature fell by more than 33°C, which is very significant when compared to a less than 1°C drop in melting temperature. This significant discrepancy can be due to the formation of multiple phase stability regions in the metal-carbon ingot in-between the graphite walls (Ti-Ti-C-Graphite). The previous has been observed upon metallurgical analysis of the Nb-C cell #11 and Mo-C cell #9, part of this group of complex metal-carbon eutectic systems.

If we look at the test performed on the Nb-C cell (figure 3.25), and focus on the first cycle. The stabilization temperature was at 2500°C or just above the pure niobium melting temperature

(2477°C). Then immediately after cooling starts, instabilities in the curve can be observed around niobium's melting temperature and again around the low temperature eutectic Nb-NbC (~2354°C); this is an indication of the formation of a primary niobium liquid phase that has afterwards wetted the solid carbon flakes and graphite walls partially forming a eutectic liquid that has solidified at lower temperature. Unfortunately, the ulterior thermal cycles do not show any discernible fluctuations in the curve that could be ascribed as an indication of some kind of phase transformation taking place. Based on this, it was determined that a metallurgical analysis could provide more information on the diffusion kinetics that took place during the thermal cycling. As previously asseverated in section 3.9, the niobium-carbon cell micrographs in figure 3.26 show distinct regions, were not only color and morphology differences are perceived, but also a series of concave marks that serve as interface of this multiple phase stability region. By putting together the niobium-carbon phase diagram, thermal curve no. 1, and micrographs we can deduct that, indeed there was an initial melting of niobium to form a eutectic liquid that could be observed during the first test. But in the following thermal cycles, as the cell was heated up a solid-state diffusion of carbon continued into the niobium rich phase, favoring the formation of Nb_2C, and higher carbon containing carbides. The diffusion of carbon into metallic niobium was fast enough, that during the second thermal test no more phase transformation were detected, nor in the following cycles even though the stabilization temperature was increased just above 2500°C. If we look at the Nb-C phase diagram (Figure 3.24) we can observe that the melting temperature of Nb_2C and NbC lays over 2900°C and 3600°C, respectively. Hence it seems that even though there might be a portion of the alloy that preserves the eutectic composition, the latent heat of transformation might enough to be detected by the pyrometer, plus the carbide might be interfering in the conduction of heat towards the pyrometer cavity, hence the transformation is overshadowed by the presence of the metal carbides and intermediate mixed phase regions. To prove this, a Vicker's micro-hardness test was performed (shown in figure 3.27 and 3.28) to denote the various phase regions. It can be seen in the bar graph that there is a gradual, sometimes step like, variation in the phase hardness of the various regions as we move from the graphite cell wall inwards

into the graphite pyrometer cavity section. Therefore, this mechanical testing technique supports the hypothesis of the multiple-phase nucleation race, and disruption on the detection of the small fraction of the eutectic alloy, which is probably the granular phase mid-way between the graphite walls, also seen in figure 3.26 as a scratched phase, which entails the presence of a relatively softer phase.

Furthermore, we will continue with the analysis of the Molybdenum-Carbon cell test. A single test was performed on the Mo-C cell #9, and the curves are plotted in figure 3.30. In these curves we can observe two main reactions upon heating and cooling, which are seen as changes in slope upon heating (~2555°C and ~2590°C) and two recalescence peaks (at lower temperature than melting) during cool down corresponding to the solidification or inverse reaction that was observed upon heating. (Not to be mistaken by the big step changes in generator power input that are seen as very marked temperature inflections in cycle 1 and 7). Furthermore, if we take a look at the Mo-C phase diagram in Appendix A, we will identify three minima points. If we start from the niobium rich side and move towards the carbon rich side, the lowest eutectic is the Mo-βMoC at ~2205°C, then it follows the βMoC-ηMoC at ~2525°C and the highest local equilibrium point is between δMoC-C at 2605°C. In other words, there is a remarkable agreement between the observed phase transformations and the thermal curves (well below the instrumental uncertainty and very close to reference phase diagram uncertainty). Hence, a similar condition was observed for the molybdenum-carbon cell, previously discussed for the niobium-cell, where there is a preferential tendency towards the formation of carbon rich phases. Therefore, the initially low eutectic composition liquid has "jumped" to other higher temperature equilibrium point, in part because the heating stabilization temperature permitted this, but also because the carbon diffusion in any metal is so fast that, especially at the liquid state, that in the presence of more carbon the reaction will move toward the carbon rich side until it reaches the equilibrium composition in the phase diagram. Which means that diffusion of carbon should reach an overall homogeneous composition all over the cell corresponding to 88wt% Carbon and 12wt% Mo if the required temperature is reached >3000°C, very close to the graphite sublimation point. In any case the highest stabilization temperature experienced by the cell

corresponds to 2680°C, which is high enough for the formation of all the molybdenum carbides in the molybdenum-carbon system. In order to support this analysis, again a metallurgical analysis was performed where multiple micrographs are shown in figures 3.31 to 3.33 denoting a variety of morphologies in the microstructure that are the molybdenum rich phase, distinct carbide phases and regions of mixed phases. It should be understood that even though the microscopy inspection shows presence of the molybdenum rich phase, which is a constituent of the low temperature eutectic, no melting/solidification was identified in the curve at lower temperatures, probably for the same reason as for Niobium-Carbon cell. Nonetheless, a confirmatory Vickers micro-hardness analysis was performed all over the multiple phases found in the microstructure and a bar graph has been plotted in figure 3.34, where we can observe the significant range of phase hardness found, which infers the existence of multiple phases in the ingot. The gradual increase in hardness of the graph is closely tied to an increase in the carbon concentration of the multiple phases and regions of stability found in the ingot. The micro-hardness analysis confirms the formation of multiple regions of phase stability in between the metal rich side and towards the higher carbon concentration section of the phase diagram.

In conclusion, even though multiple high temperature metal-carbon eutectic systems are available, the reproducibility of the eutectic transformation is best for simple eutectic systems and it degrades as the number of other stable/metastable crystalline phases augments in the metal-carbon system. For example, if the pure metal presents metamorphism, this will affect the performance of the cell, particularly at non-equilibrium heating/cooling, but will be far less disturbed than under the formation of other intermediate phases, like intermediate metal-carbides. Since, as the number of phases, eutectic points and allotropes increases, the system tends toward an equilibrium point that will be dictated by the maximum heating temperature and overall system composition (including the carbon from the graphite cell). Nonetheless, there is current research in some very high temperature MC-C eutectics (i.e. ZrC-C, HfC-C and TaC-C) for application in very high temperature pyrometry, but their performance and stability under far from equilibrium conditions should be studied.

Therefore, from the studied metal-carbon eutectic systems, the Co-C, Ru-C and Re-C are the best candidates to be used as HTFP cells and the melting inflection temperature should be preferred over the solidification temperature.

3.10 Comparison among Metrology and Industrial Cells' Performance: Co-C, Ru-C and Re-C Eutectic Cells

3.10.1 Results of Designed Eutectic Cells Tested in VITI Induction Furnace

Furthermore, based on the previous tests and experience acquired with the previous eutectic systems and cell designs, there was an interest to conceive an improved version of the cell design and to choose the eutectic systems that were the most promising for the application as high temperature fixed points in nuclear reactor safety and severe accident experiments. Therefore, the improvements were introduced in cell design E, and three eutectic systems selected: Co-C (1324ºC), Ru-C (1954ºC) and Re-C (2480ºC). This decision was based on their performance and adequate repeatability, plus the need to cover the corium solidification range in order to use them as in-situ temperature reference points.

Moreover, after the fabrication of the graphite cells, cell fill-up was undertaken. Hence, the cells were completely filled with the hypoeutectic blend and placed inside the VITI furnace following the same standard procedure of gas purging and argon bleeding before heating. Afterwards, a steady heat-up of the cell was undertaken until a temperature just above the eutectic point was reached. Then thermal stabilization was pursued for more than 10 minutes at the liquid state in order to promote the interdiffusion among the atom species and formation of the eutectic melt. Finally, the cell was steadily cooled to room temperature under a stagnant argon atmosphere. Once the cell was cold enough, the furnace overpressure was relieved and the cell was then taken out of the vessel for complete refill with the hypoeutectic mix, before reintroducing the cell back into the induction furnace and re-melting. This procedure was performed for all the cells (Co-C cell #18, Ru-C cell #19 and Re-C cell #17) for three consecutive times, and the solid↔liquid transformation temperatures recorded and calculated in table 3.9.

Cell	Melting mean temperature μ, °C	Melting Standard deviation σ, °C	Solidification mean temperature μ, °C	Solidification standard deviation σ, °C	Reference temperature, °C
Co-C (c#18)	1317.2	0.6	1315.6	0.3	1324
Ru-C (c#19)	1952.0	1.2	1948.8	1.6	1954
Re-C (c#17)	2463.0	1.4	2448.3	11.1	2480

Table 3.9. Compilation of melting/solidification results on design-E eutectic cells tested in VITI.

Afterwards, these eutectic cells were safely packed, and carried to LNE-Cnam metrology laboratory in Paris for 10-day collaboration with the team working on high fixed points. The aim was to compare our cells' transformation temperature to LNE-Cnam reference cells, and to observe its behavior in a metrology furnace. This served to validate, transpose the results from the metrology institute down to the PLINIUS platform, so they could serve as in-house calibration cells for high temperature thermometers utilized in severe accident research. The results of these tests will be presented in the following subsection.

3.10.2 Results of Eutectic Cells Tested at LNE-Cnam in a High Temperature Resistance Furnace

The LNE-Cnam metrology laboratory possesses two high temperature resistance furnaces (Vega HTBB 3200 and Chino IR-R80 with graphite heating elements) located side-to-side, which are placed in front of a monochromatic pyrometer (KE LP5). This artifact is facing the furnaces' aperture and is supported over a rail that enables its lateral translation with the aid of an automated system. Hence, two fixed points can be simultaneously compared and furnace effects as well as pyrometer fluctuations can be minimized. See figure 3.35 for a more vivid illustration of the experimental settings at LNE-Cnam. Moreover, LNE-Cnam cells design can be observed in figure 3.36. This design permits a virtually complete fill-up of the devoted eutectic cavity in one or two steps with the aid of a piston-type filling mechanism that was described earlier in this section [8]. The cells (h: 24x Ø: 24mm) were constructed from Ringsdorff R6710 graphite, along with a carbon/carbon composite fabric surrounding the ingot in order to improve thermal homogeneity and reduce heat losses through

the radial direction. Additionally, more details on the materials utilized to fill the cell can be found in table 3.10 and 3.11.
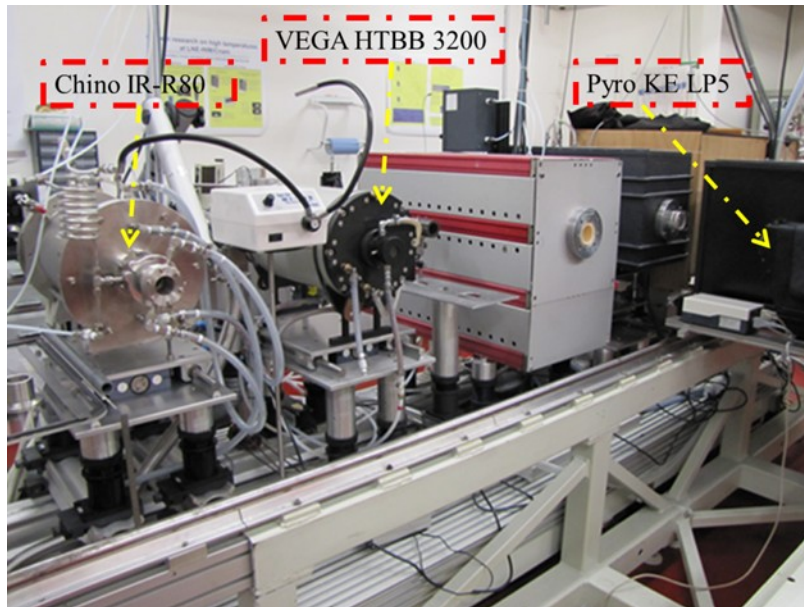
Figure 3.35. Photograph showing the LNE-Cnam laboratory room utilized for the testing of high temperature fixed points.
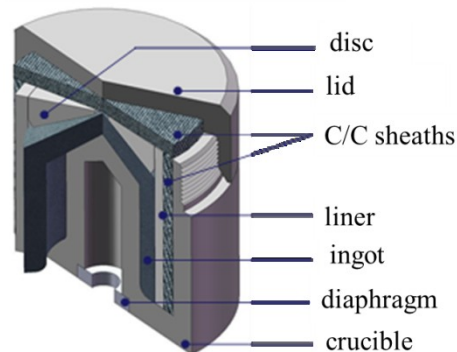
Figure 3.36. Illustration of LNE-Cnam's eutectic cell design.

Eutectic	Hypoeutectic mix composition. wt.%Carbon	Hypoeutectic mass. g	Hypoeutectic volume percent in cavity. %
Co-2.6C	1.5	10.5	~100
Ru-2.5C	1	11.4	~100
Re-1.3C	0.4	24.5	~100

Table 3.10. LNE-Cnam's eutectic cell fill-up details.

Material	Form	Particle size. mesh	Purity, %	Provider
Graphite	Powder	200	99.9999	Alfa-Aesar
Cobalt	Powder	22	99.998	Alfa-Aesar
Ruthenium	Powder	22	99.998	Alfa-Aesar
Rhenium	Powder	325	99.997	Alfa-Aesar

Table 3.11. LNE-Cnam's eutectic blend material details.

Therefore, in order to compare the eutectic transformation temperature of the cells, equivalent eutectic cells appertaining to each lab were subjected to a simultaneous thermal cycling. They were both placed in the furnaces most isothermal zone (< 1°C in temperature gradient along the cells body). Afterwards, the furnace was evacuated and argon was flown into the tube until it reached a slight over pressure. At this moment the quartz window was unscrewed to avoid any interference between the pyrometer and the black cavity thermal radiation. Afterwards, the furnace was gradually heated up (~17°C/min.) until a temperature of 30ºC below the eutectic point was reached, and stabilization achieved. Finally, the furnace input power was increased to reach a plus 30ºC temperature over the eutectic. This procedure was repeated at least four times, with slight variations in ramp with a maximum of ± 50°C around the eutectic temperature. The results on the melting/solidification temperature for LNE-Cnam's and CEA's cells can be found in tables 3.12 and 3.13, respectively. Afterwards, two bar graphs are shown (figure 3.37 and 3.38) where the difference between the reference metrology fixed point and CEA's cells are plotted in the first figure, plus a comparison between the results obtained for the CEA cells in the VITI furnace against the tests in the resistance furnace (Note that the ΔT scale is 6 time larger in the latter plot compared to the former). These results permit the use of the Co-C, Ru-C and Re-C as reference points for the calibration of high temperature thermometers by linking the ITS-90 reference value through the use of the LNE-Cnam metrology cells as an intermediary with the transposition of the reference values tied to the international standards in thermometry. They also remarked that the major source of uncertainty lies in the furnace and not with the eutectic cell, as previously thought.

Cell	Melting mean temperature μ, °C	Melting Standard deviation σ, °C	Solidification mean temperature μ, °C	Solidification standard deviation σ, °C
Co-C (6Co3)	1324.00	0.10	1323.70	0.13
Ru-C (Ru2)	1952.85	0.15	1952.75	0.16
Re-C (4Re1)	2474.25	0.20	2474.23	0.21

Table 3.12. Compilation of melting/solidification results on LNE-Cnam metrology eutectic cells.

Cell	Melting mean temperature μ, °C	Melting Standard deviation σ, °C	Solidification mean temperature μ, °C	Solidification standard deviation σ, °C
Co-C (c#18)	1323.97	0.14	1323.14	0.19
Ru-C (c#19)	1952.54	0.17	1951.65	0.21
Re-C (c#17)	2472.05	0.30	2470.77	0.42

Table 3.13. Compilation of melting/solidification results on our eutectic cells tested at LNE-Cnam.
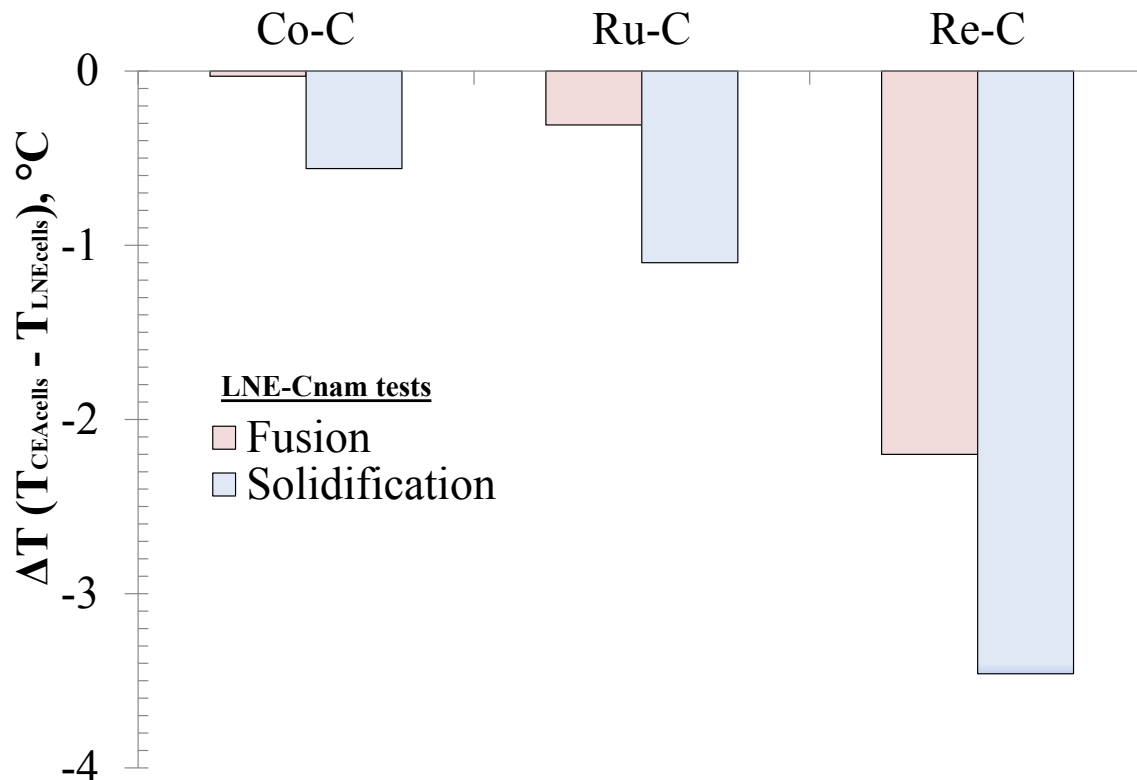
Figure 3.37. Comparison between LNE-Cnam and ours eutectic cells' transformation temperature.
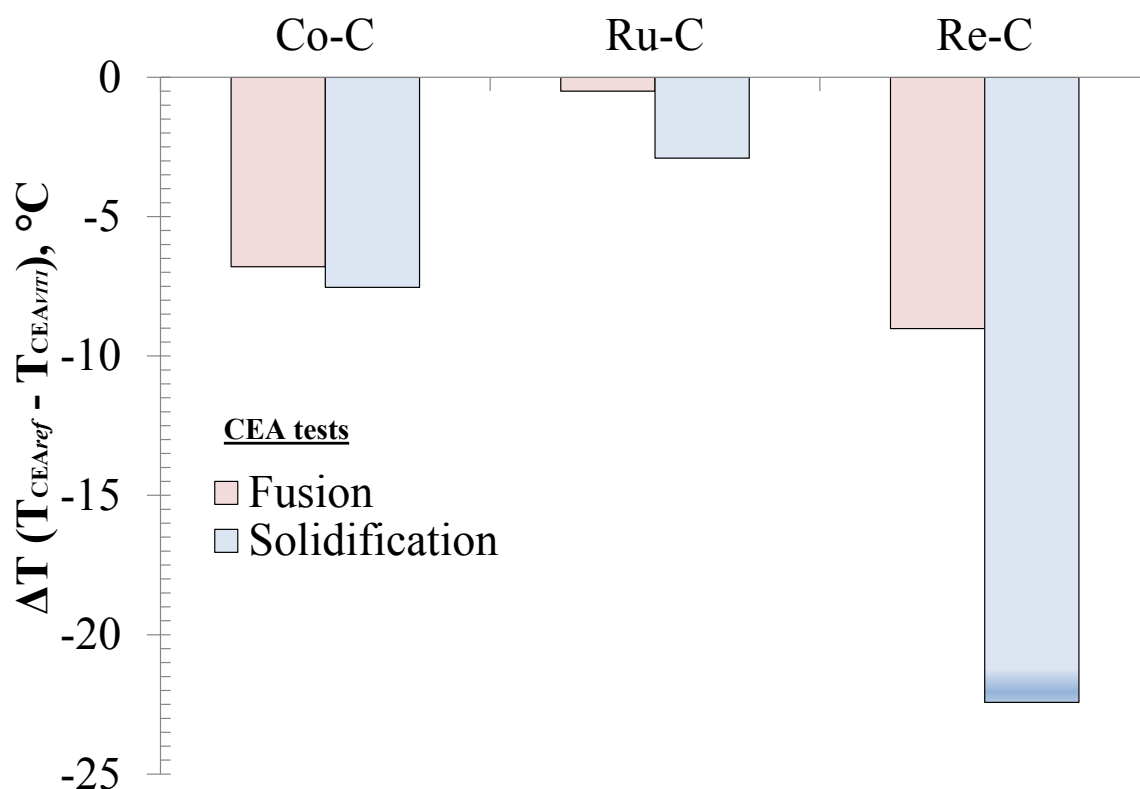
Figure 3.38. CEA eutectic cells' reference temperature comparison to VITI furnace results.

3.10.3 Calibration of High Temperature Fixed Point Cell by Comparison to Metrology Reference Cells and Analysis of Cell Drift Influenced by Furnace Peculiarities

Among the aims of the work sustained on the HTFP based on metal-carbon eutectics was to provide a mean for practical and reliable in house calibration of high temperature thermometers. For example, just before a large scale test in the PLINIUS platform the temperature sensors could be calibrated against the reference cells to have an idea of their accurateness and drift overtime, as well as the optical components and view port materials. This would avoid the need for time consuming shipping and risk of damaging sensible parts of the equipment. Therefore, in section 3.10 three cells (Co-C, Ru-C and Re-C) were prepared in the VITI furnace in Cadarache and then compared to metrology reference cells (Co-C, Ru-C and Re-C) at LNE-Cnam near Paris. The cells were characterized through comparison with the reference eutectic cells in the metrology lab and calibrated pyrometer. As can be observed, the values obtained in the induction furnace are all lower and more spread than the values obtained in the resistance furnace for the same CEA cells. This is in part due to the furnaces inherent differences, i.e. thermal homogeneity of the test section, but also cell

construction and the effect of heating and cooling rate on the transformation temperature, of particular importance for the solidification temperature. Therefore, it is recommended that when using the reference cells for calibration the temperature steps should be reduced to a minimum and the cells should be kept as thermally isolated as possible. This can be done by the addition of several layers of graphite spongy cloth (great for thermal isolation) around the cell, and only leaving a small opening to measure the black cavity radiation temperature with the apparatus to be calibrated. Additionally, this configuration is particularly efficient when using induction heating since the dense graphite utilized for the construction of the cells is basically the same type of graphite as the one utilized for the construction of the susceptor (used to indirectly heat up materials with very poor electrical conductivity). Therefore, the cell's graphite can couple with the magnetic field induced by copper coil (inductor) and directly heat up the eutectic alloy [35]; that is different from resistance furnaces in which the material is indirectly heated up by the thermal irradiation of heat by the furnace heating elements. This is advantageous since the cell can be thermally isolated in order to reduce the losses of heat by conduction, convection and particularly irradiation, since it is predominant at these high temperatures. Not to forget that the detection of the latent heat of transformation of the eutectic alloy will be maximized, by conducting preferentially towards the black cell cavity, and reducing radial heat losses.

Finally, in the frame of the HiTeMS project, three HTFP cells were provided for testing in the VITI facility. The Co-C cell was furnished by the French metrology institute (LNE-Cnam). The Ru-C cell was provided National Metrology Institute of Turkey (TÜBİTAK UME); and the Re-C cell by the National Physical Laboratory (NPL), UK's National Measurement Institute. They all had the same design in common (figure 3.37) and were prepared separately in each laboratory for testing in the VITI furnace. The aim was to test the cells' performance and robustness under significant heating/cooling rates and thermal constraints. All the cells withstood the thermal cycling in the induction furnace without fracturing [55].

3.11 Conclusions and Recommendations of the M-C Eutectic Cells and Their Practical Application in SA Tests to Reduce Temperature Measurement Uncertainty

» Based on the Fe-C eutectic tests it was determined that inclusions (impurities) depress the value of the eutectic temperature. This will also depend on the impurity nature and eutectic system.

» Upon testing of the Co-C, Ti-C, Ru-C and Re-C it was determined that there is a direct relationship between increase in heating ramp and increase in melting temperature. Similarly, as the cooling rate is increased the solidification temperature is decreased. This is adjudicated to non-equilibrium phase transformation and effects on melting and solidification transformation.

» The melting temperature is less sensible to rate changes than the solidification temperature due to their difference in transformation kinetics, rendering the solidification process a more complex transformation that depends on a finite undercooling for nucleation. Hence due to its better repeatability the melting temperature should be estimated from the inflection point and preferred over the solidification temperature for thermometer calibration. It is nevertheless reminded that there must be a first cycle of melting and solidification before accurate melting temperature measurements can be made.

» Simpler eutectic systems (i.e. Co-C, Ru-C and Re-C) show better reproducibility than more complex systems containing multiple eutectics, intermediate phases and/or multiple crystalline configurations (Ti-C, Nb-C and Mo-C).

» Furnace type, experimental set-up and graphite cell design have an important impact on the reproducibility of the eutectic cells. Improvement of thermal homogeneity of test zone through the addition of thermal isolation material will greatly reduce the heat losses and improve the performance of the eutectic cell. VITI has been adapted to reach satisfactory level of uncertainty (<2ºC)

» Various designs of graphite cells were successfully tested under significantly high heating and cooling rates, hence thermal constraints. The cells were robust enough to handle the thermal stresses and dilatation of eutectic alloy. The various experiments on different cell designs allowed for a significant reduction in cell size and eutectic material needed. There was a gain on the performance of the cell, because as the cells size is reduced there is an inherent reduction in surface area, hence heat losses were diminished.

» Three CEA pyrometer cells (Co-C, Ru-C and Re-C) have been tied to the ITS-90 thru comparison with LNE-Cnam cells at their metrology laboratory. Therefore, now these cells can be used for in-house calibration of pyrometer through the use of the HTFP cells. A one-day training on the practical application of the cells as reference points was prepared for staff at the LMA. The Ru-C cell was thermally cycled in VITI and a pyrometer was used to measure the cavity temperature. Discussion on the basics of eutectics and important details for an adequate calibration were discussed. Finallyy a HTFP cell kit was produced including the Co-C, Ru-C and Re-C cells, plus the thermal isolation material needed to get the best performance from the cell and reduce the impact of heat losses.

Chapter 3 - References

1. Y. Yamada, H. Sakate, F. Sakuma and A. Ono, "Radiometric observation of melting and freezing plateaus for a series of metal-carbon eutectic points in the range 1330°C to 1950°C", in Metrologia, 1999, 36, pp. 207-209.

2. E.R. Woolliams, G. Machin, D. H. Lowe and R. Winkler, "Metal (carbide)-carbon eutectics for thermometry and radiometry: a review of the first seven years", in Metrologia, 2006, 43, pp. R11-R25.

3. Y. Yamada, H. Sakate, F. Sakuma and A. Ono, "High-temperature fixed points in the range 1150°C to 2500°C using metal-carbon eutectics", in Metrologia, 2001, 38, pp. 213-219.

4. D. Lowe and G. Machin, "High-temperature fixed-points at the national physical laboratory" SICE Annual Conference in Sapporo, August 4-6, 2004, pp.802-806.

5. D. Lowe, Y. Yamada, "Reproducible metal-carbon eutectic fixed-points" in Metrologia, 2006, 43 S135-S139.

6. N. Sasajima, Y. Yamada and Y. Wang, "Metal carbide-carbon eutectic and peritectic fixed points as high-temperature standards" SICE-ICASE International Joint Conference 2006, Oct. 18-21, 2006 in Bexco, Busan, Korea, pp.1903-1906.

7. M.K. Sakharov, "Thermal measurements: The use of fixed points based on metal-carbon eutectic alloys to increase the accuracy of measurements in the temperature range above 1357.77K" Measurement Techniques, Vol. 50, No. 2, 2007, pp.179-183.

8. F. Bourson, S. Briaudeau, B. Rougié and M. Sadli, "Developments around the Co-C eutectic point at LNE-INM/Cnam" in Acta Metrologica Sinica, Vol. 29, No. 4A, October 2008, pp. 1-6.

9. K. Frolov, C. Journeau, P. Piluso, M. Duclot, "Electrochemical determination of oxidic melt diffusion coefficients", International Journal of Thermophysics, vol. 26, no. 4, 2005, pp. 1181-1192.

10. P. Piluso, J. Monerris, C. Journeau, and G. Cognet, "Viscosity measurements of ceramic oxides by aerodynamic levitation", Intenational Journal of Thermophysics, vol. 23, no.5, 2002, pp. 1229-1240.

11. K. Plevacova, C. Journeau, P. Piluso, V. Zhdanov, V. Baklanov, J. Poirier, "Zirconium Carbide Coating for Corium Experiments related to Water-cooled and Sodium-cooled Reactors", Journal of Nuclear Materials, no. 414, 2011, pp. 23–31.

12. H. Ogura, M. Izuchi and M. Arai, "Evaluation of Cobalt-Carbon and Palladium-Carbon eutectic point cells for thermocouple calibration" International Journal of Thermophysics, 29, 2008, pp. 210-221.

13. T. Wang, D. Lowe and G. Machin, "Manufacturing of MC eutectics and reproducibility of Pt-C eutectic fixed points using a thermogauge furnace" International Journal of Thermophysics, 30, 2009, pp. 59-68.

14. C. J. Parga, C. Journeau, A. Tokuhiro, "Development of metal-carbon eutectic cells for application as high temperature reference points in nuclear reactor severe accident tests: Results on the Fe-C, Co-C, Ti-C and Ru-C alloys' melting/freezing transformation temperature under electromagnetic induction heating" High Temperatures-High Pressures, Vol. 41, No. 6, 2012, pp. 423-448.

15. W.F. Smith, J. Hashemi, "Foundation of Materials Science and Engineering" McGraw-Hill College, 2003, pp. 326-327.

16. W.D. Callister Jr."Materials Science and Engineering: An Introduction" 5th edition, John Wiley and Sons, Inc., New York, 2000, pp. 255-267, 274-277.

17. T. B. Massalski (Ed.): "Binary Alloy Phase Diagrams Vol. 1", American Society for Metals, Materials Park, OH, 1986.

18. D. Bandyopadhyay, R. C. Sharma and N. Chakraborti, "The Ti-Co-C system (Titanium-Cobalt-Carbon)" Journal of Phase Equilibria, 2000, Vol. 21, No 2, pp. 179–185.

19. M. Singleton and P. Nash, "The C-Ni (Carbon-Nickel) System", Bulletin of Alloy Phase Diagrams, Vol. 10, No. 2, 1989, pp.121-126.

20. C.W. Bale, A.D. Pelton and W.T. Thompson, "FACT Sage 6.0, THERMFACT Ltd.", École Polytechnique de Montréal, Génie chimique / Chemical Eng., 447 Berwick, Mount-Royal, Montreal, Quebec, Canada, 2011, Pd-C, Pt-C, Rh-C, Ru-C, Ir-C.

21. D. Bandyopadhyay, B. Haldar, R.C. Sharma, and N. Chakraborti, "The Ti-Mo-C system (Titanium-Molybdenum-Carbon)" Journal of Phase Equilibria 1999, Vol. 20, No 3, pp. 332–336.

22. J.K. Hughes, "A survey of the Rhenium-Carbon system" Journal of the Less Common Metals, Volume 1, issue 5, October 1959, pp. 377-381.

23. D. Bandyopadhyay, R. Sharma and N. Chakraborti, "The C-Nb-Ti system (Carbon-Niobium-Titanium)" Journal of phase equilibria 2000, Vol. 21, No 1, pp. 102–104.

24. G. Failleau, T. Deuzé, C. J. Elliott, J. V. Pearce, G. Machin, S. Briaudeau and M. Sadli, "Development of an Fe-C eutectic fixed-point for the calibration and in-situ monitoring of thermocouples" Proceedings of 2nd IMEKO TC 11 International Symposium Metrological Infrastructure, June 15-17, 2011 in Cavtat, Dubrovnik Riviera, Croatia.

25. M. Sadli, M. Matveyev, F. Bourson, V. Fuksov, Yu. A. Sild and A. I. Pokhodun "Comparison of pyrometric Co-C and Re-C eutectic-point cells between VNIIM and LNE-Cnam" International Journal of Thermophysics, Vol. 32, No. 11–12, pp. 2657–2650.

26. G. Lowe and G. Machin, "Development of Metal-Carbon Eutectic Blackbody Cavities to 2500°C at NPL" Proceedings: TEMPMEKO 2001: 8th International Symposium on Temperature and Thermal Measurements in Industry and Science, 19-21 June 2001 in Berlin, Germany.

27. G. Machin, G. Beynon, F. Edler, S. Fourrez, J. Hartmann, P. Jimeno-Largo, D. Lowe, R. Morice, M. Sadli, M. Villamanan, K. Anhalt, F. Bourson, and E. Morel "Progress with the development of

high temperature fixed-points in the EU through the HIMERT project/Projet européen HIMERT: le point sur la réalisation de points fixes à hautes temperature" Congress Proceedings – 11th International Metrology Congress, Toulouse, France, October 20-23, 2003, pp. 1-6.

28. S. Fourrez, G. Bailleul, R. Morice and G. Machin, "HIMERT: Industrial calibration of type S, B and C thermocouples by comparison to metal-carbon eutectic cells: interest and perspectives (Etalonnage industriel de couples thermoélectriques type S, B et C par comparaison à des cellules eutectiques métal-carbone : intérêt et perspective)" Congress Proceedings, 11th International Metrology Congress, Toulouse, France, October 20-23, 2003, pp. 1-5.

29. V.N. Korobenko and A.I. Savvatimskiy, "Blackbody Design for High Temperature (1800 to 5500K) of Metals and Carbon in Liquid States under Fast Heating" Temperature: Its Measurement and Control in Science and Industry. Vol. 7 (AIP Conf. Proc. Vol. 684/Ed. D. C. Riplle. Melville, NY, AIP, 2003. P. 783–788.

30. B. Rousseau, J. F. Brun, D. De Sousa Meneses and P. Echegut, "Temperature Measurement: Christiansen Wavelength and Blackbody Reference" International Journal of Thermophysics, Vol. 26, No. 6, July 2005, pp.1277-1286.

31. J.R. Howell, R. Siegel, M.P. Mengüç, "Thermal Radiation Heat Transfer" 5th Ed. CRC Press, ISBN: 978-1-4398-0533-6, Boca Raton, Florida, 2011, pp. 241-242.

32. V. Rudnev, D. Loveless, R. Cook and M. Black, "Handbook of Induction Heating" published by Marcel Dekker Inc. New York, 2003, pp. 11-184.

33. C. Parga, C. Journeau and J-F Haquet, "Tungsten sheath effect on thermocouple measurement around 2000K (Effet de gaines en tungstène sur la mesure par thermocouples autour de 2000 K)" Congress Proceedings - Société Française de Thermique - SFT 2011: Énergie solaire et thermique, May 27, 2011, pp. 1-6.

34. M. Tarnopolsky and I. Seginer, "Leaf temperature error from heat conduction along thermocouple wires" Agricultural and Forest Metrology vol. 93, 1999, pp. 185-194.

35. R. Morice, M. Lihrmann, J. Favreau, E. Morel and M. Megharfi "Study on the fabrication of a thermo-electric couple in a graphite environment up to 2200K (Etude d'une gaine de mise en oeuvre des couples thermoélectriques en environnement graphite jusqu'à 2200K)" Congress Proceedings – 11th International Metrology Congress, Toulouse, France, October 20-23, 2003, pp. 1-5.

36. J.L. Rempe, D.L. Knudson, J.E. Daw and S.C. Wilkins, "Type C thermocouple performance at 1500°C" Measurement Science and Technology, no. 19, 2008, pp.1-9.

37. J.L. Rempe, D.L. Knudson, K. G. Condie, S.C. Wilkins, J.C. Crepeau and.E. Daw "Options Extending the Applicability of High-Temperature Irradiation-Resistant Thermocouples" American Nuclear Society, vol. 167, no 1, La Grange Park, IL, USA, 2009, pp. 169-177.

38. J. Larrain and C.F. Bonilla, "Cross-conduction errors in thermocouples: Correction of long swaged thermocouples at high temperatures" Nuclear Engineering and Design, Vol. 8, North-Holland Publishing Co., Amsterdam, 1968, pp. 251-272.

39. Ir. W. Van der Perre, "Temperature measurement in liquid metal" Heraeus Electro-Nite International N.V., 2000, pp. 1-15.

40. N. Birks and G.H. Meier, " Introduction to high temperature oxidation of metals" Edward Arnold Publishers Ltd., London, 1983, pp. 31-64, 91-144, 159-174.

41. Z. Ahmad "Principles of corrosion and corrosion control" Publisher: Butterworth-Heinemann/IChemE Series, Oxford, pp. 382-548.

42. K. Glasner, "Solute trapping and the non-equilibrium phase diagram for solidification of binary alloys" Physica D 151, 2001, pp. 253-270.

43. V. Y. Chekhovskoi and V. D. Tarasov, "Melting of Metals during Rapid Bulk Heating" Russian Metallurgy (Metally), Vol. 2009, No. 4, pp. 297–302.

44. M.C. Flemings: "Materials Science and Engineering Series: Solidification Processing" McGraw-Hill, New York, NY, USA, 1974.

45. D. A. Porter, K. E. Easterling, M. Sherif, "Phase Transformations in Metals and Alloys", 3rd Ed., CRC-Press, 2009.

46. M. Li, and K. Kuribayashi, "Free Solidification of Undercooled Eutectics" Materials Transactions, Vol. 47, No. 12, 2006 pp. 2889-2897.

47. M. Li, K. Nagashio, T. Ishikawa, A. Mizuno, M. Adachi, M. Watanabe, S. Yoda, K. Kuribayashi and Y. Katayama, "Microstructure formation and in situ phase identification from undercooled Co–61.8 at.% Si melts solidified on an electromagnetic levitator and an electrostatic levitator" Acta Materialia 56, 2008, pp. 2514-2525.

48. M. Leonhardt, W. Löser, and H.-G. Lindenkreuz, "Solidification kinetics and phase formation of undercooled eutectic Ni-Nb melts" Acta Materialia, Vol. 47, No. 10, 1999, pp. 2961-2968.

49. Y.Ping Lu, T.Ju Li, H.Tao Teng, Y.Bo Fu, D.Wei Luo and G.Cang Yang, "Microstructure evolution and non-equilibrium solidification of undercooled Ni-29.8at% Si eutectic alloy melts" Science China-Technological Sciences, Vol.53, No.4, April 2010, pp. 1043–1048.

50. B. Vinet, E. Cini, S. Tournier and L. Cortella, "Microstructures de Solidification de Métaux et Alliages Réfractaires Elaborés dans le Tube à Chute Libre de Grenoble (Solidification microstructure of refractory metals and alloys fabricated in the Grenoble free-fall tube)" Journal de Physique III, Volume 5, April 1995, pp. C3-217 to C3-224.

51. M. Singleton and P. Nash, "The C-Ni (Carbon-Nickel) System" Bulletin of Alloy Phase Diagrams Vol. 10 No.2 1989, pp. 121-126.

52. H.A. Wriedt, "The Fe-O (Iron-Oxygen) system" Journal of phase equilibria, vol. 12, no.2, 1991, pp. 170-200.

53. C.J. Parga and S.K. Varma, "Correlation between Microstructures and Oxidation Resistance in Zr-Nb-Ti Alloys" Metallurgical and Materials transactions A, Vol. 40A, December 2009, pp. 2987- 2993.

54. D. Bandyopadhyay, B. Haldar, R.C. Sharma, and N. Chakraborti, "The Ti-Mo-C system (Titanium-Molybdenum-Carbon)" Journal of phase equilibria 1999, Vol. 20, No 3, pp. 333.

55. A. Diril, M. Sadli, F. Bourson, C. Parga, "Construction and characterisation of ruthenium carbide eutectic cell at TUBITAK UME", TEMPMEKO 2013, Symposium on Temperature and Thermal Measurements in Industry and Science, Funchal, Madeira, Portugal, October 2013, pp. 14-18.

Chapter 4. Refractory Alloy Protective Sheath for MCCI Environments

4.1 Protective Sheath Material Selection

Among the multiple experimental facilities in the PLINIUS platform in Cadarache, the VULCANO facility is currently used to perform MCCI tests focused on the interactions between prototypic oxide/metallic molten corium (UO_2-ZrO_2 and stainless steel based melts) and typical reactor basemat and core-catcher materials being used. This research permits the study of the concrete ablation rate, plus analysis of physico-chemical and thermodynamic reactions in a variety of core melt scenarios in which long term exposure between oxide/metallic corium and concrete could lead to stratification of immiscible molten phases and solidification ranges of over a thousand degrees centigrade [1]. Contact and non-contact temperature measurement techniques are utilized in order to track temperature progression throughout the test. Several type-C thermocouples (W5Re/W26Re) are imbedded into the test section to monitor in-melt temperature during the ablation of the concrete crucible. Unfortunately, the temperature sensors encounter a very high temperature-chemically aggressive environment in which they need to perform in contact with biphasic oxide/metallic melts, along with hot gases as steam and carbon monoxide/dioxide. The expected performance of these tungsten-rhenium thermocouples is to be able to track the melt temperature as the experiments progresses. Nonetheless, the thermocouple as-manufactured sheaths (molybdenum or tantalum based) do not withstand the melt attack and additional thick refractory materials (metals and ceramics) have been used to extend the service life of thermocouples during corium melt-concrete interaction tests. Even though, the tungsten or cement filled zirconia sheaths can resist the attack of oxide based corium for periods of two hours or so [2], they are immediately destroyed when a superheated metallic liquid is added to the corium mix. Therefore, in order to extend the service life of thermocouples in oxide/metallic corium melt (>2000ºC) one of the tasks of the author was to conduct literature search and experimental research to propose materials and test them under this aggressive scenario. With this aim, several alloys of the Re-W-Ta system with boron additions were proposed as candidates and exposed to superheated stainless steel (up to 2000ºC) in the VITI furnace to study

their liquid metal corrosion behaviour. A detailed explanation on the refractory sheath selection and design approach will be presented, along with a metallurgical analysis of their as-cast properties and post-test condition.

4.1.1 Complex Oxide-Metallic Molten Corium Mix in MCCI Tests

The following sketch (Figure 4.1) represents an illustration of the VULCANO concrete test section. There is an emphasis on the high temperature complex multi-material system in which the type-C thermocouple need to measure temperature and perform satisfactorily under the aggressive attack of various chemical species and interactions taking place. Nonetheless, this picture is a simplification, since the interface between metal and oxide layers is not at a fixed position, but will evolve due to concrete ablation and metal oxidation throughout the test. Also, drops of metal of various sizes have been found in the oxide layer, hence a solution with two distinct phases of oxide and metal is not possible. More details on the origin of this scenario can be found in Chapter 1, in which a detailed explanation on nuclear reactor severe accidents phenomenology has been included.
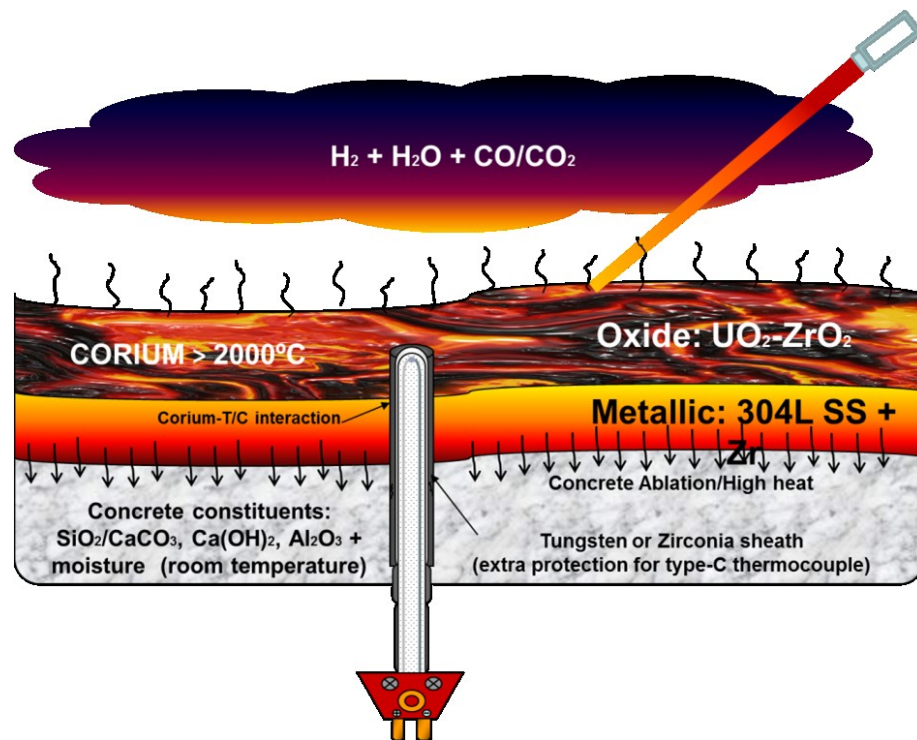

Figure 4.1. Illustration of the MCCI test section along with contact and non-contact thermometers depiction.

4.1.2 Liquid Metal Corrosion Basics Overview

In general, corrosion is defined as a material's degradation that takes places when two or more materials, usually in physical contact, interact in a chemical or electrochemical manner resulting on a net transfer of electrons. Moreover, corrosion of a material, we will focus in corrosion related to metals, is usually exacerbated as temperature increases. There are several high temperature corrosion types, i.e. oxidation, sulfidation, halogenation, carburization, nitriding and molten products attack. Among the molten material attack type a series of special cases are considered depending on the nature of the fluid reacting with the solid substrate and/or nature of the degradation process, thus in this category we include the liquid metal corrosion or attack. In contrast to the rest of the corrosion basic mechanisms, the liquid metal corrosion is not strictly a process controlled by electron or ion transfer, but a process that depends on the solubility limit and diffusivity among different metallic species, initially a liquid and solid phase in physical contact, in which the liquid phase might be stagnant or flowing (dynamic). There are different categories of liquid metal attack based on the characteristics of their degradation mechanism and are as follows:

- Simple solution.- This takes place when there is an even removal of material from the solid metal or alloy substrate usually by a pure liquid metal until the equilibrium saturation limit at temperature is reached.

- Alloying between liquid metal and solid metal.- In this case the liquid metal atoms will diffuse preferentially into the solid substrate to form a solid solution or often an intermetallic phase.

- Intergranular penetration.- This is a very aggressive type of liquid metal corrosion in which the liquid atoms diffuse through the grain boundaries of the solid, typically an alloy, and selectively attack certain elements for which they have more affinity or higher solubility. This results in a concentration decrease of the particular element in the microstructure and voids are typically left behind, or the opposite could happen where the formation of distinct alloy phases or intemetallics takes place at the grain junctions. In both cases this can greatly

modify the substrate properties, promote decohesion of the grains, and/or form crack-initiation sites.

- Impurity reactions.- If the liquid metal contains even dissolved quantities of impurities such as oxygen, nitrogen, carbon, and other very reactive species as chlorine and fluorine, it can very aggressively attack a substrate that was relatively inert to the liquid metal. In other words, foreign solutes can significantly influence the corrosion rate and corrosion mechanism between the liquid and solid metal.

- Temperature gradient-mass transfer.- This type of liquid metal corrosion takes place when there is a mass transfer or removal of solid in a liquid metal that flows through a loop under considerable temperature gradients. The driving force is the difference in solubility of the solid substrate species in the liquid metal at different temperatures. In this case the metallic container/pipe atoms de-alloy from the solid and flow through the liquid metal until they arrive at a colder section where they precipitate from the liquid, due to oversaturation, and then diffuse, plate or crystallize on the solid walls of the same type of substrate, to form sediments that will reduce and eventually impede the flow of the fluid.

- Concentration-gradient mass or dissimilar-metal mass transfer.- The mass transfer between two dissimilar solid alloys through diffusion or flow in the liquid metal concerns this type of corrosion. The driving force is the decrease in Gibbs free energy that results from the relocation of certain atom species from one substrate to the other. The rate of mass transfer will highly depend on the difference in electronegativity and solubility among the two distinct solids; hence temperature will be determining factor.

The previous serve as guidelines to detect different types of corrosion mechanisms during liquid metal attack. Nonetheless, it is important to understand that a combination of mechanisms can take place in which one might initially prevail under certain concentration and temperature, but a change in corrosion behavior can take place in other conditions, as when the system is constantly going through temperature and composition changes. The MCCI test is a very representative example

of a complex system in which high temperature gradients, physical contact of dissimilar solid/molten materials, convective flow of different liquid phases and bubbling of oxidant or reducing gases is dynamically taking place through the evolution of the test. Hence, the aim was to study this particular environment (molten oxide/metallic corium in concrete crucible), to propose and test materials that could extend the service life and temperature measurements, or at least result in an improvement over the previously utilized sheath materials, which have not been successful in protecting the thermocouple, but immediately degrade when in contact with molten oxide/metallic corium [1-11].

4.2 Refractory Metals and Alloys

Within the metallic elements there exists a category designated as the refractory metals group. In this group we usually include the five highest melting point metals: Tungsten (3422ºC), Rhenium (3186ºC), Tantalum (3017ºC), Molybdenum (2623ºC) and Niobium (2477ºC), even though some authors also include in this category other lower temperature metals (Hf, Zr, Cr) and the Pt-group metals. Besides their high melting point, these metals possess good high temperature strength, creep resistance and high modulus of elasticity, along with a low coefficient of thermal expansion, plus an excellent electrical and thermal conductivity typical of most metals. Although they have an exceptional corrosion resistance, they suffer from extensive oxidation in air at intermediate temperatures and they are often utilized under vacuum or inert atmosphere. Nonetheless they are widely used in high temperature applications as in the lightning, aerospace and chemical industry, or as alloying elements to improve the high temperature strength of Fe-, Ni- and Co- superalloys, among other applications.

4.2.1 Why Use a Re-W-Ta-(B) Refractory Alloy as Protective Sheath in MCCI?

Based on the analysis of several VULCANO MCCI experiments (VBS-U1, VBS-U3, VBS-U4 and VB-ES-U4) it has been observed that the initial temperature of the molten corium, just after it has been poured into the test section, shows an initial temperature spike of around 2300ºC, but then it sharply drops to a temperature just below 2000ºC, then it gradually cools down due to mixing with

melted concrete even though induction heating is maintained. Therefore, the 2000ºC temperature has been chosen as the reference temperature value for the selection of thermocouple sheath candidate materials for in-melt thermometry.

First, the engineering and selection of materials for application into specific environments is ruled by the expected performance and constraints encountered during service. Therefore, an review of candidate materials must be based on parameters as mechanical strength, corrosion behavior, density, thermal stability, and other as physical, chemical, thermal, mechanical, electrical, optical, among other properties, will play a more or less important role depending on the service environment and expected aim or utilization. In the case of a thermocouple sheath in general, there are certain parameters which need to be considered for the selection of an adequate material:

- Thermal: Service temperature, thermal conductivity, thermal shock resistance, recrystallization temperature, thermal expansion/contraction.
- Mechanical: Formability/machinability, strength and deformation behavior at room temperature, up to service temperature and beyond (safety margin). Structural failure type as a function of stress, stress rate, temperature.
- Corrosion behavior: chemical reactivity in contact with other substances present in the working medium, impurities (i.e. oxygen).
- Availability: scarcity and cost.

Although pure materials are sometimes used in engineering applications, most of the time is the mixture of different elements in varying proportions that result on the manifestation of properties that would not be possible in their pure form. Therefore by alloying, which is the process of adding one or more elements or compounds to interact with a base metal, we can obtain beneficial changes in the mechanical, physical, or chemical properties or manufacturing/processing characteristics of metals. Taking this into consideration, the tungsten-rhenium-tantalum system with boron additions was chosen as a potential sheath material for in-melt (molten oxide/metallic corium) thermometry. The

choice of several alloy compositions in this system was based on the specific needs of the VULCANO MCCI test, along with an extensive literature search, binary/ternary phase diagram study, metal properties, Hume-Rothery rules for alloying, and information on already existent binary alloys appertaining to this system. Therefore the aim was to produce an alloy which would perform in metallic/oxide corium, hence emphasizing the following characteristics:

- "Very high melting point": The absolute melting temperature of the alloy and its constituents should be below 60% of the aimed reference service temperature of 2000ºC. This was important in order to stay around the temperature margin at which there is an activation or profound increase on the diffusion rate or atom migration in metals and alloys ($\sim0.6T_m$). Consequently, this would reduce the rate of loss of sheath material into the corium melt.

- "Resistance" to attack by oxide based molten corium (urania-zirconia): The standard free energies of formation of the oxides present in the corium and concrete should be higher than the constituents of the thermocouple sheath, in order to avoid red-ox type reactions between the multiple melt constituents and the thermocouple shielding material. Therefore, it was imperative to look at the Ellingham diagrams of the various species expected in the oxide corium and concrete, and their position with respect to the sheath materials and tendency with temperature. Additionally, it was of importance all the feedback acquired by discussing with technical staff and engineers working in this facility, since it provided first-hand experience on what sheath materials had been already utilized in previous VULCANO MCCI tests (i.e. zirconia, tungsten and tantalum). Additionally, even though rhenium had never been used as thermocouple sheath material, search in technical literature provided evidence on the inertness of pure metallic rhenium in contact with molten uranium dioxide [14]. Also, ultrasonic temperature sensor sheaths (W-Re alloys) have been successfully utilized in contact with UO_2 [15].

- Adequate thermal and mechanical stability over the span of service temperature: the sheath material should be robust enough to withstand loading/stress and thermal shock, during storage and expected molten corium solidification temperature range. Tungsten's high temperature strength is contrasted to its poor low temperature fracture toughness. Consequently, the addition of rhenium and tantalum to the alloy has shown to greatly reduce tungsten ductile-to-brittle transition temperature substantially below water's freezing temperature, along with a significant increase on the alloys high temperature strength and recrystallization temperature. Furthermore, the addition of boron will serve both as a grain refiner and also add-up to an increase on the recrystallization temperature of the alloy, increasing its application at very high temperatures after being cold or hot worked.

- Resistance to molten 304L stainless steel corrosion: the sheath material should be able to withstand the corrosive attack of superheated stainless steel. The thermocouple sheath should be able to outperform currently utilized materials used for in-melt thermometry of molten metallic/oxide corium above 2000ºC. Tantalum's has shown resistance to attack by acids and other liquid metals due to the growth of self-limiting protective oxide layer based on Ta_2O_5 (at least up to its melting point of 1872ºC). Formation of two distinct intermetallic phases in the Re-W and Re-Ta system and extension/stabilization of its formation range in the Re-W-Ta system. Due to their covalent bonding, intemetallics are thermally and chemically more stable than the metallic bonding of their parent metals. Finally, the addition of boron is meant to improve the corrosion/oxidation resistance of high temperature alloys, and can be used as a grain refiner in the alloy.

Finally, Table 4.1 has been produced in order to provide a resume of a variety of selected properties of each constituent of the selected alloy system. Table 4.1 contains information on the properties of each individual element [14-34].

Properties		*Tungsten*	*Rheniu*	*Tantalum*	*Boron*
Crystal structure	Lattice	BCC	HCP	BCC	Rhombohedral
Physical	Density (g/cc)	19.3	21.03	16.65	2.6
	Atomic radii (nm)	0.137	0.137	0.143	0.083
Chemical	Atomic number Z	74	75	73	5
	Electronegativity	1.7	1.9	1.5	2.04
	Thermal Neutron Absorption Cross Section (barns/atom)	18.3	89.7	20.6	767
Mechanical	Vickers Hardness	310/480	170/550	100/200	3300 (Knoop)
	Modulus of elasticity (GPa)	400(RT)/ 300(1800°C)	469	186	0.44
	Poisson Ratio	0.28	0.296	0.35	N/A
	Shear Modulus (GPa)	156	176	69	N/A
	Yield Tensile Strength (Mpa)	750	290	172	N/A
	Ultimate Tensile Strength (Mpa)	980/1510	1130/2100	450/900	2.85
Electrical	Magnetic susceptibility (cgs/g)	3.30E-07	3.63E-07	9.00E-07	-6.20E-07
	Electrical Resistivity (Ohm.cm)	5.56E-06	1.93E-05	1.25E-05	6.50E+03
Thermal	Heat of Fusion (J/g)	184.2	178	170	2050
	CTE (µm/m·°C)	4.4	6.2	6.5	8.2
	Specific Heat Capacity, (J/g·°C)	0.134	0.138	0.153	1.285
	Thermal Conductivity (W/m·K)	163.3(RT)/ 117(1000°C)	39.6	54.4(RT)/ 83.7(2127°C)	27.4
	Melting point (°C)	3370°C	3180	2996	2300

Table 4.1. Properties of elements in the Tungsten-Rhenium-Tantalum-Boron system.

Afterwards, the binary phase diagrams of the rhenium, tungsten and tantalum are presented in Figure 4.2, to show the variation in phase stability over a wide temperature-composition range. It can be observed that in the solid state, tungsten and tantalum have complete solid solubility and maintain their body-centered-cubic crystal structure. On the contrary, the rhenium-tungsten and rhenium-tantalum systems have four possible crystalline phases: namely two solid solutions conformed by a rhenium-rich hexagonal-closed-packed (HCP) phase and a tungsten/tantalum-rich body centered cubic phase, along with two intermediate phases denominated with the Greek letters χ and σ. The χ-phase has a complex cubic lattice structure (A12) which resembles α-Manganese and the σ-phase has a tetragonal structure (D8$_b$) with a Re$_3$(W, Ta)$_2$ chemical formula. Finally, in Figure 4.3 we can observe the respective binary phase diagrams between each of these three refractory metals and boron. Boron forms a wide range of metal borides with each respective refractory metal over the span of the composition range [43-49].
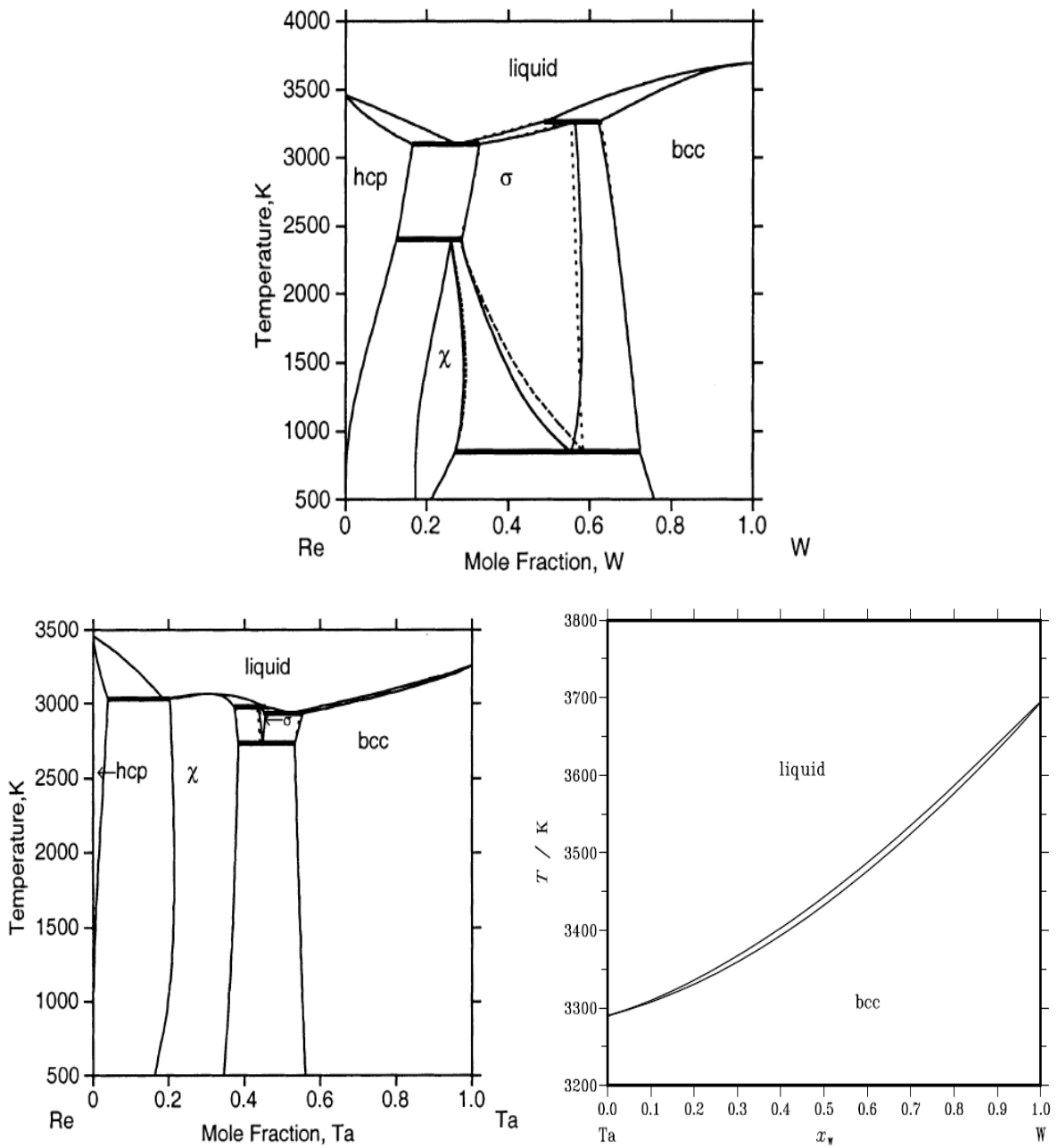
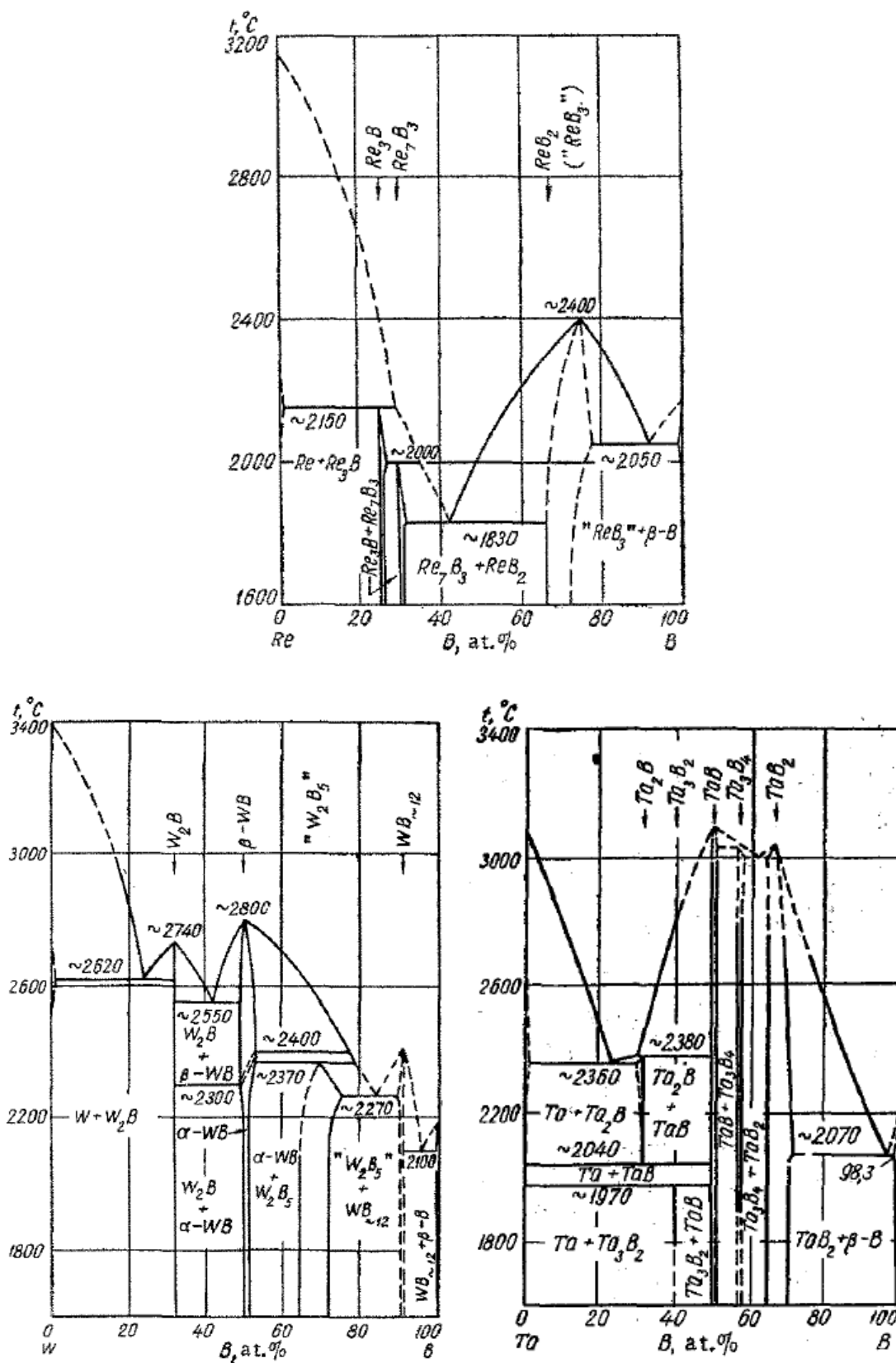Figure 4.2. The binary phase diagrams of Re-W, Re-Ta and Ta-W.

Figure 4.3. The binary phase diagrams of boron with rhenium, tungsten and tantalum, respectively.

4.2.2 Alloy Fabrication

The Re-W-Ta based alloys were prepared by the Ames National Laboratory as part of the Department of Energy and administrated by the Iowa State University in a water-cooled copper-hearth using the arc melting technique under an argon atmosphere. The base materials had at least 99.99% purity. Multiple melting steps were implemented to ensure the complete and uniform mixing of the pure metals. Due to the appearance of oxide islands after the first melting process (presumably due to an excess oxygen in the primary metallic powders provided by Zhuzhou Kete Industries Co. Ltd.), an intermediate purification step, under vacuum, was implemented in order to decompose the oxides and extract the oxygen.

Moreover, four main alloy compositions were selected, plus another four identical alloys with an addition of a small quantity of boron (0.1molar% B). The alloys have the following compositions (in molar%): Re-10W-10Ta-(0.1B), Re-25W-35Ta-(0.1B), Re-40W-20Ta-(0.1B) and Re-05W-52Ta-(0.1B). From now on, the alloys will be identified as "Re" followed by the molar percent tungsten and tantalum, and if boron is present a capital "B" will be used at the end (i.e. Re1010B). The ternary phase diagram of the Re-W-Ta system can be observed in Figure 4.4, in which the selected alloys have been pin-pointed with colored circles. All of the alloys, but three, specimens were sectioned from the as cast bars by electric discharge machining (EDM) or spark eroding with final dimension of 5 x 5 x 5 mm. The Re1010, Re1010B and Re4020B were too brittle and would break when clamped into the EDM machine before performing the sectioning. Therefore, it was decided to melt them into 12 gram-buttons and keep them in their as cast, globular form for testing.
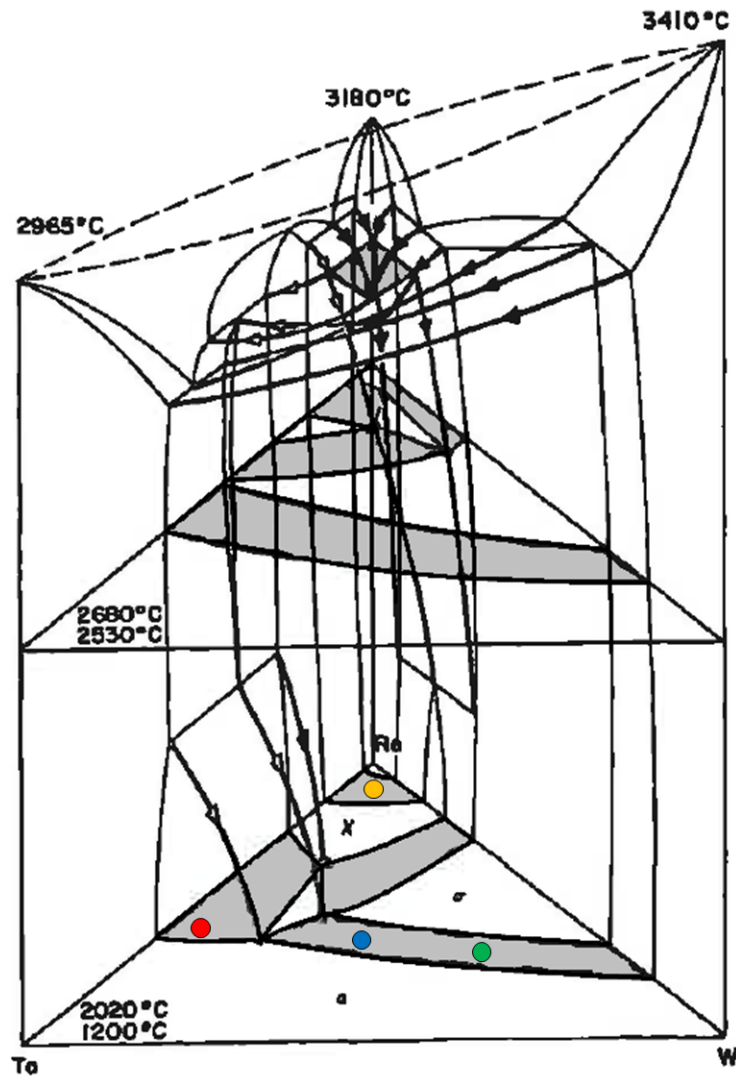
Figure 4.4. The Re-W-Ta ternary phase diagram with highlights of the selected alloy.

The alloy compositions were selected in order to promote a biphasic microstructure combining the crystal structure of one of the parent metals (BCC or HCP) along with an intermetallic phase (χ or σ). The aim was to get the inherent properties of each crystal structure, for example the good mechanical properties and ease of formability of the parent phase, along with the chemical and thermal stability of the intermetallic phase. The alloys selected maintain their two-phase microstructure from room temperature up to at least 2500ºC. The micro-alloying with boron is not expected to alter the two-phase stability range, since the additions are below the solubility limit; on the contrary, the fine precipitation of fine metal borides at the grain boundaries restrains the growth of the grains and therefore maintains the high temperature strength of the alloy to even higher

temperatures. Furthermore, the plan was to explore several combinations of the multiple phases present in the system in order to study its properties and to be gain insight on its corrosion behavior under molten 304L stainless steel attack. Each alloy has been given an ID name and they will be identified in the following manner from now on:

- Re-10W-10Ta (identified as **Re1010**).- This alloy was selected to evaluate the corrosion properties of the χ intermetallic along with the strenght of the HCP phase.

- Re-40W-20Ta (identified as **Re4020**) and Re-25W-35Ta (identified as **Re2535**).- These alloys are both composed by a BCC + σ microstructure. They were selected in the same phase region in order to understand the effect of higher tungsten or tantalum content in the alloy's corrosion resistance and mechanical properties.

- Re-05W-52Ta (identified as **Re0552**).- This alloy falls in a relatively small region in which BCC + χ phases are stable. It was selected because the cubic structure (BCC) has more closed packed directions than the HCP, hence it has better formability, even during cold-working. Additionally, the very dense χ phase can provide an improved corrosion resistance over the relatively less densely packed σ lattice structure.

- Boron addition: another set of four alloys with similar composition as the previous was prepared with 0.1 molar percent boron added to the previous alloys. Boron was added to the previous alloys to get insight on the effect of the boron microalloying on the corrosion and mechanical properties of the alloys.   The alloys with boron are clearly identified with a B at the end of their name, i.e. **Re1234B**.

The preparation of the samples for the corrosion experiments was the following:

1. Samples were ground down to 800-grit using SiC sand papers in order to remove surface scratches and imperfections left by the EDM sectioning, along with any oxide layer in order to expose a fresh metallic surface.

2. Dimension of the samples where measured using a micrometer in order to calculate surface area exposed in the corrosion experiments. Then their weight was acquired and recorded using a precision balance.

3. A 10-15 minute ultrasonic bath in ethanol for each samples was performed in order to remove any impurities and organic debris on the surface of alloy.

4. The containers utilized for the corrosion experiments were zirconia ceramic crucibles (ZrO_2 stabilized with CaO). Before each experiment the crucibles were baked in a box furnace for 24 hours at 350ºC.

5. Under flowing argon and inside a glove box, the samples were placed in a zirconia crucible and then the crucible was filled to the top with 304L stainless steel powder (-100 mesh) bought from Alfa Aesar. The nominal composition of 304L in weight percent is: Fe-balance, 18-20% Cr, 8-12% Ni, max. 0.03% C, max. 2% Mn, max. 0.045% P, max. 0.030% S, max. 0.75% Si and max. 0.1% Ni. Figure 4.5 shows the basis of this type of stainless steel with an illustration of the Fe-Cr-Ni ternary phase diagram and location of the austenitic 304L SS.
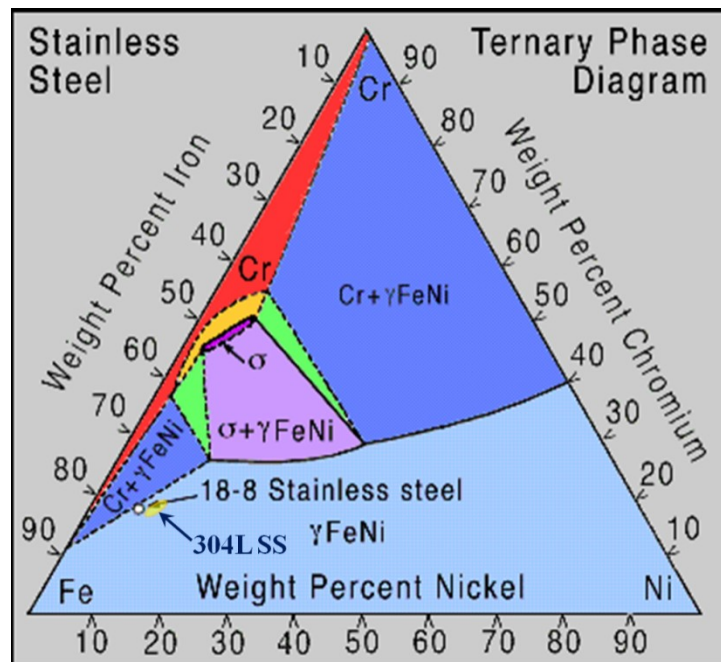

Figure 4.5. Fe-Cr-Ni ternary phase diagram with the position of 304L stainless steels.

4.2.3 Very High Temperature Liquid Metal Corrosion Test

In this section we will go through the experimental details of the test section. Some details on furnace and instrumentation might be briefly mentioned, since they had been previously introduced in Chapter 3.

The prepared zirconia crucible, containing the refractory sample and stainless steel powder, was transferred into the VITI furnace. The test section details can be observed in Figure 4.6. Then the furnace was hermetically closed and three evacuation/argon cycles were performed to remove any oxygen inside the vessel. When argon pressure of 0.8 bar gauge was reached, then the generator was turned on and the heating initiated. The heat-up was performed in multiple power increase steps, it would heat-up during 1-hour reach 1450ºC and subsequently the stainless steel melting, then around 30 minutes to reach the desired testing temperature of 2000ºC which was held for 5 minutes then a fast cooling would start (average of 30º/minute). Depending on the alloy being tested, the cooling curve would have different features as solidification spikes and other phase's transformation that could also be observed with the pyrometer camera looking vertically onto the melt surface. A detailed explanation for each test will be given in the test results section.

4.2.4 As-Cast and Post-Test Metallurgical Analysis

The as-cast and post-test samples were prepared for characterization following these steps:

1. All the as-cast were mounted or encapsulated in epoxy resin, opposite to the corrosion tested samples were kept in their stainless steel casting for grinding and polishing.

2. Samples were ground down using silicon carbide paper (SiC). The samples were subjected to multiple grinding steps starting with 80 then 120, 220, 320, 400, 500, 600, 800, 1200 and down to 2400 (sand-paper particle grid size). The as-cast samples were ground in groups of 8 samples using an automatic grinding machine. Each side of the cubic sample was ground for 5 minutes, at 300rpm with a 20N force. The same steps were followed for the corrosion samples, except they were manually ground down using a mechanical turntable.

3. The samples were then polished on an MD-Mol disc using a fine diamond powder (6, 3 and 1μm) suspended in an alcohol based lubricant (DP-S Red). The samples were polished for 5 minutes, at 150rpm with a 15N force. A final fine polish with 0.04μm silica particles (SiO_2) suspended in water was performed with the same parameters as for the diamond polish. The corrosion samples undergo similar steps but they were manually polished.

4. All the samples were rinsed in water, and subsequently in ethyl alcohol before drying by blowing warm air with a blow-dryer.

5. Then the samples were labeled and the polished surface was covered with cotton and introduced in a plastic container with multiple compartments.
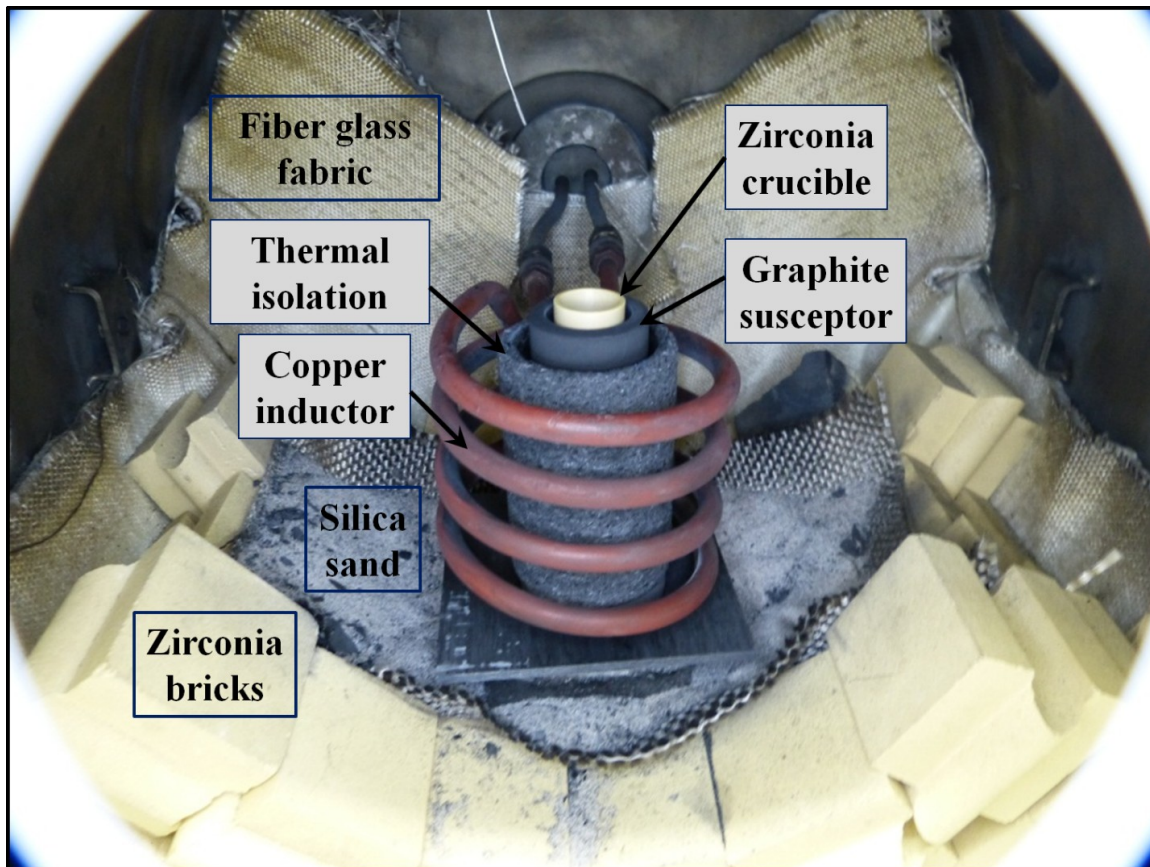
Figure 4.6. Corrosion experiments test section configuration inside VITI furnace.

4.3 Characterization/Metallurgical Analysis of As-Cast and Corrosion Samples

Sample characterization of the as-cast alloys and oxidized samples was performed with scanning electron microscopy (SEM) in backscattered electron imaging (BSD) mode, and chemical analysis using energy dispersive spectroscopy (EDS). Additionally, X-ray diffraction (XRD) was used to identify the crystal structure of the phases present in the as-cast alloys. Finally, Vickers microhardness was also performed for the as-cast samples. Sample characterization was performed in facilities provided

4.3.1 Optical and Scanning Electron Microscopy

The micrographs were captured with an Olympus BX51M optical microscope (OM) coupled to a video camera system controlled via computer software (Analysis 5.0, Soft Imaging System GmbH). For the SEM analysis all samples were coated with carbon and carbon tape was also used to connect the sample and the metallic sample holder, hence ground the sample; this was done to prevent the accumulation of electrical charge on the samples. The microstructures were analyzed by scanning electron microscope (SEM), in backscatter electron imaging modes using a Zeiss EVO MA-15 (FE-SEM), and the chemical composition of the phases was determined by energy dispersive spectroscopy (EDS) using Oxford Instruments detector with an INCA EDS System software. The use of backscatter electron imaging mode provides image contrast as a function of elemental composition, and energy dispersive spectroscopy provides a qualitative analysis of elemental concentration. EDS and BSD analysis was performed on the metal surface in order to identify distinct phases present in the microstructure; at least 5 readings were taken of different microstructural features to obtain a more confident reading on concentration of elements in different phases. Readings were performed with an elapsed time of 50 seconds. Before any analysis an initial calibration of EDS detector was performed using a very pure cobalt sample and following calibration procedures provided for the INCA software. EDS analysis was correlated with the XRD technique. The parameter used for SEM, BSD, and EDS were 20kV accelerating voltage, with a probe current of 20µA and a working distance ranging from 10.5mm to 16.5mm.

4.3.2 X-Ray Diffraction

Previously stated grinding and polishing steps were performed on the as-cast samples to remove any surface impurities before XRD. The X-ray diffraction (XRD) was used to identify the phases using a Siemens-5000 diffractometer with a monochromatic CuKα (λ=1.540562 Angstroms) radiation. The parameters used for XRD analysis are the following: Generator voltage (45kV), generator current (45mA), step size (0.02º), time at each step (1.5 seconds) and 2θ angle range (15 to 90º). Identification of the phase's crystal lattice was made with DIFFRAC-EVA software for X-ray powder diffraction data evaluation and analysis.

4.3.3 Microhardness Testing

In order to evaluate the strength of the alloys and to differentiate the properties of the multiple phases present the Vickers microhardness testing was performed on the alloys. The micro indentures were made in 20 seconds with a 100 lbs. force using a PolyVarMet/Micro-Duromat 4000 microscope/hardness equipment by Reichert-Jung.

4.4 Results

4.4.1 Microstructure and Phase Identification of As-Cast Samples

The characterization of the as-cast samples was performed using multiple techniques in order to correlate the results. The scanning electron microscope (SEM) in secondary electron (SE) and backscatter diffraction mode (BSD), along with a chemical analysis using electron diffraction spectroscopy (EDS) was used for phase identification. Also, the X-ray diffraction (XRD) was utilized to identify the phases present in the microstructure and crystallographic features. Furthermore, the SEM in secondary electron imaging and the optical microscope were used as a mean to identify the surface morphology. Finally, Vickers microhardness testing was performed to indirectly get insight on the alloys strength and when possible, differentiate between the multiple phases.
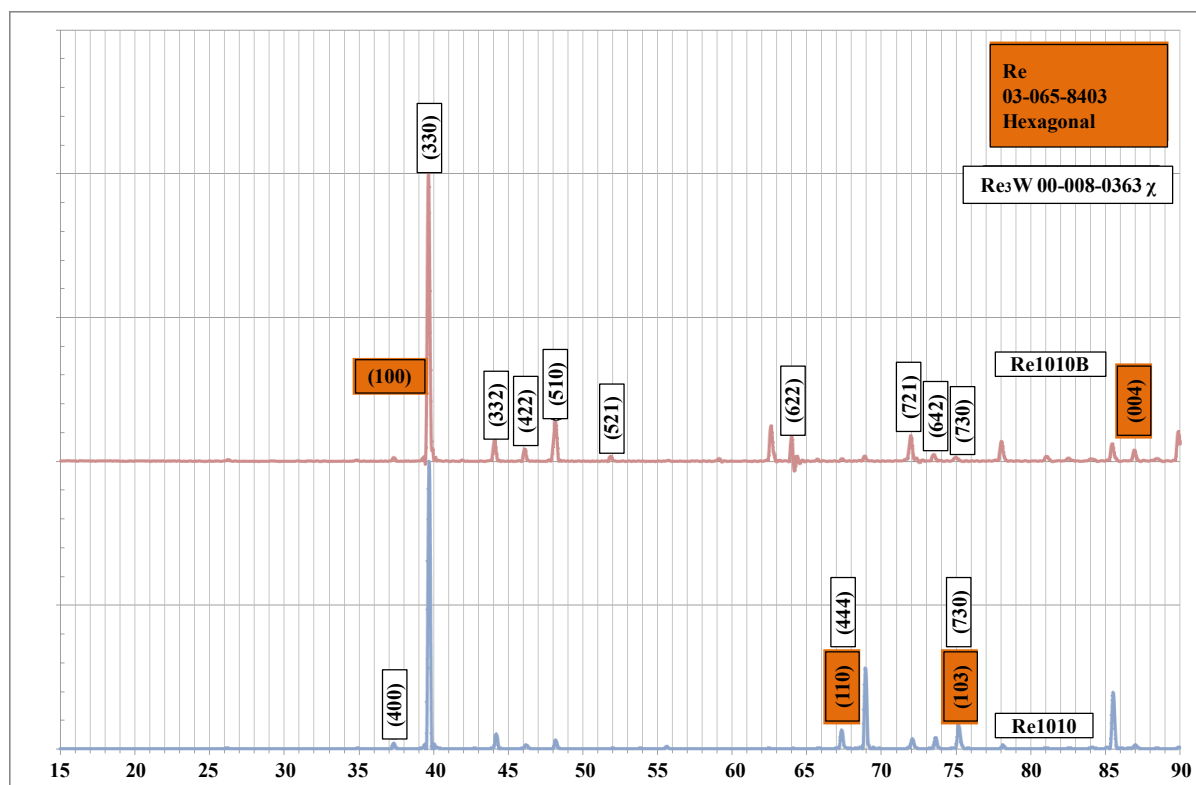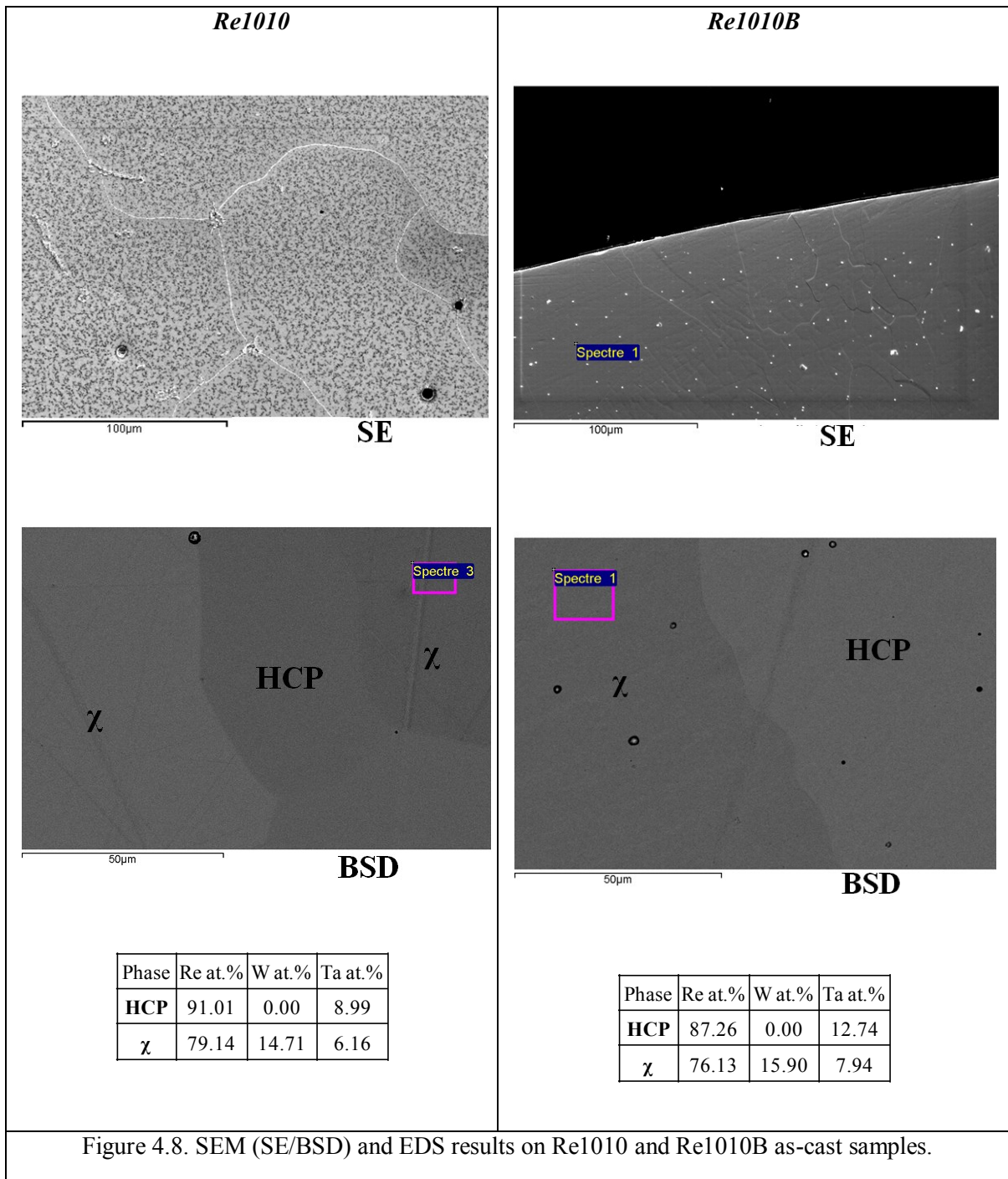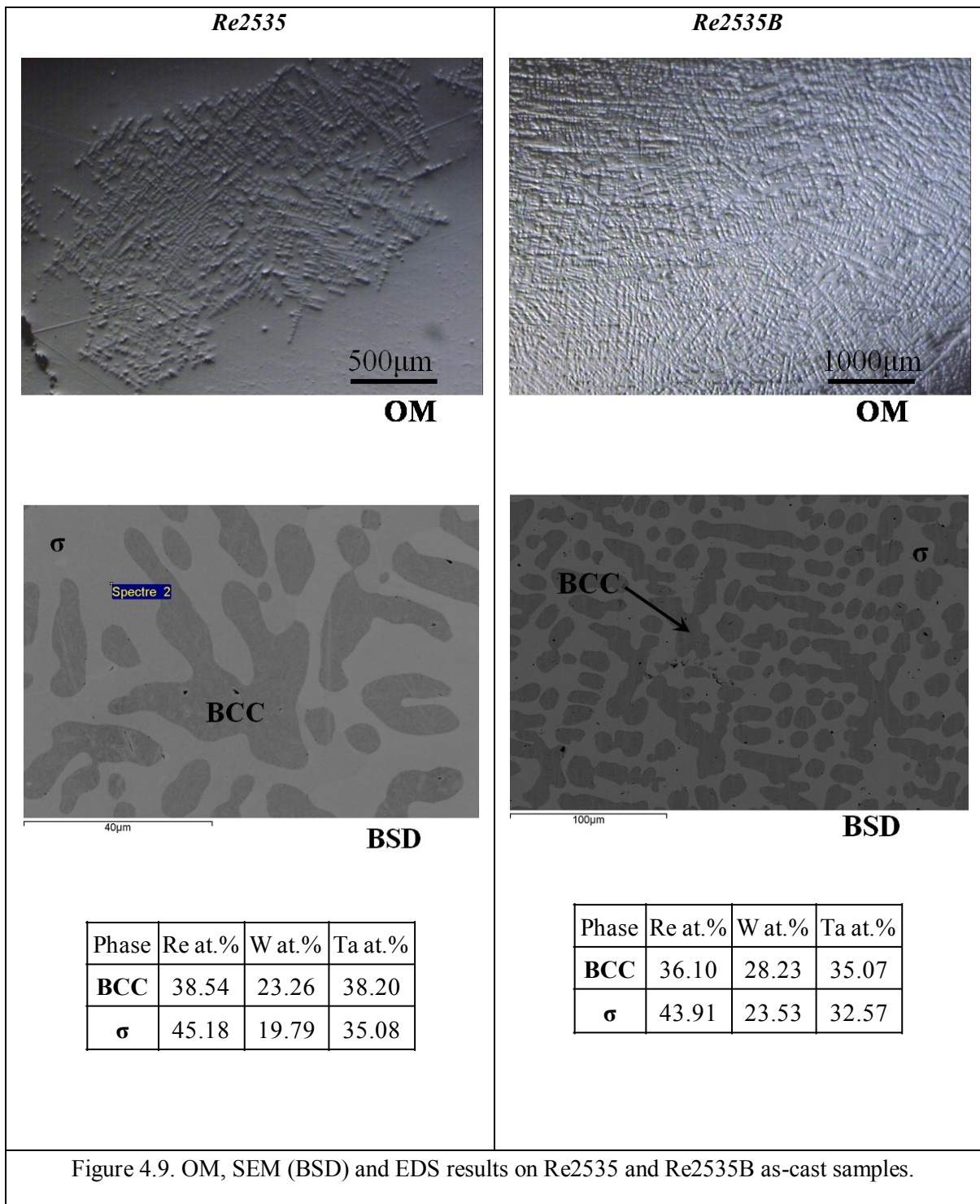
Figure 4.7. X-ray diffraction pattern of the Re1010 and Re1010B as-cast alloys.

The XRD patterns obtained on the Re1010 and Re1010B alloys (Figure 4.7) were tied to two main crystal structure cards found in the Powder Diffraction Database: HCP-Re (Card#: 03-065-8403) Re_3W corresponding to χ (Card#: 00-008-0363). Furthermore, the studies performed with the electron microscope (Figure 4.8) confirm the existence of two distinct phases having a different crystal structure and chemical composition. Utilizing the EDS chemical analysis, two distinct phases were found, one corresponds to a rhenium-rich phase with approx. 10at.% Ta identified as the hexagonal structure, along with another phase composed mainly by rhenium (~78at.%) but also with the other two metallic constituents, W(~15at.%) and Ta(~7at.%). The SE imaging shows that the microstructure is composed of asymmetrical elongated grains, which are sometimes filled by smaller more equiaxed grains (probably newly recrystallized grains). At low-magnitude the grains show an undulating texture, but at higher magnitudes the topography can be described as pointillism painting style. Additionally, the presence of some dispersed bubbles can be observed, this is gas porosity that originated due to the coalescence of dissolved gases during the alloy fabrication at the liquid state.

Finally, some worm-like phases were found, especially on the Re1010 alloy; these correspond to segregated rhenium which nucleated at the grains boundaries and triple-points.
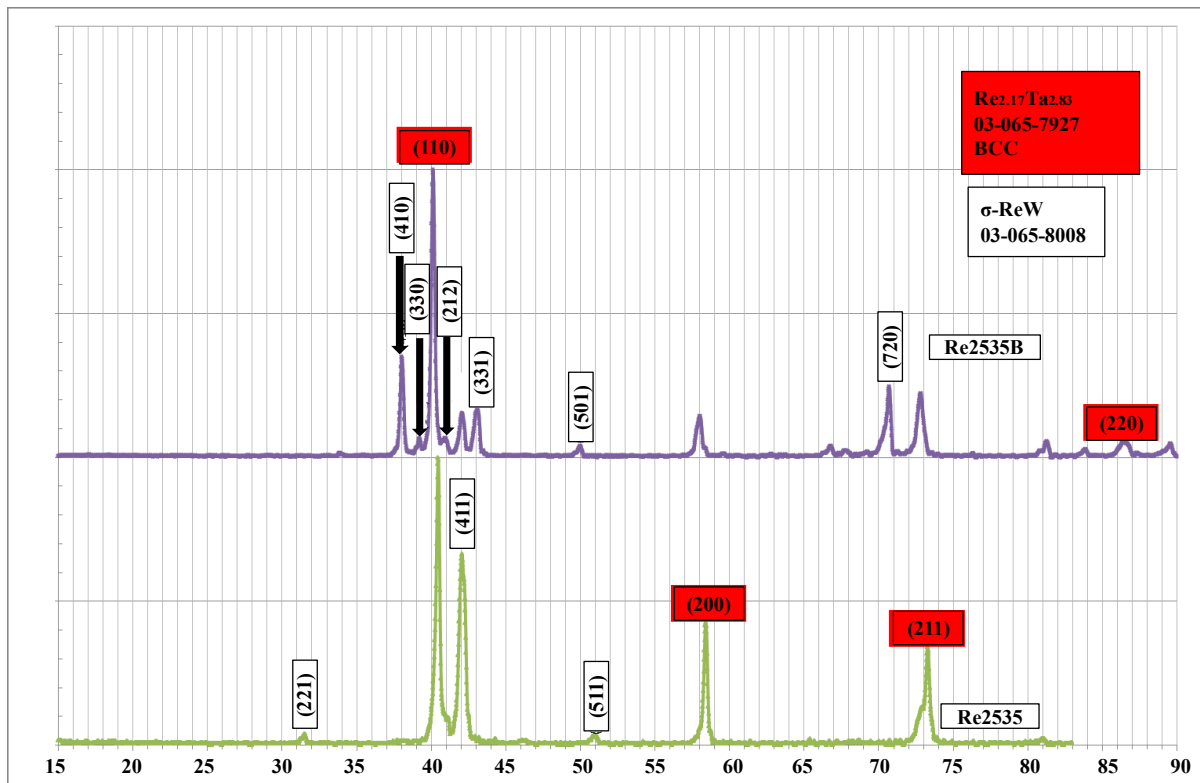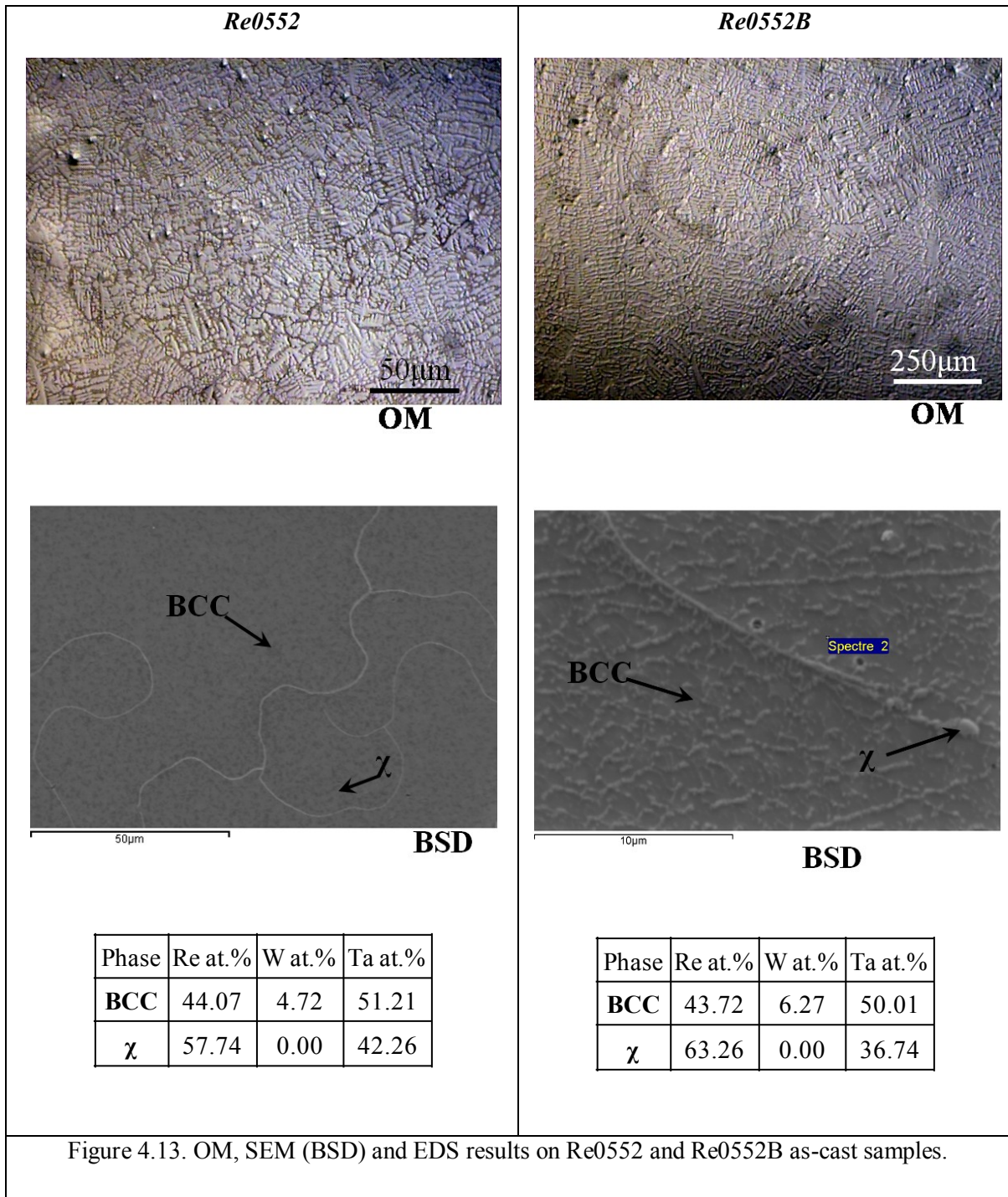

	Re1010	Re1010B

Re1010 (SE, BSD)

Phase	Re at.%	W at.%	Ta at.%
HCP	91.01	0.00	8.99
χ	79.14	14.71	6.16

Re1010B (SE, BSD)

Phase	Re at.%	W at.%	Ta at.%
HCP	87.26	0.00	12.74
χ	76.13	15.90	7.94

Figure 4.8. SEM (SE/BSD) and EDS results on Re1010 and Re1010B as-cast samples.

Phase	Re at.%	W at.%	Ta at.%
BCC	38.54	23.26	38.20
σ	45.18	19.79	35.08

Phase	Re at.%	W at.%	Ta at.%
BCC	36.10	28.23	35.07
σ	43.91	23.53	32.57

Figure 4.9. OM, SEM (BSD) and EDS results on Re2535 and Re2535B as-cast samples.

Figure 4.10. X-ray diffraction pattern of the Re2535 and Re2535B as-cast alloys.
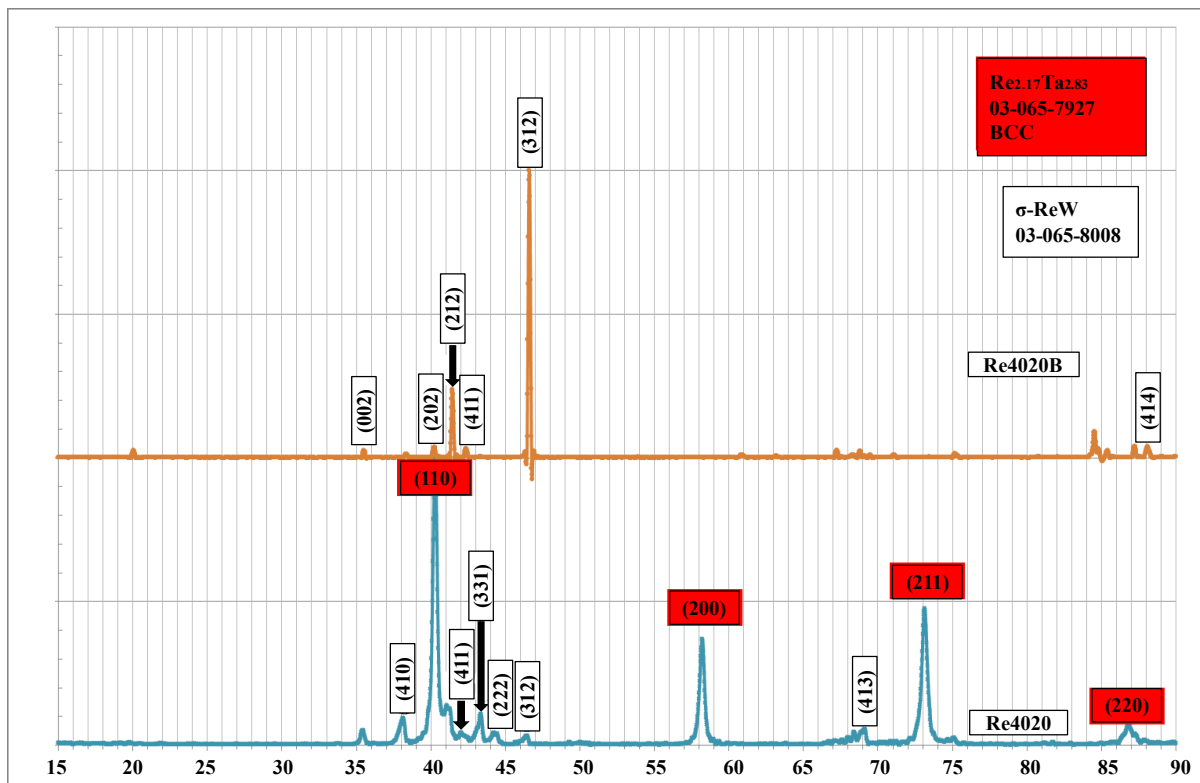
Figure 4.11. X-ray diffraction pattern of the Re4020 and Re4020B as-cast alloys.

The XRD pattern of the Re2535 (and B) and Re4020 (and B) samples (Figures 4.10 and 4.11) show the presence of two crystal structures identified as body-centered-cubic and σ-intermetallic. The peaks were matched to the following powder diffraction cards: $Re_{2.17}Ta_{2.83}$ alloy with a BCC lattice (Card#: 03-065-7927) and ReW alloy corresponding to the σ-phase crystal (Card#: 03-065-8008). Even though the alloys fall in the same bi-phase region and are conformed by similar structure phases, the XRD patterns are not identical because the samples utilized were solid cubes; therefore they will show a preference on crystal plane-directionality which depends on the fabrication and position of the cubes during the x-ray diffraction. Furthermore, upon optical microscopy and SEM analysis of the previous alloys (Re2535(B) and Re4020(B)) we can identify two-main phases as in the XRD. The first phase to solidify has a dendritic structure (dark-phase) and corresponds to the BCC-structure, it coexists with a continuous/matrix phase (light-phase) which solidified at the end, and corresponds to the σ-intermetallic. The alloys with boron additions show a more homogeneous and finer microstructure. The previous features can be due to the boron effect, since it acts as a nucleation site for crystals from the liquid phase; and during grain coarsening boron impinges the grain boundaries and acts as an impediment to grain growth, hence resulting on a finer structure with smaller grains. Upon chemical analysis (EDS) of the Re2535(B) and Re4020(B) alloys it has been observed that the phases have different proportion of metallic elements. In both alloys the phases have similar amount of tantalum (~20 at.%), but the tungsten/rhenium ratio is higher in the BCC phase than in the σ-phase. The variation in the composition of both phases corresponds to what is expected in the two-phase region of the Re-W-Ta ternary phase diagram.

Phase	Re at.%	W at.%	Ta at.%
BCC	30.08	49.61	20.31
σ	40.19	40.29	19.52

Phase	Re at.%	W at.%	Ta at.%
BCC	28.31	53.53	18.16
σ	38.65	44.15	17.20

Figure 4.12. OM, SEM (SE/BSD) and EDS results on Re4020 and Re4020B as-cast samples.

	Re0552	*Re0552B*

Figure 4.13. OM, SEM (BSD) and EDS results on Re0552 and Re0552B as-cast samples.
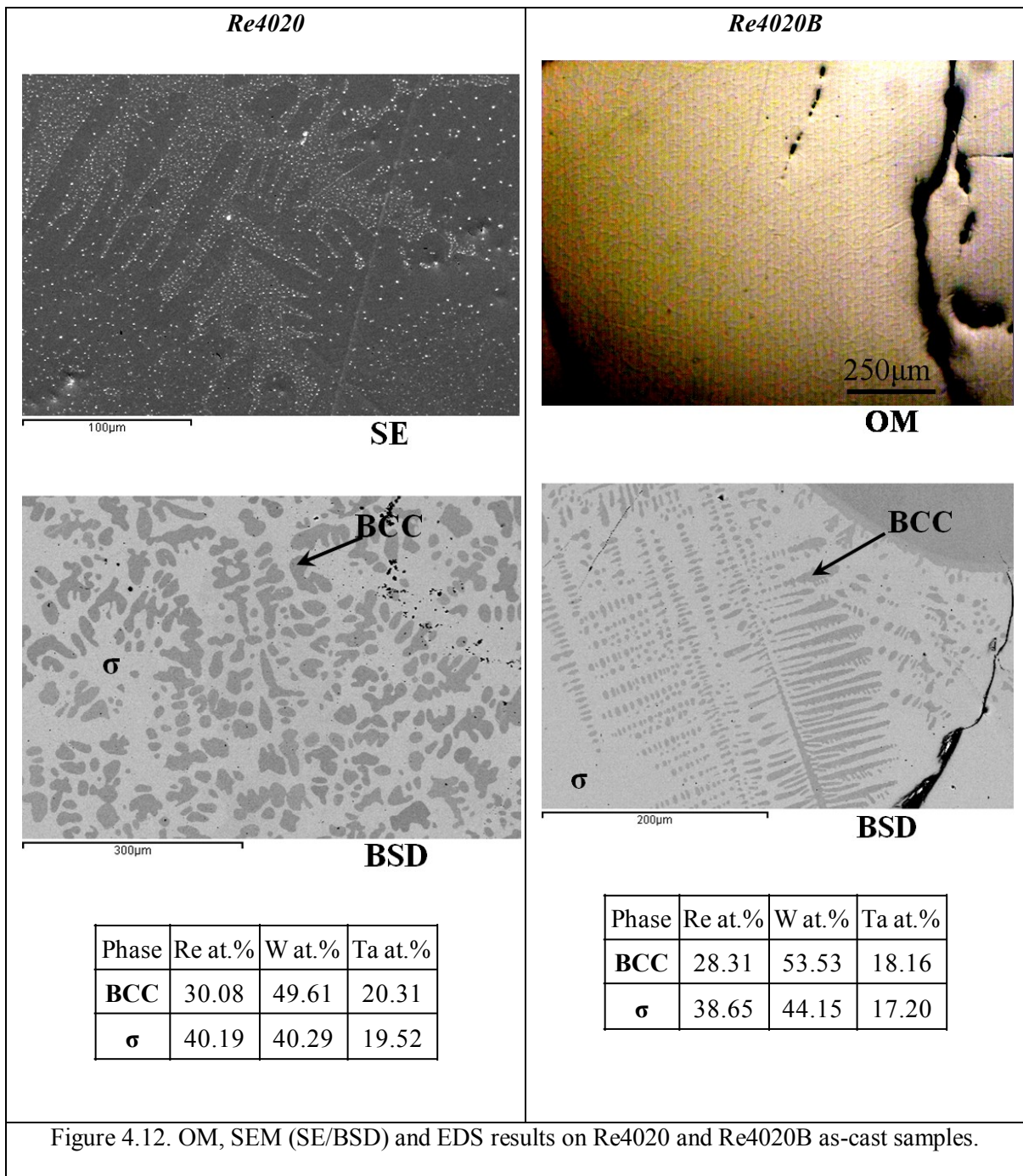
Finally, the characterization of the Re0552 and Re0552B alloy shows the presence of two-phases, BCC and χ-phase. The XRD peak pattern was tied to the crystal structure of two phases formed by Re and Ta, due to the alloy's low tungsten content of 5molar%. The powder diffraction patterns correspond to: $Re_{2.17}Ta_{2.83}$ alloy with a BCC lattice (Card#: 03-065-7927) and TaRe crystal corresponding to the χ-phase (Card#: 00-008-0364). Furthermore, upon OM and SEM(BSD) analysis

of the samples it can be observed that the microstructure morphology of these alloys resembles something in between the HCP/χ and BCC/σ alloys microstructural features. For example, the macrostructure is composed by large irregular grains (similar to the elongated grains observed in the Re1010(B) alloy) and inside these grains a dendrite-like structure is observed (similar to the Re2535(B) and Re4020(B) alloys). The SEM chemical analysis confirms the existence of two distinct phases, these phases and its elemental composition (analyzed with the EDS) have almost the same proportions as the chemical formula of the XRD cards. For example, approximately half-Re and half-Ta in the χ-phase and, if we replace the W-atoms as Ta-atoms in the BCC phase the ratio is also quite close. This interchange is allowed since tungsten and tantalum dissolve completely, or act as substitutional atoms, in the BCC solid-solution phase found in the W-Ta binary system.
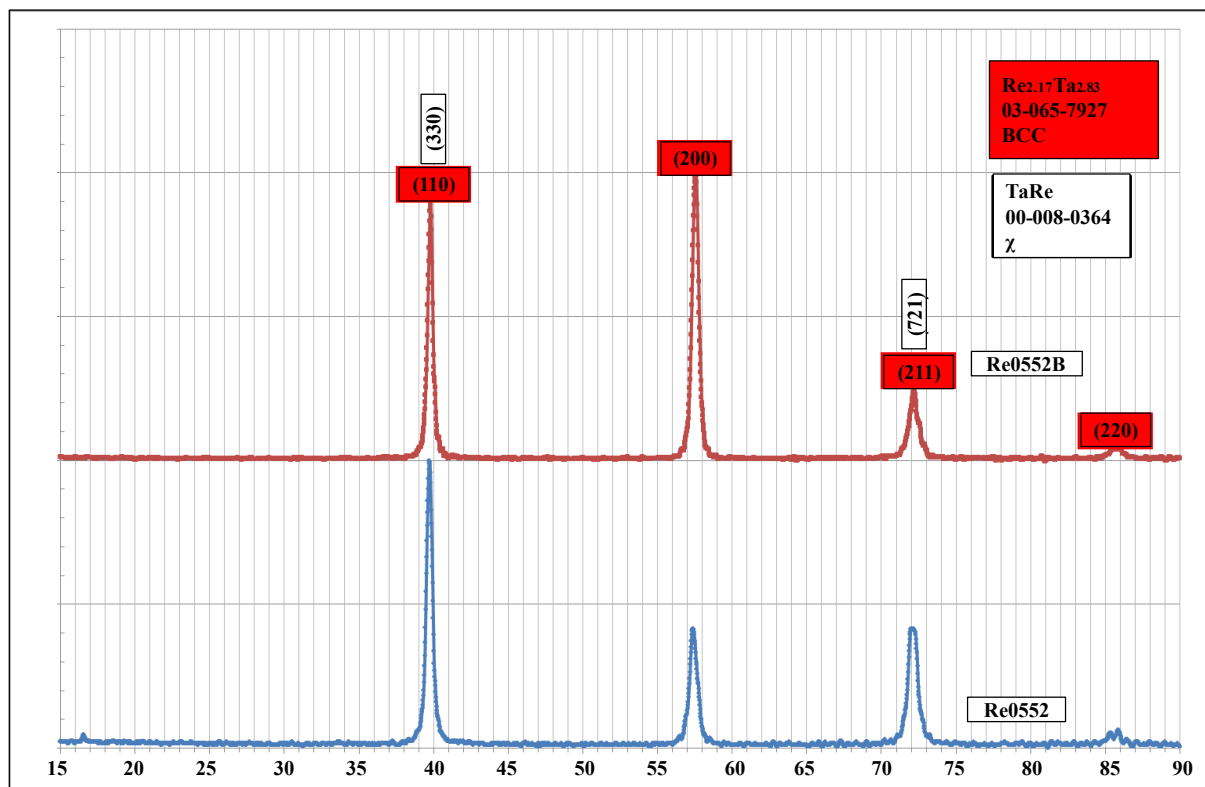
Figure 4.14. X-ray diffraction pattern of the Re0552 and Re0552B as-cast alloys.
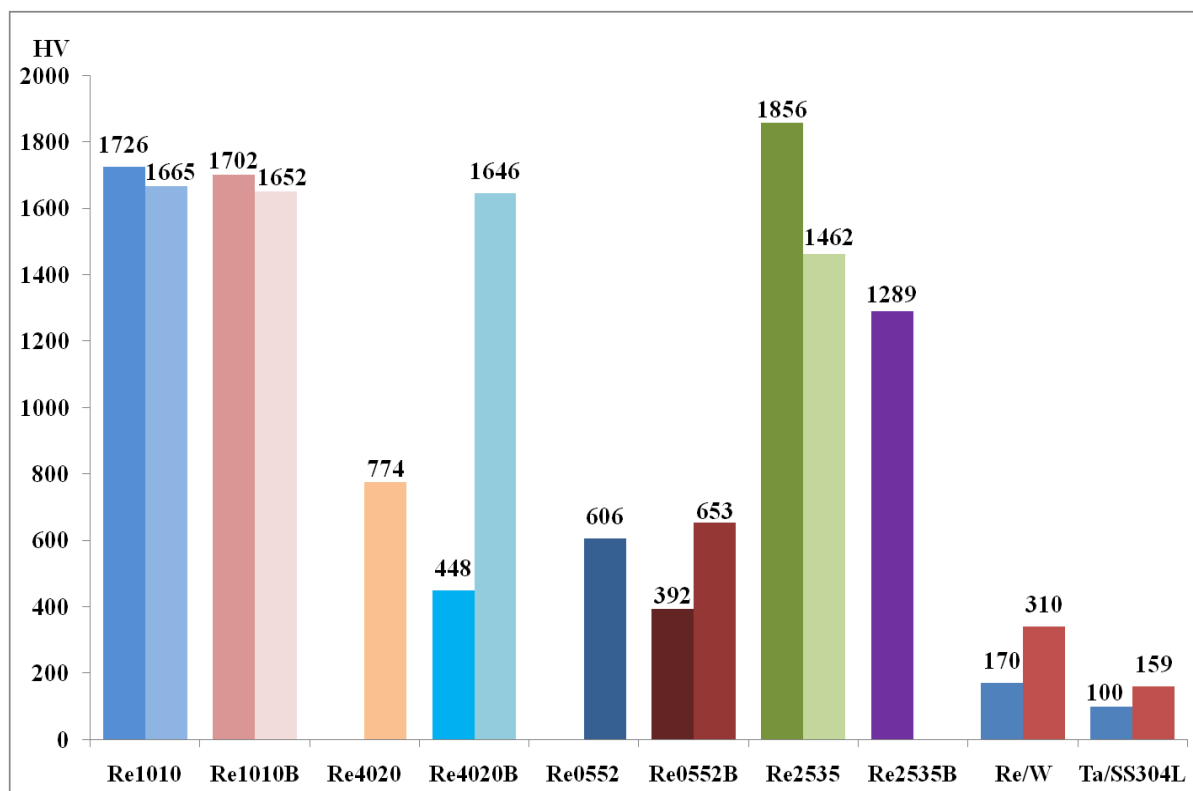
Figure 4.15. Vickers microhardness measurements of the Re-W-Ta-(B) as-cast alloys.

In order to get some insight on the mechanical properties of the Re-W-Ta-(B) alloys, an evaluation of the Vickers microhardness was performed on the as-cast samples (Figure 4.15). Additionally, in order to set a basis for comparison, the HV value of annealed Re, W, Ta and 304LSS were included since they serve to elucidate the non-negligible changes that can be obtained by alloying. If we analyze the HV values plotted in Figure 4.15, we can readily observe that there was a significant increase in the hardness of the alloyed samples, when compared to the metals in their pure non-worked hardened form. This significant increase in hardness can be due to both the presence of the extremely hard intermetallic phase along with the strengthening of the BCC or HCP phase thru solid-solution hardening mechanism. Furthermore, when possible the HV value of individual phases was evaluated, and they are presented as two separate bars in the plot. In all cases, the hardest phase, or highest HV value, corresponds to the intermetallic phase. If averaged, the Re-rich alloys are the hardest followed by Re2535(B), then Re4020(B) and the softest alloys are the Tantalum-rich alloys (Re0552(B)), as could be expected. During the machining (EDM) of the alloys it was observed that

Re1010, Re1010B and Re4020B were too brittle to section into cubes, and would break during clamping. In the case of the Re-rich alloys this can be ascribed to the very low fracture toughness of the intermetallic phase present in the microstructure, and to the limited availability of slip planes in the HCP phase. Additionally, in the case of the Re4020B alloy it is hard to determine the failure mechanism without conducting a more detailed analysis and other tests, but the significant disparity between the very hard and relatively soft phases present could be the cause of failure. On the other hand, the other three alloys which lay in the same bi-phase region (BCC/σ) show an improved strength and fracture toughness could be due to the higher tantalum content in Re2535-(B) alloys, and the finer more homogeneous microstructure of Re4020 alloy. Nevertheless, the evaluation of the mechanical properties of these alloys is not the main purpose of this research and in order to get more detailed information, a more precise study is needed using variety of mechanical tests and fracture analysis.

4.5 Results and Discussion of the Molten 304L Stainless Steel Liquid Metal Attack on Tungsten, Tantalum and Re-W-Ta-(B) Alloys Up to 2000ºC

A liquid metal attack test was performed on each Re-W-Ta-(B) alloy, along with tungsten and tantalum samples for comparison. The information on the heating cycle is included in subsection 4.2.2. The details on the sample characteristics and amount of 304L stainless steel powder utilized in each test are shown in Table 4.2. This information not only serves as an indication on the quantities of materials utilized and sample shape, but includes the sample surface area to 304L stainless steel volume which is a very important parameter in corrosion research. Furthermore, in order to facilitate the interpretation of the test solidification curves and SEM/EDS chemical analysis of the phases present Table 4.3 has been produced. This table includes individual mass and calculation of the weight percent of the totality of the corrosion experiment reacting elements, hence metallic elements (Fe, Cr, Ni, Re, W, Ta and boron when applicable). The table has been "simplified" and other alloying elements included in the 304L SS (C, Si, Mn, S, P…) have been omitted in order to make the analysis of the results less complex, also since no know thermodynamic software includes a database

combining the pertinent elements. Therefore, in order to analyze each corrosion experiment it was necessary to utilize multiple tools, i.e. cooling curves, SEM/BSD microscopy along with EDS chemical analysis, pertinent phase diagrams, thermodynamic and metallurgy knowledge. When applicable, any assumptions made will be stated with corresponding.

Test #	SS mass, grs	SS vol., cc	Sample	Form	Sample mass, grs	X, mm	Y (diameter), mm	Z (height), mm	Area, cm²	Sample Area/SS Vol
10	46.290	5.786	W	Cylinder	9.506	N/A	11.11	5.23	5.59	0.97
11	46.410	5.801	Re4020	Cube	2.151	4.80	4.90	4.77	1.40	0.24
12	48.570	6.071	Re0552	Cube	1.672	4.46	4.43	4.51	1.20	0.20
13	46.636	5.830	Re1010	Blob	14.850	N/A	14.12	6.50	4.70	0.81
14	48.160	6.020	Re2535	Cube	2.144	4.90	4.89	4.94	1.45	0.24
15	48.940	6.118	Ta	Cylinder	5.226	N/A	8.03	6.80	4.44	0.73
16	50.827	6.353	Re0552B	Cube	2.102	4.80	4.81	4.86	1.40	0.22
17	55.181	6.898	Re2535B	Cube	1.980	4.69	4.74	4.68	1.33	0.19
18	52.870	6.609	Re1010B	Blob	14.164	N/A	13.74	6.58	4.45	0.67
19	50.485	6.311	Re4020B	Blob	15.136	N/A	14.27	6.79	4.80	0.76

Table 4.2. Corrosion experiment sample details.

Test #	Sample	Fe, grs	Cr, grs	Ni, grs	Re, grs	W, grs	Ta, grs	B, grs	Total mass, grs	Fe wt%	Cr, wt%	Ni, wt%	Re, wt%	W, wt%	Ta, wt%	B, wt%
10	W	30.52	9.74	6.03	0.00	9.51	0.00	0.0000	55.80	54.70	17.45	10.81	0.00	17.04	0.00	0.00000
11	Re4020	30.60	9.76	6.05	0.87	0.86	0.42	0.0000	48.56	63.01	20.10	12.46	1.79	1.77	0.87	0.00000
12	Re0552	32.02	10.22	6.33	0.73	0.08	0.86	0.0000	50.24	63.74	20.33	12.60	1.45	0.17	1.71	0.00000
13	Re1010	30.75	9.81	6.08	11.93	1.47	1.45	0.0000	61.49	50.01	15.95	9.89	19.40	2.39	2.36	0.00000
14	Re2535	31.75	10.13	6.28	0.87	0.54	0.74	0.0000	50.30	63.12	20.14	12.48	1.73	1.07	1.47	0.00000
15	Ta	32.27	10.29	6.38	0.00	0.05	5.17	0.0000	54.17	59.57	19.01	11.78	0.00	0.10	9.55	0.00000
16	Re0552B	33.51	10.69	6.63	0.92	0.10	1.08	0.0001	52.93	63.31	20.20	12.52	1.74	0.20	2.04	0.00023
17	Re2535B	36.38	11.61	7.19	0.80	0.50	0.68	0.0001	57.16	63.65	20.31	12.58	1.41	0.87	1.19	0.00020
18	Re1010B	34.86	11.12	6.89	11.37	1.41	1.38	0.0008	67.03	52.00	16.59	10.28	16.97	2.10	2.06	0.00123
19	Re4020B	33.28	10.62	6.58	6.13	6.03	0.03	0.0009	62.67	53.11	16.94	10.50	9.77	9.63	0.05	0.00142

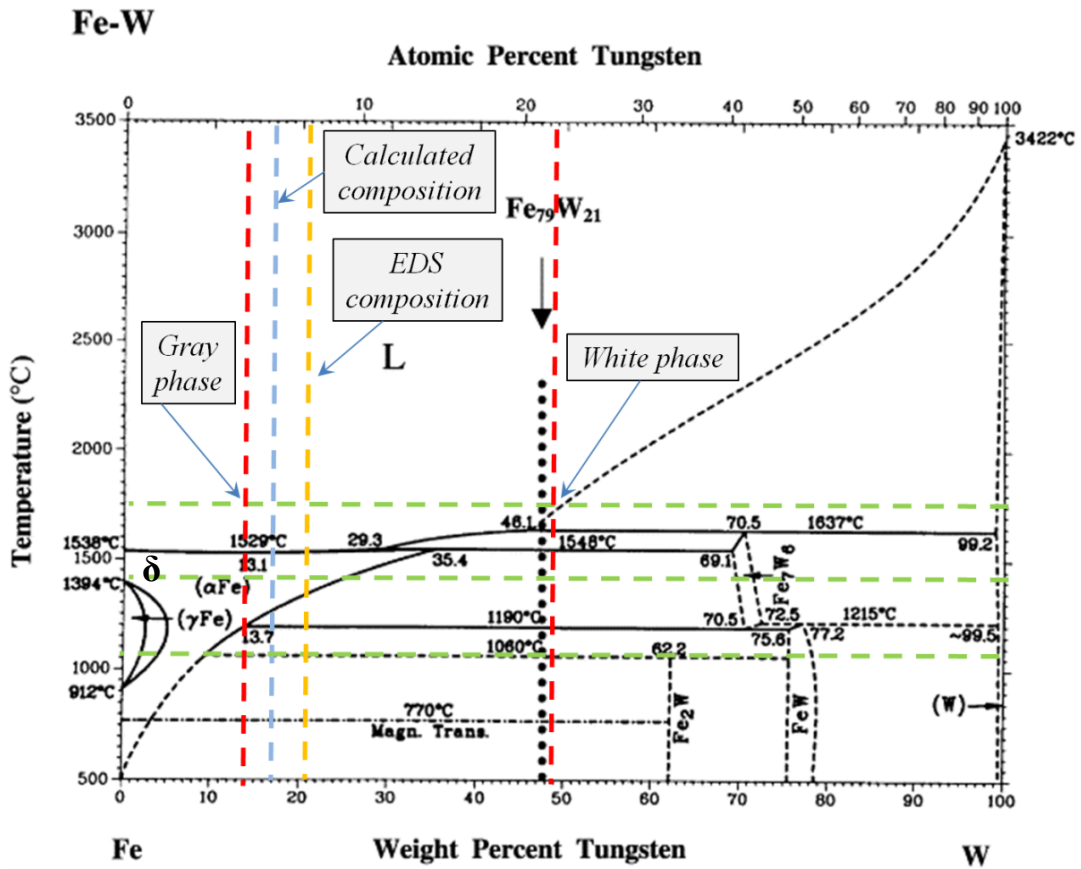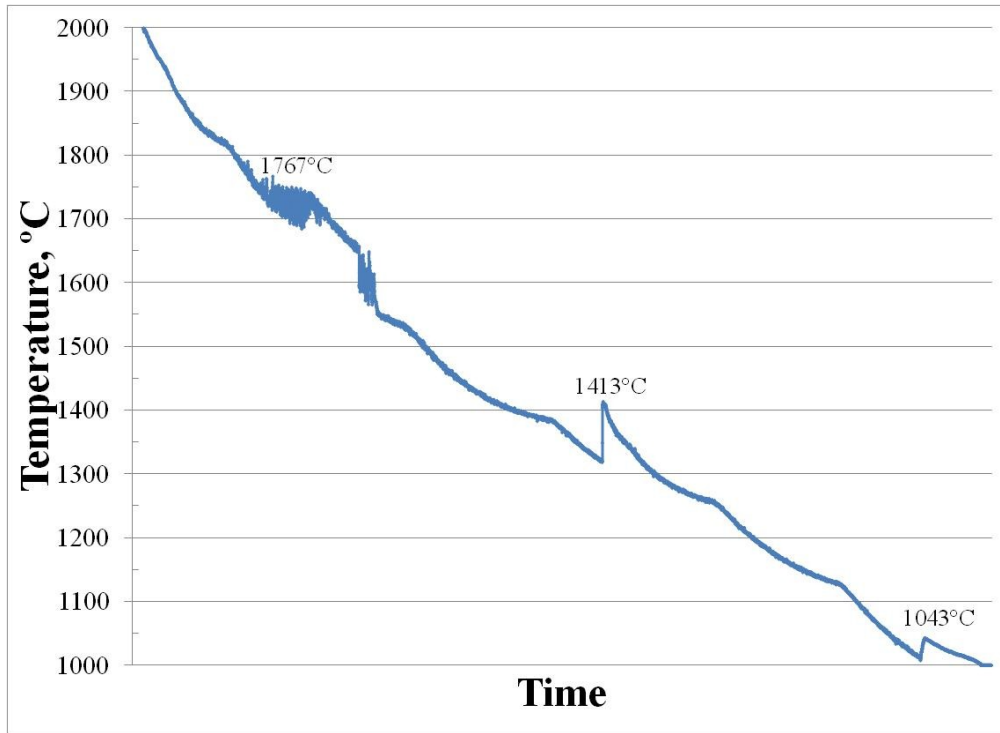Table 4.3. Reacting components mass and weight percent in each experiment.

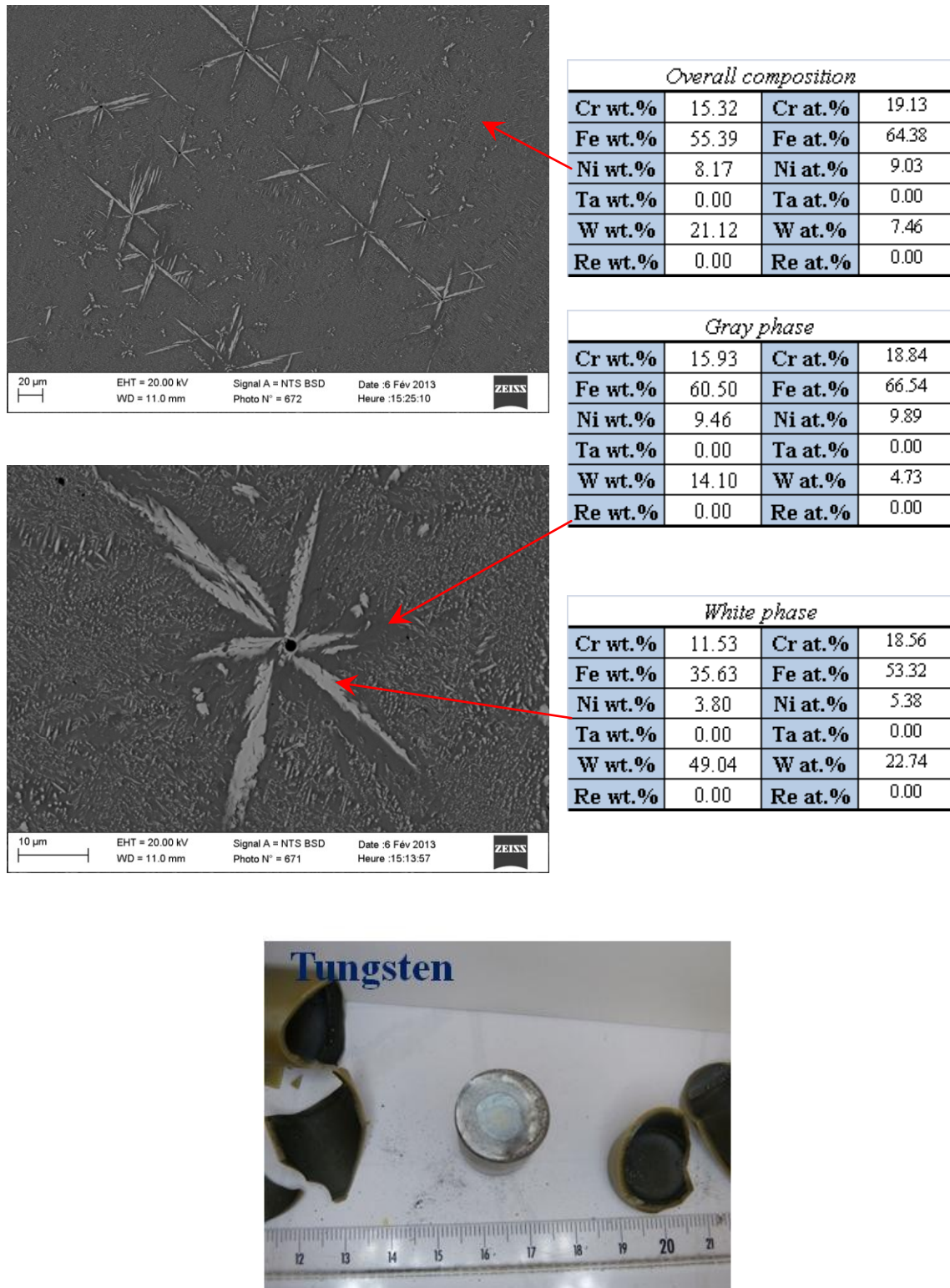Figure 4.16. Tungsten – Test 10 (Temp. 2000ºC) – Solidification curve and phase diagram.

Overall composition			
Cr wt.%	15.32	Cr at.%	19.13
Fe wt.%	55.39	Fe at.%	64.38
Ni wt.%	8.17	Ni at.%	9.03
Ta wt.%	0.00	Ta at.%	0.00
W wt.%	21.12	W at.%	7.46
Re wt.%	0.00	Re at.%	0.00

Gray phase			
Cr wt.%	15.93	Cr at.%	18.84
Fe wt.%	60.50	Fe at.%	66.54
Ni wt.%	9.46	Ni at.%	9.89
Ta wt.%	0.00	Ta at.%	0.00
W wt.%	14.10	W at.%	4.73
Re wt.%	0.00	Re at.%	0.00

White phase			
Cr wt.%	11.53	Cr at.%	18.56
Fe wt.%	35.63	Fe at.%	53.32
Ni wt.%	3.80	Ni at.%	5.38
Ta wt.%	0.00	Ta at.%	0.00
W wt.%	49.04	W at.%	22.74
Re wt.%	0.00	Re at.%	0.00

Figure 4.17. Tungsten – Test 10 (Temp. 2000ºC) – SEM/EDS Results and post-test ingot.

4.5.1 Tungsten - Test 10 (Temp. 2000ºC) – Analysis and Discussion

The analysis of the tungsten corrosion experiment, not only serves as the basis for explanation of ulterior experiments, but also elucidates the metallurgical explanation behind the tungsten sheath failure in the VULCANO MCCI tests (metallic/oxide corium). The Fe-W diagram (Figure 4.6) was chosen since iron is the main element in stainless steel and tungsten is the sheath element, hence the element of interest. Even though, the system is composed of more than four elements, the utilization of a binary phase diagram is valid if we assume one or more elements are acting as substitutional atoms. For example, in the analysis we have made the assumption that chromium and nickel are behaving as iron substitutional elements, hence they will be counted as iron atoms to reduce the system to a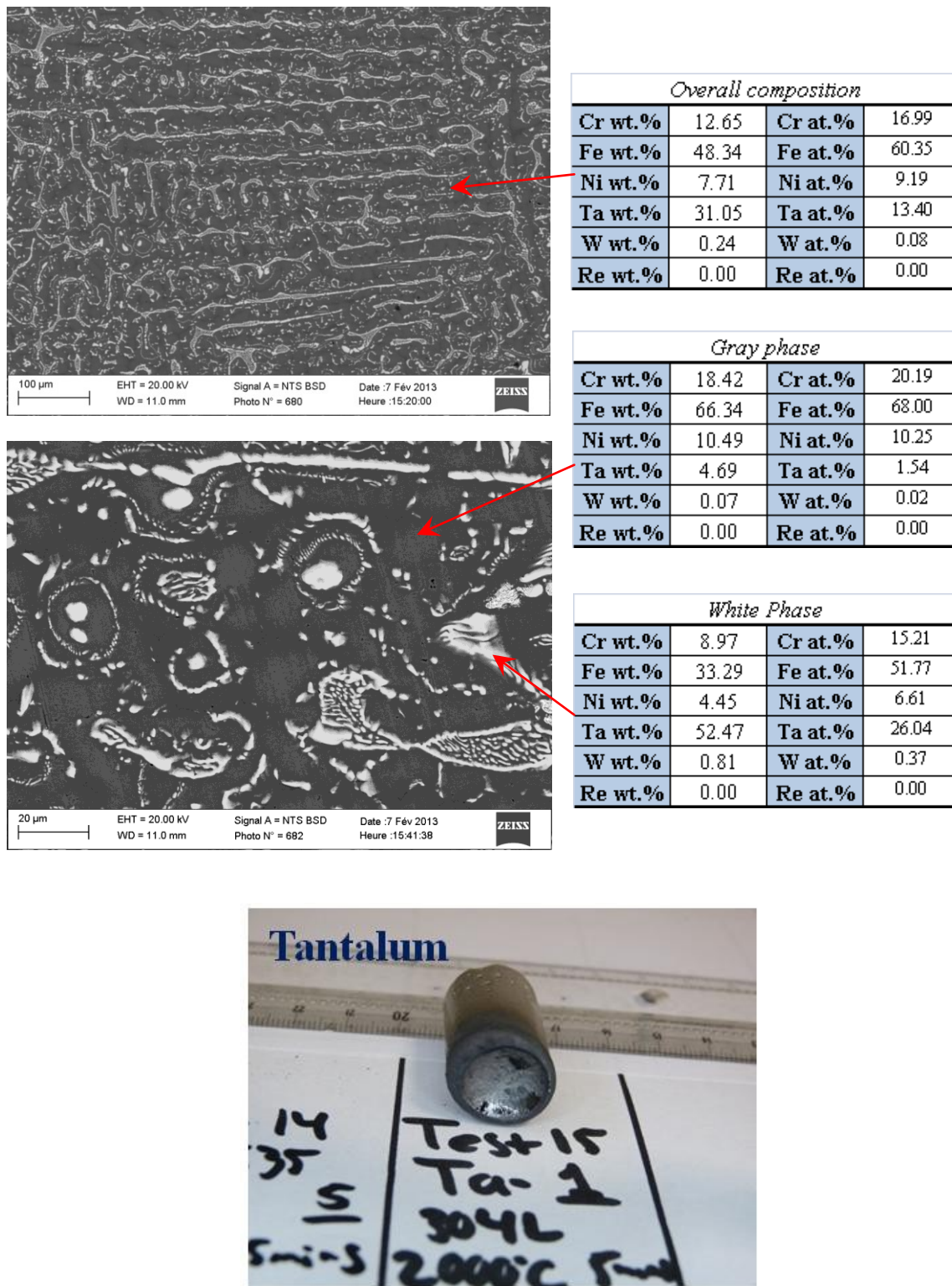 binary degree. The Fe-W diagram includes colored lines which pinpoint important information, as calculated weight percent of each metallic element in the crucible (blue), along with the macro EDS chemical composition (yellow), plus the recalescence peak temperatures or phase transformation (green), and finally the EDS elemental analysis of each found in the microstructure (red).

First, we need to consider the fact that the non-equilibrium cooling will result in a solidification behavior that could vary from the expected ideal (phase diagram) transformation, nonetheless the thermodynamic analysis through the use of the phase diagram can be a great aid in order to explain the non-equilibrium phase transformation observed from the liquid state to complete solidification. Now, by looking at the Fe-W phase diagram we will focus on a point intersected by the cooling curve's first fluctuation at 1767ºC and the white phase composition. This point approximately corresponds to the lowest L+ W_{solid} equilibrium temperature, and can be due to the formation of the tungsten-rich white phase, or big star-like morphology. Afterwards, the remaining liquid solidification is observed as a second peak at 1413ºC, which is within the solidification range of 304L SS (1400ºC-1450ºC), but this point probably corresponds to the formation of the high temperature δ-(Fe,Cr,Ni) gray phase, instead of the austenitic phase because the tungsten addition favors the formation of BCC δ-Fe . The fact that it is seen at a lower

temperature than the minimum at 1529ºC shown in the diagram, can be due to the significant presence of chromium and nickel, which can depress the equilibrium point, specially nickel (T_m: 1455ºC) which has a lower melting point than iron (T_m: 1535ºC). Finally, at relatively low temperature, a third recalescence peak is observed at 1043ºC, which seems to correspond to the solid state transformation of the tungsten-rich white phase into some form of $(Fe,Cr,Ni)_3W$ intermetallic. In the microstructure, it can be identified as the smaller platelet-like white phase. Due to fast cooling, the reaction might not have come to completion, which explains the presence of the bigger star-like phase surrounded by the evenly dispersed platelet phase.

In conclusion, the reason behind the low corrosion resistance of tungsten to molten 304L SS can be due to effective wetting and fast dissolution of tungsten by the liquid steel, followed by the incorporation of the refractory metal atoms into the stainless steel matrix. The speed of dissolution is quite high and this will be proved in a subsequent experiment in which tungsten rod was immersed into molten stainless steel at 2000ºC. After 5 minutes the sample is lifted and the immersed part of the W-bar has completely disappeared. Hence, a tungsten sample will not resist dissolution by 304L stainless steel at temperatures above the solubility limit of iron in solid tungsten at approximately 1767ºC for 304L SS.
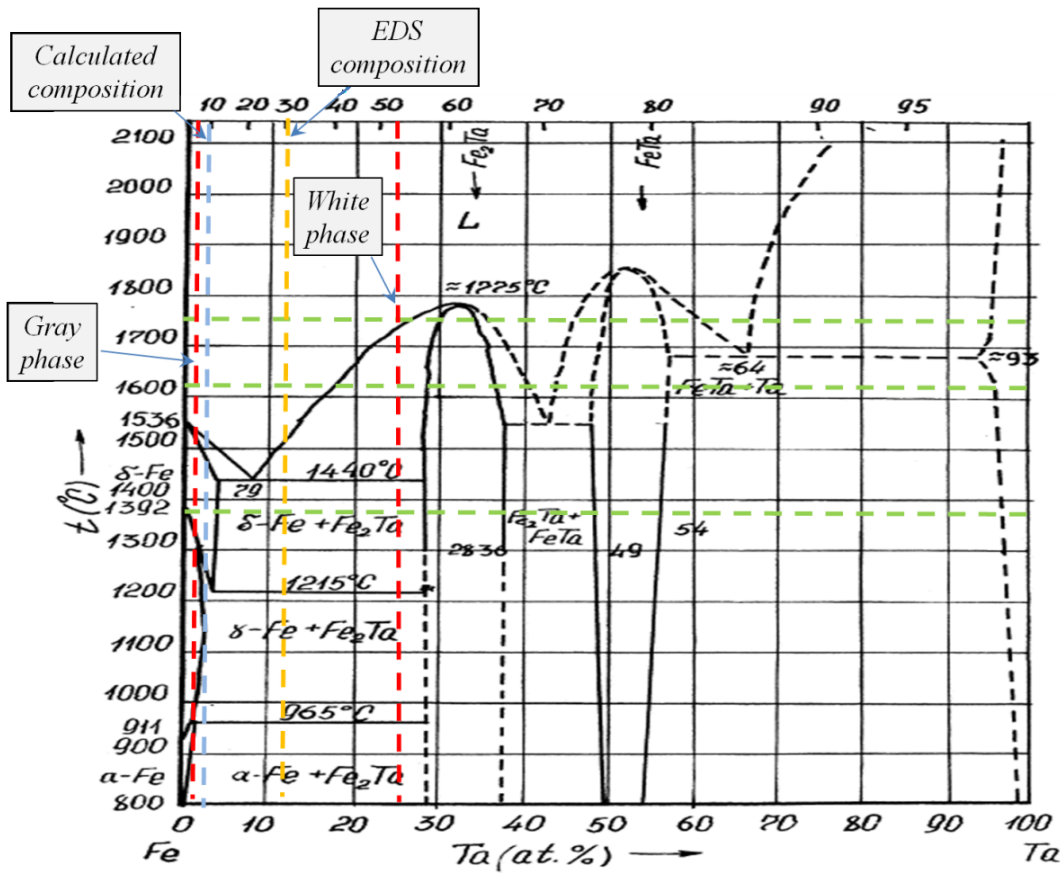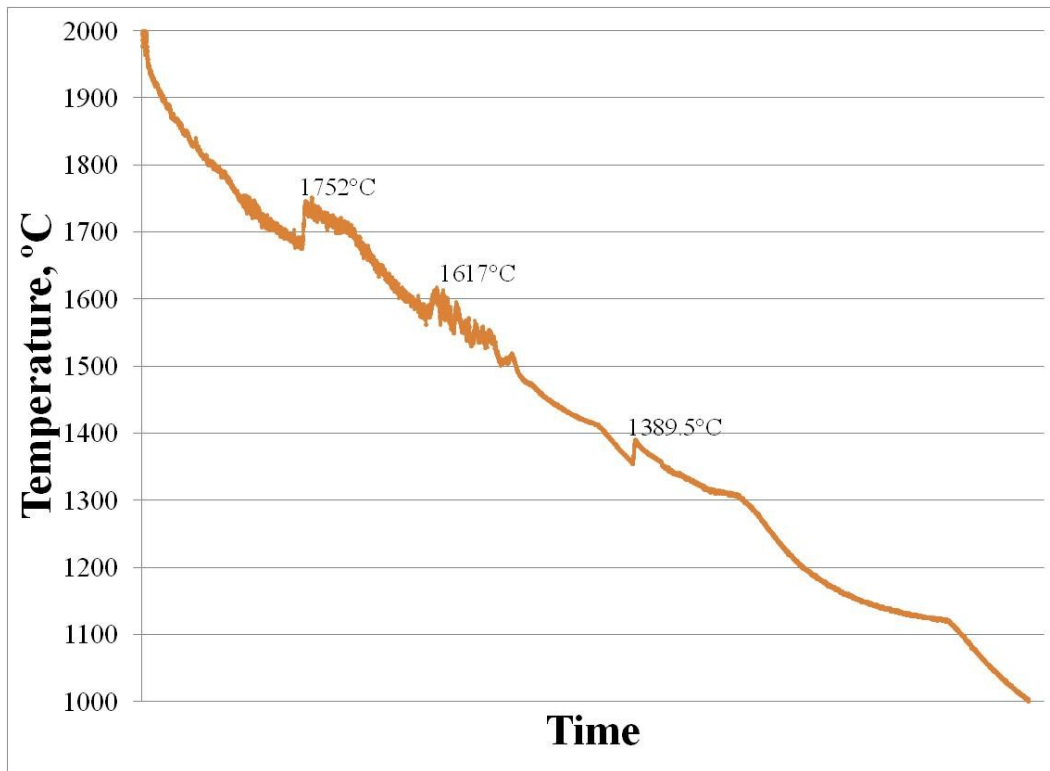
Figure 4.18. Tantalum - Test 15 (Temp. 2000ºC) – Solidification curve and phase diagram.

Overall composition			
Cr wt.%	12.65	Cr at.%	16.99
Fe wt.%	48.34	Fe at.%	60.35
Ni wt.%	7.71	Ni at.%	9.19
Ta wt.%	31.05	Ta at.%	13.40
W wt.%	0.24	W at.%	0.08
Re wt.%	0.00	Re at.%	0.00

Gray phase			
Cr wt.%	18.42	Cr at.%	20.19
Fe wt.%	66.34	Fe at.%	68.00
Ni wt.%	10.49	Ni at.%	10.25
Ta wt.%	4.69	Ta at.%	1.54
W wt.%	0.07	W at.%	0.02
Re wt.%	0.00	Re at.%	0.00

White Phase			
Cr wt.%	8.97	Cr at.%	15.21
Fe wt.%	33.29	Fe at.%	51.77
Ni wt.%	4.45	Ni at.%	6.61
Ta wt.%	52.47	Ta at.%	26.04
W wt.%	0.81	W at.%	0.37
Re wt.%	0.00	Re at.%	0.00

Figure 4.19. Tantalum - Test 15 (Temp. 2000ºC) – SEM/EDS Results and post-test ingot.

4.5.2 Tantalum - Test 15 (Temp. 2000ºC) – Analysis and Discussion

In order to analyze the corrosion behavior of tantalum in 304L SS we will use the Fe-Ta binary phase diagram as an aid, making the same assumptions as previously made for tungsten behavior. In Figure 4.18 the phase diagram of Fe-Ta has been highlighted with important temperature and compositions compiled from the corrosion test cooling curve and ingot EDS analysis. Analyzing the Fe-Ta diagram we can see a cross-section corresponding to the first peak of the cooling curve (1752ºC) and the white phase composition. This transformation can be due to the solidification of part of the liquid into primary intermetallic phase $(Fe,Cr,Ni)_3Ta$. Afterwards, there is a recalescence observed around 1600ºC which corresponds to the transformation of some liquid into primary δ-(Fe,Cr,Ni) phase with a BCC lattice (gray phase). Finally, we observe a last recalescence at 1389.5ºC which corresponds to the eutectic transformation L→δ-(Fe,Cr,Ni)+(Fe,Cr,Ni)$_3$Ta and formation of the lamellar structure.

In conclusion, the low corrosion resistance of tantalum can be due to the presence of multiple eutectic points and the aggressive mixing between 304L SS and tantalum. For this reason, tantalum cannot be utilized as protective TC sheath in contact with 304L SS above the lowest observed eutectic point at 1389.5ºC. The reason being that at temperatures above the eutectic, tantalum in contact with an iron-rich alloy, especially under liquid metal wetting, will combine until it reaches the low Gibbs free energy eutectic point composition and melts Ta. Nonetheless, the corrosion resistance of tantalum could be improved by pre-oxidizing in a controlled low-oxygen environment until it grows a sufficiently thick and well adhered protective Ta_2O_5 which would act as a diffusion barrier to liquid metal atoms inward migration into the tantalum substrate.
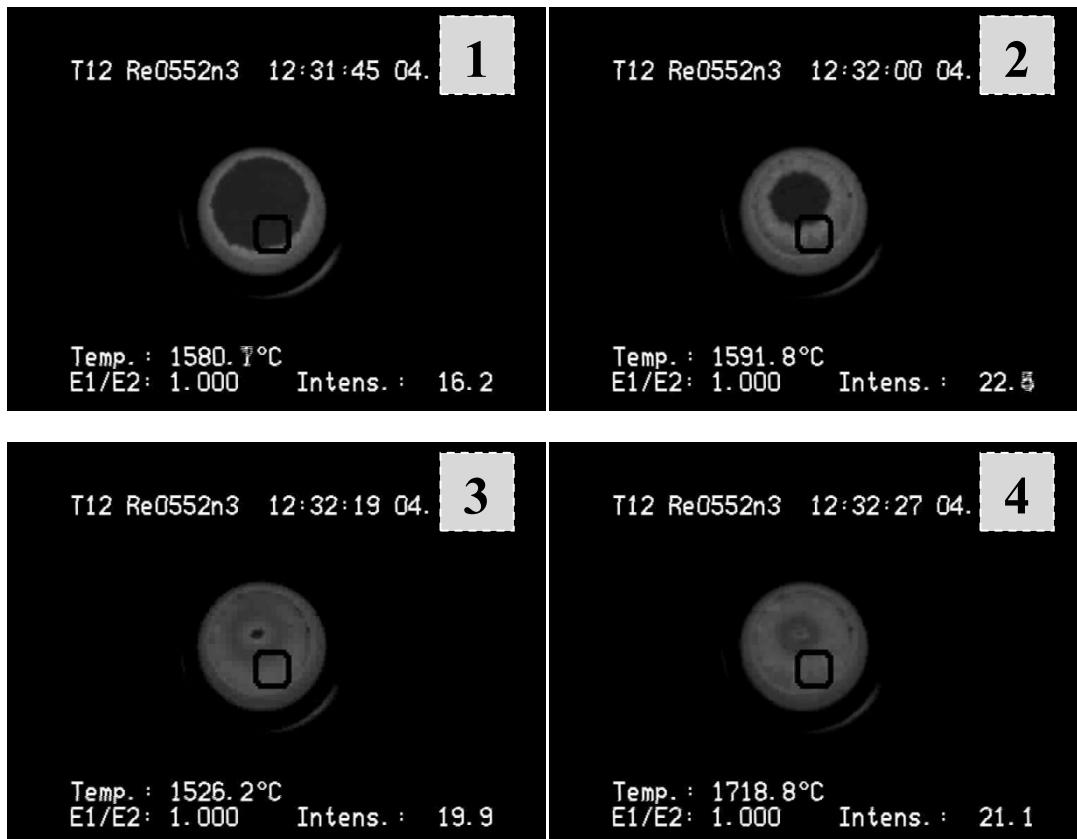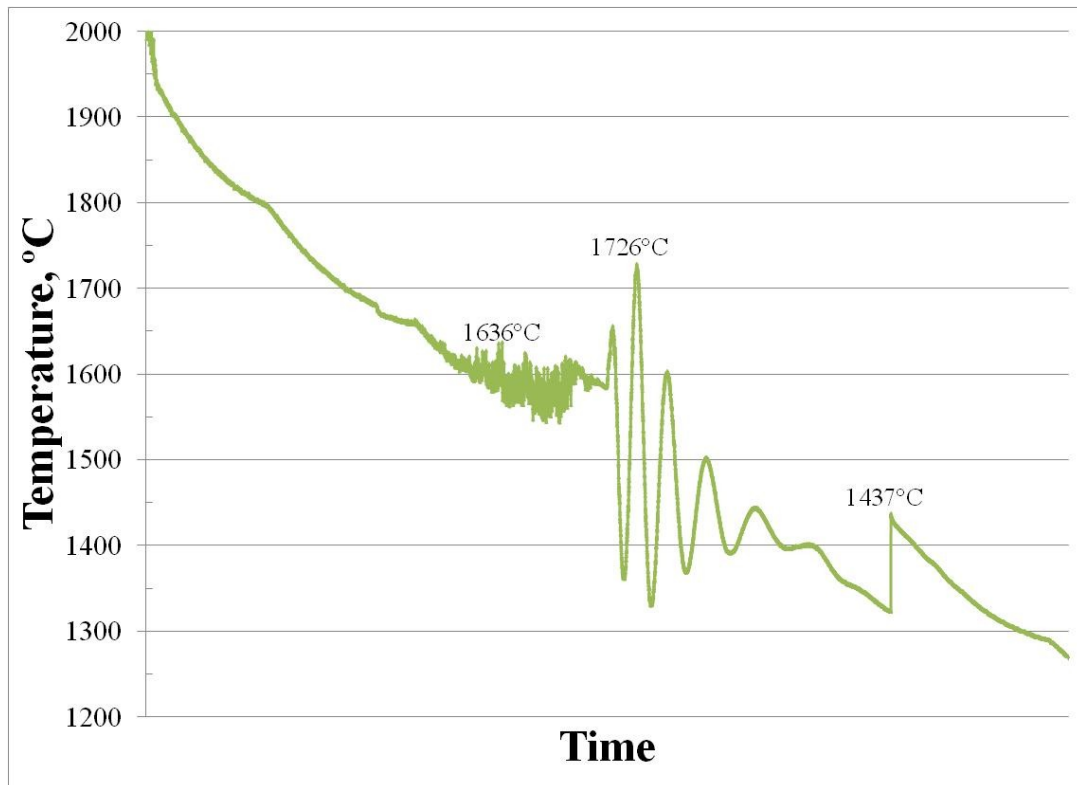
Figure 4.20. Re0552 - Test 12 (Temp. 2000ºC) – Solidification curve and test photos.

Overall composition			
Cr wt.%	19.18	Cr at.%	20.41
Fe wt.%	70.28	Fe at.%	69.65
Ni wt.%	10.54	Ni at.%	9.93
Ta wt.%	0.00	Ta at.%	0.00
W wt.%	0.00	W at.%	0.00
Re wt.%	0.00	Re at.%	0.00

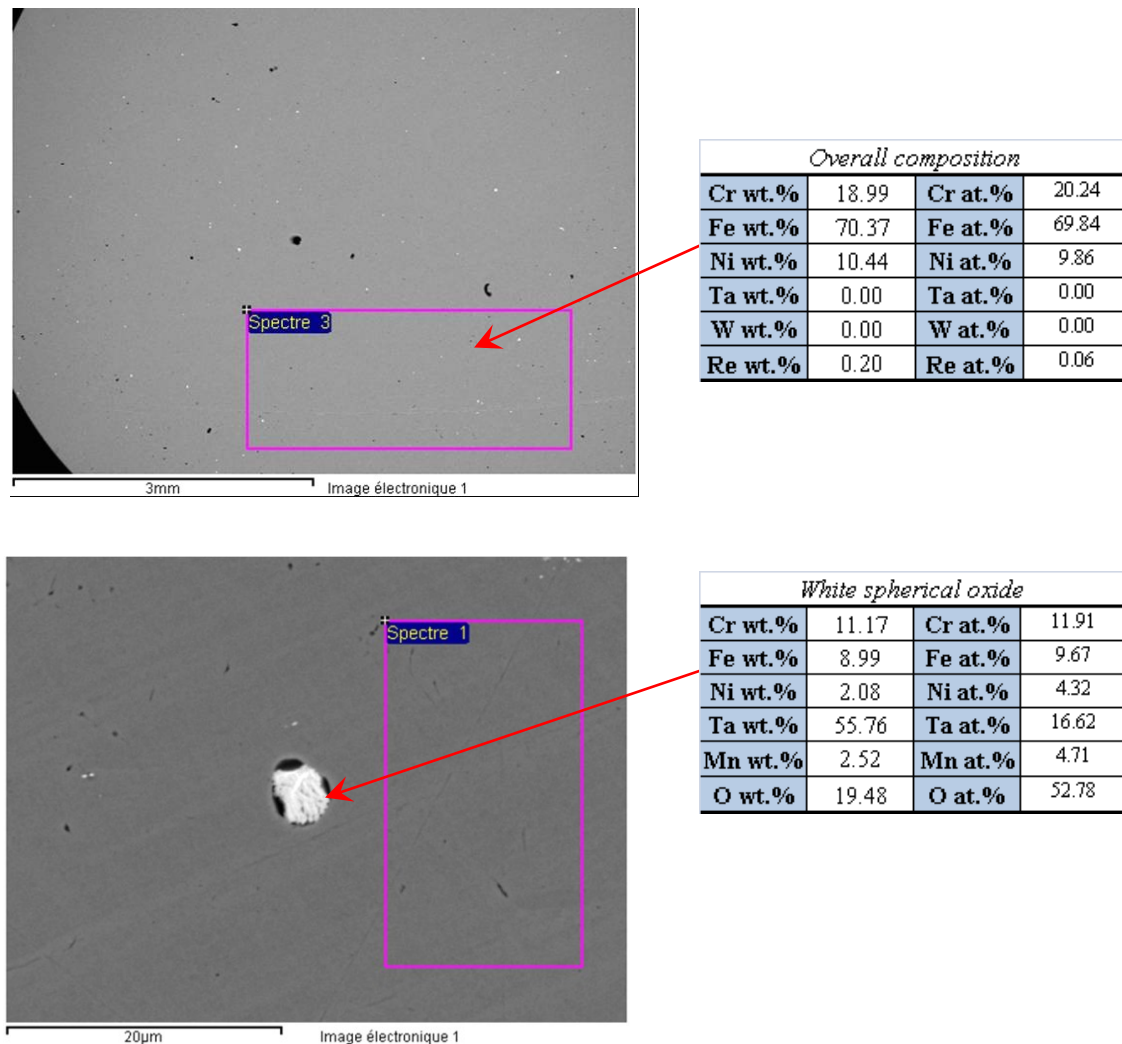| White spherical oxide			
Cr wt.%	9.98	Cr at.%	10.91
Fe wt.%	3.07	Fe at.%	5.59
Ni wt.%	0.00	Ni at.%	0.00
Ta wt.%	59.33	Ta at.%	17.02
Mn wt.%	3.29	Mn at.%	5.77
O wt.%	24.33	O at.%	60.74
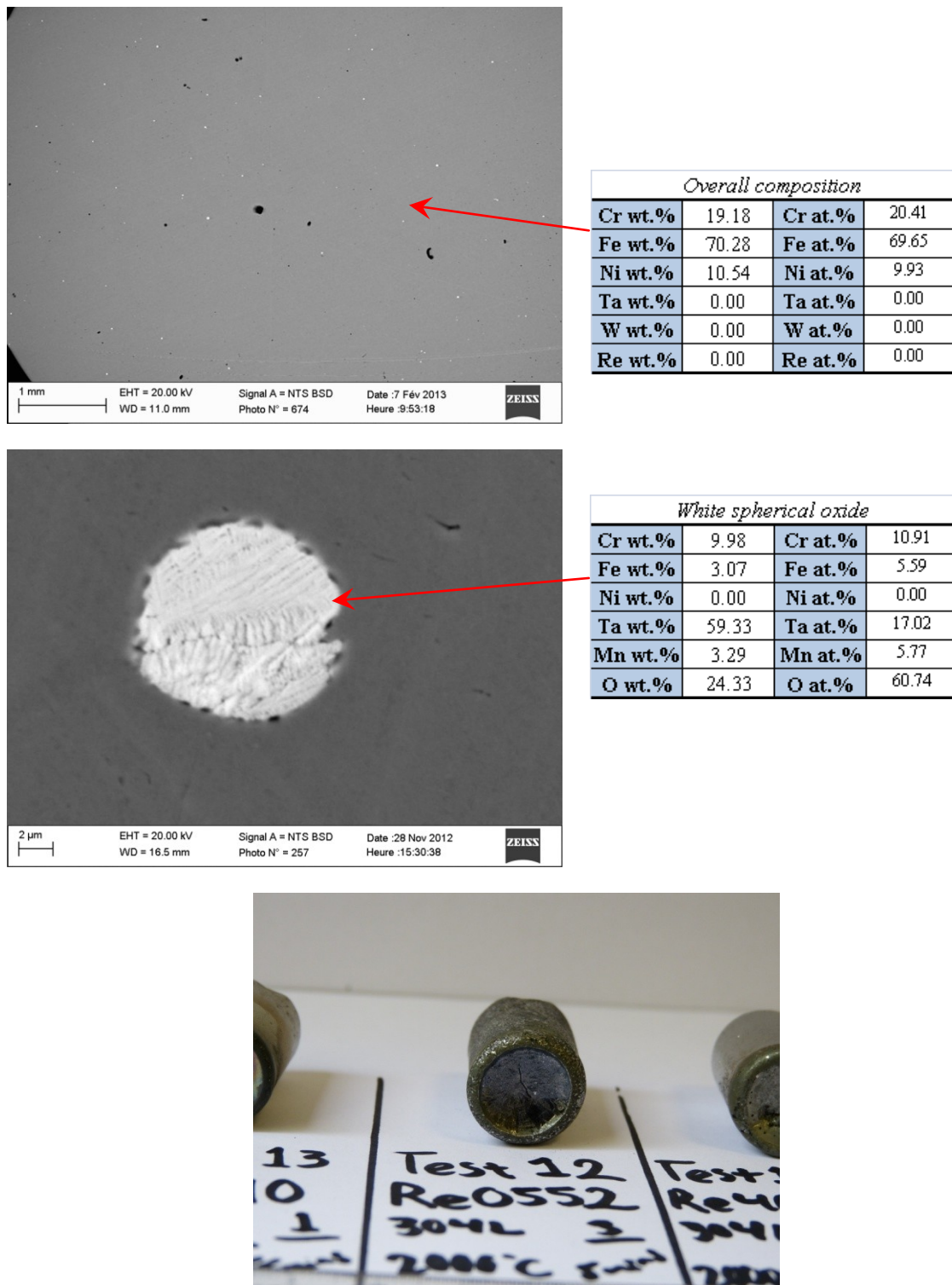
Figure 4.21. Re0552 - Test 12 (Temp. 2000ºC) – SEM/EDS Results and post-test ingot.

4.5.3 Re0552 - Test 12 (Temp. 2000ºC) – Analysis and Discussion

In this experiment the calculated Re-W-Ta content in the melt is so low (3wt.%) that at least in the bottom part of the ingot none of this elements were detected via EDS. Furthermore, according to the Fe-W, Fe-Ta and Fe-Re phase diagrams, the content falls below the solubility limit of each refractory metal in iron, respectively. Therefore, a slightly different approach is utilized for the interpretation of the results. Furthermore, as can be observed the Re0552 corrosion experiment shows a particular solidification curve, particularly in the middle were an oscillation similar to a damped sinusoidal curve is encountered. But let us start from the beginning, upon cooling from 2000ºC, this curve shows a small fluctuation around 1600ºC, with similar behavior as the one observed for the virtually pure tantalum sample, within the same temperature ballpark and with very close composition, therefore it has been due to the formation of the δ-(Fe,Cr,Ni) phase. Afterwards, there is this region in which the temperature-time curve starts fluctuating up and down, as the sinusoidal part of the curve varies the peak amplitude. Going back to the pyrometer video recording of the melt surface (snapshots in figure 4.20), it has been observed that this temperature fluctuation correspond to the nucleation and growth of the solid phase from the crucible walls into the melt. Upon literature search, no information was found on a similar phenomena taking place during alloy solidification. The more plausible explanation to this could be an optical effect on the bichromatic pyrometer, due to the difference in emissivity between the liquid and growing solid phase, the impact of the coarsening of the solid grains and its relatively higher surface roughness than the smooth liquid surface. Furthermore, the curve shows a quite energetic ultimate recalescence peak at 1437ºC which falls within the 304L SS solidification range, and might correspond to part of the melt that might not have been contaminated with the heavy atoms from the refractory alloy. Finally, traces of a spherical white oxides with a chemical formula $(Ta,Cr,Fe,Mn,Ni)_2O_3$ were found in the microstructure, the oxide phase seem to have solidified first, based on its very round shape.
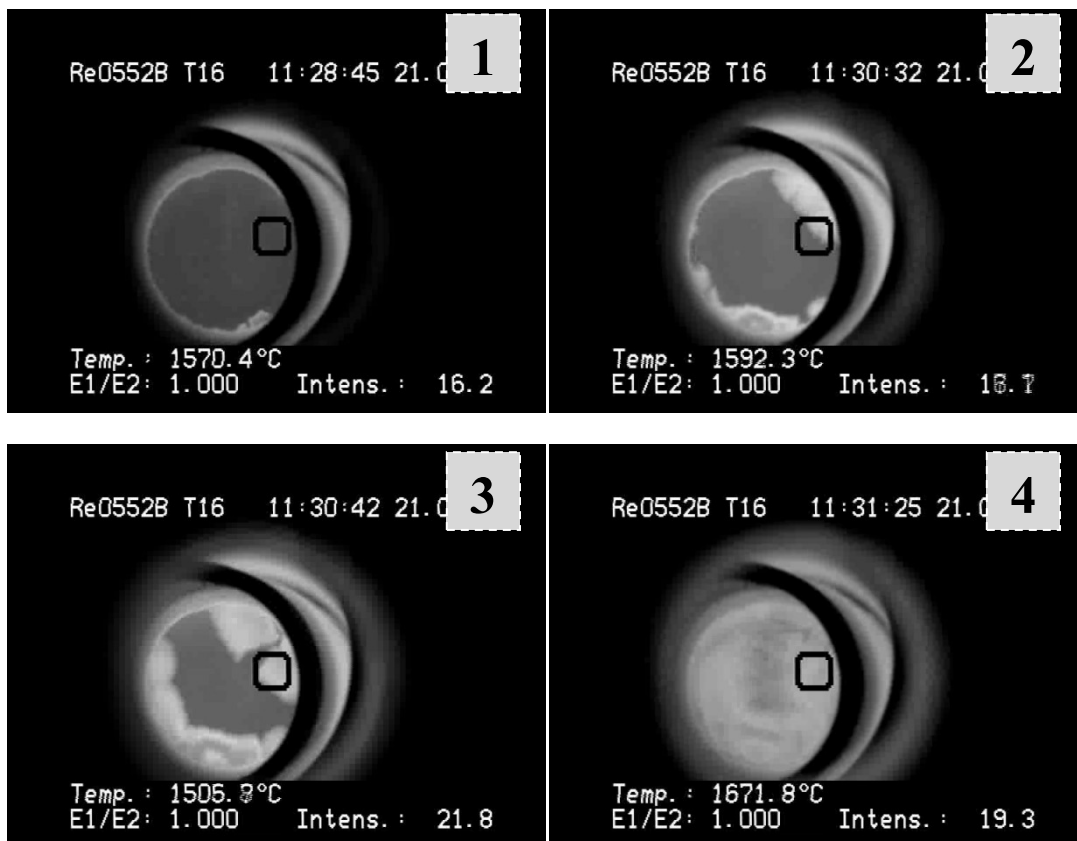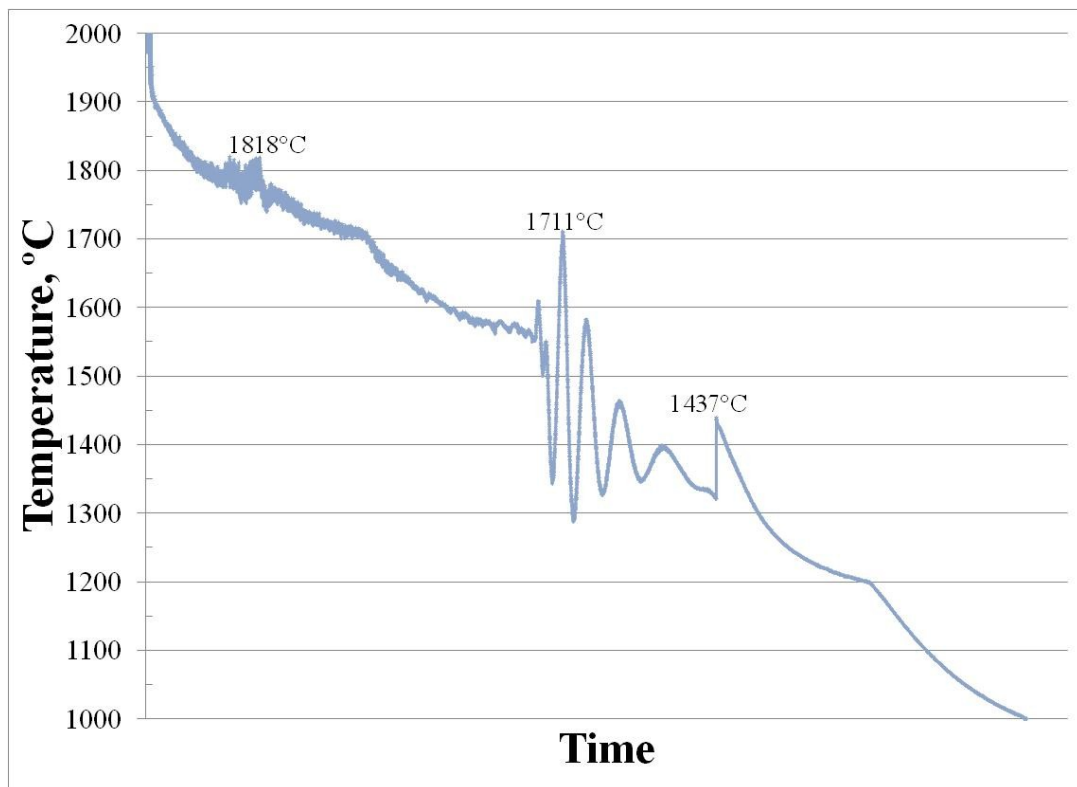
Figure 4.22. Re0552B - Test 16 (Temp. 2000ºC) – Solidification curve and test photos.

Overall composition			
Cr wt.%	19.44	Cr at.%	20.69
Fe wt.%	69.93	Fe at.%	69.30
Ni wt.%	10.62	Ni at.%	10.01
Ta wt.%	0.00	Ta at.%	0.00
W wt.%	0.00	W at.%	0.00
Re wt.%	0.00	Re at.%	0.00

Eutectic			
Cr wt.%	16.37	Cr at.%	20.82
Fe wt.%	51.66	Fe at.%	61.15
Ni wt.%	8.24	Ni at.%	9.29
Ta wt.%	23.72	Ta at.%	8.74
W wt.%	0.00	W at.%	0.00
Re wt.%	0.00	Re at.%	0.00

Eutectic white phase			
Cr wt.%	12.13	Cr at.%	18.99
Fe wt.%	35.13	Fe at.%	51.20
Ni wt.%	4.97	Ni at.%	6.94
Ta wt.%	47.77	Ta at.%	22.86
W wt.%	0.00	W at.%	0.00
Re wt.%	0.00	Re at.%	0.00
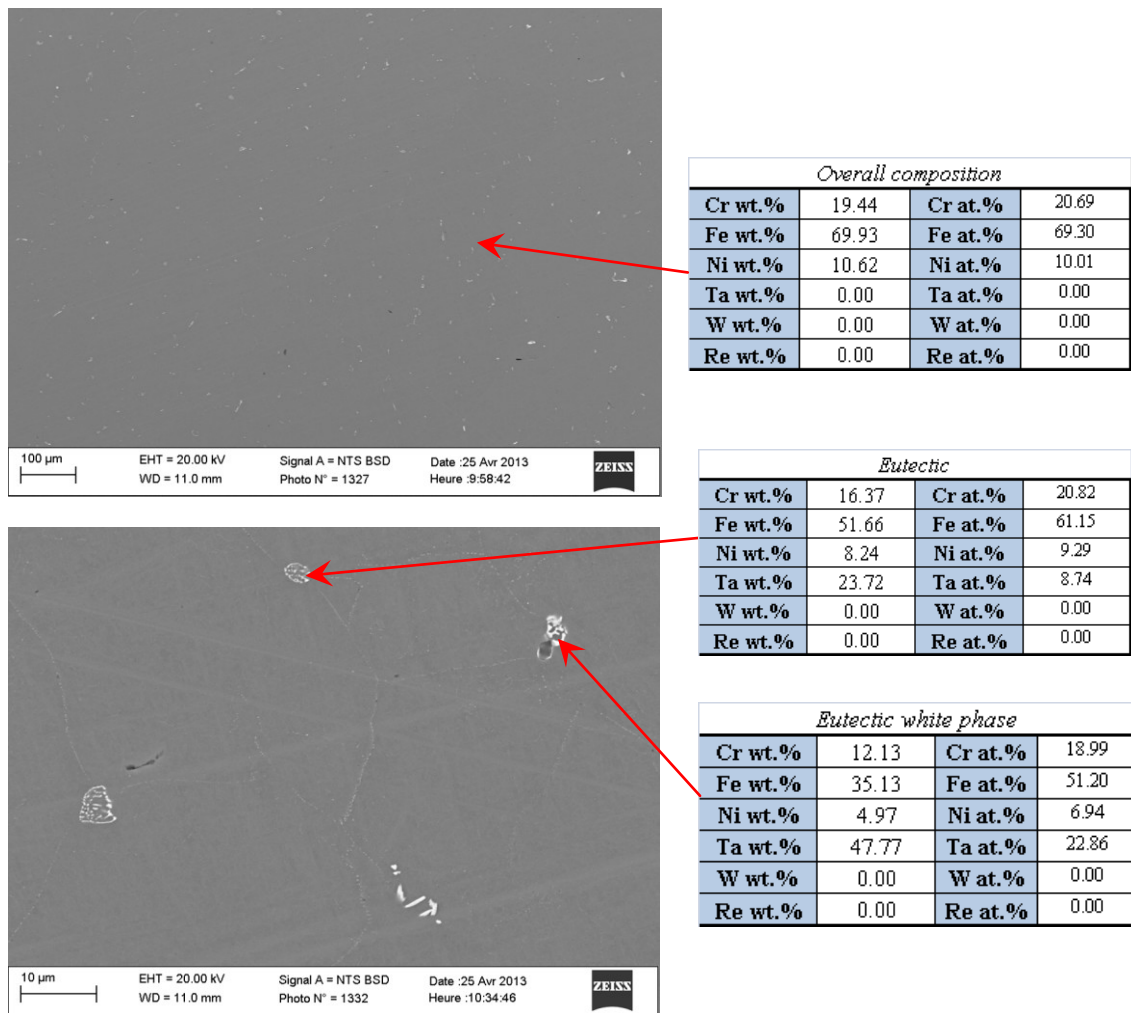
Figure 4.23. Re0552B - Test 16 (Temp. 2000ºC) – SEM/EDS Results and post-test ingot.

4.5.4 Re0552B - Test 16 (Temp. 2000ºC) – Analysis and Discussion

The Re0552B corrosion experiment has very similar behavior as the Re0552, as expected due to the similar alloy composition besides the boron addition to the mix. The sinusoidal behavior of the curve was again observed during this experiment, and the pertinent video snapshots have been included in Figure 4.22, where a similar solid front growth is observed as in the Re0552 test. Nonetheless, a peak at 1818ºC can be observed in the curve. It is hard to tell what phase might have solidified since it cannot be confirmed with the SEM/EDS analysis, but it is possible that one of the high temperature refractory metal borides (Figure 4.2) had crystallized. Unfortunately the use of another chemical analysis technique as wavelength-dispersive X-ray spectroscopy (WDS) is needed in order to detect the boron element. However, we did find the precipitation of the eutectic phase, δ-$(Fe,Cr,Ni)+(Fe,Cr,Ni)_3Ta$ at the grain boundary junctions and triple points. The composition of the tantalum-rich constituent of the eutectic (white phase) is very close to the intermetallic composition and the overall chemical analysis of the eutectic is within the Fe-Ta lowest temperature eutectic point. It is not certain if the last peak corresponds to the solidification of the basic 304L SS melt, and/or the eutectic, since their respective transformation temperatures are near. Nonetheless, it can be concluded that the addition of boron to the melt does have an impact on the stabilization of high temperature intemetallics even under such low proportions of foreign elements in the 304L matrix. Therefore, this infers that the addition of boron does improve the corrosion behavior of the alloy and it would be relevant to study the benefits of further increasing the boron proportion. Moreover, the addition of other elements as Si is also recommended in conjunction with boron, since they form silicon borides (or boron silicides), that form glassy compounds. These compounds are used as protective barriers to reduce oxidation, due to their compact structure. Also, since in their liquid state they have a viscous flow which heals any cracks formed in the oxidation barrier and impede the migration of oxygen to the substrate.
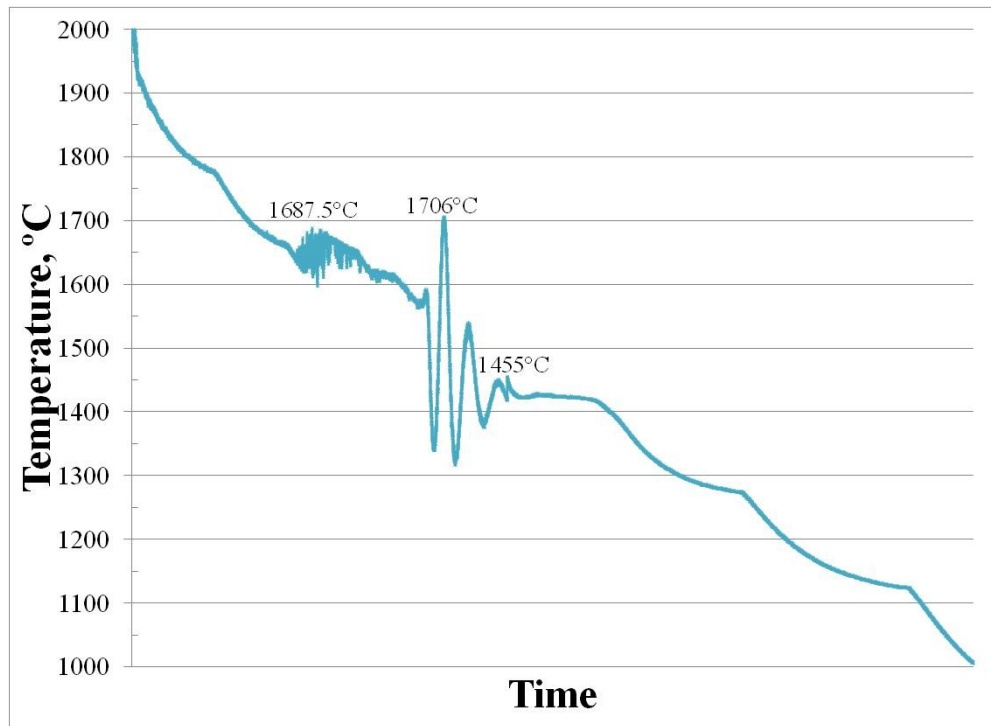
Figure 4.24. Re2535 - Test 14 (Temp. 2000ºC) – Solidification curve and post-test ingot.

Overall composition			
Cr wt.%	18.99	Cr at.%	20.24
Fe wt.%	70.37	Fe at.%	69.84
Ni wt.%	10.44	Ni at.%	9.86
Ta wt.%	0.00	Ta at.%	0.00
W wt.%	0.00	W at.%	0.00
Re wt.%	0.20	Re at.%	0.06

White spherical oxide			
Cr wt.%	11.17	Cr at.%	11.91
Fe wt.%	8.99	Fe at.%	9.67
Ni wt.%	2.08	Ni at.%	4.32
Ta wt.%	55.76	Ta at.%	16.62
Mn wt.%	2.52	Mn at.%	4.71
O wt.%	19.48	O at.%	52.78

Figure 4.25. Re2535 - Test 14 (Temp. 2000ºC) –SEM/EDS Results and phase identification.

4.5.5 Re2535 - Test 14 (Temp. 2000ºC) – Analysis and Discussion

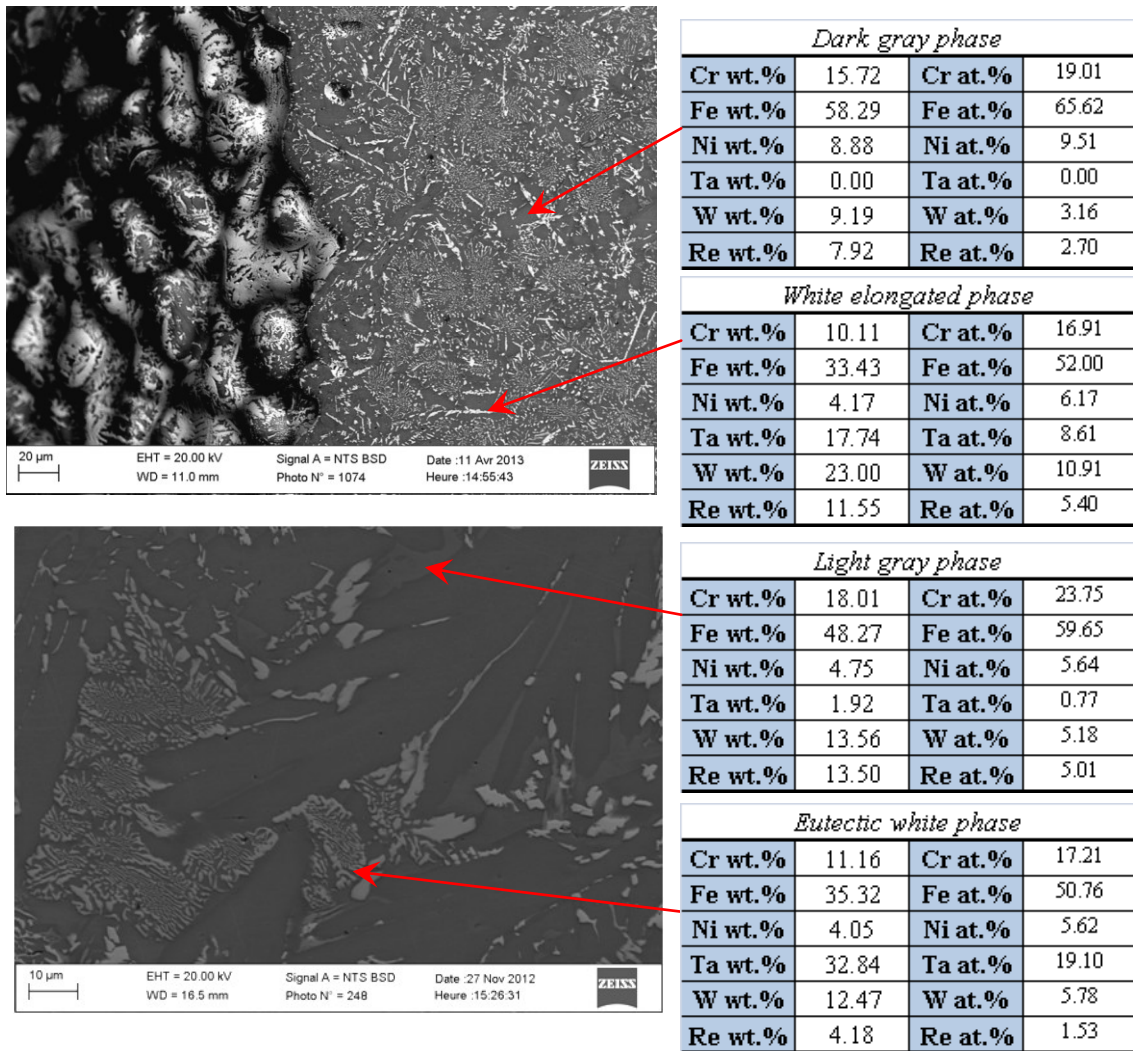The Re2535 solidification curve and EDS analysis is very similar to the one observed in the Re0552 behavior. The phase transformation is within the same temperature range and the overall composition of the monophase is the same besides the detection of some small proportion of rhenium. Additionally, the nucleation of a high temperature white spherical oxide $(Ta,Cr,Fe,Mn,Ni)_2O_3$ has also been encountered in the microstructure. This compound is of interest since it might hold the key to the production of an effective protective oxide layer.
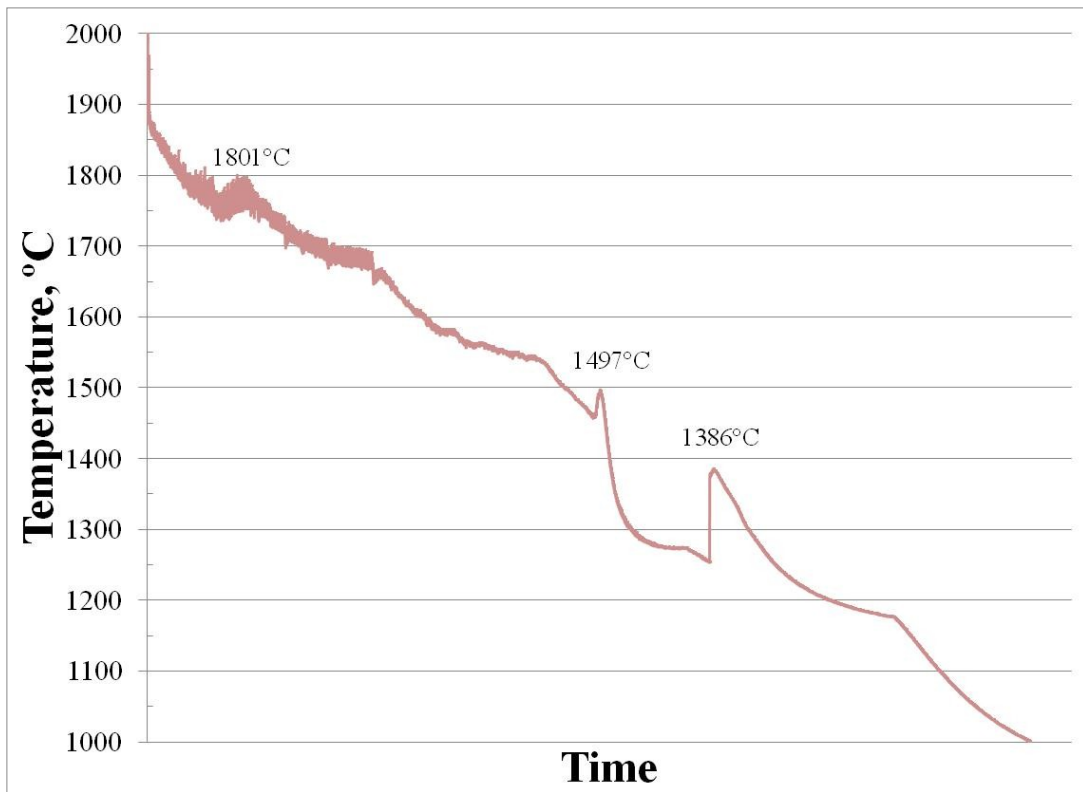
Figure 4.26. Re2535B - Test 17 (Temp. 2000ºC) – Solidification curve and post-test ingot.

Overall composition			
Cr wt.%	18.99	Cr at.%	20.21
Fe wt.%	70.37	Fe at.%	69.78
Ni wt.%	10.44	Ni at.%	10.01
Ta wt.%	0.00	Ta at.%	0.00
W wt.%	0.00	W at.%	0.00
Re wt.%	0.20	Re at.%	0.00

White spherical oxide			
Cr wt.%	10.90	Cr at.%	10.63
Fe wt.%	5.91	Fe at.%	6.30
Ni wt.%	2.75	Ni at.%	3.84
Ta wt.%	54.50	Ta at.%	15.91
Mn wt.%	2.96	Mn at.%	4.03
O wt.%	23.00	O at.%	59.30
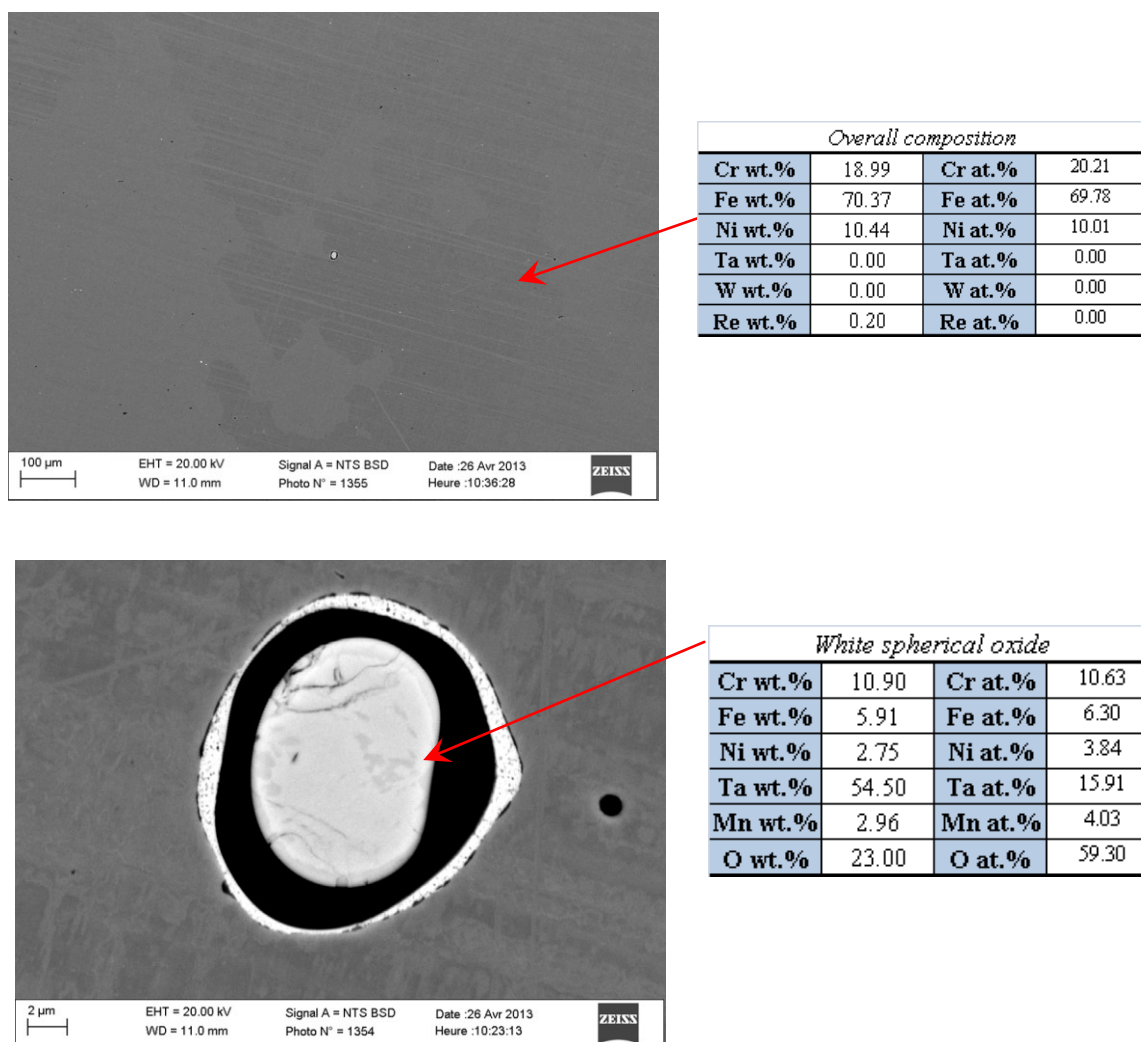
Figure 4.27. Re2535B - Test 17 (Temp. 2000ºC) – SEM/EDS Results and phase identification.

4.5.6 Re2535B - Test 17 (Temp. 2000ºC) – Analysis and Discussion

The Re2535B ingot and solidification curve shows a recalescence peak at 1801ºC, which resembles the one observed in the boron containing alloy Re0552B test. Afterwards, we observe a peak at 1497ºC which corresponds to the delta-(Fe,Cr,Ni) phase. And finally the δ→γ solid state transformation takes place at 1386 ºC, and this relates to the transformation steps expected for very dilute solutions of Re, W, Ta dissolved in an Fe-rich matrix. The spherical oxide seems to have formed upon reaction with oxygen dissolved in the met.
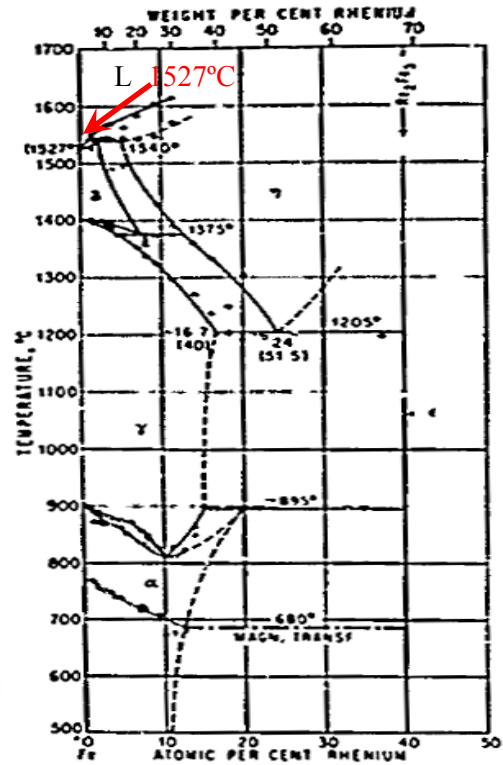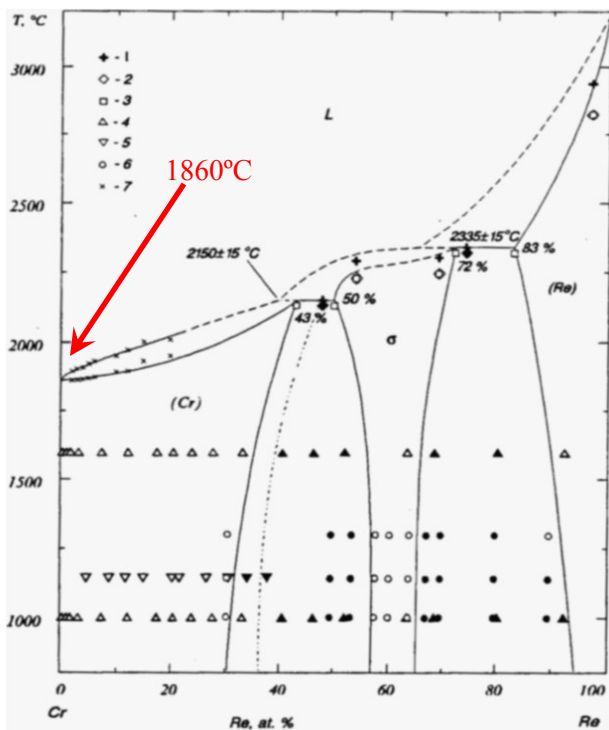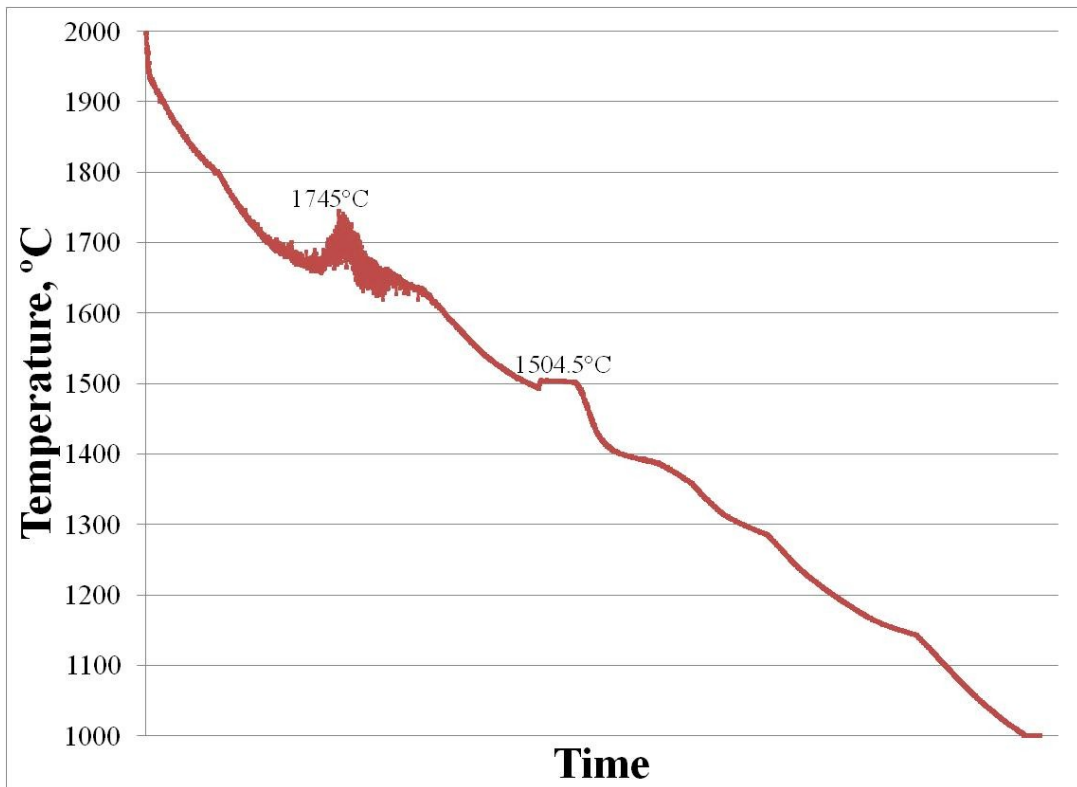
Figure 4.28. Re4020 - Test 11 (Temp. 2000ºC) – Solidification curve and phase diagrams.

Overall composition			
Cr wt.%	18.99	Cr at.%	21.40
Fe wt.%	70.37	Fe at.%	68.50
Ni wt.%	10.44	Ni at.%	8.89
Ta wt.%	0.00	Ta at.%	0.00
W wt.%	0.00	W at.%	1.06
Re wt.%	0.20	Re at.%	0.15

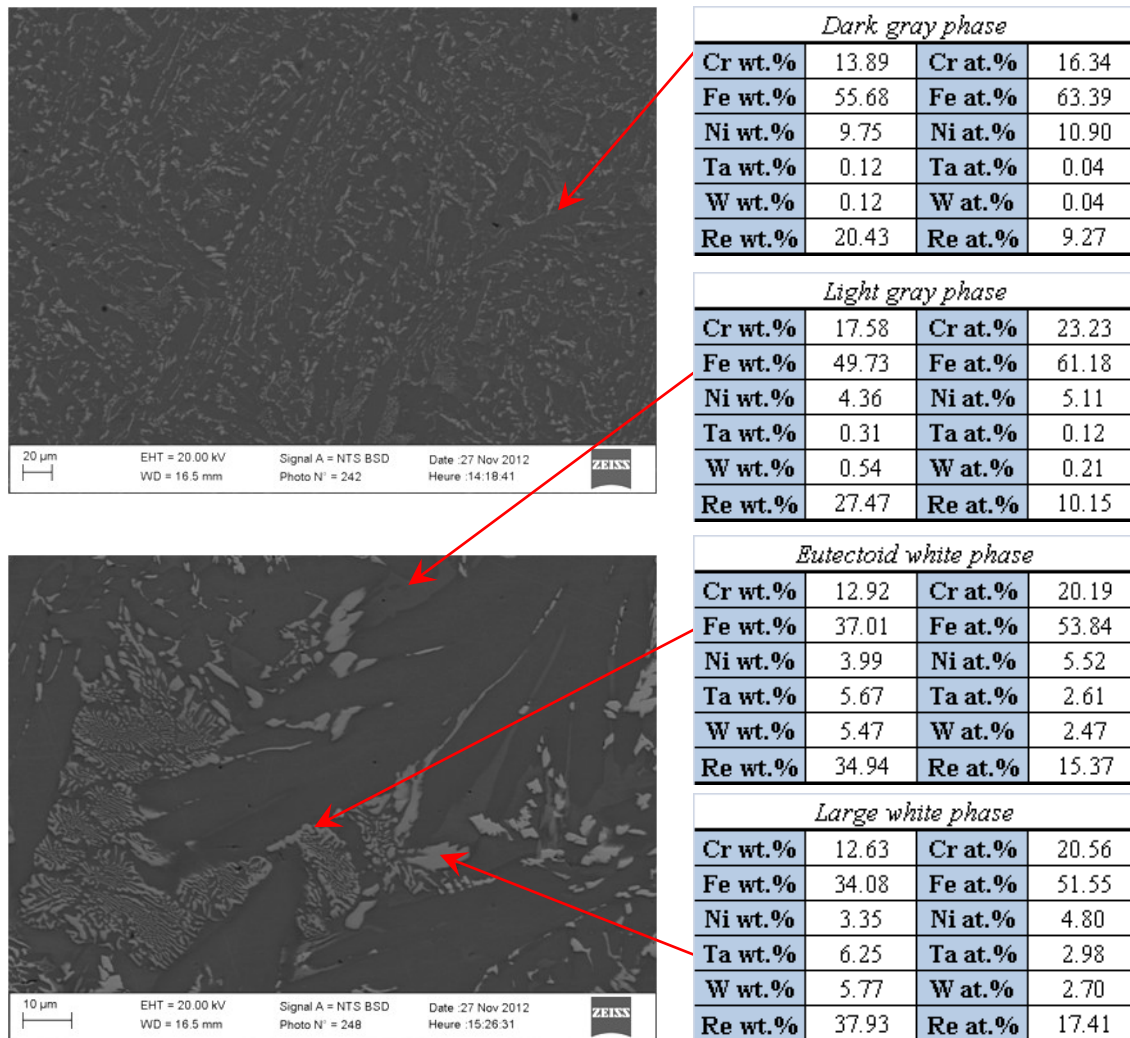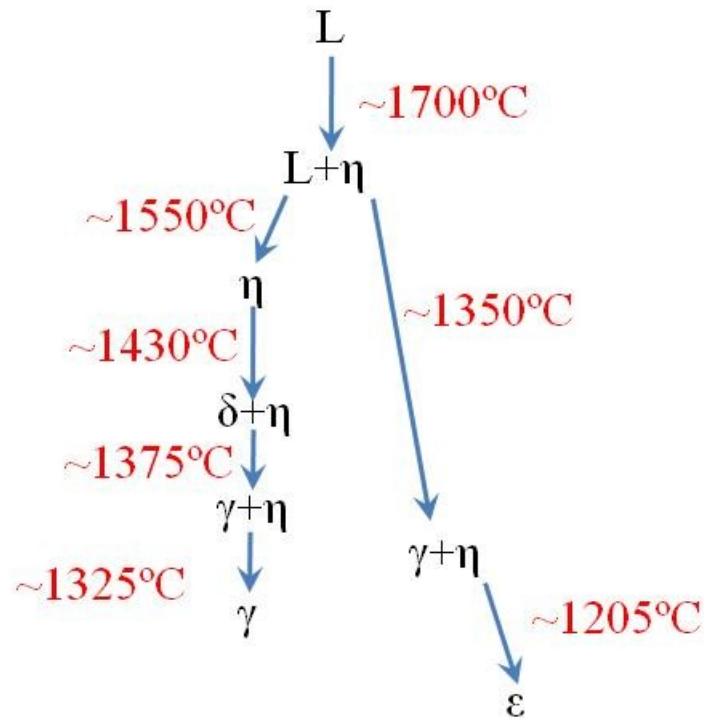| White spherical oxide			
Cr wt.%	10.14	Cr at.%	11.04
Fe wt.%	3.78	Fe at.%	6.46
Ni wt.%	0.00	Ni at.%	0.00
Ta wt.%	56.34	Ta at.%	16.16
Mn wt.%	4.18	Mn at.%	6.75
O wt.%	25.56	O at.%	59.58
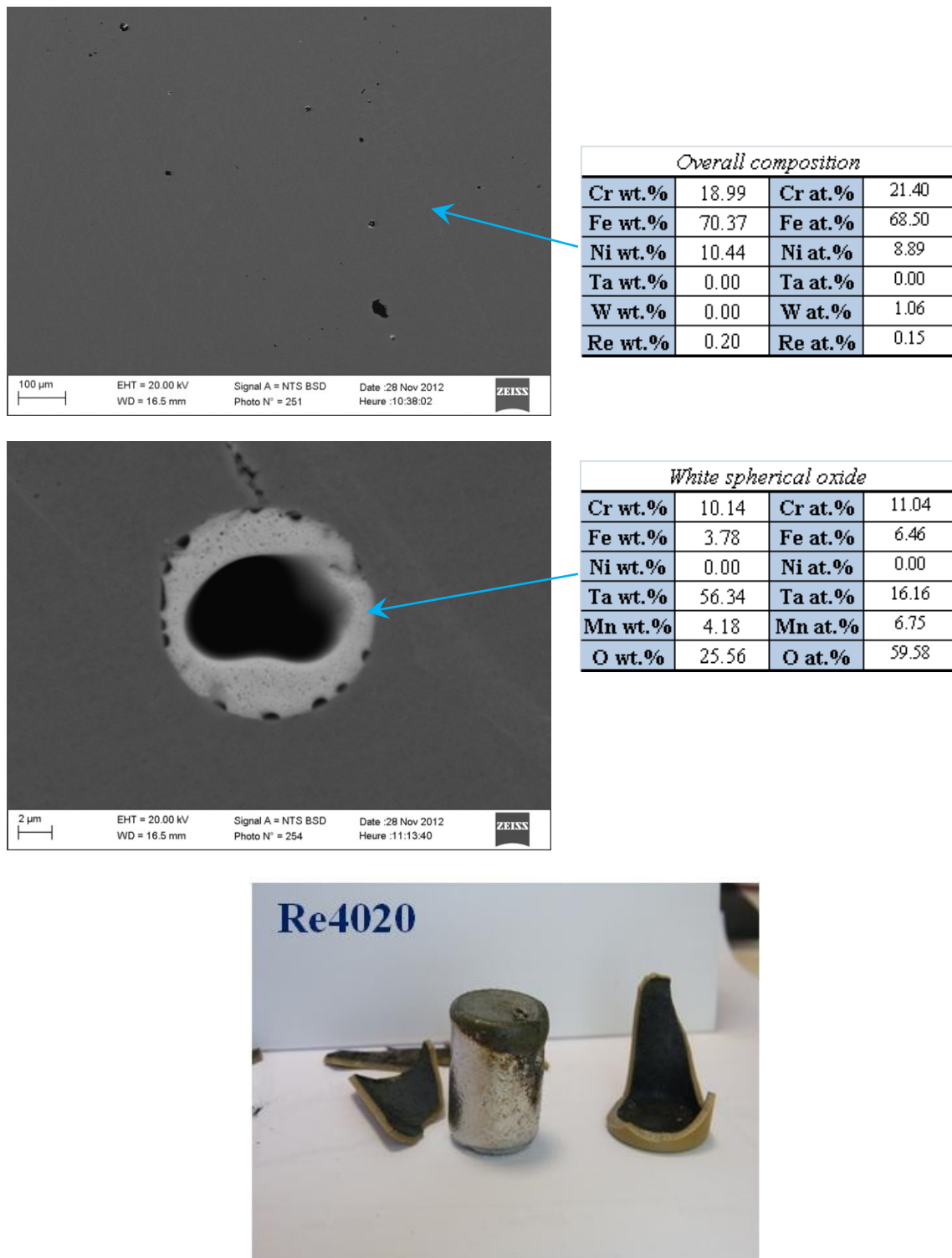
Figure 4.29. Re4020 - Test 11 (Temp. 2000ºC) – SEM/EDS Results and phase identification.

4.5.7 Re4020 - Test 11 (Temp. 2000ºC) – Analysis and Discussion

This alloy contains the same atomic percent of rhenium and tungsten which makes the interpretation more difficult due to the scarcity of phase diagrams between rhenium and iron, plus the fact that rhenium has an hexagonal closed packed lattice which is more compatible with the original austenitic stainless steel FCC lattice. According to the SEM analysis it is evident that a single metallic phase composed in its majority by the stainless steel constituents, along with some dissolved rhenium and tungsten, is the end result of the dissolution of the alloy by the liquid metal. The weight percent of the refractory alloys in the melt adds up to 4.43wt.%, which falls within the solubility limit of the 304L SS metallic constituents. Nonetheless, it is apparent that the higher rhenium and tungsten concentration has a tendency to increase the solidus line of the stainless steel. This makes sense since these two refractory metals have the highest melting point in the periodic table, just below carbon. Even though, the recalescence peak marked at 1745ºC, seems a bit high for iron by itself, when combined with the chromium it falls in between the melting temperature of both metals, and it should correspond to the L→δ reaction. Afterwards, a second peak is signaled at that 1504ºC which corresponds to the δ→γ transformation at a higher temperature, favored by rhenium's hexagonal crystal lattice. This information will help to improve the database on the complex Fe-Cr-Ni-Re-W-Ta system. Additionally, the formation of the complex white oxide has b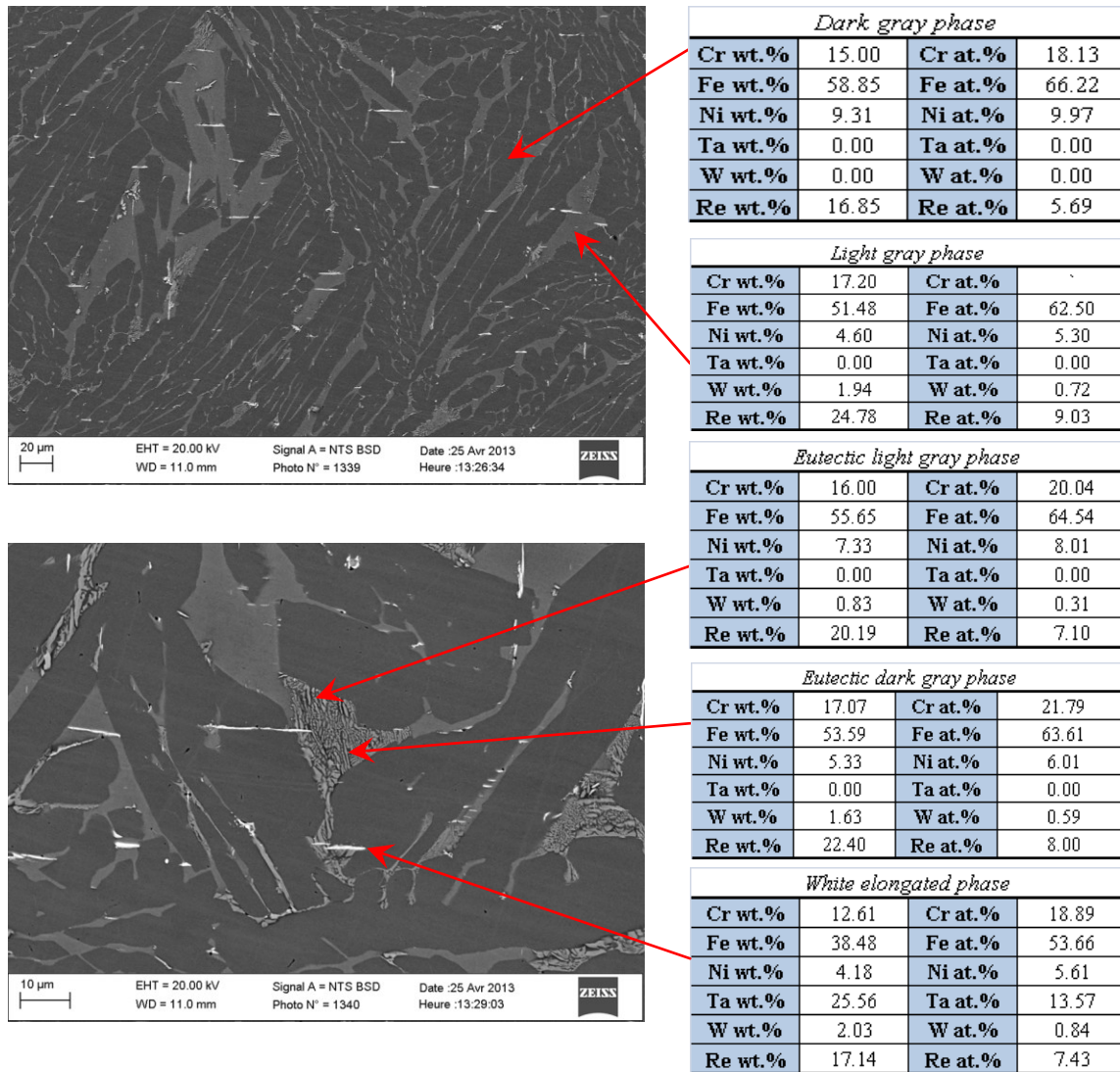een observed in the post-test ingot. The intersection of the oxide phase (Figure 4.29) exposes the interior of the spherical compound, showing an empty interior and outer layer. This infers that the oxide was originally an agglomeration of dissolved oxygen that clustered, leaving the metallic solution. Afterwards, reacting with the complex metallic melt and oxidizing selected metallic elements, to form a shell that is inert to the metallic melt. This might be due to the structure of the oxide being constituted by base metals as Fe, Cr, Mn and Ta which form dense protective oxides.
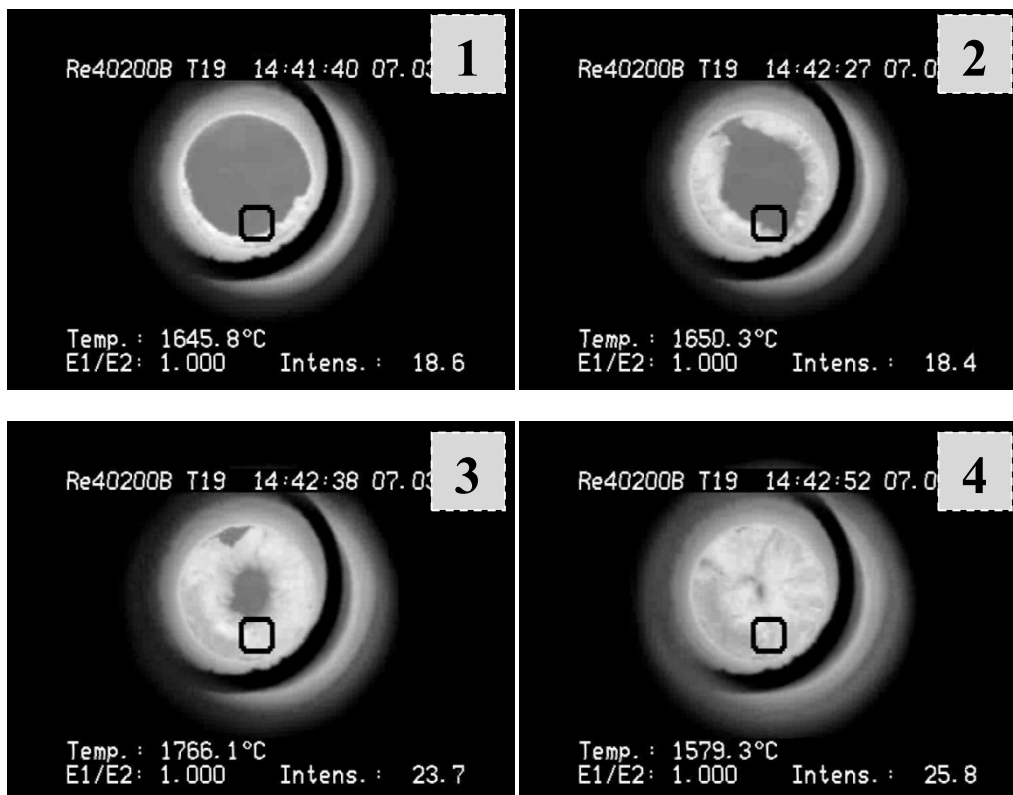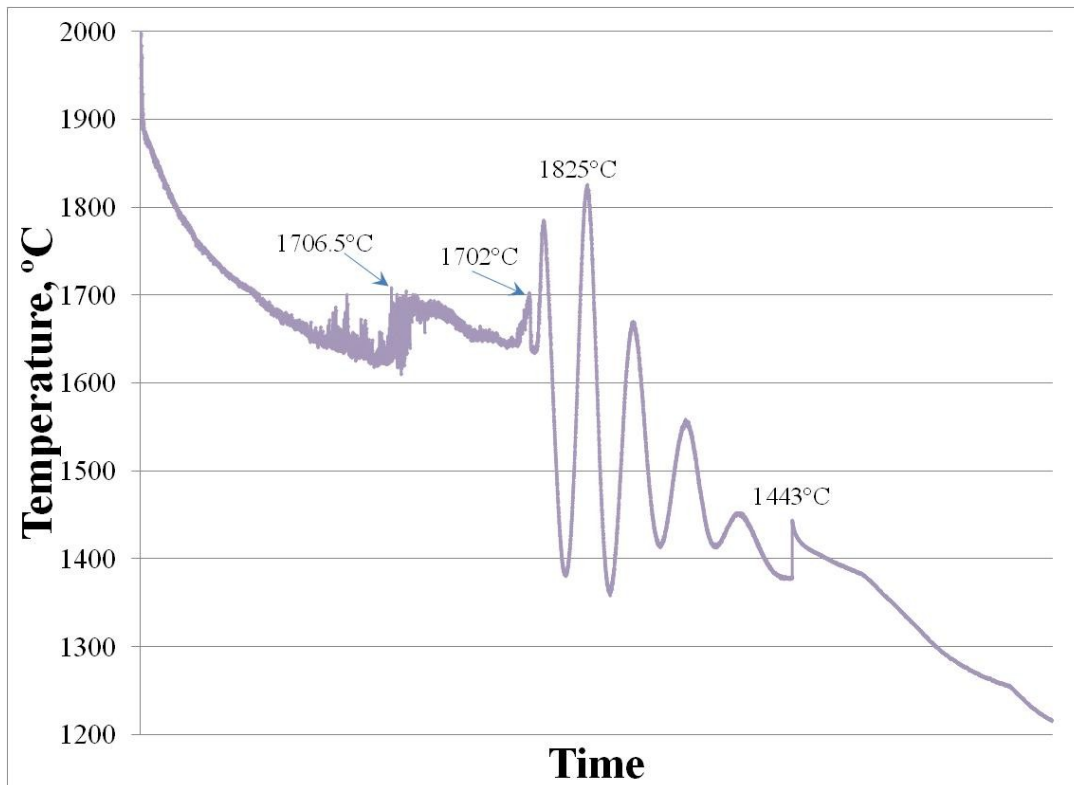
Figure 4.30. Re4020B - Test 19 (Temp. 2000ºC) – Solidification curve and test photos.

Dark gray phase		
Cr wt.%	15.72	Cr at.% 19.01
Fe wt.%	58.29	Fe at.% 65.62
Ni wt.%	8.88	Ni at.% 9.51
Ta wt.%	0.00	Ta at.% 0.00
W wt.%	9.19	W at.% 3.16
Re wt.%	7.92	Re at.% 2.70

White elongated phase		
Cr wt.%	10.11	Cr at.% 16.91
Fe wt.%	33.43	Fe at.% 52.00
Ni wt.%	4.17	Ni at.% 6.17
Ta wt.%	17.74	Ta at.% 8.61
W wt.%	23.00	W at.% 10.91
Re wt.%	11.55	Re at.% 5.40

Light gray phase		
Cr wt.%	18.01	Cr at.% 23.75
Fe wt.%	48.27	Fe at.% 59.65
Ni wt.%	4.75	Ni at.% 5.64
Ta wt.%	1.92	Ta at.% 0.77
W wt.%	13.56	W at.% 5.18
Re wt.%	13.50	Re at.% 5.01

Eutectic white phase		
Cr wt.%	11.16	Cr at.% 17.21
Fe wt.%	35.32	Fe at.% 50.76
Ni wt.%	4.05	Ni at.% 5.62
Ta wt.%	32.84	Ta at.% 19.10
W wt.%	12.47	W at.% 5.78
Re wt.%	4.18	Re at.% 1.53

Figure 4.31. Re4020B - Test 19 (Temp. 2000ºC) – SEM/EDS Results and phase identification.

4.5.8 Re4020B - Test 19 (Temp. 2000ºC) – Analysis and Discussion

The variety of phases found in the Re4020B ingot is in part due to the higher mass of the tested sample. The refractory metals calculated proportion in the melt corresponds to 9.77wt.% Re, 9.63wt.% W and 0.05wt.% Ta. According to the solidification curve the 1706.5ºC peak corresponds to the large needle-like phase, which has the same proportions of the summed up refractory metals and morphology as the tungsten-rich intermetallic compound observed in Test 10. Just after the first peak there is a depression in the curve and a second peak resulting from the solidification of the primary δ-(Fe,Cr,Ni) which again has the same proportion of refractory metals as the gray phase observed in Test 10. Then the sinusoidal part of the curve can be related to the massive solidification growth of the matrix phase and the pertinent fluctuation in the emissivity of the solid and liquid phases (Figure 4.30). Afterwards, there is a solidification peak observed at 1443ºC which corresponds to the eutectic temperature observed in the Ta-Fe diagram. The composition of the white constituent corresponds to a $(Fe,Cr,Ni)_3(Ta,W,Re)$ intermetallic phase. Finally, in some areas a light gray phase was identified at the grain boundaries, but it is unclear if it is due to the segregation of elements or if it corresponds to the η intermediate phase found in the Fe-Re phase diagram.
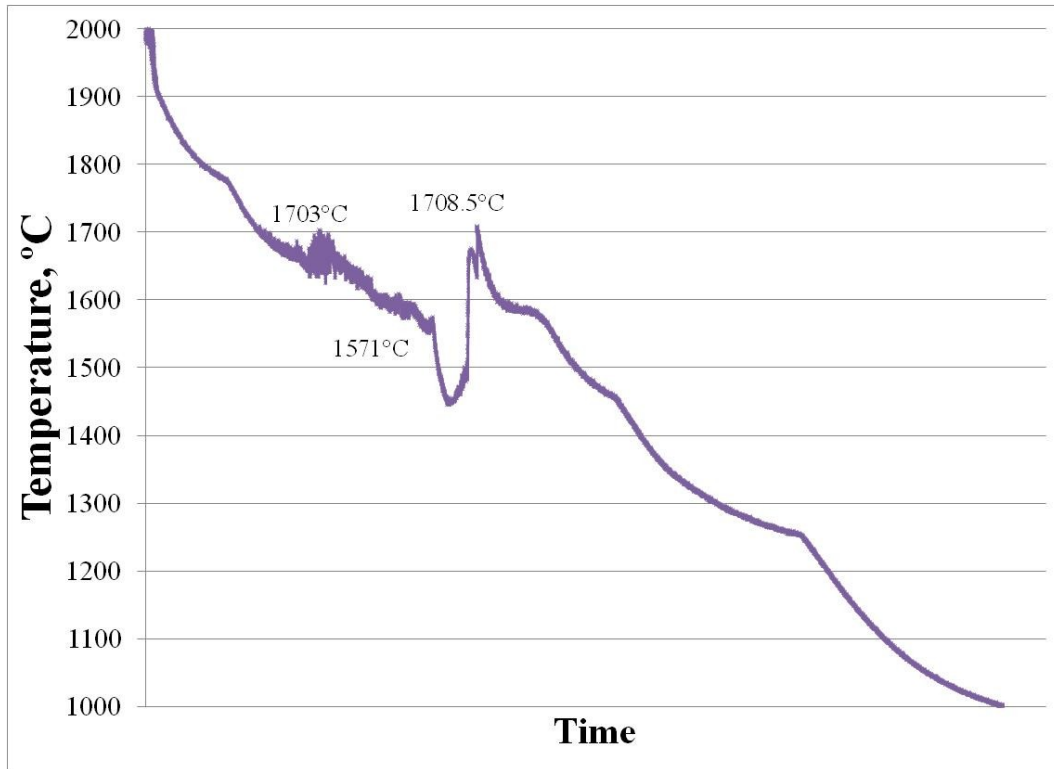
Figure 4.32. Re1010 - Test 13 (Temp. 2000ºC) – Solidification curve and post-test ingot.
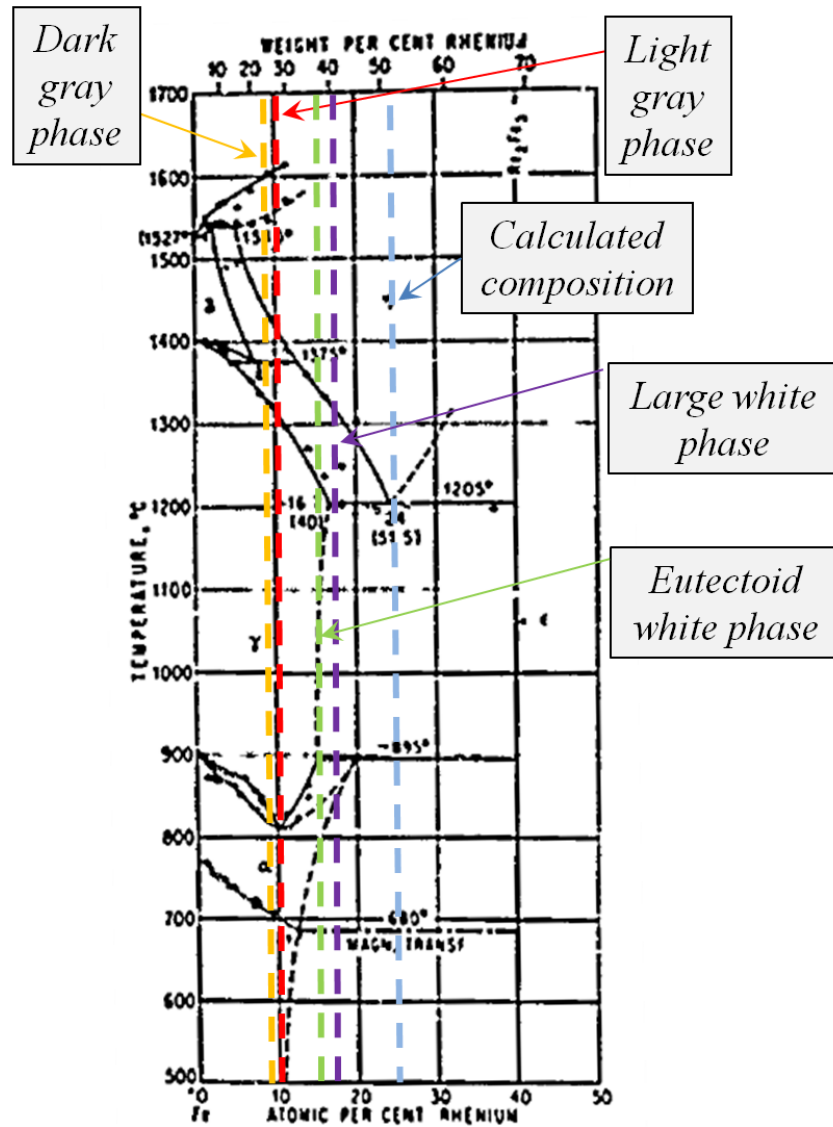
Figure 4.33. Re1010 - Test 13 (Temp. 2000ºC) – Fe-Re phase diagram.

Dark gray phase			
Cr wt.%	13.89	Cr at.%	16.34
Fe wt.%	55.68	Fe at.%	63.39
Ni wt.%	9.75	Ni at.%	10.90
Ta wt.%	0.12	Ta at.%	0.04
W wt.%	0.12	W at.%	0.04
Re wt.%	20.43	Re at.%	9.27

Light gray phase			
Cr wt.%	17.58	Cr at.%	23.23
Fe wt.%	49.73	Fe at.%	61.18
Ni wt.%	4.36	Ni at.%	5.11
Ta wt.%	0.31	Ta at.%	0.12
W wt.%	0.54	W at.%	0.21
Re wt.%	27.47	Re at.%	10.15

Eutectoid white phase			
Cr wt.%	12.92	Cr at.%	20.19
Fe wt.%	37.01	Fe at.%	53.84
Ni wt.%	3.99	Ni at.%	5.52
Ta wt.%	5.67	Ta at.%	2.61
W wt.%	5.47	W at.%	2.47
Re wt.%	34.94	Re at.%	15.37

Large white phase			
Cr wt.%	12.63	Cr at.%	20.56
Fe wt.%	34.08	Fe at.%	51.55
Ni wt.%	3.35	Ni at.%	4.80
Ta wt.%	6.25	Ta at.%	2.98
W wt.%	5.77	W at.%	2.70
Re wt.%	37.93	Re at.%	17.41

Figure 4.34. Re1010 - Test 13 (Temp. 2000ºC) – SEM/EDS Results and phase identification.

4.5.9 Re1010 - Test 13 (Temp. 2000ºC) – Analysis and Discussion

The Re1010 corrosion test solidification curve has two main peaks at a similar recalescence temperature but at different time frames. The phase diagram has been magnified in order to analyze the sluggish transformations that took place. Even though, the calculated proportion of metals seems to be positioned at the eutectoid transformation ($\eta \rightarrow \gamma + \varepsilon$), observed in the Fe-Re phase diagram, it is actually closer to the iron-rich according to EDS analysis of the phases. However the phase transformation path is complex since the initial liquid phase subsequently transformed into multiple distinct solids. Assuming the simplified real composition

lies around Fe-33wt.%Re and under very slow equilibrium cooling the transformation path is the following:

$$\text{L} \xrightarrow{\sim 1700°C} \text{L+η}$$

From L+η:
- $\xrightarrow{\sim 1550°C}$ η $\xrightarrow{\sim 1430°C}$ δ+η $\xrightarrow{\sim 1375°C}$ γ+η $\xrightarrow{\sim 1325°C}$ γ
- $\xrightarrow{\sim 1350°C}$ γ+η $\xrightarrow{\sim 1205°C}$ ε

However, under the cooling rate undertaken the transformation path is hard to evaluate with a bichromatic pyrometer reading, since the solid-state transformation are very sluggish and usually are not energetic enough to be measured as a temperature fluctuation in the curve. Nonetheless, assuming that the sample did not transform below 1300°C and according to the EDS analysis the large white phase corresponds to primary η-phase, the eutectoid white phase is the secondary η-phase (eutectoid), then the dark gray-phase corresponds to (Fe,Cr,Ni)-rich to secondary δ-phase, and the light gray phase corresponds also to η-phase but with a higher content of stainless steel constituents.
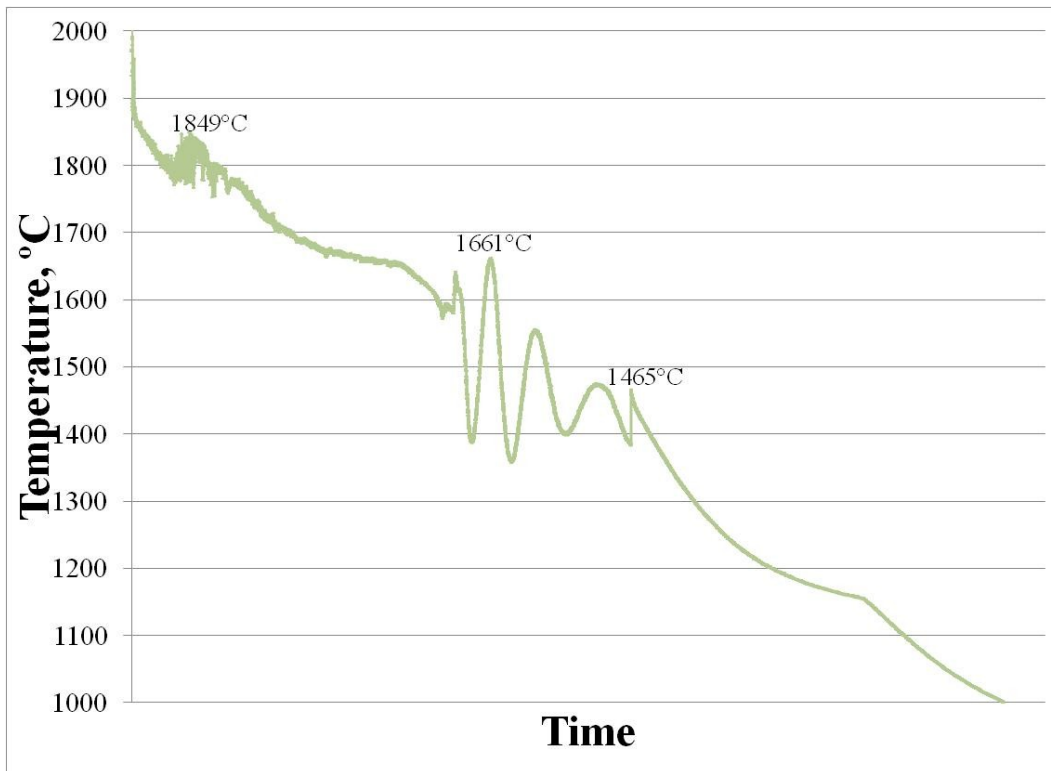
Figure 4.35. Re1010B - Test 18 (Temp. 2000ºC) – Solidification curve and post-test ingot.

Dark gray phase			
Cr wt.%	15.00	Cr at.%	18.13
Fe wt.%	58.85	Fe at.%	66.22
Ni wt.%	9.31	Ni at.%	9.97
Ta wt.%	0.00	Ta at.%	0.00
W wt.%	0.00	W at.%	0.00
Re wt.%	16.85	Re at.%	5.69

Light gray phase			
Cr wt.%	17.20	Cr at.%	`
Fe wt.%	51.48	Fe at.%	62.50
Ni wt.%	4.60	Ni at.%	5.30
Ta wt.%	0.00	Ta at.%	0.00
W wt.%	1.94	W at.%	0.72
Re wt.%	24.78	Re at.%	9.03

Eutectic light gray phase			
Cr wt.%	16.00	Cr at.%	20.04
Fe wt.%	55.65	Fe at.%	64.54
Ni wt.%	7.33	Ni at.%	8.01
Ta wt.%	0.00	Ta at.%	0.00
W wt.%	0.83	W at.%	0.31
Re wt.%	20.19	Re at.%	7.10

Eutectic dark gray phase			
Cr wt.%	17.07	Cr at.%	21.79
Fe wt.%	53.59	Fe at.%	63.61
Ni wt.%	5.33	Ni at.%	6.01
Ta wt.%	0.00	Ta at.%	0.00
W wt.%	1.63	W at.%	0.59
Re wt.%	22.40	Re at.%	8.00

White elongated phase			
Cr wt.%	12.61	Cr at.%	18.89
Fe wt.%	38.48	Fe at.%	53.66
Ni wt.%	4.18	Ni at.%	5.61
Ta wt.%	25.56	Ta at.%	13.57
W wt.%	2.03	W at.%	0.84
Re wt.%	17.14	Re at.%	7.43

Figure 4.36. Re1010B - Test 18 (Temp. 2000ºC) – SEM/EDS Results and phase identification.

4.5.10 Re1010B - Test 18 (Temp. 2000ºC) – Analysis and Discussion

The Re1010B experiment is comparable to the Re1010 test with the exception of the first peak. The peak at 1849ºC can be due to the addition of boron, hence the formation of a high temperature metallic boride. The rest of the phases can be related to the ones observed in Re1010 ingot, but the phase fraction in the microstructure favors the (Fe,Cr,Ni)-rich phases over the refractory-alloy phases. This is evident if we compare the same scale micrographs from Figure 4.34 to 4.36.

4.6 Tungsten Bar 5-minute Immersion into Molten 304L Stainless Steel at 2000ºC and Re2535 Cube 6-minute Immersion at 1800ºC

Originally, an elevator system was designed in order to be able to immerse the samples at an exact temperature and for a limited time lapse. However, due to the aggressiveness of superheated stainless steel the experiment was simplified to its previously mentioned set-up. Nonetheless, the elevator mechanism was successfully tested and two immersion experiments were performed:

- The first experiment consisted of immersing a Re2535 cubic sample for 6 minutes in liquid stainless steel (299.55grs) at 1800ºC. The test was performed using two carbon crucibles, which is not ideal due to the contamination of the melt with carbon, but it was tried since the originally-intended zirconia crucibles suffered from continuous breakage even at mildly low heating rates.

- The second experiment consisted of immersing the same type of tungsten bar as the sheaths used to protect the TC's in VULCANO MCCI tests (length: 45mm, diameter: 11mm), during 5 minutes in liquid 304L stainless steel (174.89grs) at 2000ºC. The W-bar was pending from a W-5Re wire which was tied to the elevator system.

The experimental set-up utilized with the elevator system is shown in Figure 4.37. The experiment consisted of a large (zirconia or carbon) crucible in which the stainless steel was heated until melted and up to the desired temperature. Then the sample was slowly lowered into the molten metal until it was immersed, subsequently the countdown would start, until the time range achieved then the sample was lifted up and the reaction stopped.
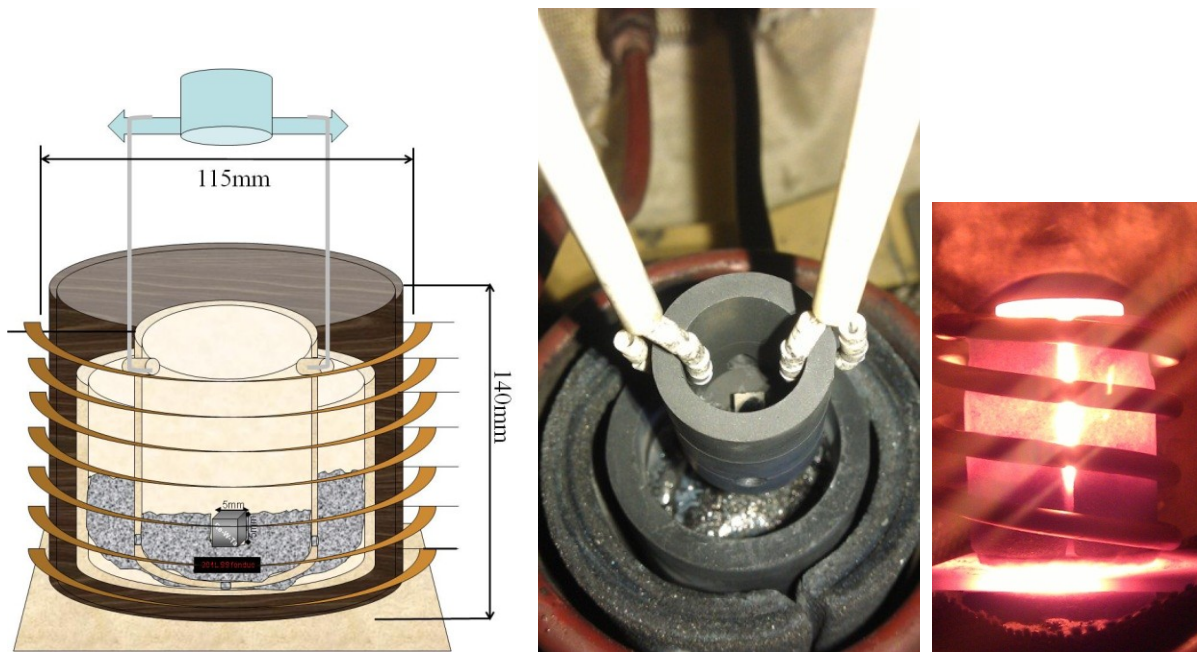
Figure 4.37. Experimental set-up utilized with the elevators mechanism.

4.6.1 Results of the Re2535 Alloy cube 6-minute Immersion in Molten Stainless Steel at 1800ºC

The materials details of the corrosion test performed on the Re2535 cube details are included in Table 4.4. Additionally, in Figure 4.38 we have included a snapshot of the pyrometer video recording showing the moment just before the immersion of the Re2535 cube into the superheated stainless steel.

Re2535B-Test 9	Fe	Cr	Ni	C	Total
SS Powder Mix in grams	158.7	100.1	37.0	3.8	299.55 grs.
Weight %	53.0	33.4	12.4	1.3	100 wt.%

Re2535B Cube Dimensions	Z, mm	X, mm	Y, mm	Weight, grs
	4.73	4.68	4.7	2

Table 4.4. Re2535 alloy cube immersion corrosion test details.

Figure 4.38. Pyrometer snapshot of sample inside crucible just before immersion.
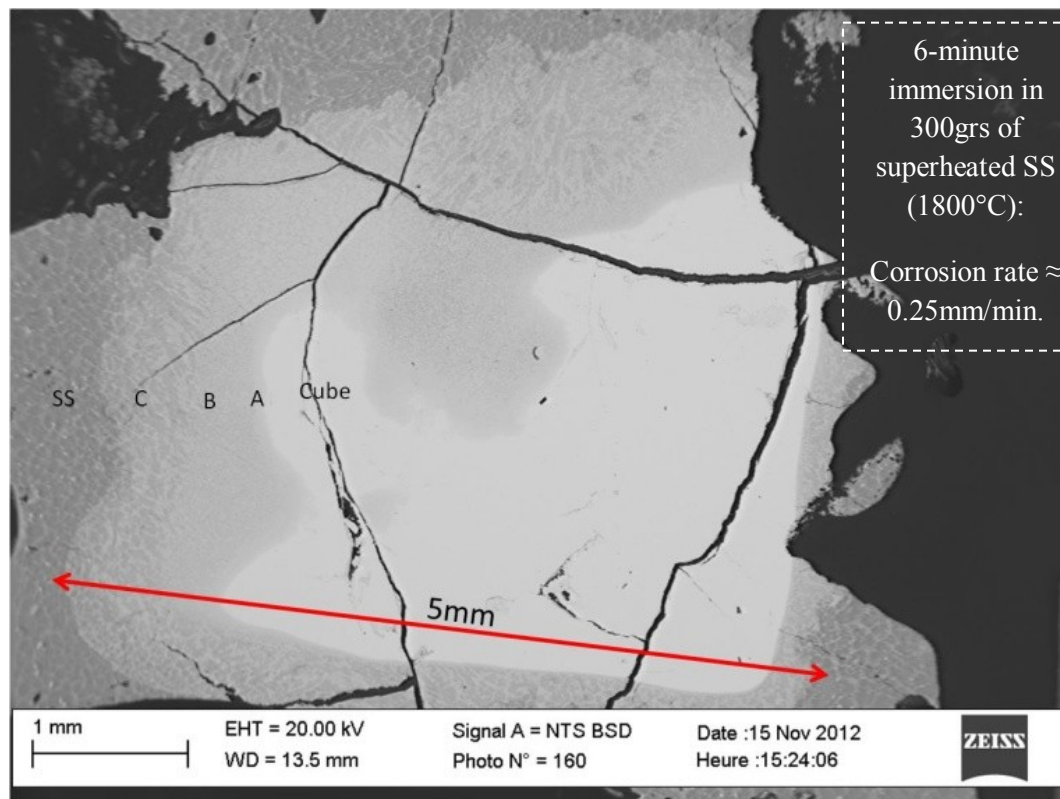
Figure 4.39. SEM/BSD analysis of the post-test Re2535 cube with calculated corrosion rate.

Furthermore, an extensive electron microscope analisys was undertaken on the Re2535 cube/304L SS interface. The BSD micrograph (figure 4.38) shows the multiple layers found in between the original refractory alloy substrate and the molten stainless steel region. They have been identified with letters and their chemical composition is presented in Figure 4.40.
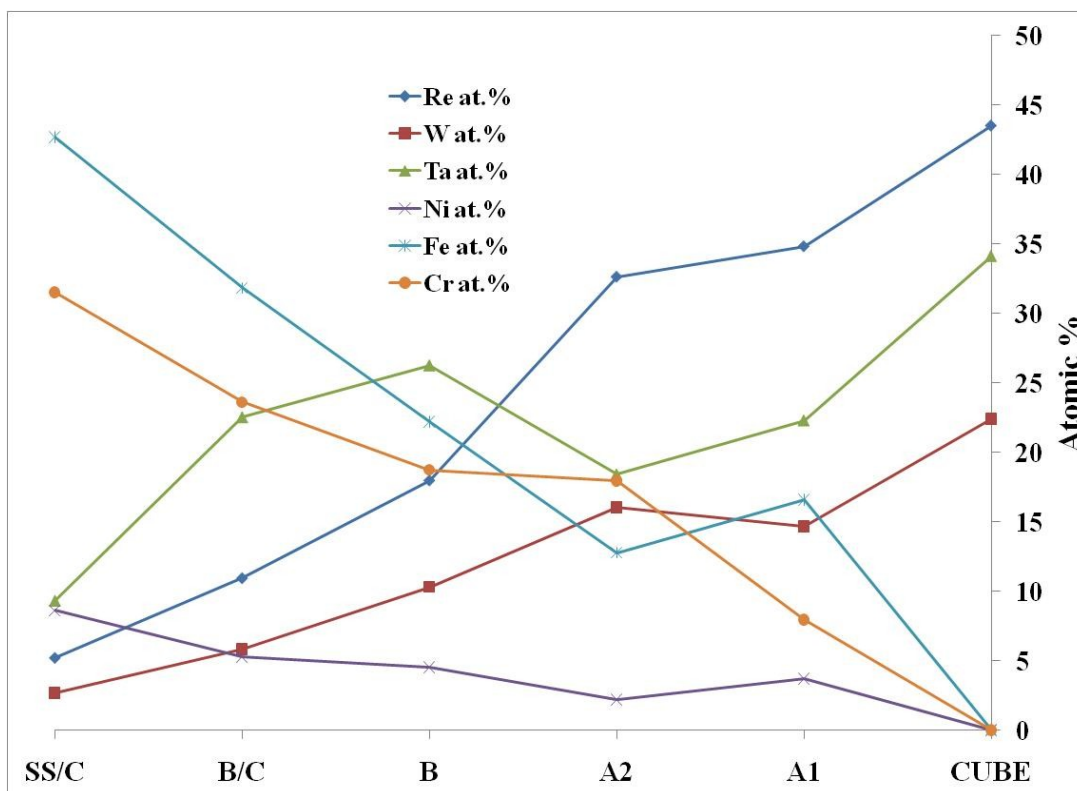
Figure 4.40. Overall EDS analysis of the Re2535/SS reaction zone multiple layers.
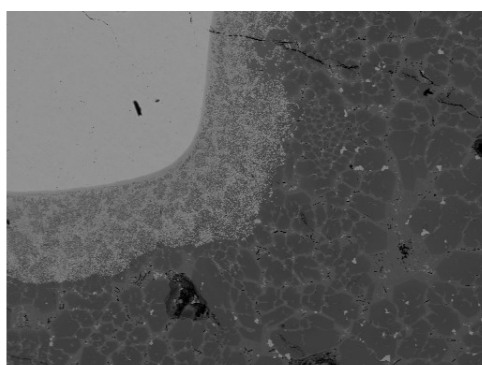
Image électronique 1
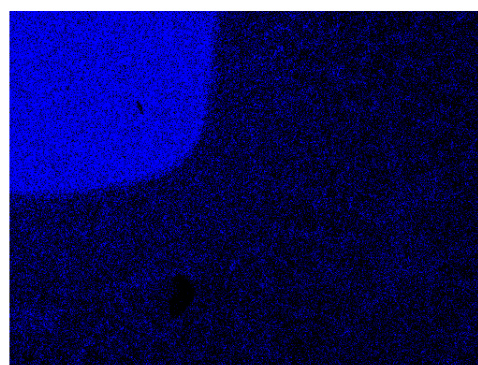
Re La1
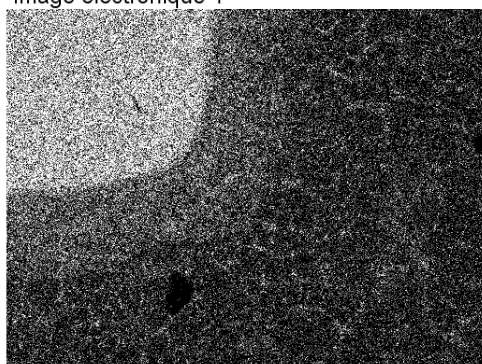
W La1
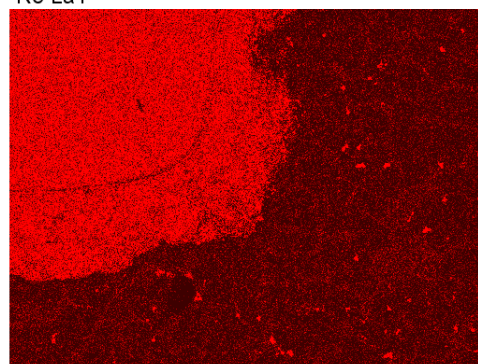
Ta La1
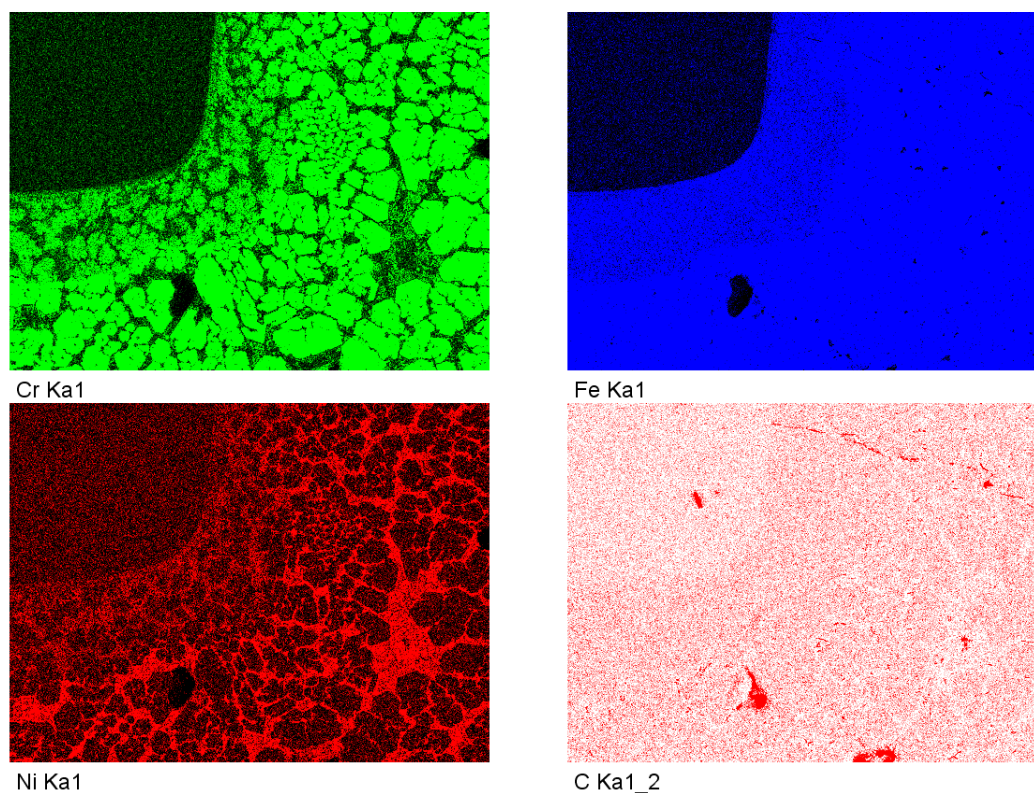
Figure 4.41. X-ray mapping of the Re2535/SS reaction zone.

Additionally, an X-ray mapping of the lower-right corner of the sample is presented in Figure 4.41, to visualize the phases morphology and the concentration of elements in each phase.

4.6.2 Discussion and Conclusions of the Re2535 Alloy Cube 6-minute Immersion in Molten SS at 1800ºC

The Re2535 sample surface area to stainless steel volume ratio corresponds to 0.09. The measured Re2535 alloy corrosion rate in superheated SS at 1800ºC corresponds to 0.25mm/min. The elemental analysis profiles plotted in Figure 4.40 show internal diffusion of the 304L-SS constituents into the Re4020 cubic sample. The curves have an overall logarithmic shape, except at the reaction front (region A1-A2) where the liquid/solid interface was positioned and accumulation of the element is observed. The X-ray mapping (Figure 4.41) show a homogeneous distribution of the Re2535 alloy constituents in the 304L-SS with some segregation at the Cr-rich phase grain boundaries where nickel is preferentially concentrated. Coalescence and nucleation of a tantalum-rich phase is observed as bright spots at the grain boundaries. The iron atoms are evenly dispersed along the reaction zone. The

analysis infers that the Re2535 elements have a tendency to combine with iron and nickel, but are more depleted in the chromium grains. Also, there is a preferential inward diffusion of the lighter atoms (Fe, Ni, Cr) and a less marked migration of the heavier atoms (Re, W, Ta) into the liquid. Based on the previous information we could infer that there are three types of corrosion mechanisms taking place depending on the element evaluated. For example nickel seems to corrode through intergranular penetration. Chromium selectively attacks or alloys with certain elements to form a Cr-rich phase. Iron seems to simply dissolve all elements since it is homogenously dispersed. Finally, carbon has been included to get insight on its behavior in the melt; C seems to be fairly dispersed everywhere, with some slight enrichment at the Cr-rich grains.

4.6.3 Results of the Tungsten rod 5-minute immersion in molten SS at 2000ºC
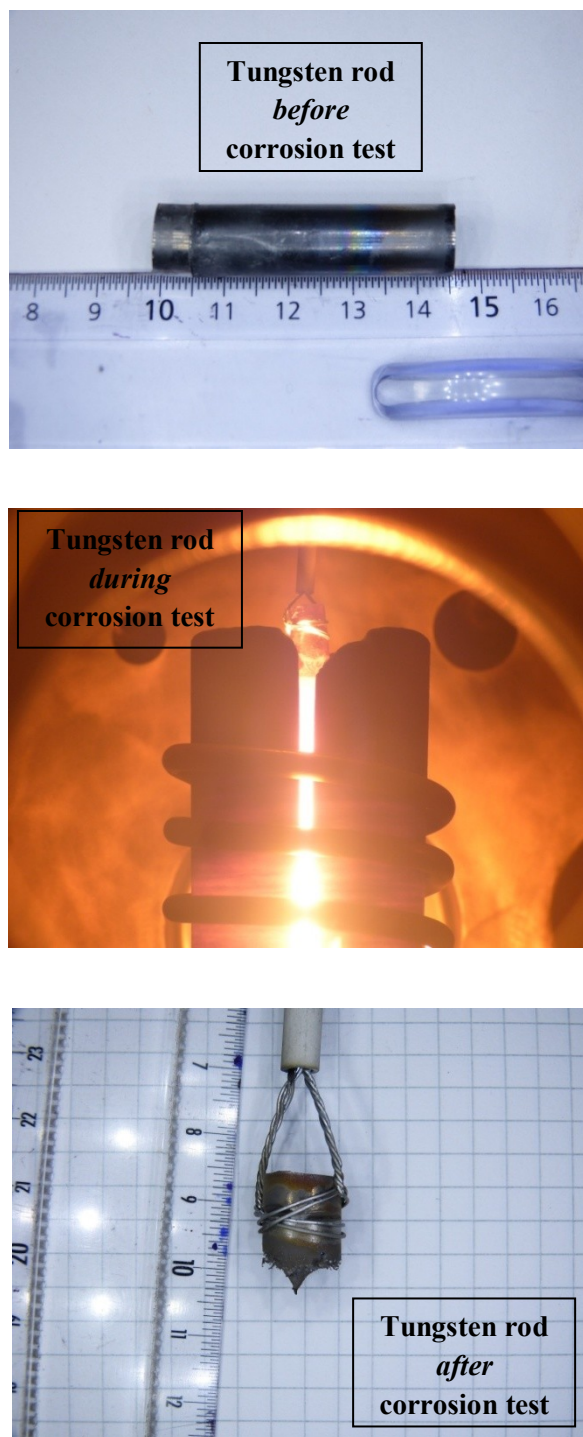
Figure 4.42. Tungsten rod before and after the 5-minute immersion in stainless steel at 2000ºC

4.6.4 Discussion and Conclusions of the Tungsten Rod 5-minute Immersion in Molten SS at 2000ºC

The 5-minute immersion of a tungsten rod in a stainless steel bath at 2000ºC (Figure 4.42), is a test that was performed in order to support the analysis previously done in Section 4.5 and to set a higher limit on the corrosion rate of tungsten in molten stainless steel at 2000ºC. The reacting section of the tungsten surface area to stainless steel volume corresponds to 0.65. The dissolution of the immersed section of the tungsten sample was approximately 4.64 grs/cm^2 (during five minutes) or 0.93 grs/cm^2·min. Nonetheless, since it is not possible to establish at what exact moment the whole section was dissolved, the calculated value serve as a minimum limit on the corrosion rate, since the corrosion front could move faster than evaluated. A 5-mm section in the bottom of the sample denotes the remaining part of the reaction zone. The conical shape observed at the end of the reaction zone is an indication of the simple dissolution mechanism under which corrosion of the tungsten bar proceeded in molten stainless steel. The calculated corrosion ratio for the Re2535 cube in stainless steel at 1800ºC was calculated as 0.25mm/min. The sample can be compared to the tungsten rod corrosion experiment if we assume that the bar is mostly dissolved laterally. Eventhough, the corrosion experiment performed on tungsten took place at 2000ºC, we can observe a ten fold increase in the corrosion rate (approximately ~2.2mm/min).

4.7 Conclusions of the Molten Metal Attack Experiments

» Rhenium-rich and Re-Ta based alloys show better corrosion resistance to 304L SS (than the other materials) up to 2000ºC due the formation of complex intermetallic phases with the stainless steel constituents. These complex intermediate compounds act in effect as retardation to the dissolution of the substrate.

» Tungsten and tantalum in pure form show poor resistance to molten stainless steel attack due to the formation of low temperature phases with stainless steel constituents, or low eutectic points that sharply decrease the service temperature of the sheath.

» Boron additions improve the as-cast microstructure by producing a finer and more homogeneous microstructure.

» The boron microalloying improves the corrosion resistance of the Re-W-Ta alloys through the nucleation of high temperature metallic borides. Increase in boron content could further improve the alloys corrosion resistance.

» Re-10W-10Ta-0.1B can be utilized in molten 304L stainless steel below 1850ºC. This represents more than a hundred-degree improvement over the tungsten bar. It could be used in MCCI tests after temperature has dropped below 1800ºC.

» The characterization of the post-test ingots will serve to improve the thermodynamic and phase stability data available on the Fe-Cr-Ni/Re-W-Ta system.

» The complex spherical oxide observed in multiple ingots might be a material worth testing as a protective layer on a thin TC refractory sheath. If we lump the metals together, this oxide has approximately the following chemical formula $(Ta,Cr,Fe,Mn,Ni)_2O_3$. It resembles the chemical formula of chromia (Cr_2O_3), the protective oxide responsible for stainless steel corrosion/oxidation resistance.

Chapter 4 - References

1. C. Journeau, P. Piluso, "Molten Core Concrete Interaction" in Comprehensive Nuclear Materials, R. Konnings, ed., Elsevier, Amsterdam, 2012.

2. V. Bouyer, C. Journeau, C. Parga, N. Cassiaut-Louis, "High Temperature Measurements in Severe Accident experiments on the PLINIUS platform", Int. Conf. Advances Nuclear Instrum. Meas. Methods and their Applications, Marseille, France, 23-27 June 2013.

3. Z. Ahmad "Principles of corrosion and corrosion control" Publisher: Butterworth-Heinemann/IChemE Series, Oxford, pp. 9-266.

4. N. Birks and G.H. Meier, "Introduction to high temperature oxidation of metals" Edward Arnold Publishers Ltd., London, 1983, pp. 31-158.

5. P. Elliott, "Choose Materials for High-Temperature Environments" Based on a paper presented at CORROSION/2000 (NACE International 55th Annual Conference and Exhibition), Mar.26–31, 2000, Orlando, FL, USA, pp. 75-81.

6. W.D. Manly, "Fundamentals of liquid metal corrosion" Oak Ridge National Laboratory-2055, Metallurgy and Ceramics, TID-4500, 11th ed., 1956, pp. 1-10.

7. D.R. Adkins, K.S. Rawlinson, C.E. Andraka, S.K. Showalter, J.B. Moreno, T.A. Moss, and P.G. Cordiero, "An investigation of corrosion in liquid-metal heat pipes", Sandia National Laboratories-98-1393C, 1998, pp. 1-10.

8. E. M. Lyutyi, O. I. Eliseeva, and R. I. Bobyk, "Corrosion of refractory metals and alloys in liquid lithium (A review)" Original article submitted September 1, 1988G. V. Karpenko Physicomechanical Institute, Academy of Sciences of the Ukrainian SSR, L'vov. Translated from Fiziko-Khimicheskaya Mekhanika Materialov, Vol. 26, No. 6, pp. 3-16, November-December, 1990, pp. 611-621.

9. J.S. Huang and G.F. Gallegos, "Embrittlement by Liquid U in Some Group VB and VIB Metals and Alloys during Tensile Loading at 1473 K" Metallurgical Transactions A, Volume 21A, July 1990, pp. 1959-1967.

10. A. Robin, H.R.Z. Sandim, "Degradation behavior of niobium in molten aluminum" International Journal of Refractory Metals & Hard Materials 20, 2002, pp. 221–225.

11. R. L. Klueh, "Oxygen Effects on the Corrosion of Niobium and Tantalum by Liquid Lithium" Metallurgical Transactions, Volume 5, April 1974, pp. 875-879.

12. MatWeb LLC. "Material property data" www.Matweb.com, Copyright 1996-2013.

13. J.R. Davis, "Alloying: Understanding the basics" ASM International, ISBN: 0-87170-744-6, Materials Park, OH, USA, pp. 1-16, 255-344.

14. D. Kaoumi, "Investigations of the chemical compatibility of rhenium with uranium dioxide at elevated temperatures" MS Thesis University of Florida, 2001, pp. 1-42.

15. J. Richter, M. Campara, G. Fayl, "The TRESON experiment: Measurements of temperature profiles in nuclear fuels by means of ultrasonic thermometers", High Temp High Pres 9, 1977, pp. 347-406.

16. A. Naor, N. Eliaz, E. Gileadi, S.R. Taylor, "Properties and Applications of Rhenium and Its Alloys" The AMMTIAC Quarterly, Vol. 5, No. 1, pp. 11-15.

17. T. Leonhardt, "Properties of Tungsten-Rhenium and Tungsten-Rhenium with Hafnium Carbide" Journal of Materials, Vol. 61, No. 7, July 2009, pp.68-71.

18. B.D. Reed and J.A. Biaglow, "Rhenium Mechanical Properties and Joining Technology" NASA Technical Memorandum 107317 AIAA–96–2598, pp.1-12.

19. T.A. Millensifer, "Rhenium and rhenium compounds" Kirk-Othmer Encyclopedia of Chemical Technology, Copyright John Wiley & Sons, Inc., pp. 1-18.

20. T. Kunieda, K. Yamashita, Y. Murata, T. Koyama, M. Morinaga, "Effect of Rhenium addition on Tungsten diffusivity in Iron-Chromium alloys" Materials Transactions, Vol. 47, No. 8, 2006, pp. 2106-2108.

21. J. Rösler, D. Mukherji, T. Baranski, "Co-Re-based alloys: a new class of high temperature materials?" Advanced engineering materials, Vol.9, No. 10, 2007, pp. 876-881.

22. Y.B. Kuzma, V.I. Lakh, B.I. Stadnyk and Y.V. Voroshilov, "Phase equilibria in the system Zr-Re-B and W-Re-B" Test methods and properties of materials, translated from Poroshkovaya Metallurgiya, No. 6 (66), pp. 47-53, June 1968. Original article submitted March 23, 1967, pp. 462-466.

23. A.R. Poster, "Note on the powder metallurgy of Rhenium", Journal of Less-Common Metals, Vol. 4, No. 2.8, 1962, pp. 2-8.

24. M. Garfinkle, W.R. Witzke and W.D. Klopp, "Superplasticity in Tungsten-Rhenium Alloys" NASA Technical Note D-4728, Washington D.C., August 1968, pp. 1-22.

25. A. Cezairliyan and A.P. Miiller, "Thermophysical Measurements on Tungsten-3 (Wt %) Rhenium Alloy in the Range 1500-3600 K by a Pulse Heating Technique" International Journal of Thermophysics, Vol. 6, No. 2, 1985, pp. 191-202.

26. S. Wurster, B. Gludovatz, R. Pippan, "High temperature fracture experiments on tungsten–rhenium alloys" International Journal of Refractory Metals & Hard Materials, Volume 28, Issue 6, November 2010, Pages 692–697.

27. R.P. Simpson, G.J. Dooley and T.W. Haas, "Study of Grain Boundary Fracture Surfaces in Doped Tungsten-Rhenium Alloys" Metallurgical Transactions, Vol. 5, March 1974, pp. 585-591.

28. H-K. Kang, "Thermal properties of plasma-sprayed tungsten deposits" Journal of Nuclear Materials, No. 335, 2004, pp. 1-4.

29. T. Ishikawa and P-F. Paradis, "Thermophysical properties of molten refractory metals measured by an electrostatic levitator" Journal of electronic materials, Vol. 34, No. 12, 2006, pp.1526-1532.

30. L.A. Gypen, M. Brabers and A. Deruyttere, "Corrosion resistance of tantalum base alloys. Elimination of hydrogen embrittlement in tantalum by substitutional alloying" Materials and Corrosion, Vol. 35, Issue 2, , February 1984, pp. 37–46

31. F. Cadarelli, P. Taxil and A. Savall, "Tantalum protective thin coating techniques for the chemical process industry: Molten salts electrocoating as new alternative" International Journal of Refractory Metals & Hard Materials, Vol. 14, 1996, pp. 365-381.

32. H. Wang, Y. Xu, M. Goto, Y. Tanaka, M. Yamazaki, A. Kasahara and M. Tosa, "Thermal conductivity measurement of tungsten oxide nanoscale thin films" Materials Transactions, Vol. 47, No. 8, 2006, pp. 1894-1897.

33. P.L. Raffo and W.D. Klopp, "Influence of boron additions on physical and mechanical properties of arc-melted Tungsten and Tungsten-1%Tantalum alloy" NASA Technical Note D-3247, Washington D.C., February 1966, pp. 1-20.

34. A.N. Minkevich, "Diffusion boride layers in metals" Metal Science and Heat Treatment of Metals, Volume 3, Issue 7-8, July–August 1961, pp. 347-351.

35. G.A. Cottrell, "Sigma phase formation in irradiated tungsten, tantalum and molybdenum in a fusion power plant" Journal of Nuclear Materials 334, 2004, pp. 166-168

36. J.A. Yeomans, T.F. Page, "Studies of ceramic-liquid metal reaction interfaces" Journal of materials science, vol. 25, 1990, pp. 2312-2320.

37. O. Dezellus, N. Eustathopoulos, "Fundamental issues of reactive wetting by liquid metals" Journal of Materials Science, , Volume 45, Issue 16, August 2010, pp. 4256-4264.

38. V. Nalivaev, "Investigation of interaction of the structural elements of high temperature thermoelectric converters with the structural materials of a fuel element and a cassette and the working medium" Scientific industrial association, LUTCH Research Institute, Poland, 1991, pp. 1-12.

39. C.E.D. Row, "Tantalum, niobium and zirconium as corrosion resistant materials" SMF Ltd., 21801 Tungsten Rd., Cleveland, Ohio, pp. 121-124.

40. S.J. Zinkle, "Thermomechanical Properties of W-Re Alloys & Initial Survey of Molten Tin Corrosion Data" APEX Study Meeting UCLA, November 2-4, 1998, pp. 1-10.

41. J. Lee, W. Gao, Z. Li, Y. He, "Corrosion behavior of Ti3Al and Ti3Al–11 at.% Nb intermetallics" Materials Letters 57, 2003,pp. 1528-1538.

42. J.H. Brophy, M.H. Kamdar and J. Wulff, "The Ta-W-Re System" Transactions of the metallurgical society of AIME, Vol. 221, December 1961, pp. 1137-1140.

43. I.A. Tregubov, L.N. Evseyeva, O.S. Ivanov, I.D. Marchukova, "Investigation of the W-Ta-Re constitution diagram by the diffusion layer method" Russ. Metall. (Engl. Transl.), 1973, pp. 144-148.

44. Springer Materials "Binary Systems: Ta-W" The Landolt-Börnstein Database, New Series IV/19B, pp. 1-4.

45. S.H. Zhou and Zi-Kui Liu, "Evaluation of the thermodynamic properties and phase equilibria of the Re-W-Ta system" Metallurgical and Materials Transactions A, Vol. 33A, Sept. 2002, pp. 2781-2787.

46. Z.-K. Liua and Y.A. Chang "Evaluation of the thermodynamic properties of the Re–Ta and Re–W systems" Journal of Alloys and Compounds, no. 299, 2000, pp. 153–162.

47. K.I. Portnoi and V.M. Romashov "Binary constitution diagrams of systems composed of various elements and boron-A review" Test methods and properties of materials, translated from Poroshkovaya Metallurgiya, No. 5 (113), pp. 48-56, May, 1972. Original article submitted March 18, 1971, pp. 378-384.

48. C. Bagnall, P.F. Tortorelli, S.J. Pawel, J.H. DeVan and S.L. Schrock, "Corrosion Tests and Standards Manual: Chapter 40-Liquid Metals" ASM International, pp. 465-475.

49. ASTM International, "Standard practice for laboratory immersion corrosion testing of metals" Designation: G 31-72, 2004, pp. 1-8.

Conclusions and Recomendations

This PhD research focused on the improvement of very high temperature thermometry (1100ºC to 2500ºC), with special emphasis on the application to the field of nuclear reactor safety and severe accident research. Two main projects were undertaken to achieve this objective:

- The development, testing and transposition of high-temperature fixed point (HTFP) metal-carbon eutectic cells, from metrology laboratory precision (±0.001ºC) to applied research with a reasonable degradation of uncertainties (±3-5ºC).

- The corrosion study and metallurgical characterization of Type-C thermocouple (service temp. ≤ 2300ºC) prospective sheath material was undertaken to extend the survivability of TCs used for molten metallic/oxide corium thermometry (≤ 2000ºC).

Extensive research on high-temperature metal-carbon eutectics [Fe-4.3wt.%C (1153°C), Co-2.6wt.%C (1324°C), Ti-0.4wt.%C (1646.5ºC), Ru-2.5wt.%C (1954°C), Mo-2.5wt.%C (2205°C), Nb-1.5wt.%C (2354ºC) and Re-1.3wt.%C (2480°C)] was undertaken in order to explore their feasibility as HTFP for in-house calibration of thermometers that are used in experimental facilities in which radioactive materials are handled, therefore not suitable for calibration elsewhere; along with their potential as in-melt temperature reference points. Furthermore, based on the tests performed on three Fe-C eutectic cells within a range of iron purity (Fe purity ranging from 99 to 99.998%), it was determined that impurities depress the eutectic temperature. However, the magnitude of this effect depends on the type of impurity and eutectic system. Therefore, in order to use the metal-carbon eutectic cells for calibration of thermometers it is recommended to use HTFP eutectic cell constituent materials with a purity of at least 99.99% to avoid cell inaccuracy and erroneous calibration. Also, several metal-carbon eutectic cells (Co-C, Ti-C, Ru-C and Re-C) were tested under high heating and cooling rates (~50-200ºC/min). Based on the results it was determined that there is a direct relationship between increase in heating rate and increase in experimentally measured melting

temperature due to lack of thermal homogeneity causing a non-equilibrium transformation. Similarly, as the cooling rate is increased, the experimentally measured solidification temperature is decreased. However, the melting temperature is less sensible to rate changes than the solidification temperature due to the difference in their transformation kinetics, rendering the solidification process a more complex transformation, which depends on a finite undercooling for nucleation. Therefore, the melting temperature, estimated from the temperature-time curve, should be preferred over the solidification temperature for thermometer calibration and heating rate restricted to a maximum of 25ºC/minute. Furthermore, it was determined that simpler eutectic systems (i.e. Ru-C, Co-C and Re-C) show better reproducibility than more complex systems containing multiple eutectics, intermediate phases and/or polymorphic transformations (i.e. Ti-C, Nb-C and Mo-C). This is due to the competition for the formation of multiple distinct phases and the formation of phase fields and concentration gradients. Nonetheless, furnace type, experimental set-up and graphite cell design have an important impact on the the eutectic cell performance. And improvement of thermal homogeneity of test zone through the addition of thermal isolation material will greatly reduce the heat losses and improve the performance of the eutectic cell. VITI has been adapted to reach a satisfactory level of uncertainty (<3-5ºC). Various designs of graphite cells were successfully tested under significantly high heating and cooling rates (thermal constraints). The cells were robust enough to handle the thermal stresses and dilatation of eutectic alloy. The extensive research on different cell designs allowed for a significant reduction in cell size and eutectic material needed. Accordingly a gain on the performance of the cell was obtained, due to the reduction in surface area and concomitant reduction of heat losses. Numerous eutectics and cell designs were studied, leading to the realization of three HTFP (Co-C, Ru-C and Re-C) cells which are now available for on-site calibration of temperature sensors utilized in facilities in which radioactive materials are manipulated, therefore not suitable for calibration elsewhere. These cells were characterized in the LNE-Cnam French metrology facilities and their equilibrium melting/solidification transformation temperature established. One-day training on the practical application of the cells as reference points was offered to staff at the LMA. The Ru-C

cell was thermally cycled in VITI and a bichromatic pyrometer was utilized to measure the cavity temperature. Discussion on the basics of eutectics and important details for an adequate calibration were discussed. The HTFP cell kit includes the Co-C, Ru-C and Re-C cells, plus the thermal isolation material needed to get the best performance from the cell and through a reduction on the impact of heat losses. The cells were tested in LNE-Cnam French metrology institute near Paris and their transformation temperature defined. The Co-C (cell #18) has a melting/solidification mean temperature of 1323.97ºC /1323.14ºC and a standard deviation of 0.14ºC/0.19ºC, respectively. The Ru-C (cell #19) has a melting/solidification mean temperature of 1952.54ºC/1951.65ºC and a standard deviation of 0.17ºC/0.21ºC, respectively. The Re-C (cell #17) has a melting/solidification mean temperature of 2472.05ºC/2470.77ºC and a standard deviation of 0.30ºC/0.42ºC, respectively. Even though our cells have a slightly inferior reproducibility (i.e. lower transformation temperature and higher standard deviation) than the metrology reference cells [Co-C (T/σ: melting - 0.03ºC/+0.04ºC and solidification: -0.56ºC/+0.06ºC), Ru-C (T/σ: melting: -0.31ºC/+0.02ºC and solidification: -1.1ºC/+0.05) and Re-C (T/σ: melting: -2.2ºC/+0.1ºC and solidification: -3.46ºC/+0.21)]; they represent a significant improvement to the first generation of cells performance:

The development and testing of Re-W-Ta-(B) refractory alloys protective sheath for MCCI environments provided the following information. Rhenium-rich and ReTa-based alloys show better corrosion resistance to molten 304L SS up to 2000ºC. This is due to the formation of complex intermetallic phases with the stainless steel constituents which act as retardation to the dissolution of the substrate, along with higher tantalum availability for the formation of Ta_2O_5 protective oxide. Pure tungsten and tantalum, show poor corrosion resistance to molten stainless steel and are dissolved by stainless steel constituents to form low temperature Fe-rich phases (<1700ºC) or eutectics (~1389.5ºC), respectively, which sharply decrease the service temperature of the sheath. Boron microalloying in Re-W-Ta alloys improves the corrosion resistance to molten 304L SS, along with a microstructural refinement and homogenization of the as-cast refractory alloys. Re1010B alloy

shows the best corrosion resistance among the pure tungsten, tantalum and Re-W-Ta-(B) alloys studied. It could be utilized as protective sheath in 304L SS below 1850ºC. Nonetheless, due to its brittleness a thin layer could be plasma sprayed on a tantalum substrate for TC sheath protection. The characterization of the as-cast and post-test ingots will serve to improve the thermodynamic phase stability database available on the Fe-Cr-Ni/Re-W-Ta system, which is currently very scarce or non-existent. The high temperature complex spherical oxide, $(Ta,Cr,Fe,Mn,Ni)_2O_3$, imbedded in the microstructure of multiple post-test ingots might be a material worth testing as a protective layer on a TC refractory sheath.

This PhD research allowed for an improvement in the experimental capabilities for molten corium thermometry through better calibration of thermometers (Co-C, Ru-C and Re-C HTFP cells). Also, it provided a sheath alloy (Re-10W-10Ta-0.1B) with better corrosion resistance and thermal stability to molten oxide/metallic corium than commercial TC sheath material (tungsten, tantalum and ZrO_2 ceramic). Within the HiTeMS project it also contributes with the work performed in the investigation of high-temperature metal-carbon eutectic, for their introduction as HTFP in the next ITS. Finally, it provided academic and technical data in the complex Re-W-Ta-Fe-Cr-Ni system for thermodynamic database and ulterior alloy development for high-temperature applications.

Appendix A

Metal-Carbon Eutectic System's Phase Diagram

Appendix A

Fe-C Phase Diagram
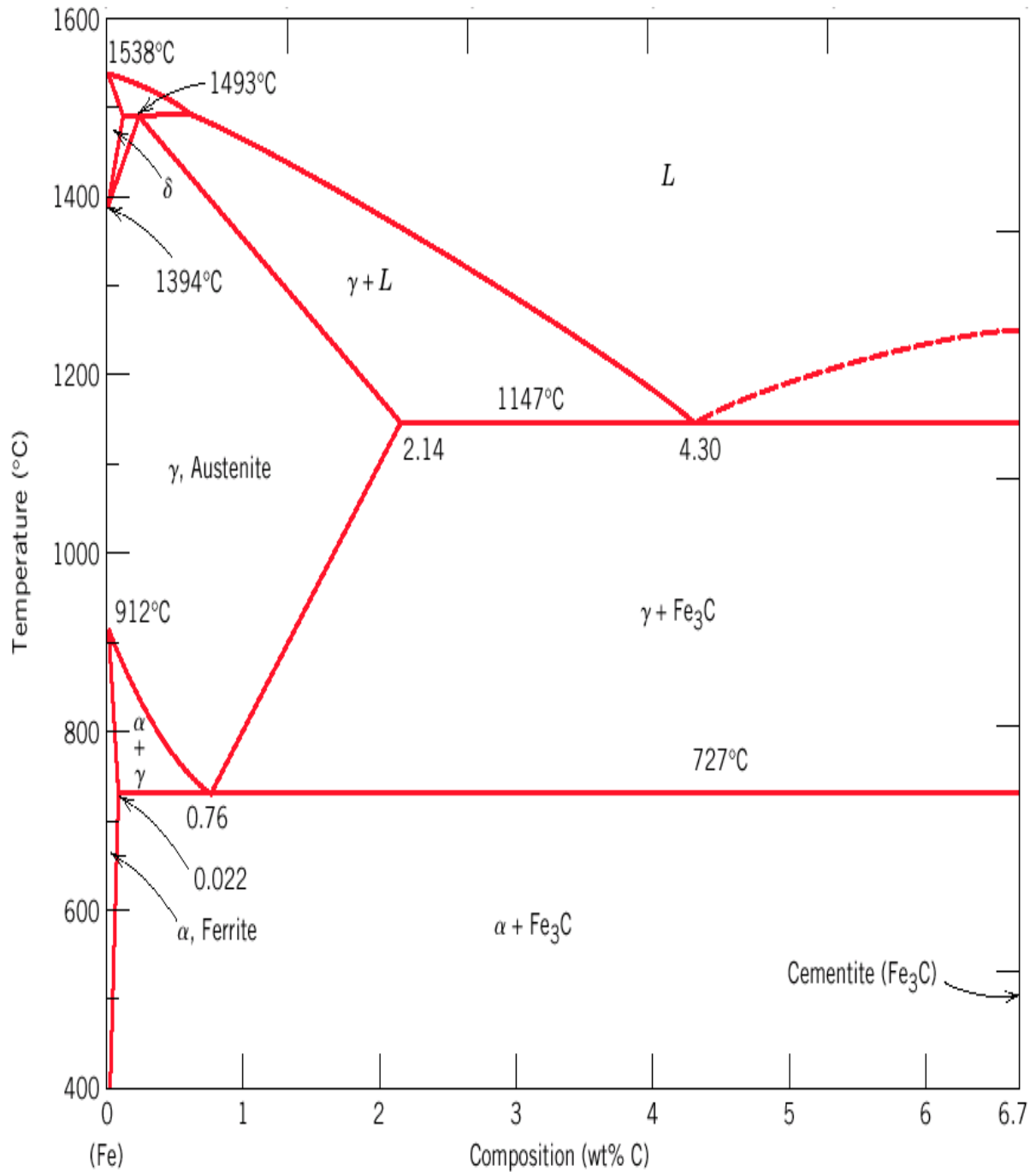
The iron-iron carbide phase diagram: W.D. Callister Jr."Materials Science and Engineering: An Introduction" 5th edition, John Wiley and Sons, Inc., New York, 2000, pp. 274

Adapted from Binary Alloy Phase Diagrams, 2nd edition, Vol. 1, T.B. Massalski, Editor-in-chief, 1990.

Co-C Phase Diagram
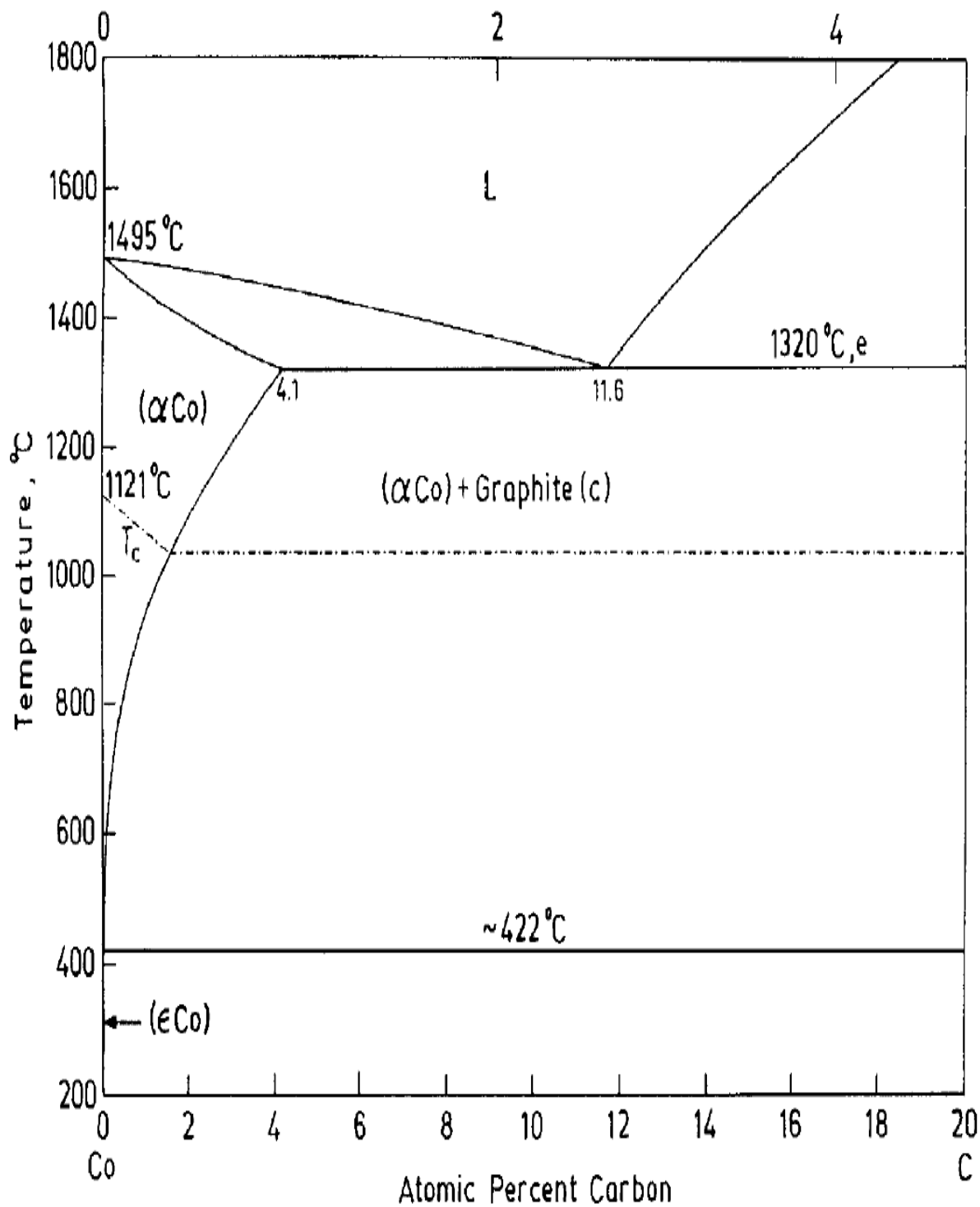
D. Bandyopadhyay, R. C. Sharma and N. Chakraborti, "The Ti-Co-C system (Titanium-Cobalt-Carbon)" Journal of phase equilibria 2000, Vol. 21, No 2, pp. 181.

Original source: K. Ishida and T. Nishizawa: J. Phase Equilibria, 1991, vol. 12 (4), pp. 417-24.

Ti-C Phase Diagram
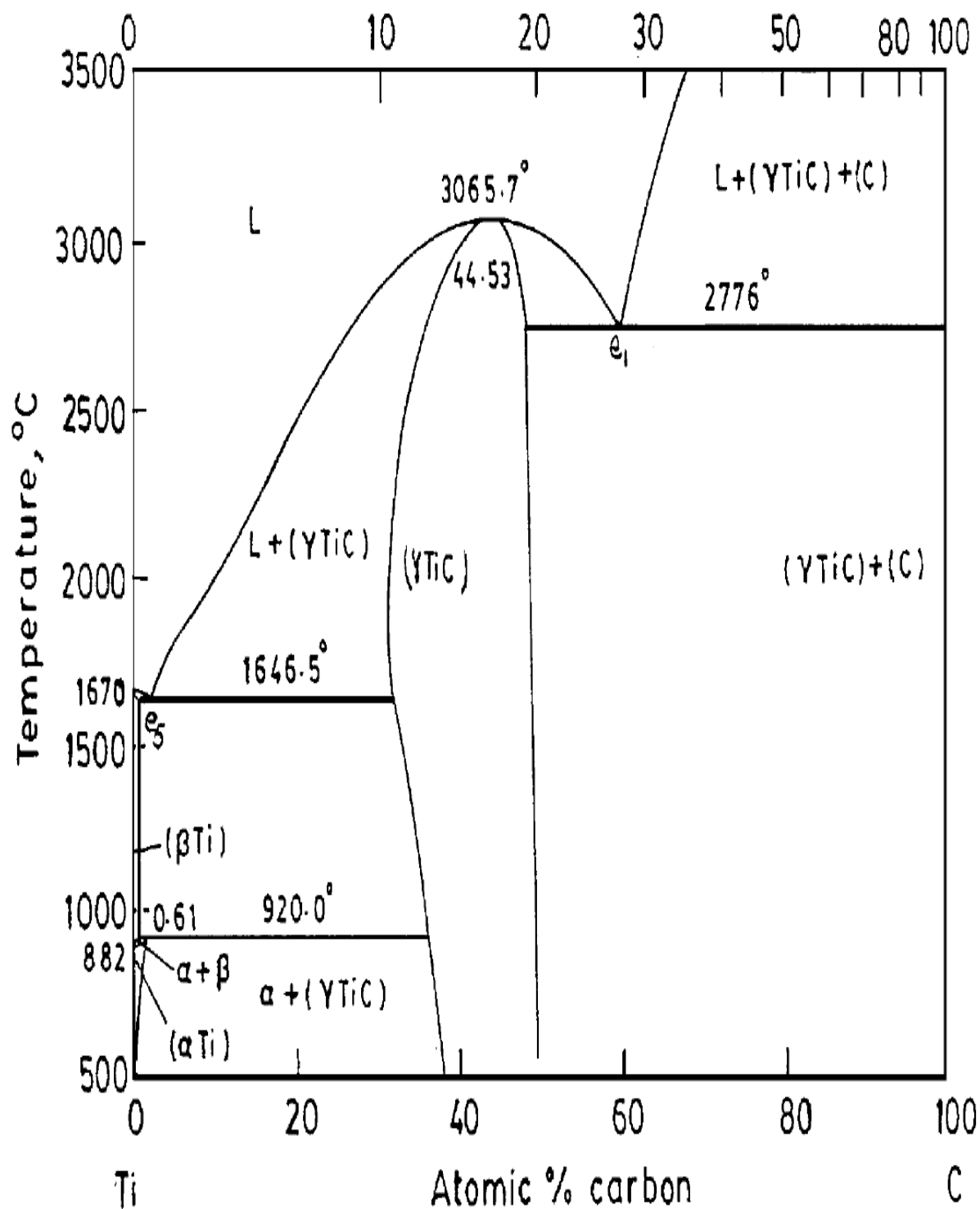
D. Bandyopadhyay, R.C. Sharma, and N. Chakraborti, "The Ti - Co - C System (Titanium - Cobalt - Carbon) ", Journal of Phase Equilibria Vol. 21 No. 2, 2000, pp. 179.

Original source: H. Okamoto: J. Phase Equilibria, 1998, vol. 19 (1), p. 89.

Ru-C Phase Diagram
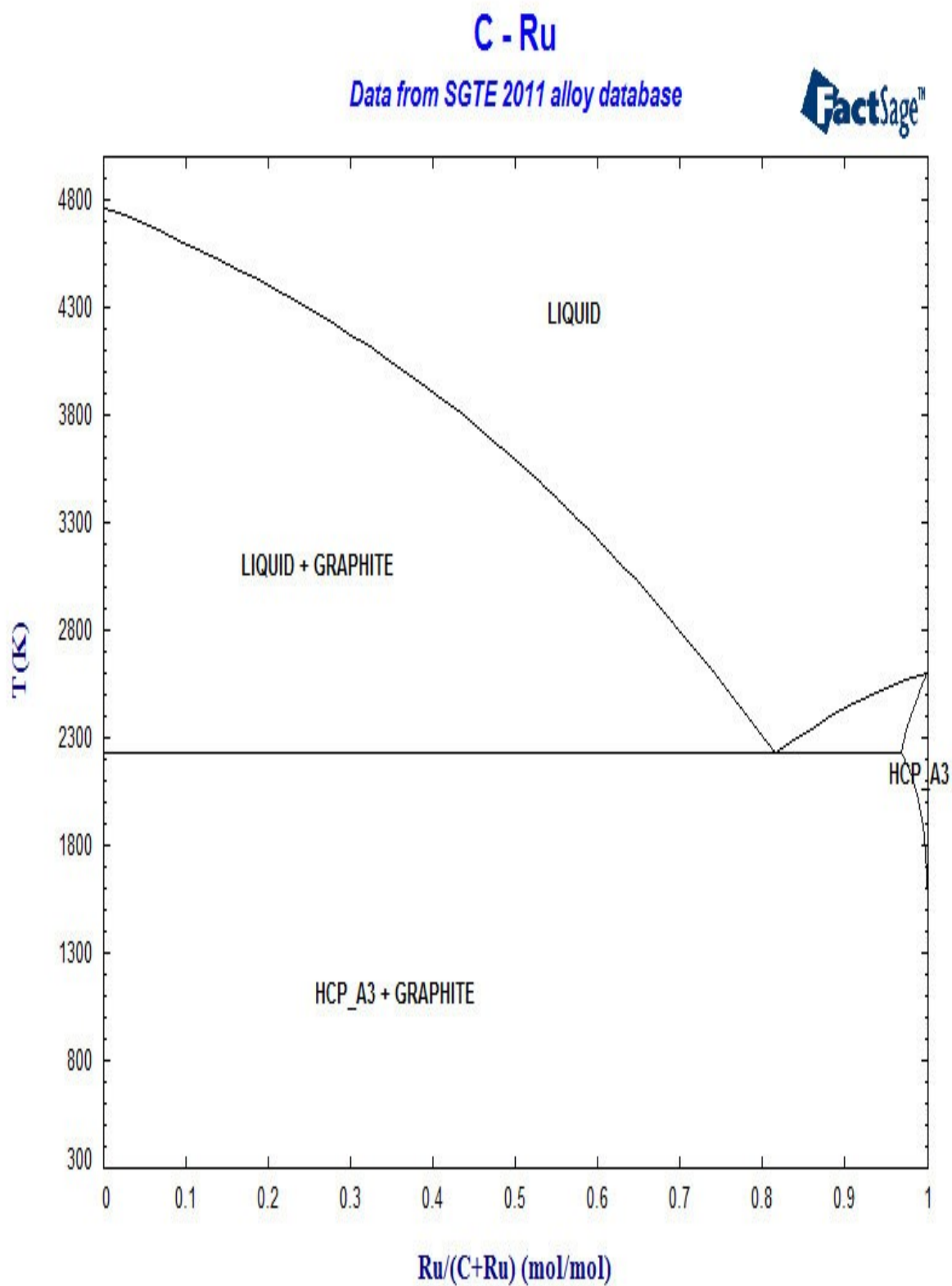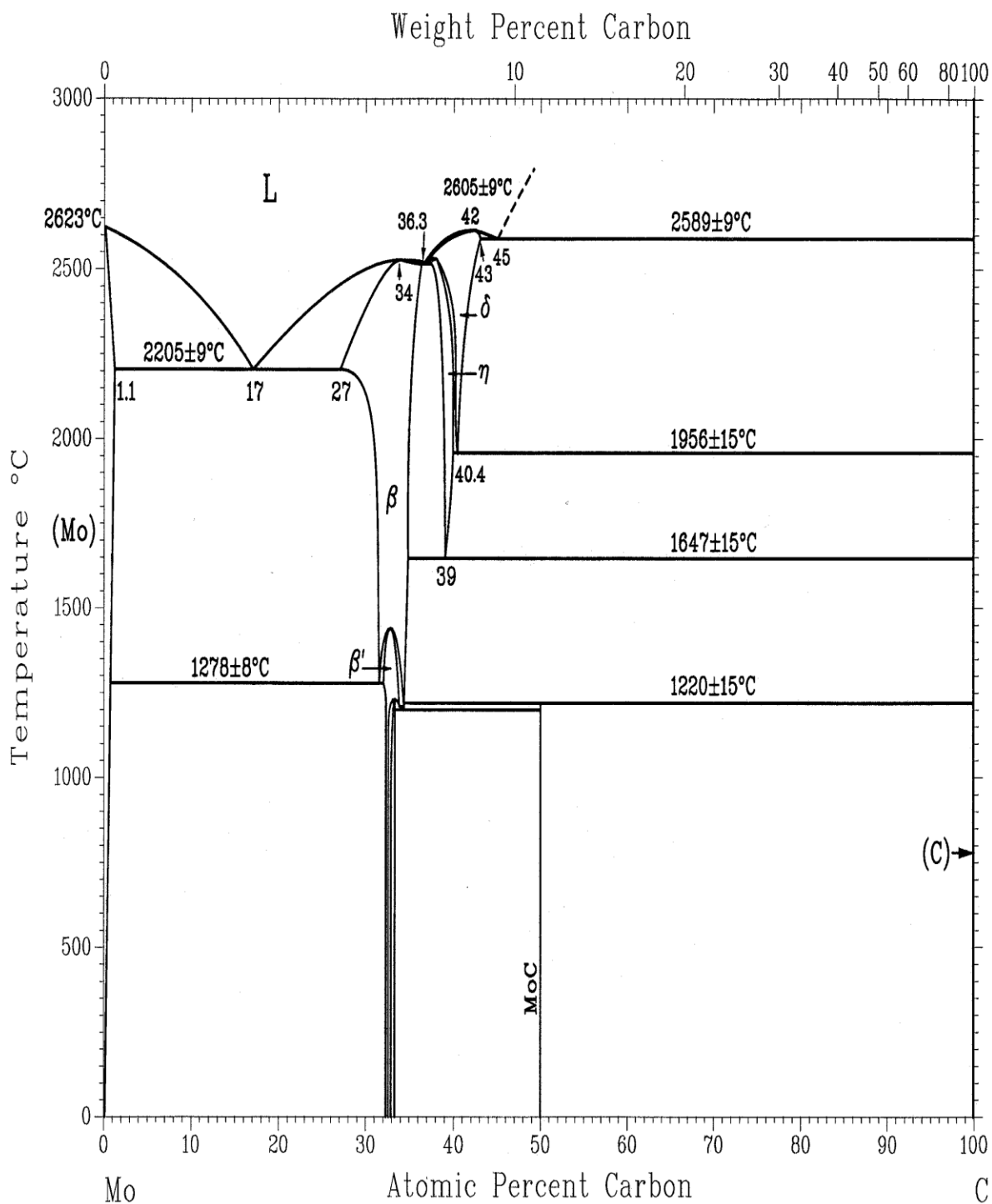
C - Ru

Data from SGTE 2011 alloy database

FactSage™

T(K)

4800

4300

3800

3300

2800

2300

1800

1300

800

300

LIQUID

LIQUID + GRAPHITE

HCP_A3

HCP_A3 + GRAPHITE

0   0.1   0.2   0.3   0.4   0.5   0.6   0.7   0.8   0.9   1

Ru/(C+Ru) (mol/mol)

Mo-C Phase Diagram

Weight Percent Carbon

D. Bandyopadhyay, B. Haldar, R.C. Sharma, and N. Chakraborti, "The Ti-Mo-C system (Titanium-Molybdenum-Carbon)" Journal of phase equilibria 1999, Vol. 20, No 3, pp. 333.

Nb-C Phase Diagram
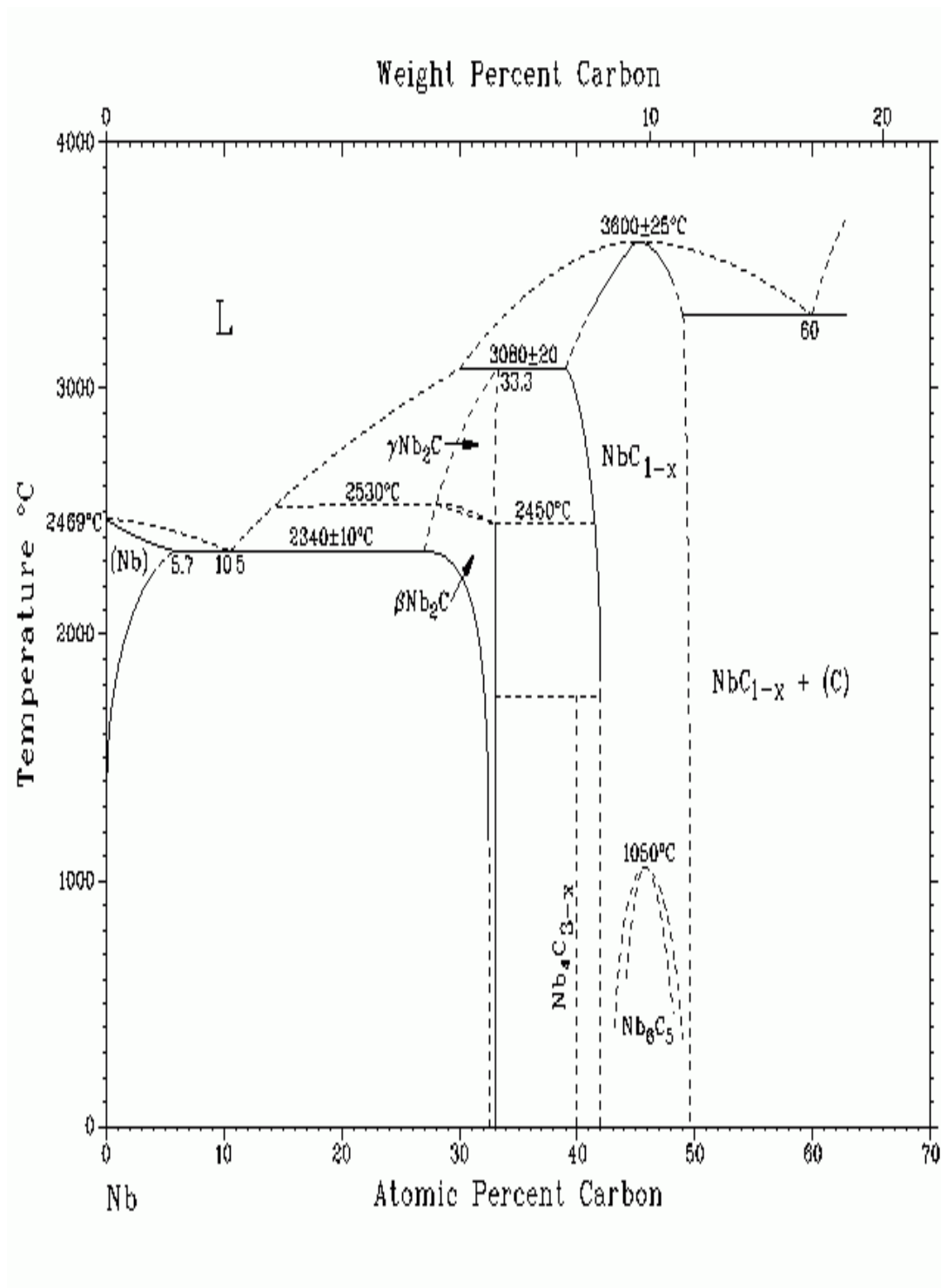
C-Nb (Carbon-Niobium) J.F. Smith, O.N. Carlson, and R.R. de Avillez.

Re-C Phase Diagram
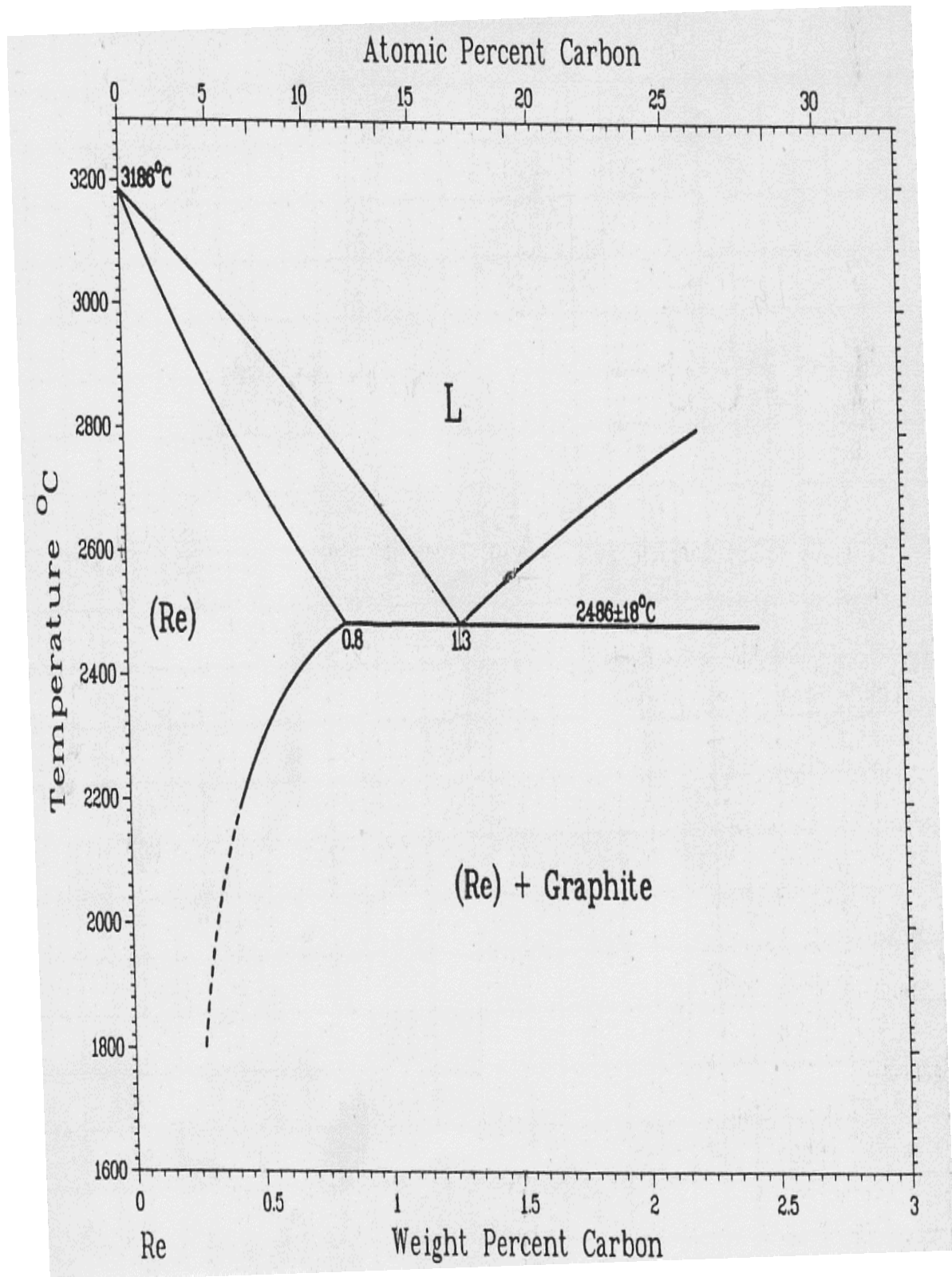
Re-C phase diagram copy provided by LNE-Cnam.

Ni-C Phase Diagram
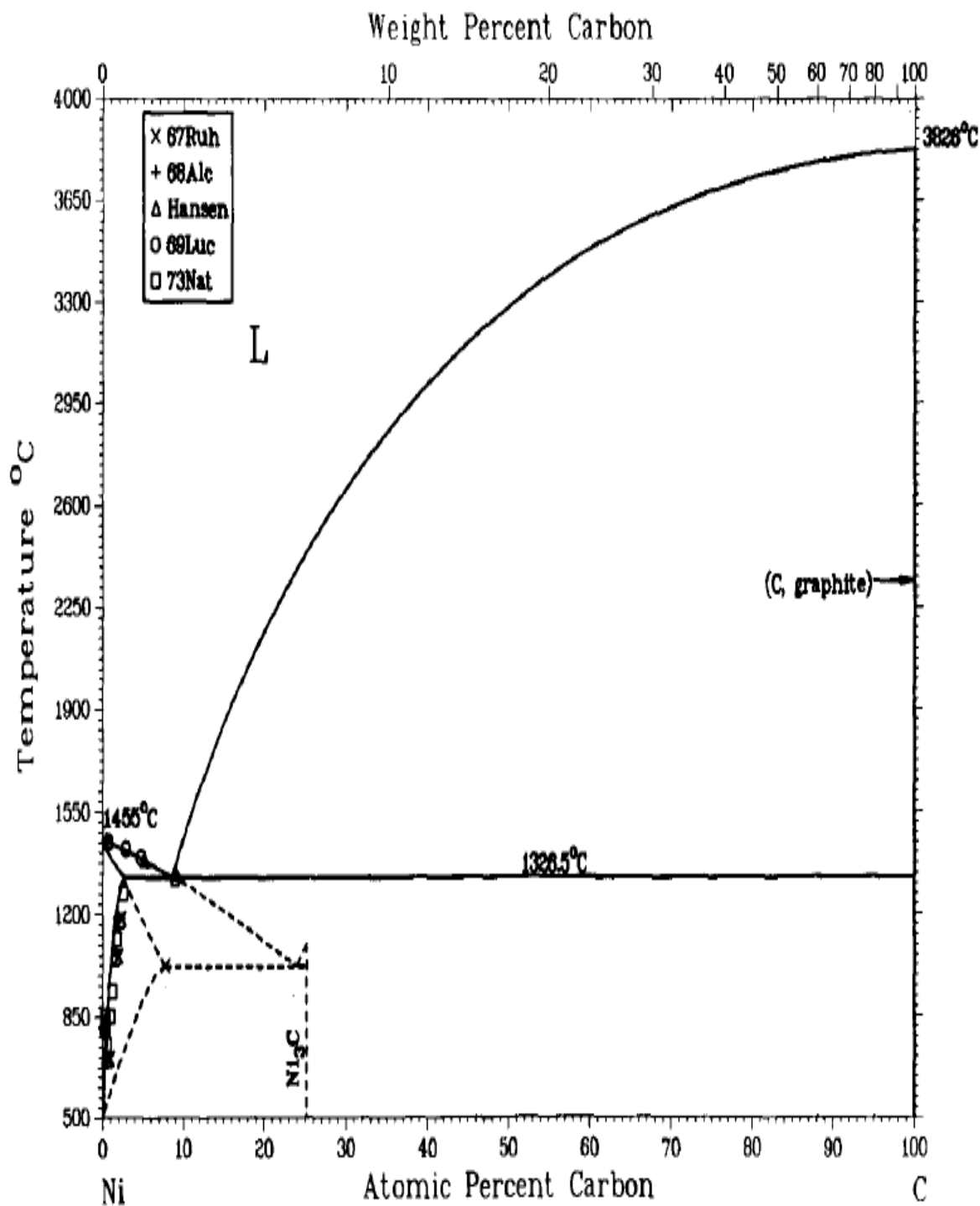
M. Singleton and P. Nash, "The C-Ni (Carbon-Nickel) System", Bulletin of Alloy Phase Diagrams, Vol 10, No. 2, 1989, pp.122.

Pd-C Phase Diagram

C - Pd

Data from SGTE 2011 alloy database

FactSage™

LIQUID

LIQUID + GRAPHITE

FCC_A1

FCC_A1 + GRAPHITE

T (K)

Pd/(C+Pd) (mol/mol)
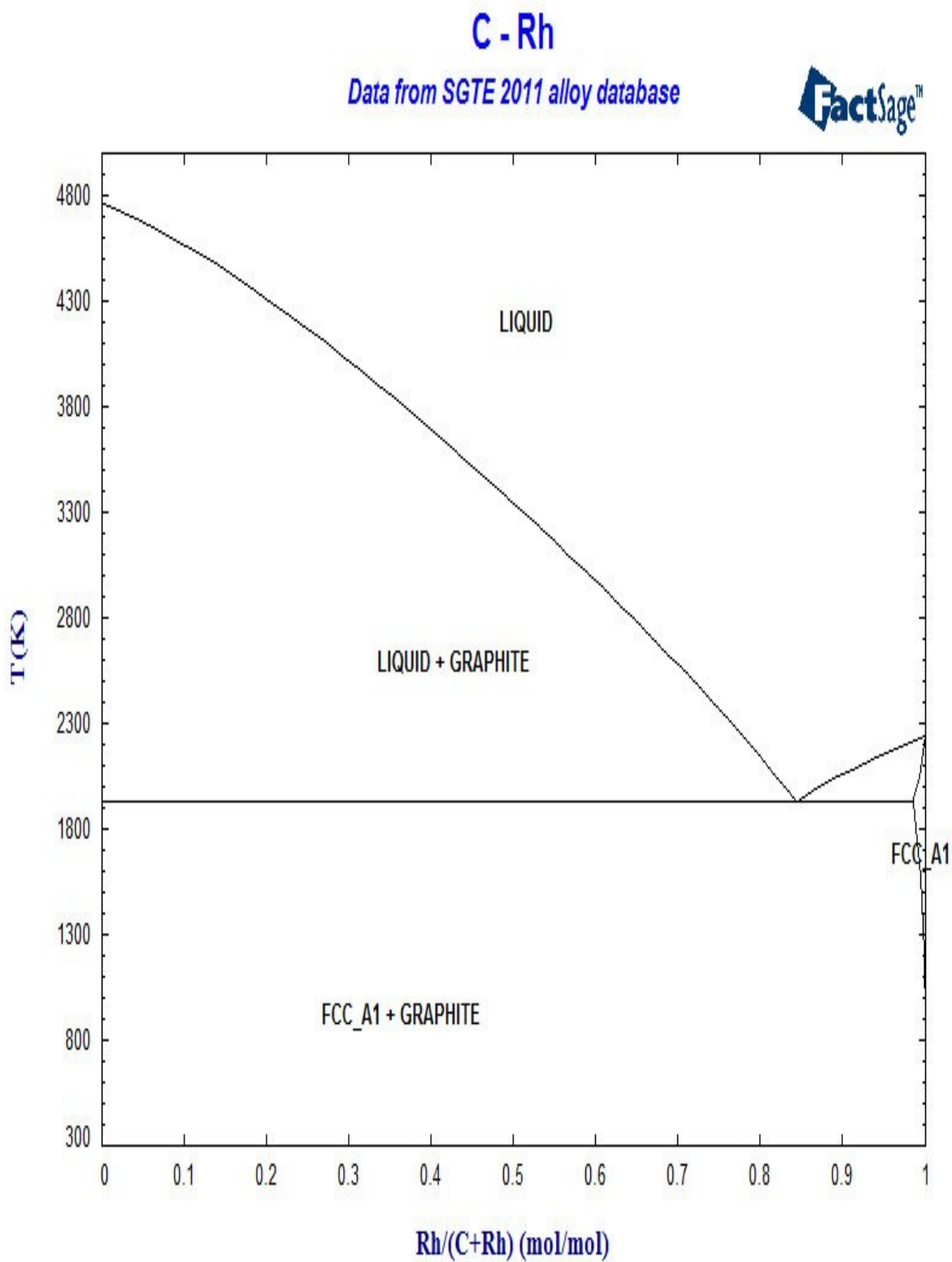
Rh-C Phase Diagram

Pt-C Phase Diagram
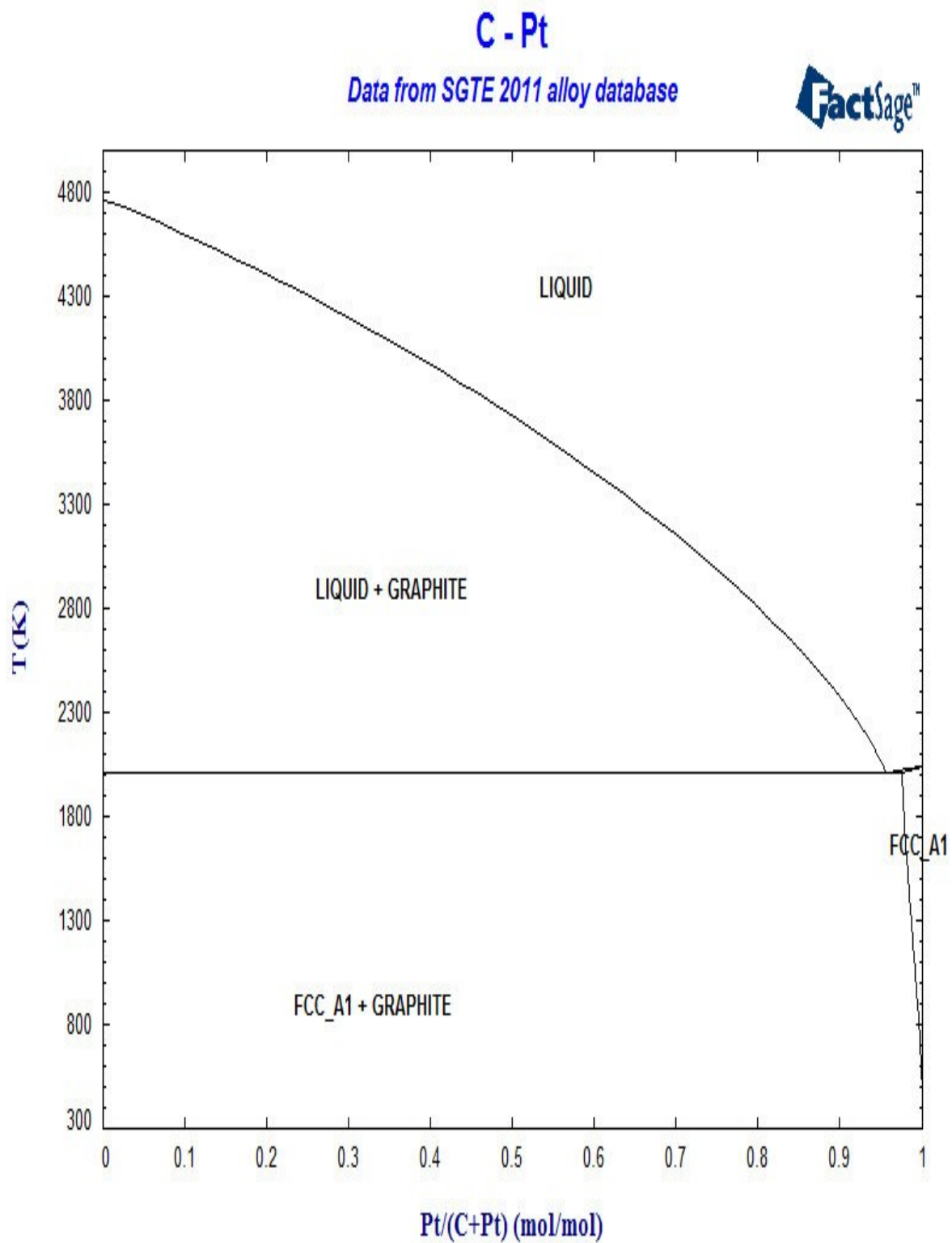
Ir-C Phase Diagram

C - Ir

Data from SGTE 2011 alloy database
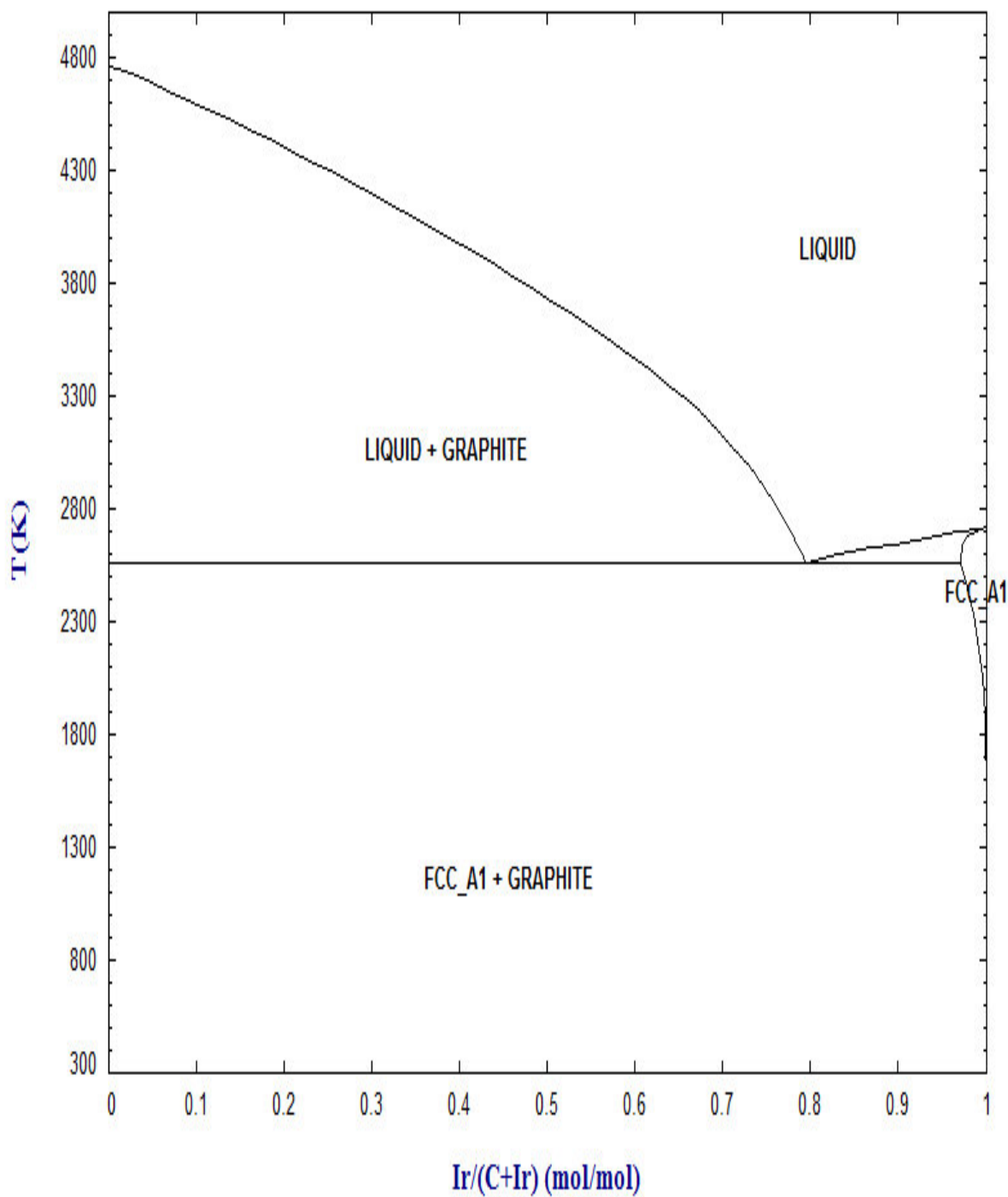
W-C Phase Diagram
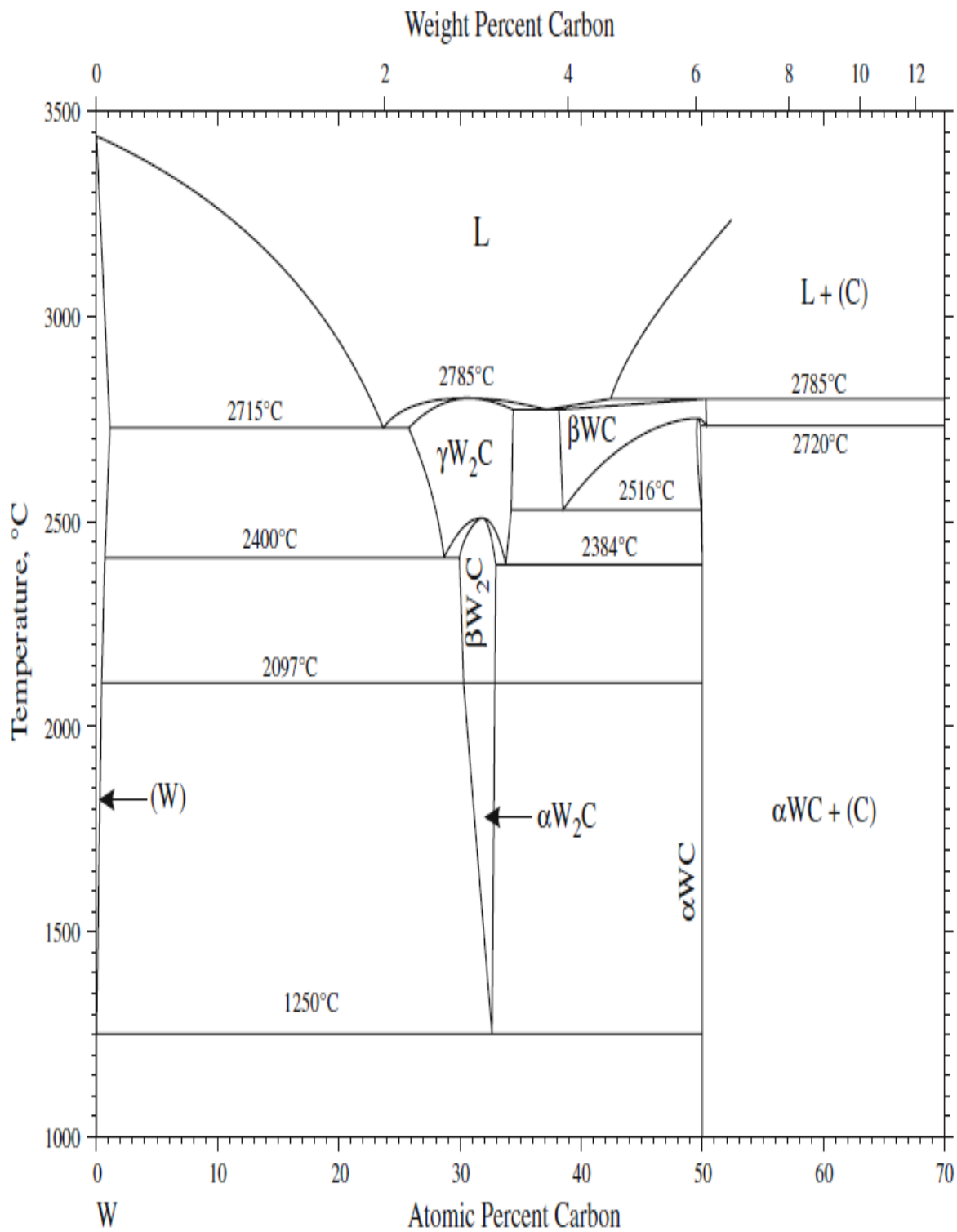
H. Okamoto, "C-W (Carbon-Tungsten)" Journal of Phase Equilibria and Diffusion Vol. 29 No. 6 2008, pp. 543.

Ta-C Phase Diagram

H. Okamoto, "C-Ta (Carbon-Tantalum)" Journal of Phase Equilibria Vol. 19 No. 1 1998, pp. 88.

Zr-C Phase Diagram
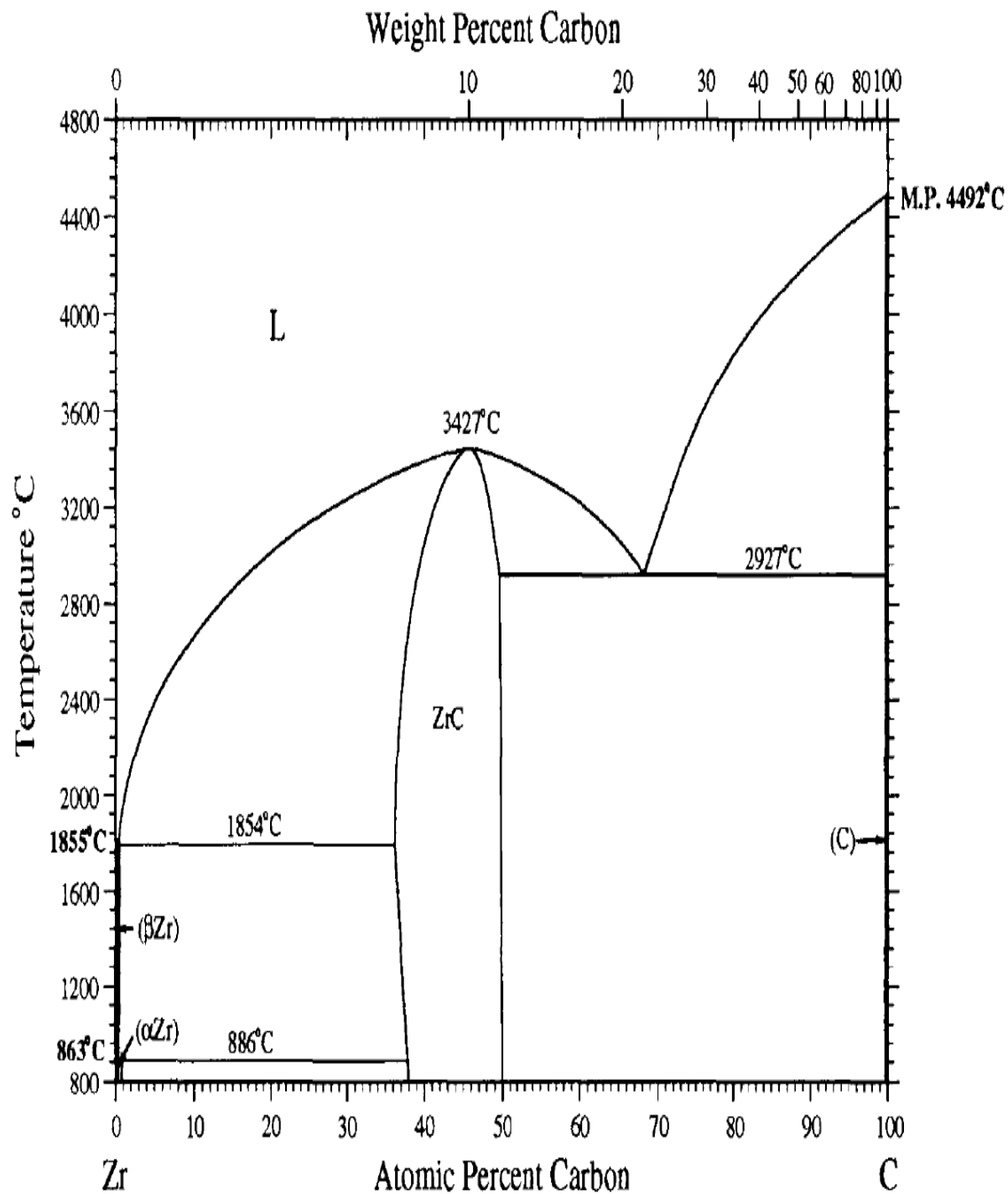
H. Okamoto, "C-Zr (Carbon-Zirconium)" Journal of Phase Equilibria Vol. 17 No. 2 1996, pp.162.

Hf-C Phase Diagram
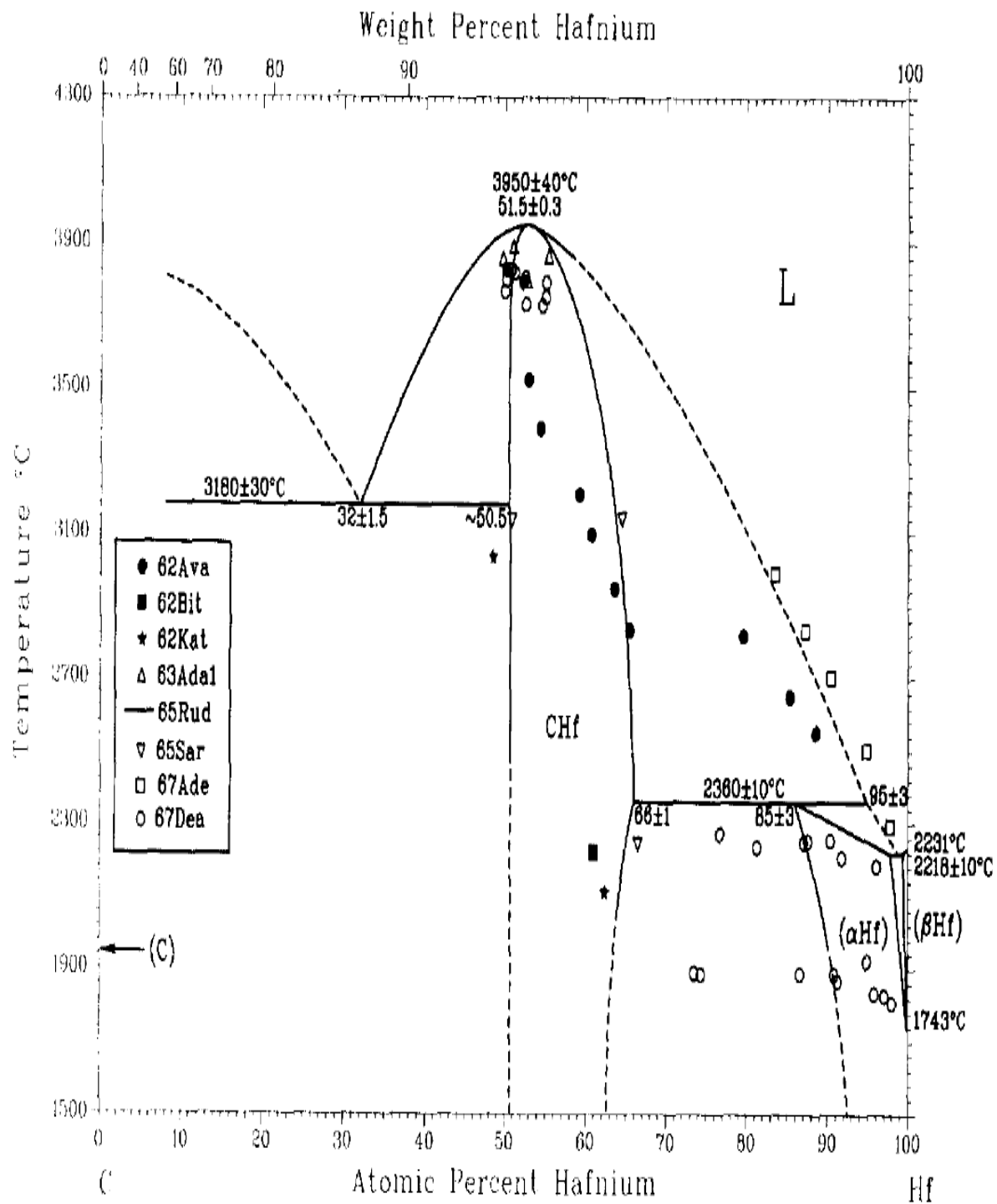
H. Okamoto, "C-Hf (Carbon-Hafnium) System" Bulletin of Alloy Phase Diagrams Vol. ii No. 4 1990, pp. 397

Appendix B

Compilation of Metal-Carbon Eutectic Cell's

Melting-Cooling Curves

Appendix B

Fe-C (99.998%) Thermal Cycling Melting/Solidification Curve 1st Test (Pyrometer)
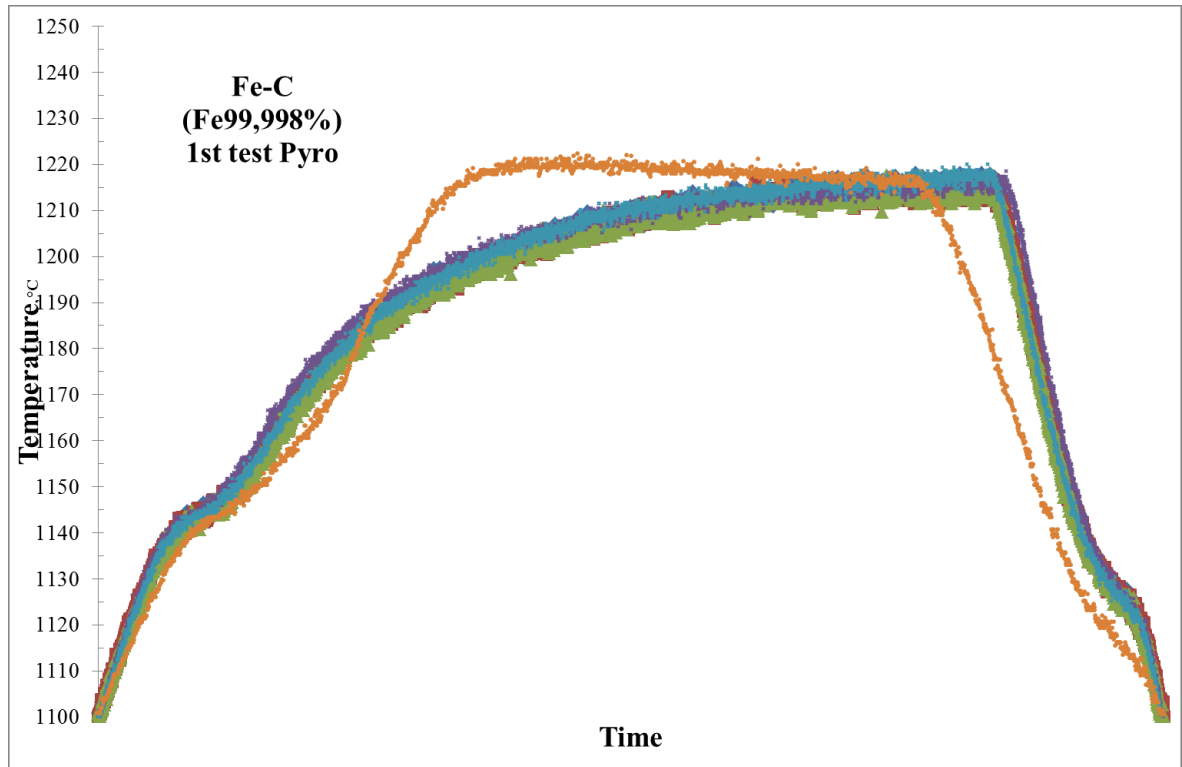
Fe-C (99.998%) Thermal Cycling Melting/Solidification Curve 2nd Test (Pyrometer)

Fe-C (99.998%) Thermal Cycling Melting/Solidification Curve 3rd Test (Pyrometer)

Fe-C (99.98%) Thermal Cycling Melting/Solidification Curve 1st Test (Pyrometer)

Fe-C (99.98%) Thermal Cycling Melting/Solidification Curve 2nd Test (Pyrometer)

Fe-C
(Fe99.98%)
2nd test Pyro

Fe-C (99.98%) Thermal Cycling Melting/Solidification Curve 1st Test (Thermocouple)

Fe-C
(Fe99,98%)
1st test TC
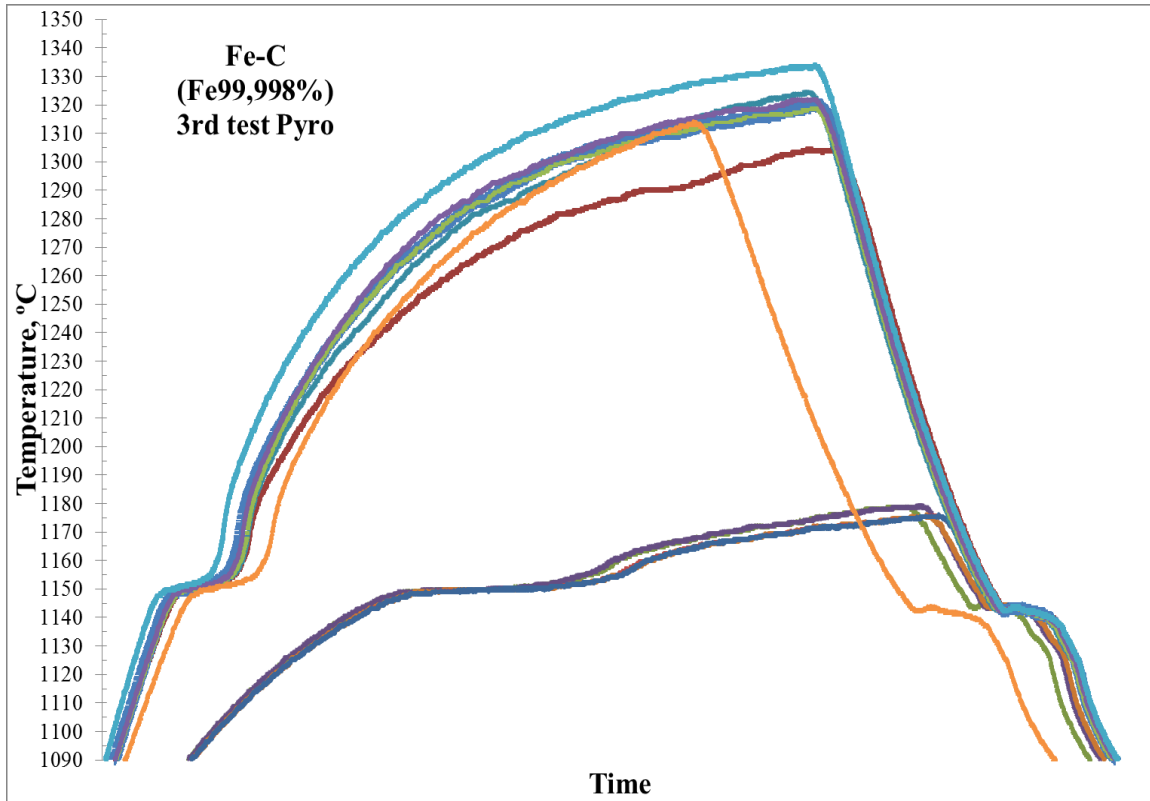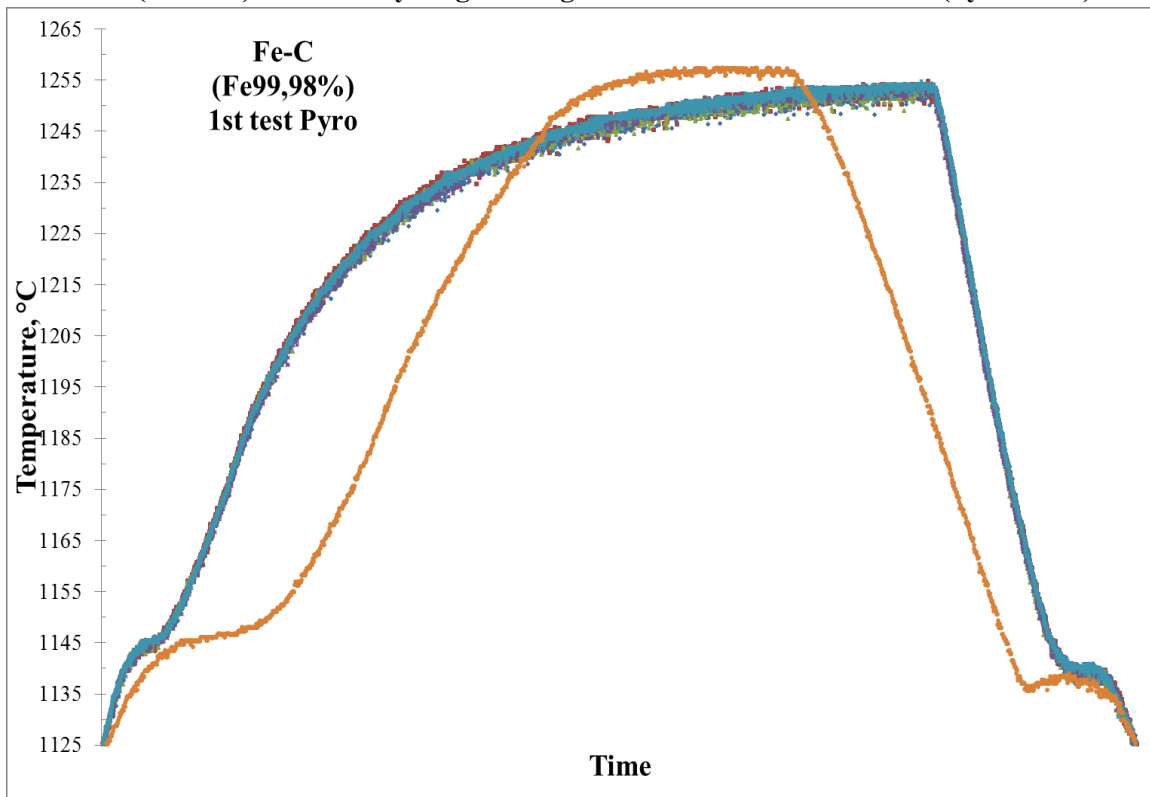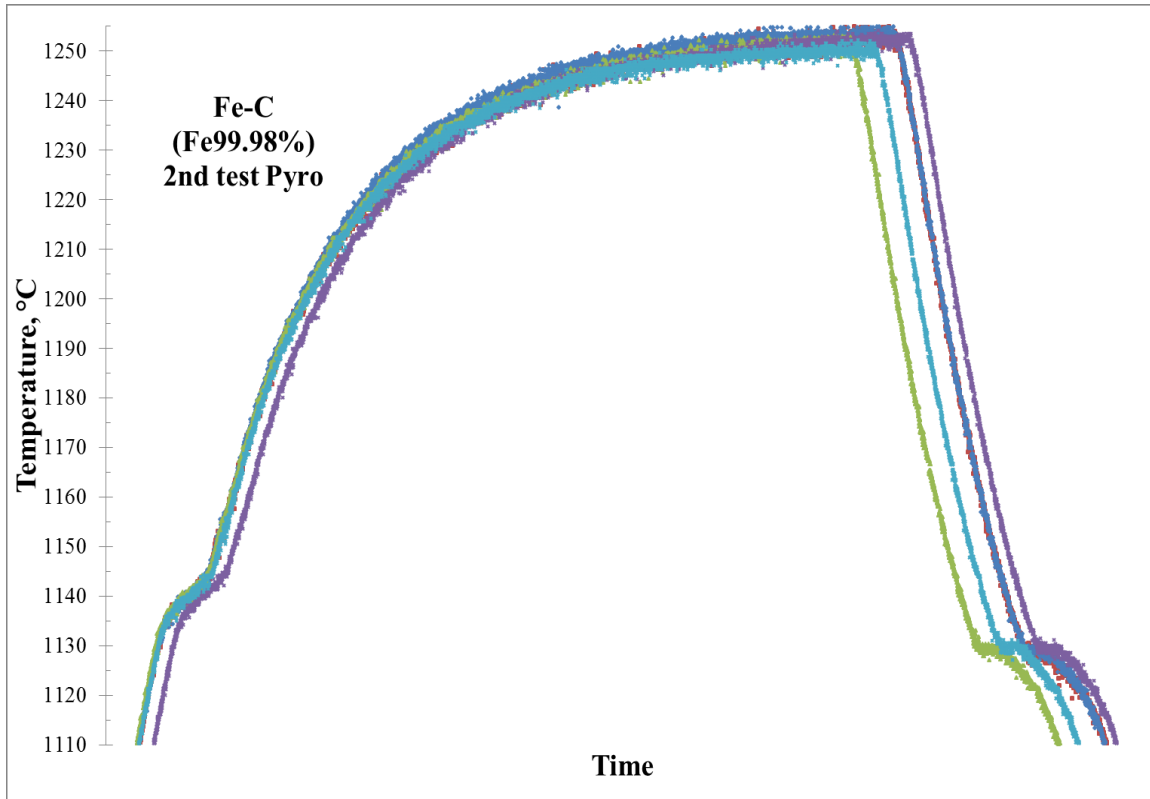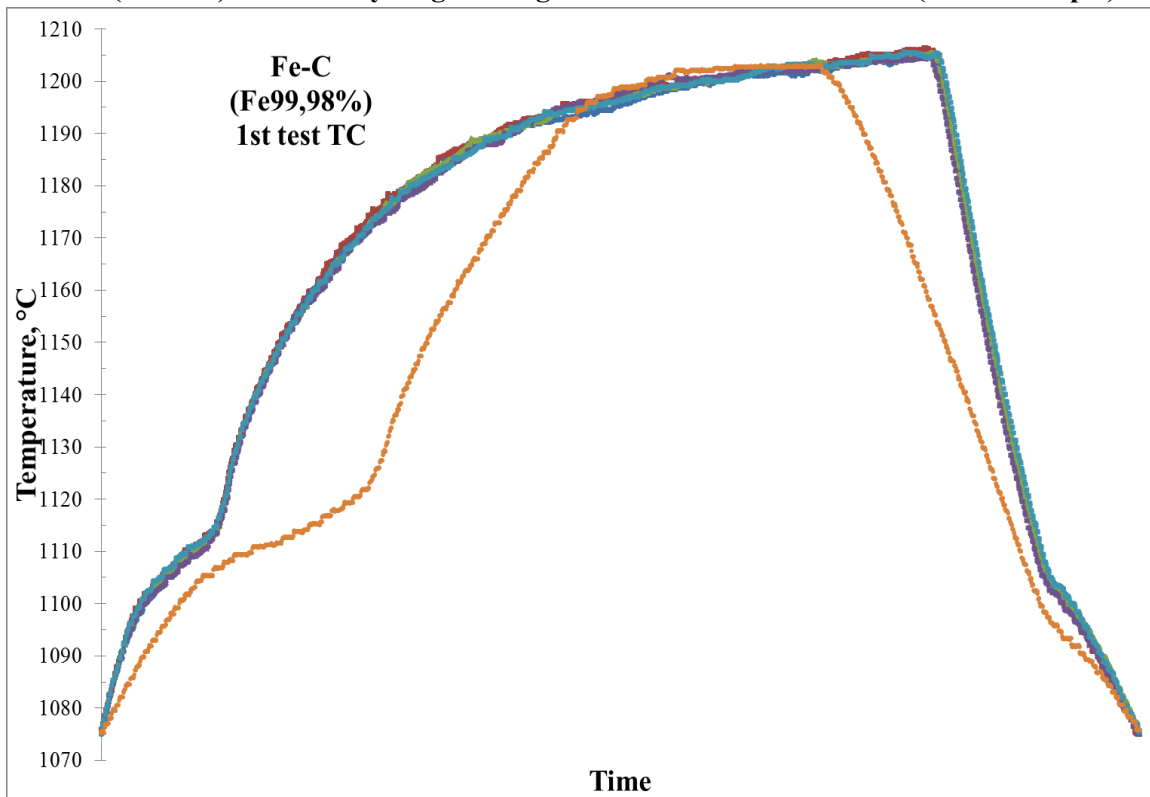
Fe-C (99.98%) Thermal Cycling Melting/Solidification Curve 2nd Test (Thermocouple)
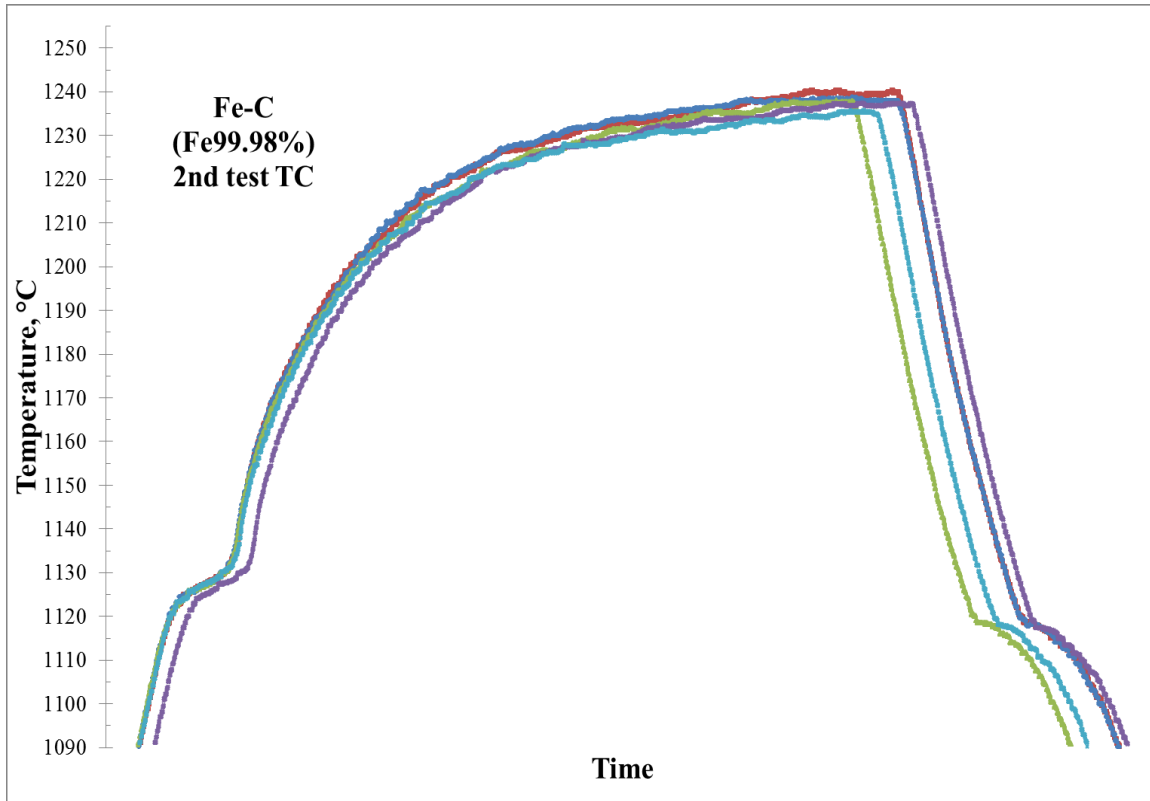
Fe-C (99%) Thermal Cycling Melting/Solidification Curve 1st Test (Pyrometer)
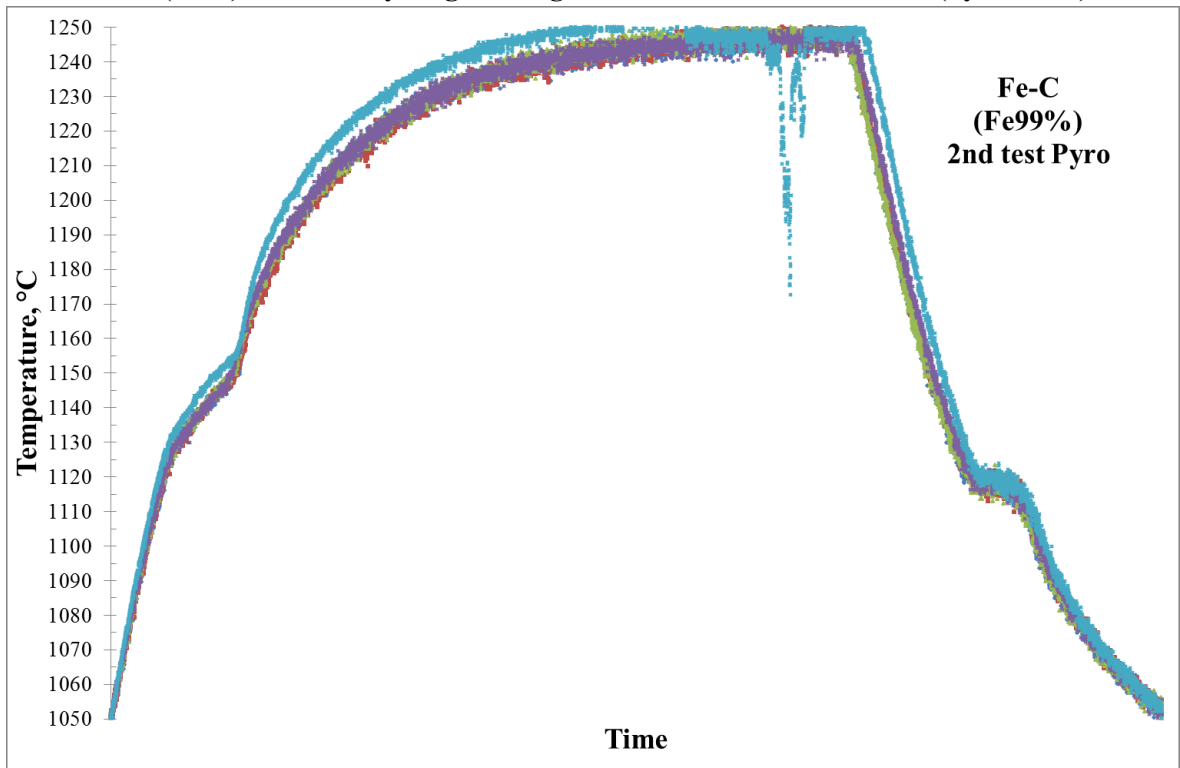
Fe-C (99%) Thermal Cycling Melting/Solidification Curve 1st Test (Thermocouple)

Fe-C (Fe99%)
1st test TC

Fe-C (99%) Thermal Cycling Melting/Solidification Curve 2nd Test (Pyrometer)

Fe-C
(Fe99%)
2nd test Pyro

Fe-C (99%) Thermal Cycling Melting/Solidification Curve 2nd Test (Thermocouple)

Fe-C (Fe99%) 2nd test TC
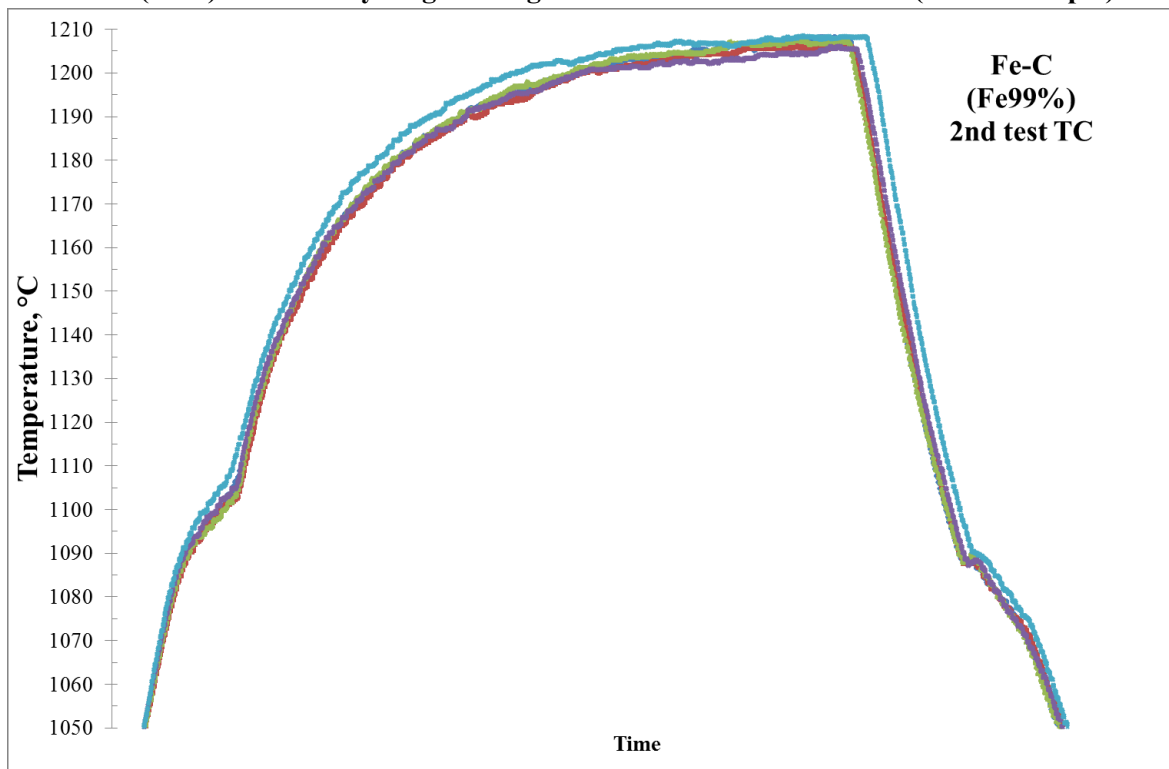
Co-C (Cell#8) Thermal Cycling Melting/Solidification Curve 1st Test
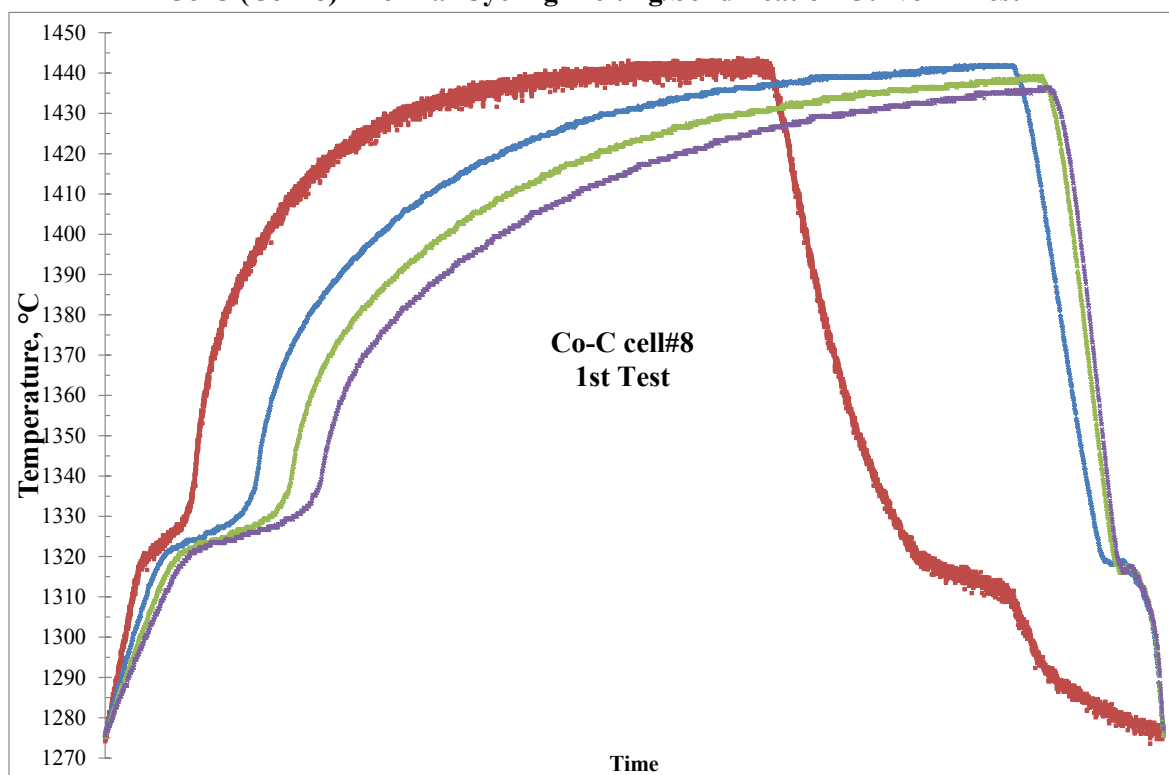
Co-C cell#8 1st Test

Co-C (Cell#8) Thermal Cycling Melting/Solidification Curve 2nd Test
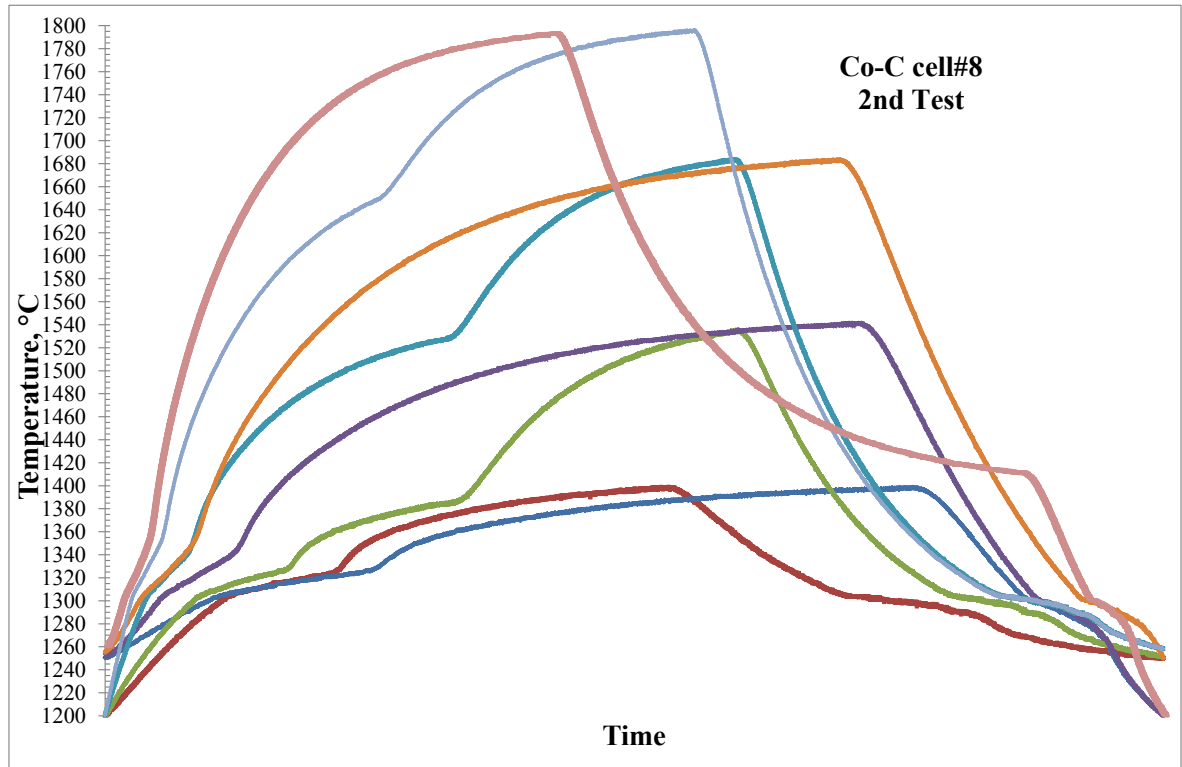
Co-C (Cell#8) Thermal Cycling Melting/Solidification Curve 3rd Test
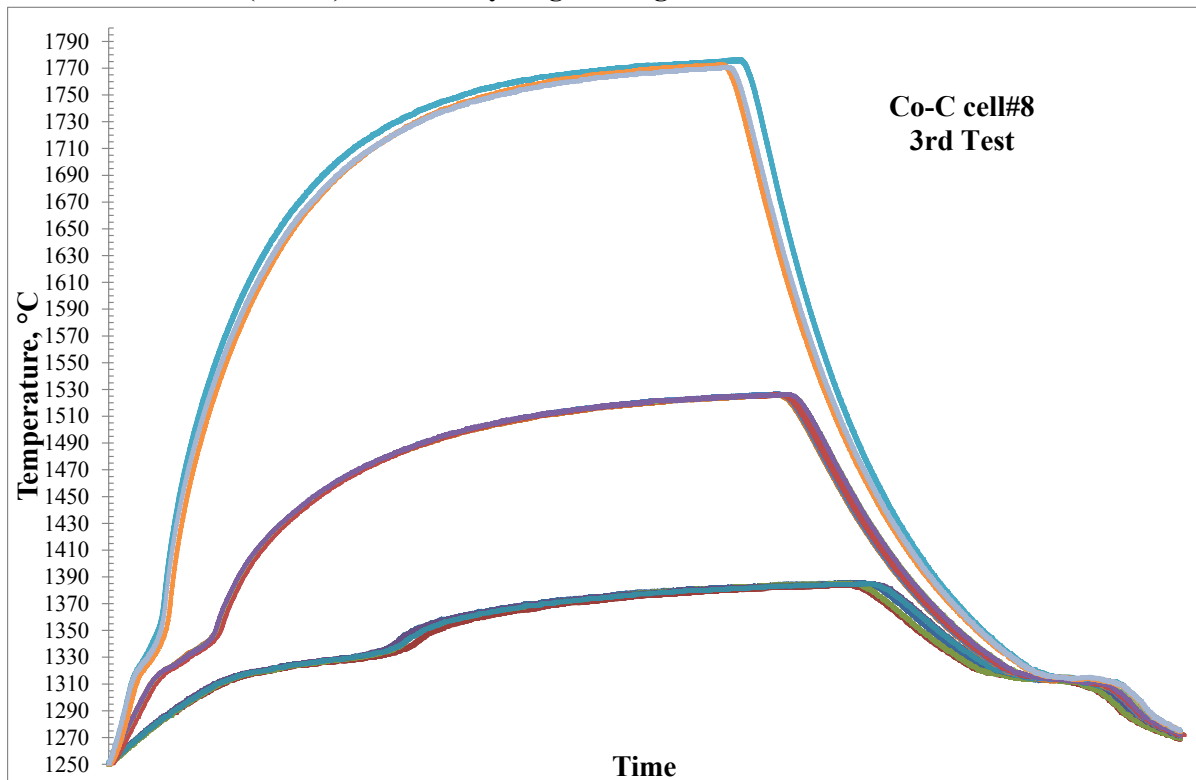
Ti-C (Cell#7) Thermal Cycling Melting/Solidification Curve 1st Test
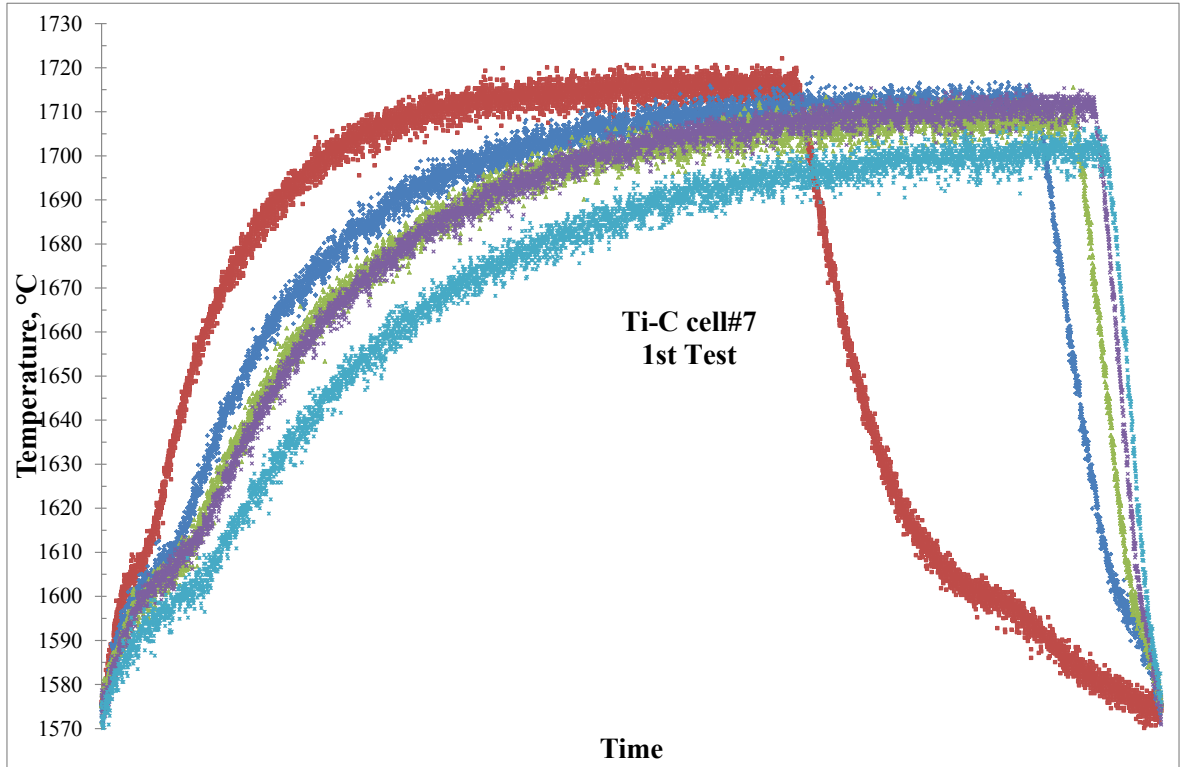
Ti-C cell#7
1st Test

Time

Ti-C (Cell#7) Thermal Cycling Melting/Solidification Curve 2nd Test

Ti-C cell#7
2nd test

Time
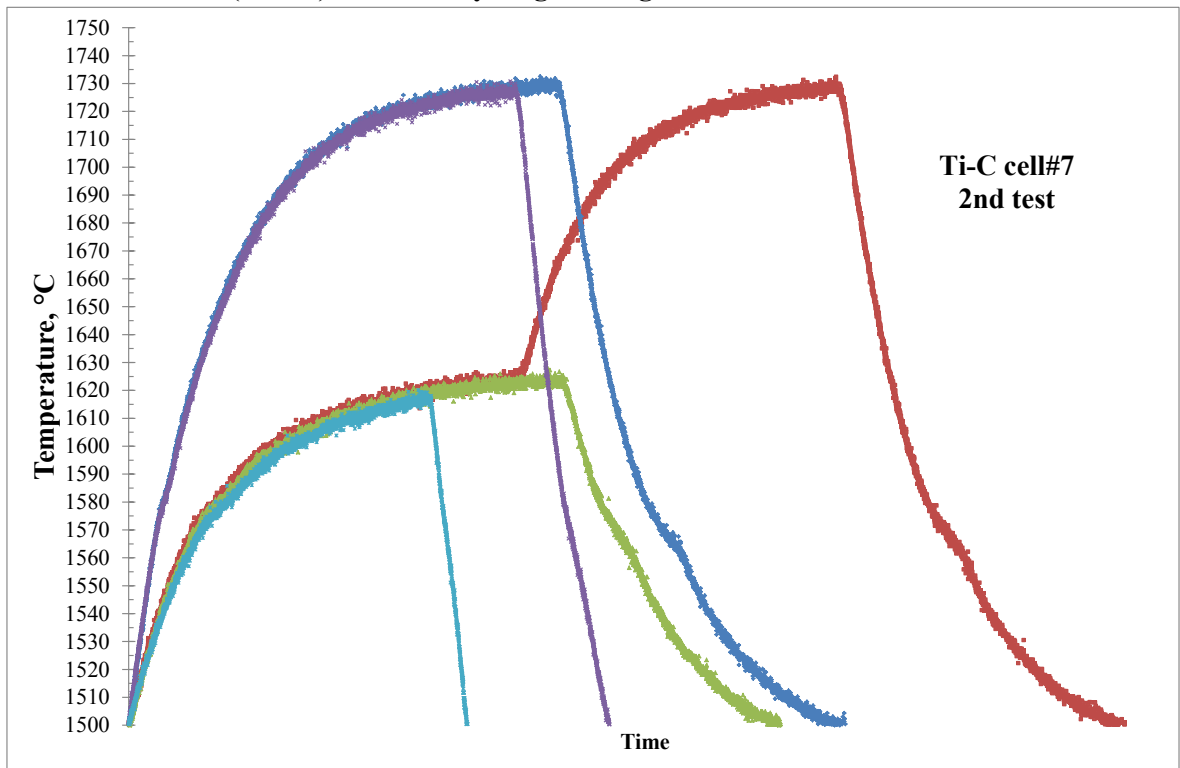
Ru-C (Cell#12) Thermal Cycling Melting/Solidification Curve 1st Test (Pyrometer)
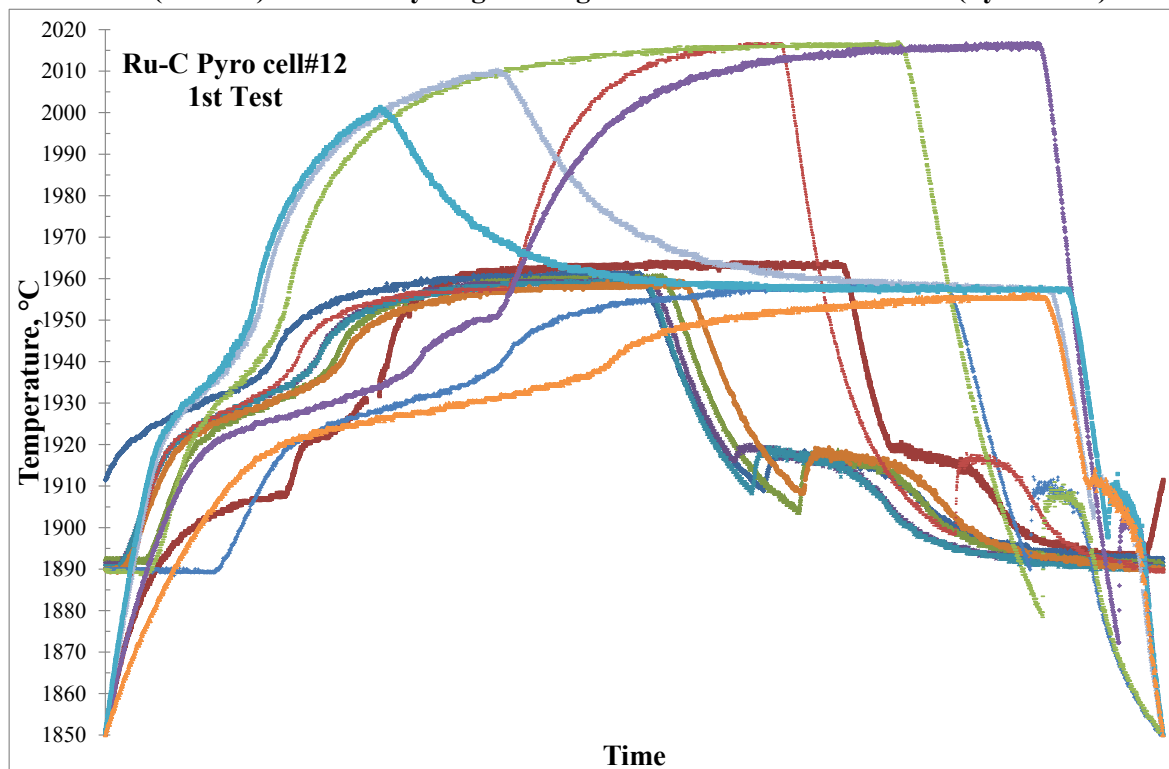
Ru-C (Cell#12) Thermal Cycling Melting/Solidification Curve 2nd Test (Pyrometer)
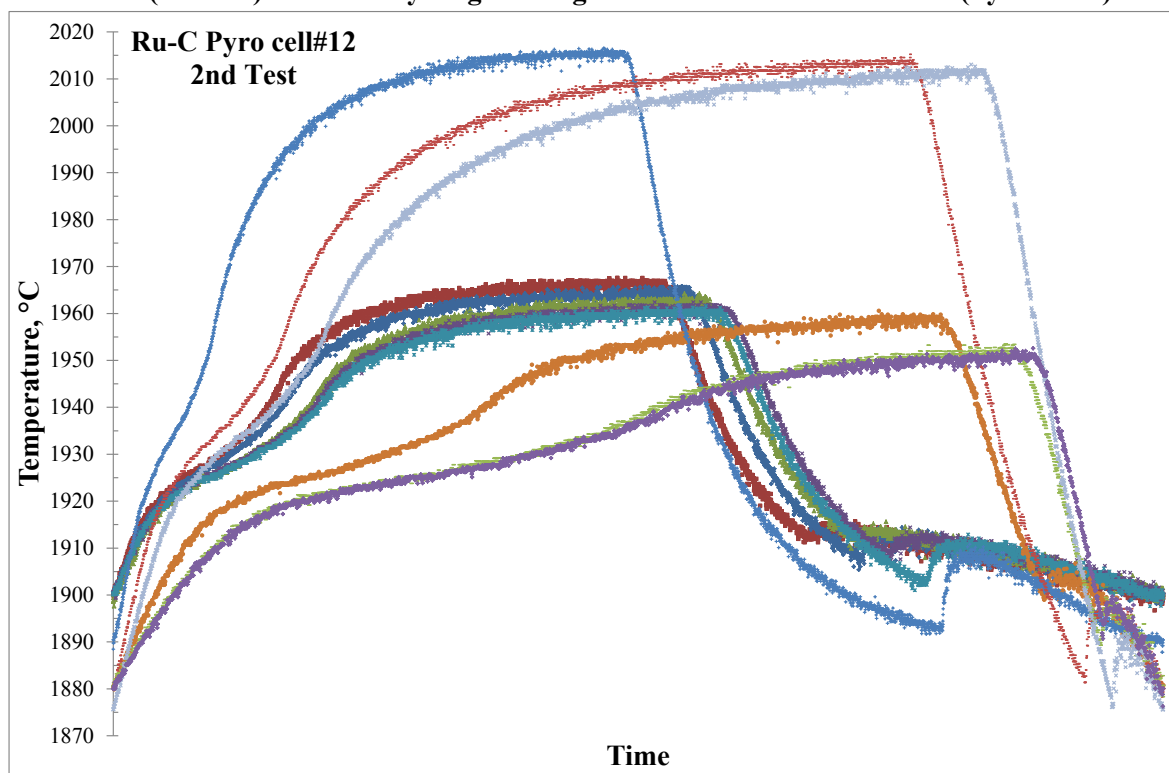
Ru-C (Cell#12) Thermal Cycling Melting/Solidification Curve 3rd Test (Pyrometer)
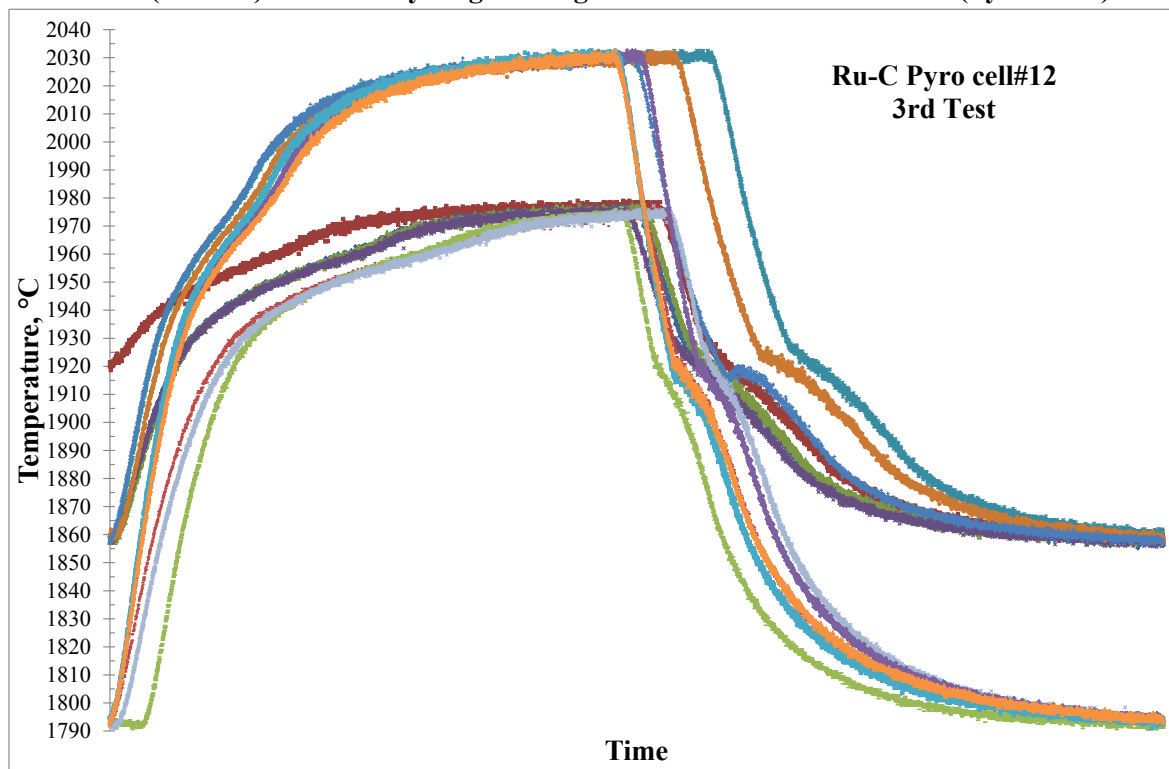
Ru-C (Cell#15) Thermal Cycling Melting/Solidification Curve 1st Test (Thermocouple)
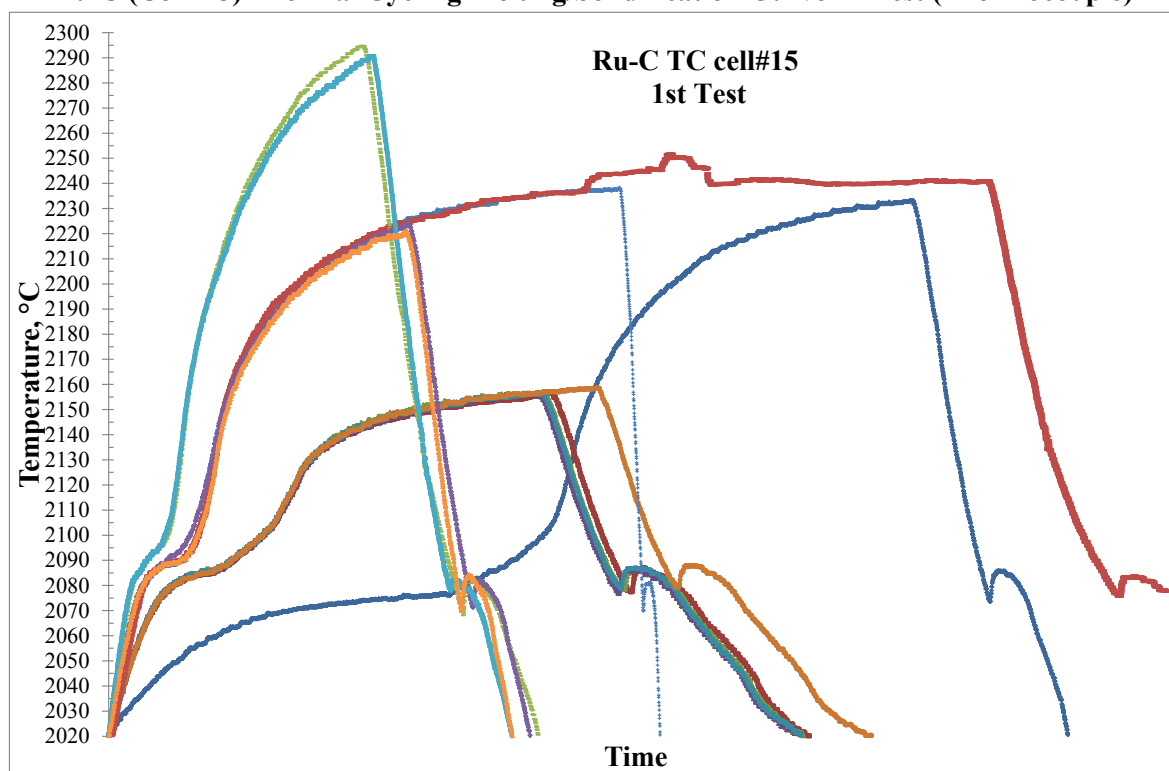
Ru-C (Cell#15) Thermal Cycling Melting/Solidification Curve 2nd Test (Thermocouple)
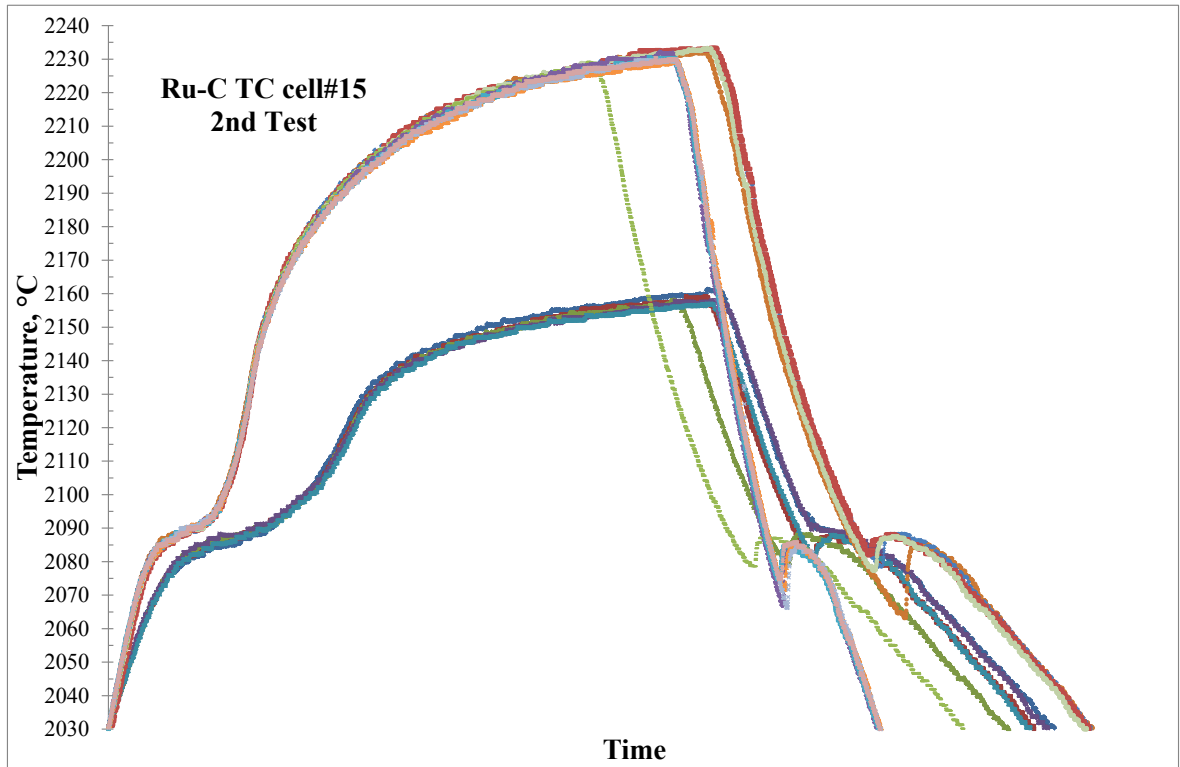
Appendix C

Material's Certificate of Inspection

Appendix C

Fe (99.998%) Certificate of Analysis

Certificate of Analysis

Alfa Aesar
A Johnson Matthey Company

Iron powder, -22 mesh, Puratronic®, 99.998% (metals basis)
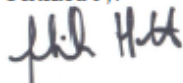
Stock Number: 10621
Lot Number: 24203

Analysis

Al	ND	Sb	ND	As	ND
Ba	ND	Bi	ND	B	ND
Cd	ND	Ca	ND	Cs	ND
Cr	7	Co	ND	Cu	1
Ge	ND	In	ND	Fe	Matrix
Pb	ND	Li	ND	Mg	ND
Mn	2	Mo	ND	Ni	1
Nb	ND	P	ND	K	ND
Rb	ND	Si	ND	Se	ND
Ag	ND	Na	ND	Sr	ND
Ta	ND	Te	ND	Tl	ND
Sn	ND	Ti	ND	W	ND
V	ND	Zn	3	Zr	ND

Values given in ppm unless otherwise noted
Analysis is weight for weight as determined by ICP-MS
ND: Not detected

Certified by:

Quality Control

Fe (99.98%) Certificate of Analysis

Certificate of Analysis

Alfa Aesar®
A Johnson Matthey Company

Iron granules, 1-2mm (0.04-0.08in), 99.98% (metals basis)
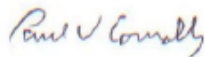
Stock Number: 39708
Lot Number: B18T031

Analysis

Carbon	0.0007 %
Sulfur	0.0013 %
Iron	Balance

+10 mesh	0.2 %
+35 mesh	99.4 %
-35 mesh	0.4 %

Certified by:

Paul V Connolly

Quality Control

Fe (99%) Certificate of Analysis

Certificate of Analysis

Alfa Aesar
A Johnson Matthey Company

Iron powder, -20 mesh, 99% (metals basis)

Stock Number: 14183
Lot Number: G17R024

Analysis

Purity	99.0 %
Particle size	-20 mesh

Gas atomized

Certified by:

Paul V Connolly

Quality Control

Co (99.998%) Certificate of Analysis

Certificate of Analysis

Alfa Aesar
A Johnson Matthey Company

Cobalt powder, -22 mesh, Puratronic®, 99.998% (metals basis)
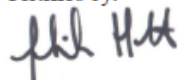
Stock Number: 10610
Lot Number: 24323

Analysis

Al	5	Sb	ND	As	ND	Ba	1
Bi	ND	B	ND	Cd	ND	Ca	ND
Cr	ND	Co	Matrix	Cu	ND	Ge	ND
In	ND	Fe	6	Pb	ND	Mg	ND
Mn	ND	Mo	ND	Ni	ND	Nb	ND
Si	ND	Ag	ND	Na	ND	Sr	ND
Ta	ND	Tl	ND	Sn	ND	Ti	ND
W	ND	V	ND	Zn	ND	Zr	ND

Values given in ppm unless otherwise noted
All figures above are weight for weight as determined by
Inductively Coupled Mass Spectroscopy
ND: Not detected

Certified by:

Ti (99.995%) Certificate of Analysis

Certificate of Analysis   *Alfa Aesar*
A Johnson Matthey Company

Titanium slug, 3.175mm (0.125in) dia x 3.175mm (0.125in) length, Puratronic®,
99.995% (metals basis)

Stock Number: 42394
Lot Number: J28W058

Analysis

Ti   99.998 %
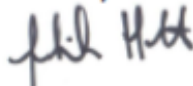
Ag	< 0.05	Al	1	As	< 0.01	Au	< 0.05
B	0.03	Ba	< 0.005	Be	< 0.005	Bi	< 0.01
Br	< 0.05	C	93	Ca	< 0.2	Cd	< 0.05
Ce	< 0.005	Cl	0.09	Co	0.05	Cr	0.3
Cs	< 0.01	Cu	0.35	F	< 0.05	Fe	9.45
Ga	< 0.05	Ge	< 0.05	H	1.5	Hf	< 0.01
Hg	< 0.1	I	< 0.01	In	< 0.05	Ir	< 0.01
K	< 0.01	La	< 0.005	Li	< 0.005	Mg	< 0.05
Mn	0.033	Mo	< 0.05	N	15.5	Na	< 0.01
Nb	< 0.2	Nd	< 0.005	Ni	0.215	O	309
Os	< 0.01	P	0.3	Pb	< 0.01	Pd	< 0.01
Pt	< 0.05	Rb*	< 5	Re	< 0.01	Rh	< 0.15
Ru	< 0.01	S	6	Sb	< 0.05	Sc	< 0.05
Se	< 0.05	Si	1.35	Sn	< 0.05	Sr*	< 3000
Ta**	< 5	Te	< 0.05	Th	< 0.0005	Tl	< 0.01
U	< 0.0005	V	0.09	W	< 0.01	Y*	< 200
Zn	< 0.05	Zr	0.8				

Values given in ppm unless otherwise noted
Carbon, hydrogen, nitrogen, oxygen and sulfur determined by LECO
All other elements determined by GDMS
* Ion interference
** Instrument contamination

Certified by:

Quality Control

Ru (99.9%) Certificate of Analysis

ACROS ORGANICS

Certificate of Analysis

Product 19810
Ruthenium,99.9%,(trace metal basis),-200 mesh
, powder

General Product Data

Version	0
CAS No	7440-18-8
Country of origin	UNITED STATES OF AMERICA
Molecular weight	101.07
Molecular formula	Ru
Linear formula #	

Product Specifications

Appearance	GREY POWDER
Total trace metal imp.	=<0.1 %

Lot Specific Data : A0312992

Appearance	GREY POWDER
Total trace metal imp.	=<0.1 %

Issued: 12-06-13
L. Van den Broek, QA Manager

Acros Organics   ENA23, zone 1, nr 1350, Janssen Pharmaceuticalaan 3a, B-2440 Geel, Belgium
Tel +32 14/57.52.11 - Fax +32 14/59.34.34 Internet: http://www.acros.com
1 Reagent Lane, Fair Lawn, NJ 07410,USA
Fax 201-796-1329

Mo (99.999%) Certificate of Analysis

Certificate of Analysis — Alfa Aesar
A Johnson Matthey Company

Product No.:   12972

Product: Molybdenum powder, -22 mesh, Puratronic®, 99.999%
                  (metals basis excluding W), W <1000ppm

Lot No.:   22982

Al	ND	Sb	ND	Ba	ND
Bi	ND	B	5	Cd	ND
Ca	ND	Cr	ND	Co	ND
Cu	ND	Ga	ND	Ge	ND
In	ND	Fe	ND	Pb	ND
Mg	ND	Mn	ND	Ni	ND
Nb	ND	Si	ND	Ag	ND
Sr	ND	Ta	ND	Tl	ND
Sn	ND	Ti	ND	W	< 10
V	ND	Zr	ND		

Values given in ppm unless otherwise noted
Values are weight for weight as determined by Emission Spectroscopy
Tungsten determined by ICP
ND: Not determined

Nb (99.8%) Certificate of Analysis

Certificate of Analysis

Niobium powder, -325 mesh, 99.8% (metals basis)

Stock Number: 10275
Lot Number: H15L41

Analysis

Al	0.003	Cr	0.005	Fe	0.02
Mn	0.001	Mo	0.003	Ni	0.0035
Si	0.003	Ti	0.003	W	0.004
H	0.01	C	0.008	O	0.3
N	0.07	Nb	Balance		

Values given in wt% unless otherwise noted

Certified by:

Paul V Connolly

Quality Control

Appendix D

Material's Purity Certificate

Appendix D

W (99.998%) Certificate of Analysis

KETE

株 洲 凯 特 实 业 有 限 公 司
ZHUZHOU KETE INDUSTRIES CO. LTD

产 品 质 量 证 明 书
CERTIFICATE OF QUALITY

超 纯 钨 粉

Ultrapure Tungsten Powder

生产批号：

Batch No. UW10-601

主含量：W ≮ 99.998%

Main Content: W 99.998%min

杂质成份：(%，不大于)

Impurities: (%， max)

K <0.000005	Na<0.00007	Ca 0.000021	Fe 0.00012
Ta<0.0001	Pb<0.000008	Cu<0.000005	Sn<0.000005
Ba<0.000005	Mn<0.0000001	Be<0.000001	Pt<0.000001
Co<0.000001	Cd<0.000001	Cr 0.00053	Mo<0.000029
Mg<0.000005	Zn<0.000005	Sb<0.000001	Al<0.000017
Ni 0.000018	Ti<0.000004	Bi<0.000005	As<0.000004
Re 0.00025	Si<0.00023	Ge<0.000001	P<0.00012
Cl<0.00022	Th< 0.0000006	U<0.00000002	

签 发 人：
Signature:

日期：2010-06-09
DATE: June/9th/2010

Ta (99.99%) Certificate of Analysis

株 洲 凯 特 实 业 有 限 公 司
ZHUZHOU KETE INDUSTRIES CO., LTD

产 品 质 量 证 明 书
CERTIFICATE OF QUALITY

金 属 钽 粉
Tantalum Powder

生产批号：
Batch No.　TA10-507

主含量：
Main Content:　Ta 99.99% min

杂质成份：(%，不大于)
Impurities:　(% ,　max)

Nb < 0.0020　　Ti < 0.0001　　W < 0.0010　Mo < 0.0010
Cr < 0.0009　　Mn < 0.0001　Fe < 0.0005　Ni < 0.0005
Si < 0.0015

签 发 人：
Signature

日期：　2010-06-09
Date: June/9th/2010

Re (99.999%) Certificate of Analysis

株 洲 凯 特 实 业 有 限 公 司
ZHUZHOU KETE INDUSTRIES CO. LTD

产 品 质 量 证 明 书
CERTIFICATE OF QUALITY

超 纯 铼 粉

Ultrapure Rhenium Powder

生产批号：

Batch No. RP10-501

主含量：　　　Re ≮ 99.999%
Main Content:　Re　99.999%min

杂质成份：(%, 不大于)
Impurities: (% ,　max)

K <0.00005	Na<0.00005	Ca<0.00005	Fe<0.00005
W <0.00005	Pb<0.00001	Cu<0.00001	Sn<0.00001
Ba<0.00001	Mn<0.00001	Be<0.00001	Pt<0.00001
Co<0.00001	Cd<0.00001	Cr <0.00001	Mo<0.00005
Mg<0.00001	Zn<0.00001	Sb<0.00001	Al<0.00001
Ni <0.00002	Ti <0.00002		

签 发 人：
Signature:

日期：2010-06-09
DATE: June/9th/2010

Appendix E

PhD Thesis Defense Presentation

Appendix E

PhD Thesis Defense Presentation Slides

CEA Cadarache Research Center

» French Atomic and Alternative Energies Commission

» CEA Employees: ~16,000

» CEA Cadarache: ~4,000 people

   » Department of Nuclear Technologies (DTN) ~250

» LMA (Severe Accident Mastery Laboratory): Experimental/Code Development research. ~30

» PLINIUS experimental platform:
> VULCANO: MCCI and corium spreading (rheology) research.
> KROTOS: FCI and steam explosions research.
> COLIMA: fission products aerosol production research.
> VITI: small scale material interaction and physical properties research.
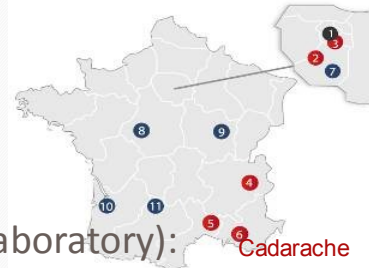
Context of PhD Subject

» Nuclear reactor core meltdown
> Lack of adequate heat extraction from the fuel elements.

» After TMI-2 accident, great need to acquire understanding on the progression and consequences of severe accidents.
> The VULCANO facility was built after the Chernobyl accident.
> Fukushima NPP accident, 3 melted BWR cores: renewed interest

» The NRSA experimental research posses many technological challenges
> Produce a urania based corium melt (>2500°C),
> Monitor its behavior as it reacts with reactor structure, containment, control and coolant materials.

» Temperature measurement are essential for the determination of the thermo-physical, -chemical and -dynamic properties of materials.

Context of PhD Subject (ITS)

» The International Temperature Scale is based on the assignment of values to a selected number of sensibly distributed fixed points
> Phase equilibrium temperatures as triple, freezing, melting and boiling points of selected substances.
> Interpolation among them is utilized with specific type of thermometers and assigned formulae.

» Highest temperatures reference points: equilibrium freezing point of
> silver (961.78°C),
> gold (1064.18°C)
> copper (1084.62°C).

» For technological reasons beyond the copper melting temperature no more melting points are available, and the scale is defined using Planck's radiation law.

$$\frac{L_\lambda(T_1)}{L_\lambda(T_2)} = \frac{\left(exp\left(\frac{c_2}{\lambda T_2}\right) - 1\right)}{\left(exp\left(\frac{c_2}{\lambda T_1}\right) - 1\right)}$$

PhD research objectives 1/3

» This PhD research is focused on the improvement of temperature measurements in severe accident experiments (MCCI), but the findings are suitable for high temperature thermometry in general.

» The need for high temperature measurements and materials in the aerospace/aeronautic industry, nuclear safety, fusion reactors, etc., demand the improvement of high temperature measurements above 1200°C, with a reasonable uncertainty (not a 100mK precision as in metrology).

» In VULCANO tests at CEA Cadarache, it is critical to trace the corium temperature, concrete ablation rate and heat convection from the melt to the concrete walls as the test progresses.

» It is of great importance to obtain reliable temperature measurements in order to interpret the severe accident tests, if not this can lead to erroneous conclusions and misunderstanding of the MCCI phenomenology.

PhD research objectives 2/3

» <u>Main sources of error in VULCANO MCCI test</u>:

> Disruption of pyrometer measurements by fine dust particles, fumes and gases evolved during MCCI tests. Influence of selective absorption bands from water vapor and carbon mono/dioxide, fluctuations in corium emissivity due to composition and temperature evolution.

➤ Electromagnetic interference on the thermocouple measurements (disruption of Seebeck thermoelectric effect) caused by induction heating (utilized to emulate fission product radioactive decay heat).

➤ In-melt thermocouple destruction by the corium due to the intense thermal shock caused by the large temperature difference between the corium melt (>2000°C) and the concrete test section (room temperature), and/or dissolution of the protective sheath materials, by highly eroding superheated oxide-metallic melt.
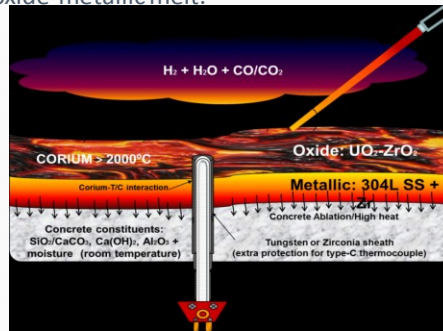
PhD research objectives 3/3

» <u>Application of Metal-Carbon Eutectic Cells as High Temperature Fixed Points</u>

> Extensive work on high temperature metal-carbon eutectic systems to gain insight on its solid↔liquid transformation temperature reproducibility and non-equilibrium behavior under extreme temperature ramps typical of SA tests.

> Fixed point cells can greatly diminish the impact of thermometer-drift by providing a practical mean for on-site calibration of instruments which are used in nuclear-grade facilities, and reduction on time-consuming recalibration at manufacturer facilities or metrology labs.

> If coupled with thermometers the cell can serve as an *in situ* reference point for in-melt corium thermometry.

» <u>Development of TC Sheath for corium melt thermometry</u>

> After extensive discussion with PLINIUS staff and literature search on oxide/metallic corium melts, a series of alloys based on Re-W-Ta-(B) were proposed as a material with adequate properties to resist molten metallic/oxide corium.

> This research expands the thermodynamic database for phase diagram estimation on this complex refractory system and its combination with SS constituents.

> Metallurgical characterization (Optical/Electron Microscopy, XRD and Vickers microhardness) along with corrosion testing will provide important information on the properties of this refractory alloy system and its phases.

261

Severe accident schematic and VULCANO facility
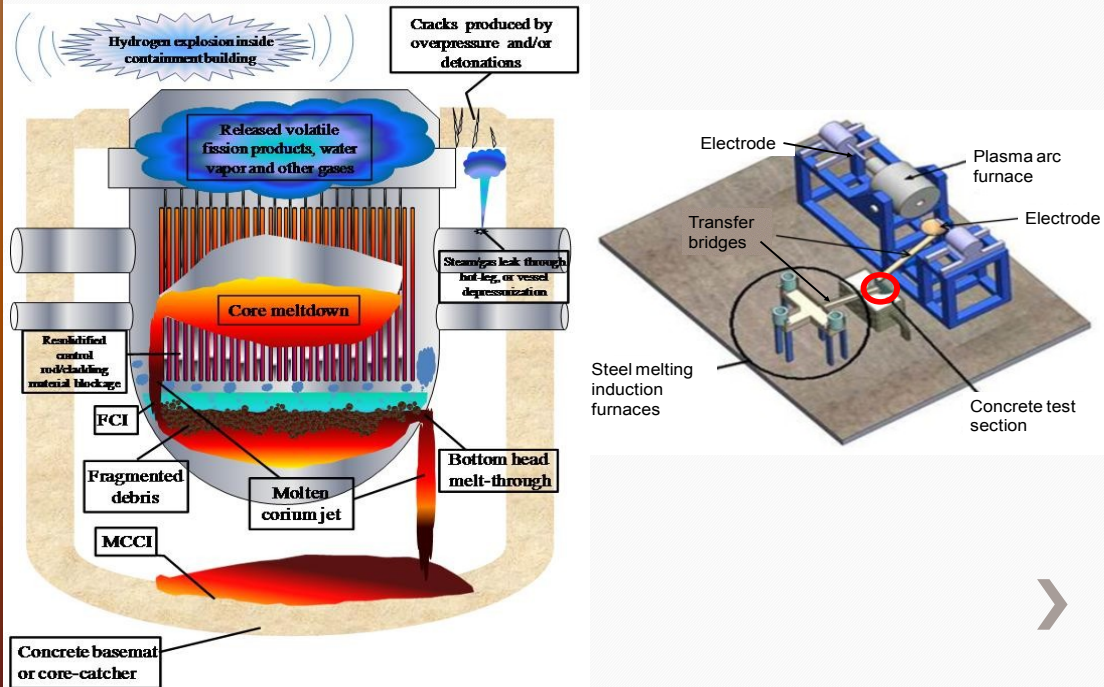
Metal-Carbon Eutectic Cells as High Temperature Fixed Points

Fixed point cells: Pure substances vs. Eutectics

» <u>Similarities</u>:
> Congruent melting/solidification temperature
> Fixed point availability in a large temperature range (~0.75 K to +3500K)

» <u>Issues at high temperatures</u>:
> As temperature increases, also the chemical reactivity of materials
> Pure substances are polluted by the crucible material above the copper point.
> Need to maintain a low uncertainty in temperature measurement (metrology).
> Planck's law extrapolation to high temperatures for blackbody (>2°C uncertainty).
> Materials emissivity is temperature/wavelength/surface/composition dependent.

» <u>Advantages of Metal-Carbon eutectics</u>:
> No contamination of fixed point material: crucible materials is part of the system (graphite).
> High repeatability of phase transformation point:
  + Thermal equilibrium <100mK in uncertainty (Metrology)
  + Non-equilibrium rapid heating/cooling ~ 3-5°C (Industrial)
> Numerous high temperature M-C eutectics systems, practical interpolation between the fixed points.

High Temperature Metal-Carbon Eutectics

rbon Eutectic Cells)

High Temperature Fixed Point Cells - Eutectic Details

M-C Eutectic Alloy	Cell Design	Cell Type	Hypoeutectic mass, grams	Hypoeutectic, wt.% Carbon	Metal Purity
Fe-4.3C	A	Pyro/TC	16.73	3.9	99%
Fe-4.3C	A	Pyro/TC	20.47	3.9	99.98%
Fe-4.3C	A	Pyro/TC	18.77	4.0	99.998%
Ti-0.4C	B	Pyro	20.30	0.4	99.995%
Co-2.6C	B	Pyro	8.60	2.0	99.998%
Mo-2.5C	B	Pyro	12.61	2.0	99.999%
Nb-1.5C	C	Pyro	5.28	1.0	99.8%
Ru-2.5C	C	Pyro	4.82	2.0	99.9%
Ru-2.5C	D	TC	9.99	2.1	99.9%
Re-1.3C	C	Pyro	13.89	1.1	99.999%
Re-1.3C	E	Pyro	12.10	1.1	99.999%
Co-2.6C	E	Pyro	4.80	2.0	99.998%
Ru-2.5C	E	Pyro	10.10	2.3	99.9%

HTFP Eutectic cells – VITI facility
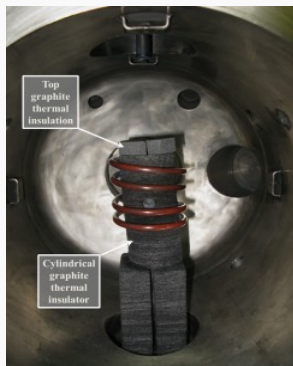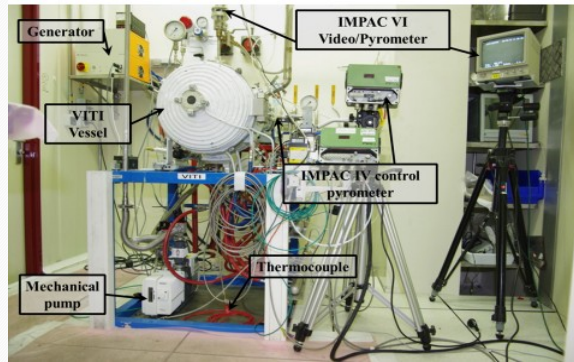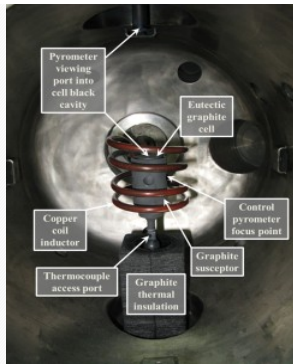
Iron – Carbon Eutectic Cells Results

Fe-C		Melting				Solidification				Eutectic
Test	Iron purity, %	Average heating rate, °C/min	Mean temperature μ, °C	Standard deviation σ, °C	Thermometer error, ±°C	Average cooling rate, °C/min	Mean temperature μ, °C	Standard deviation σ, °C	Thermometer error, ±°C	Ref. temp., °C
1st Pyro	99.998	59.0	1157.4	3.1	5.8	42.8	1127.5	1.8	5.6	
2nd Pyro	99.998	59.2	1143.6	0.4	5.7	42.2	1127.0	0.7	5.6	
3rd Pyro	99.998	70.1	1150.3	0.6	5.8	63.3	1144.0	0.5	5.7	
1st Pyro	99.98	59.0	1145.8	0.1	5.7	47.6	1140.3	0.1	5.7	1153
2nd Pyro	99.98	61.2	1139.7	0.4	5.7	38.7	1130.2	0.5	5.7	
1st Pyro	99	64.2	1144.3	1.5	5.7	40.8	1135.0	0.7	5.7	
2nd Pyro	99	56.0	1138.7	1.2	5.7	40.5	1121.1	0.3	5.6	

At least 99.99% purity should be used for the M-C Eutectic cell material

Cobalt – Carbon and Titanium-Carbon Eutectic Cell Results

Co-C	Melting			Solidification			Eutectic
Test #	Heating rate, °C/min	Mean temperature μ, °C	Standard deviation σ, °C	Cooling rate, °C/min	Mean temperature μ, °C	Standard deviation σ, °C	Reference temp., °C
1st	62-55	1324.7	0.5	23-210	1318.8	1.3	1324
2nd	50-207	1320.5	3.2	47-128	1302.0	2.2	
3rd	54-208	1327.0	1.3	53.0	1314.1	0.8	

Ti-C	Melting			Solidification			Eutectic
Test #	Heating rate, °C/min	Mean temperature μ, °C	Standard deviation σ, °C	Cooling rate, °C/min	Mean temperature μ, °C	Standard deviation σ, °C	Reference temp., °C
1st	52-71	1605.4	3.0	45-59	1599.2	4.1	1646.5
2nd	38-119	1604.7	3.6	61-143	1566.6	1.8	

Melting inflection point should be used for calibration.

Titanium is an oxygen scavenger!

Ruthenium – Carbon Pyrometry and Thermocouple Cell Results

Ru-C	Melting			Solidification			Eutectic
Test #	Heating rate, °C/min	Mean temperature μ, °C	Standard deviation σ, °C	Cooling rate, °C/min	Mean temperature μ, °C	Standard deviation σ, °C	Reference temp., °C
1st Pyro	56-167	1930.4	1.9	51-210	1914.7	4.7	1953
2nd Pyro	60-153	1928.9	3.3	39-211	1906.7	7.8	
3rd Pyro	40-179	1963.9	5.1	92-191	1924.6	3.5	

Ru-C	Melting			Solidification			Eutectic
Test #	Heating rate, °C/min	Mean temperature μ, °C	Standard deviation σ, °C	Cooling rate, °C/min	Mean temperature μ, °C	Standard deviation σ, °C	Reference temp., °C
1st TC	107-248	1921.8	2.3	99-267	1918.6	2.5	1953
2nd TC	106-188	1922.4	1.2	94-181	1921.1	1.9	

Melting point has higher reproducibility than thermometer error: ~15% sensor error!

Rhenium–Carbon Cell Results
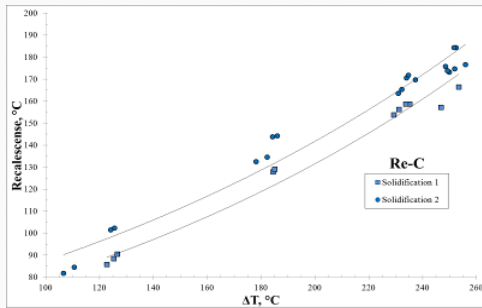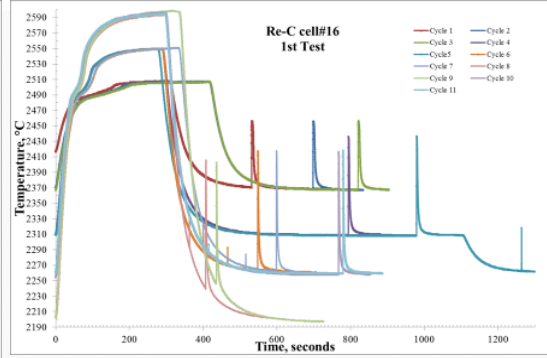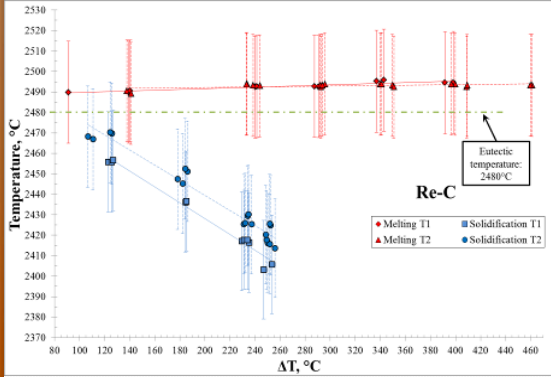
Re-C cell#16
1st Test

Re-C

- Melting T1
- Solidification T1
- Melting T2
- Solidification T2

Eutectic temperature: 2480°C

Re-C

- Solidification 1
- Solidification 2

Re-C	Melting			Solidification			Eutectic
Test #	ΔT, °C	Mean temperature μ, °C	Standard deviation σ, °C	ΔT, °C	Mean temperature μ, °C	Standard deviation σ, °C	Reference temp., °C
1st	91-398	2492.8	2.0	137-290	2429.0	19.3	2480
2nd	138-461	2493.0	1.2	129-359	2437.1	19.4	

Melting is less affected by heating rate than solidification by cooling rate.

Niobium-Carbon and Molybdenum-Carbon Eutectic Cell Results

Nb-C

- Cycle 1
- Cycle 2
- Cycle 3
- Cycle 4
- Cycle 5
- Cycle 6

Mo-C

- Cycle 1
- Cycle 3
- Cycle 4
- Cycle 5
- Cycle 6
- Cycle 7
- Cycle 8

Double recalescence
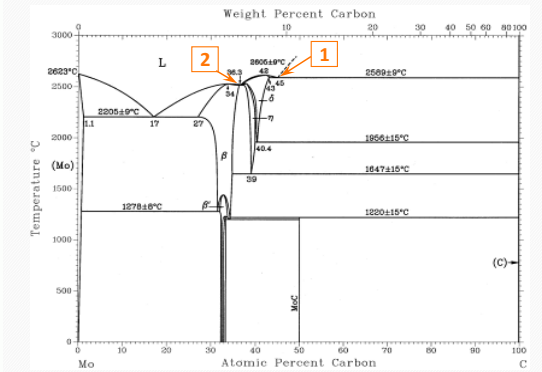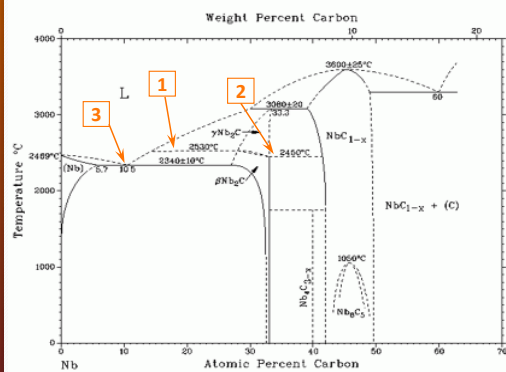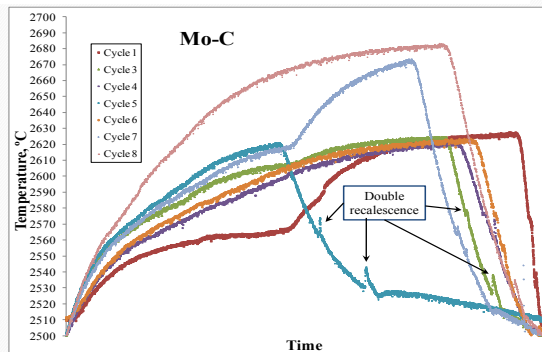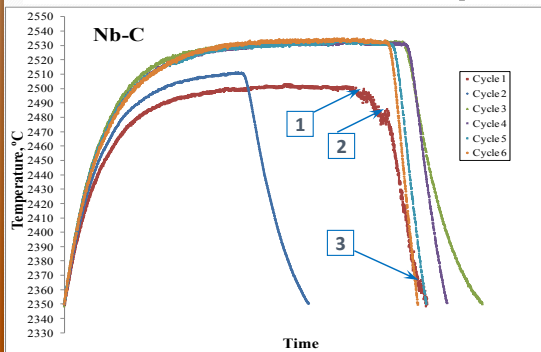
Metallography Niobium-Carbon and Molybdenum-Carbon
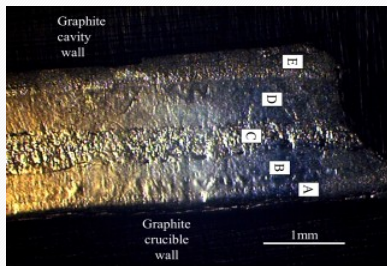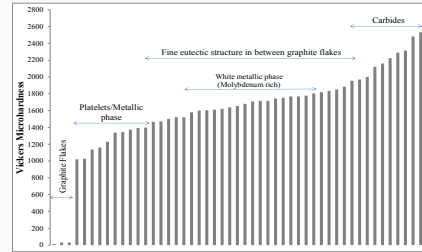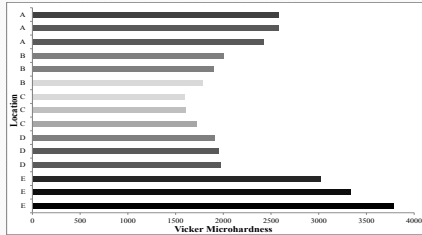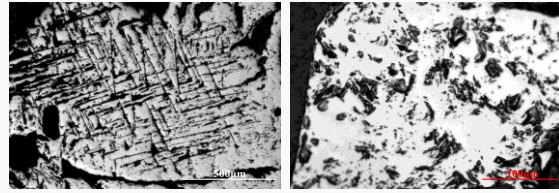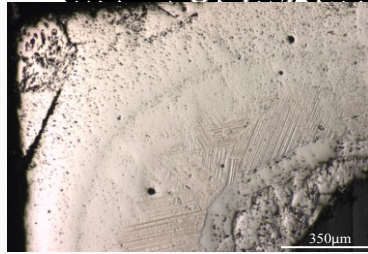
Complex eutectic systems should not be used as HTFP.
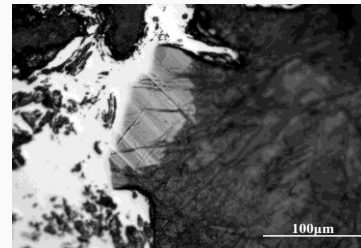
LNE-Cnam Reference cells vs. Developed cells

Cell	Melting mean temperature μ, °C	Melting Standard deviation σ, °C	Solidification mean temperature μ, °C	Solidification standard deviation σ, °C
Co-C (6Co3)	1324.00	0.10	1323.70	0.13
Ru-C (Ru2)	1952.85	0.15	1952.75	0.16
Re-C (4Re1)	2474.25	0.20	2474.23	0.21

Cell	Melting mean temperature μ, °C	Melting Standard deviation σ, °C	Solidification mean temperature μ, °C	Solidification standard deviation σ, °C
Co-C (c#18)	1323.97	0.14	1323.14	0.19
Ru-C (c#19)	1952.54	0.17	1951.65	0.21
Re-C (c#17)	2472.05	0.30	2470.77	0.42

Conclusions on the High Temperature Metal-Carbon Eutectic Cells

» Fe-C eutectic tests confirmed that impurities reduce the eutectic temperature. ≥99.99% purity recommended

» The melting temperature is less sensitive to rate changes than the solidification temperature. (Complex solidification kinetics). Melting inflection point should be used for calibration.

» Direct relationship between increase in heating ramp and increase in melting temperature (Co-C, Ti-C, Ru-C and Re-C tests). Similarly, as the cooling rate is increased the solidification temperature is decreased. (Non-Equilibrium transformation). Calibration heating rate<25°C/min. (If possible 5-10°C/min)

» Simple eutectic systems show better reproducibility than more complex systems containing carbides. **Among the systems studied Co-C, Ru-C, Re-C were selected as HTFP.**

> Simple eutectics systems: Binary metal-carbon eutectic system with a single eutectic and no solid state allotropes , carbides or metastable phases: **Pd-C, Rh-C, Pt-C, Ru-C, Ir-C & Re-C**

> Intermediate eutectic systems: Binary metal-carbon eutectic system with a single eutectic, along with an allotropic metallic phase or metastable carbide phases: **Fe-C, Co-C and Ni-C**

> Complex eutectic systems: Binary metal-carbon **di**-eutectic system comprising two eutectic points, one or several carbides, plus metallic or carbide metamorphism: **Ti-C, Zr-C, Hf-C, Nb-C, Mo-C, W-C and Ta-C**.

Achievements on the High Temperature Metal-Carbon Eutectic Cells

» Graphite cell design, furnace and test zone experimental configuration have significant impact on the reproducibility of the eutectic cells. (Better hot zone temp. homogeneity and smaller cell = better repeatability). Furnace effect>> eutectic deviation (10x)

» Various designs of graphite cells were successfully tested under high temperature ramps. This allowed for a significant reduction in cell size and eutectic material needed with improvements in performance.

» Three CEA pyrometer cells (Co-C, Ru-C and Re-C) have been calibrated by comparison with LNE-Cnam reference cells at their metrology facilities.

> Uncertainty around 1K (above 2000 K) in metrology lab (LNE) furnace

> Uncertainty around 2-5 K in applied lab (VITI) furnace

» Now there is the availability of in-house calibration of thermometers with HTFP. Which provides a mean to calibrate pyrometers that cannot be sent outside the PLINIUS platform due to their use in facilities were radioactive materials are manipulated. Calibration of "nuclear-grade" thermometers now available in PLINIUS facility!

Recommendations for future work

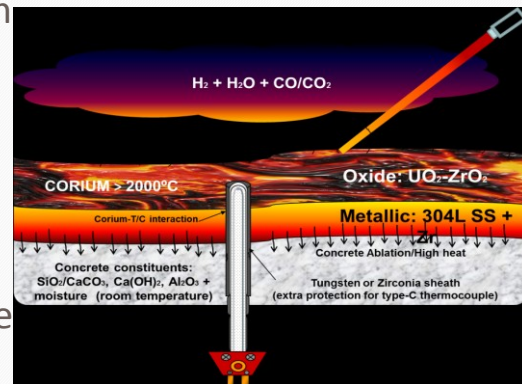» Metal-Eutectic Fixed Point Cells

> The eutectic graphite cell could be further reduced in size, while maintaining its performance, to render it more practical for utilization in-corium-melt

> To avoid damage to graphite cell thermowell, an inert material (ceramic coating?), or special thermocouple sheath, should be utilized between the thermocouple sheath and the graphite cavity to reduce chemical interaction, hence deterioration or failure of the TC/Graphite cavity.

> Thermowell eutectic cell single use for in-melt thermometry (presumably destroyed or contaminated). It should be pre-filled at least three times (for better TC thermalization) with the eutectic mix and characterized in VITI with a pyrometry looking inside the cavity (to measure the eutectic cells transition temperature and thermal behavior) to avoid inserting a TC and deteriorating the cavity.

> The melting temperature is more repeatable than solidification temperature, and should be preferred as reference point for calibration of thermometers. Nonetheless, if it is more practical, the solidification point can be utilized as reference point, even though it has relatively poorer repeatability than the melting point, but still the standard deviation is usually significantly less than the instrumental error. **Ru-C cell recommended as in-melt reference point for VULCANO MCCI experiments.**

Refractory Sheath Development for In-Melt Thermometry (Oxide/Metallic Corium)

Thermocouple sheaths

» Currently, Tungsten sheaths are used and can survive 2 hours in oxidic corium.

» Very rapid destruction in presence of steel. (Minutes!)
  > Impossible to reach reliable measurement

» Interest in tests with both oxides and metals to reproduce reactor case.

» Refractory metal alloys studied to improve TC survival in these aggressive pools.

$H_2 + H_2O + CO/CO_2$

CORIUM > 2000ºC

Oxide: UO_2-ZrO_2

Metallic: 304L SS +

Corium-T/C interaction

Concrete Ablation/High heat

Concrete constituents:
SiO_2/$CaCO_3$, $Ca(OH)_2$, Al_2O_3 + moisture (room temperature)

Tungsten or Zirconia sheath
(extra protection for type-C thermocouple)

Tungsten-bar test: 5 minute immersion in 200grs of superheated (2000°C) 304L SS

Before test

W- Bar

After test
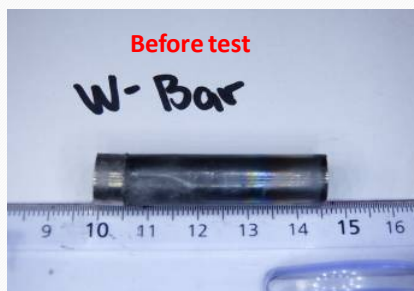
Zirconia crucible test: 80grs of 304LSS heated up to 2000°C over a 2-hour span

Fe-W

Atomic Percent Tungsten

$Fe_{79}W_{21}$

L

Temperature (°C)

Weight Percent Tungsten

Fe

W
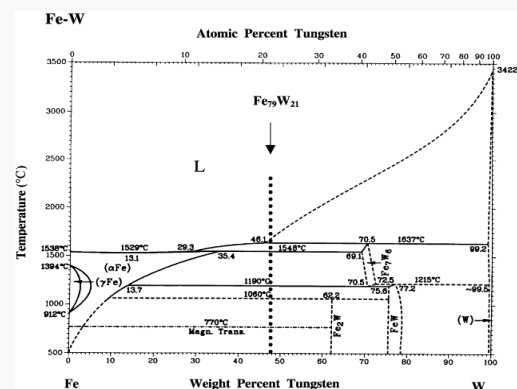
Refractory Sheath Development

- 🟡 Re-10W-10Ta-(0.1B) [Re1010(B)]
- 🔵 Re-25W-35Ta-(0.1B) [Re2535(B)]
- 🟢 Re-40W-20Ta-(0.1B) [Re4020(B)]
- 🔴 Re-05W-52Ta-(0.1B) [Re0552(B)]

Molar%
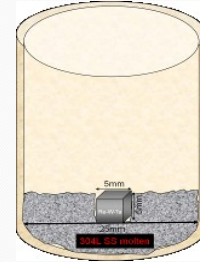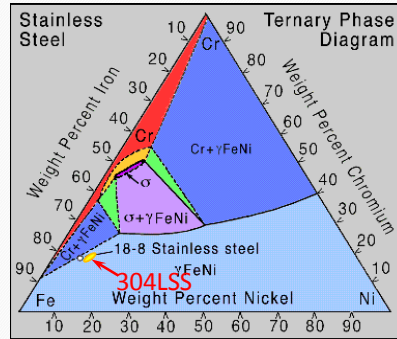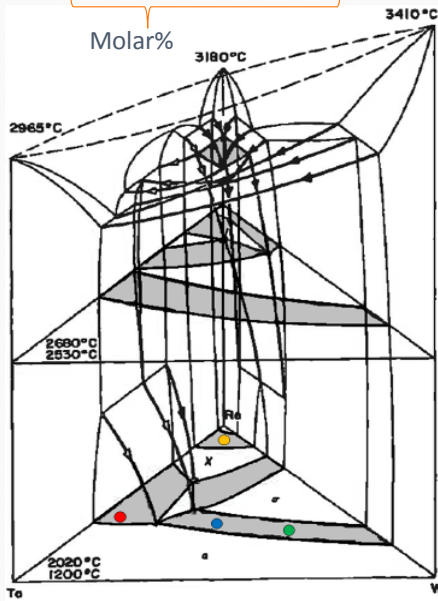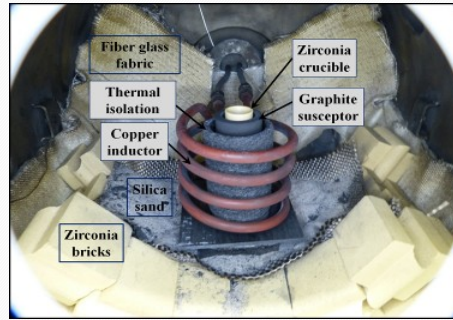
The alloys were fabricated at Ames Materials Lab part of the DoE, administrated by the Iowa State University.

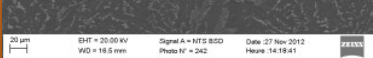# Refractory Sheath As-Cast Characterization
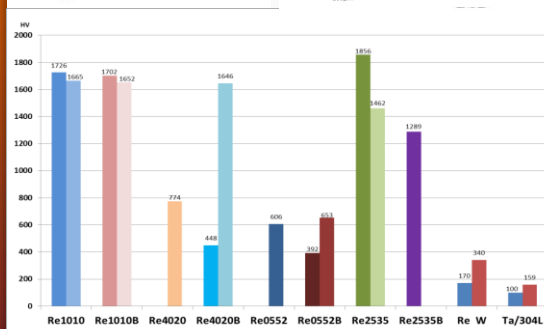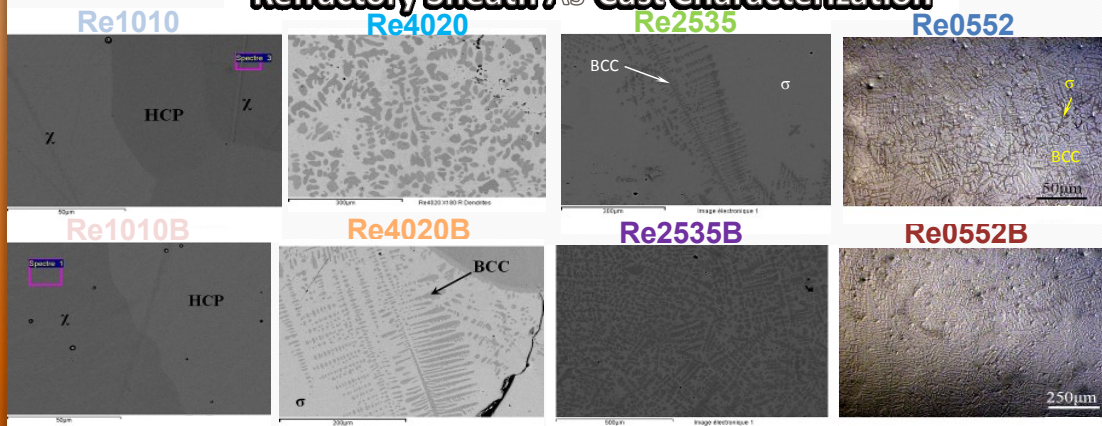
- •**OM/SEM** in **SE/BSD** mode along with **EDS** for chemical analysis.
- •**XRD** for phase identification and agreement with **SEM**.
- •**Vickers Hardness** insight on phase mechanical properties and phase id.

Non-equilibrium Solidification Curves of Samples submerged 30 minute in superheated Stainless Steel (5mins@2000°C)
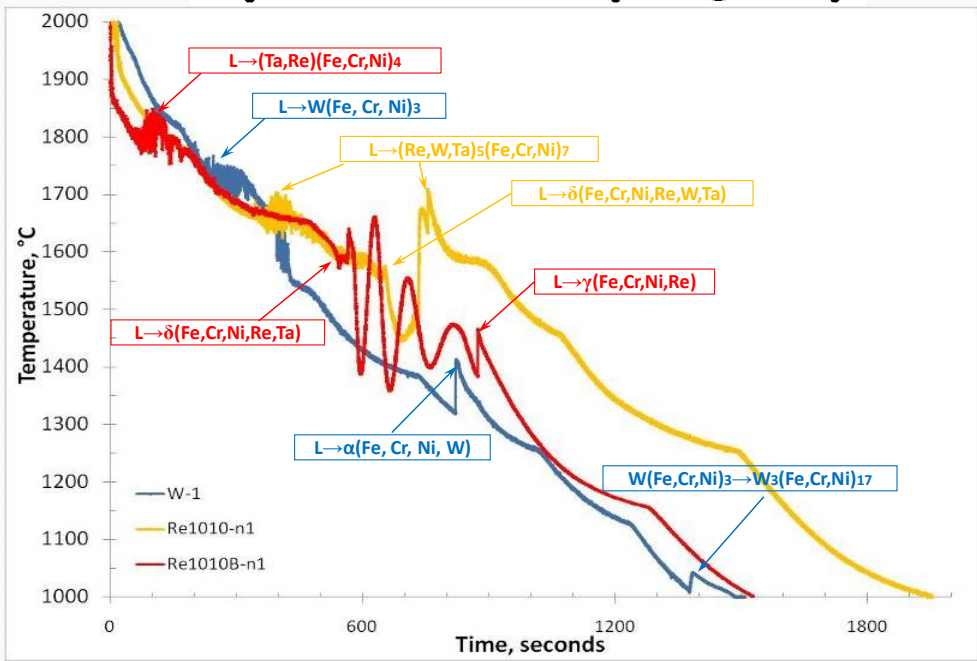
Post-test analysis

Post-test analysis
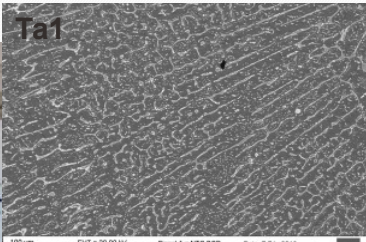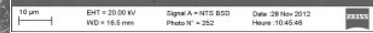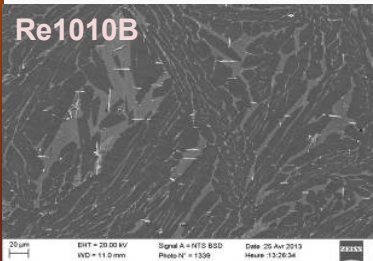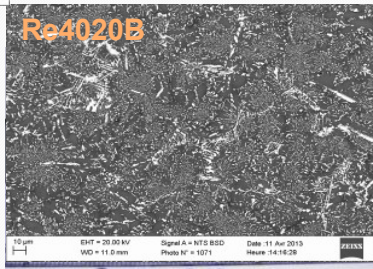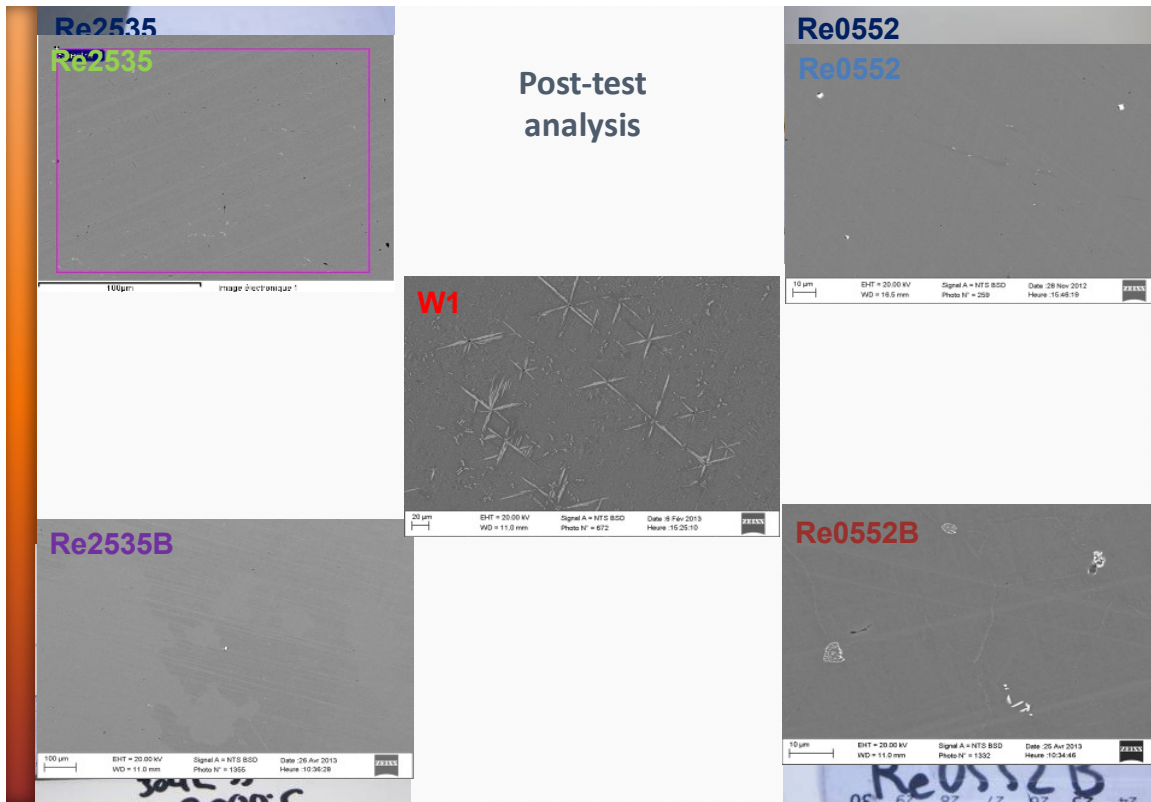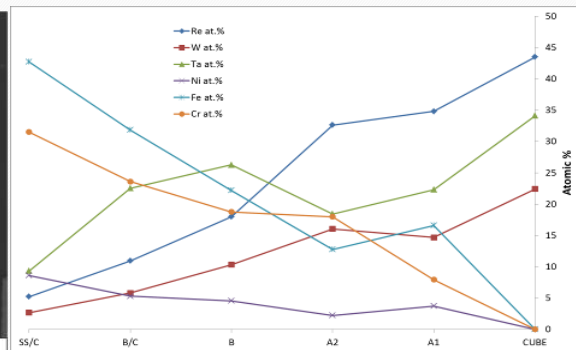
Refractory Sheath Corrosion in Molten Stainless Steel

Re2535B Test 9	Fe	Cr	Ni	C	Total Mass
Powder Mix in grams	158,7	100,1	37,0	3,8	299,6
Weight Percent	53,0	33,4	12,4	1,3	100,0

6-minute immersion in 300grs of superheated SS (1800°C): Corrosion rate ≈ 0.25mm/min.
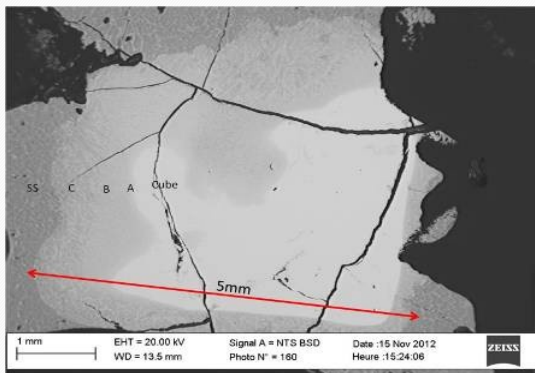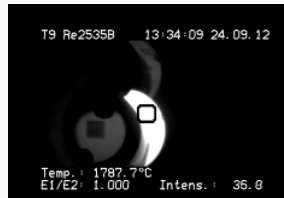
2535B Test 9: Post test SEM/EDS Analysis: X-Ray Maps

Image électronique 1 · Re La1 · W La1 · Ta La1 · Cr Ka1 · Fe Ka1 · Ni Ka1 · C Ka1_2
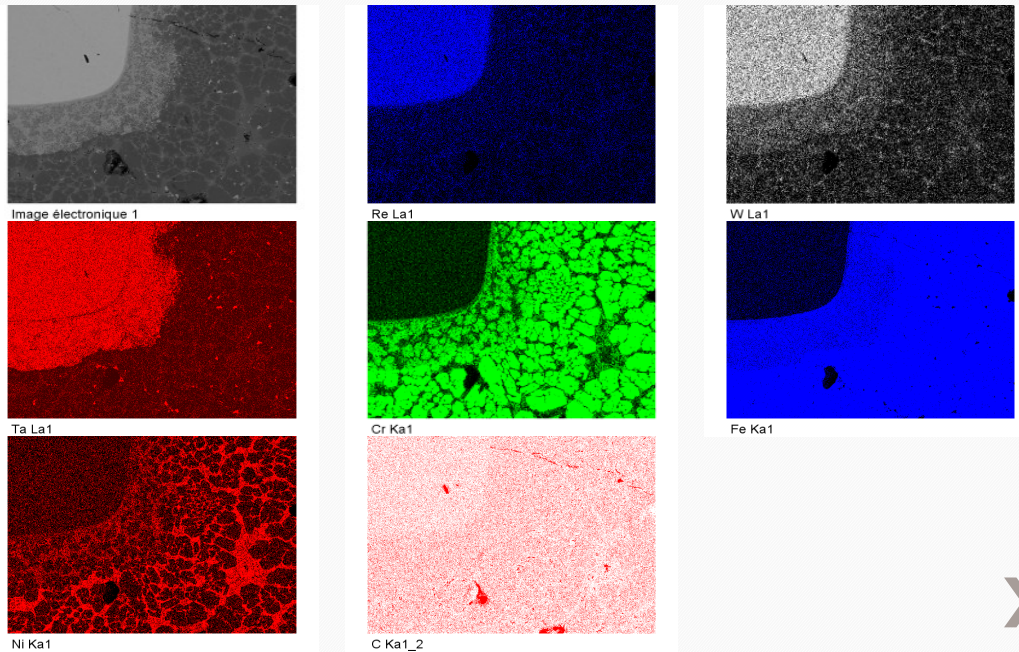
Conclusions/Achievements on the refractory sheath development

» Rhenium-rich and high Re-Ta alloys show better corrosion resistance, than W, Ta and the other alloys in molten 304L SS.

» Pure Tungsten and Tantalum show poor corrosion resistance in molten SS due to the formation of low temp. phases and eutectics.

» Boron additions improve the corrosion behavior, refine and homogenize the microstructure of the alloy.

» Re-10W-10Ta-0.1B showed the best resistance to molten SS attack ($\sim$100°C improvement over W-sheath) and It can be used <1850°C . Due to the formation of high temperature intermetallics with the 304L SS constituents.

» The complex oxide $(Ta,Cr,Fe,Mn,Ni)_2O_3$ is potential protective layer candidate.

» Characterization of the as-cast and post-test ingots will serve to improve the thermodynamic and phase stability data available on the Fe-Cr-Ni/Re-W-Ta system.

Other achievements

» Development and testing of an elevator systems, now available in VITI.

» After a lot of work, a mean to superheat stainless steel in VITI (at least up to 2000°C) was provided. This knowledge is now being applied by a current PhD student in LMA working on metallic phase oxidation during SA.

Overheating molten SS and containing it is a complicated task. Don't try it at home!!!

Recommendations for future work

» **Protective sheath for Corium In-Melt thermometry**

» Zirconia ceramic sheath could be used to protect the thermocouple during in-melt thermometry, a recommendation is to pre-heat the ceramic above its allotropic transformation temperature.

> The zirconia sheath should never be rapidly heated from room temperature.
> A moderate heating rate (~15°C/minute) up to about 1100 °C is acceptable.
> Between about 1100°C and 1300°C, a slower heating rate (7-8°C/minute) is preferred.
> Once the ceramic temperature exceeds 1300°C, every effort should be made to prevent it from cooling below that point. *(source: Zircoa)

» Re-10W-10Ta-0.1B showed the best resistance to molten SS attack (~100°C improvement over W-sheath). It can be used as a coating up to 1850°C (later phases of MCCI).

» Plasma spray coating the Re-W-Ta-B alloy on a Tantalum substrate (bar) for TC protection is an option (MSc Intern under C. Parga's tutelage).

» Improvements in alloy fabrication and processing are needed to reduce the alloys' brittleness and increase their fracture toughness. (Addition of alloying elements?)

Thanks for your attention…